**UNIVERSIDAD DEL PAÍS VASCO**
**EUSKAL HERRIKO UNIBERTSITATEA**

**ESCUELA TÉCNICA SUPERIOR DE INGENIERÍA DE BILBAO**
**BILBOKO INGENIARITZA GOI ESKOLA TEKNIKOA**

**PhD thesis**

# MODELIZATION AND ANALYSIS OF THE ELECTRIC ARC IN LOW VOLTAGE CIRCUIT BREAKERS

**PRESENTED BY**

Ms. Araitz Iturregi Aio

e-mail: araitz.iturregi@ehu.eus

**SUPERVISED BY**

Dr. Ms. Esther Torres Iglesias
Prof. Dr. Ms. Inmaculada Zamora Belver

2013

*"Insanity: doing the same thing over and over again expecting different results"*
Albert Einstein

# ACKNOWLEDGEMENTS

# Index of contents

# Index of Figures

# Index of Tables

# CHAPTER 1
## INTRODUCTION

1.1.- BACKGROUND
1.2.- AIMS OF THE DOCTORAL THESIS
1.3.- STRUCTURE

# 1  INTRODUCTION

## 1.1  BACKGROUND

In the last decades, electrical energy has become essential for the development and well-fare of industrialized societies. Energy consumption has been aligned with industrial development and nowadays it is impossible to think of anything else but an increase of this electrical demand during next years. In this context, the Power System is responsible for the supply, transmission and use of the electrical energy in an efficient way. Thus, maintenance and optimization of all its components is essential.

Among all the components, switching devices arise as important ones. A first analysis of these switching devices leads us to differentiate between circuit breakers (CBs) and fuses. Unlike fuses, which must be replaced after each use because of its rupture, CBs have reset property, which makes these devices a more attractive option.

The circuit breaker can be defined as an electrical device designed for interruption of the continuity of the current in fault situation and normal operation. Protection is focused on human beings safety and also to prevent an electrical circuit from the damage caused by overload or short circuits. The CBs can also be used to change the configuration of the network, attending to optimization needs or network reconfiguration.

All circuit breakers have common features in their mode of operation, although some details vary substantially depending on the voltage or current range the CB is intended for. For that reason, CBs are usually classified attending to the voltage level and the switching medium inside the chamber, as it can be seen in Table 1-1.

Table 1-1 Circuit breakers classification according to the voltage level and switching medium [1]

| Nominal voltage and type of circuit breakers | | | | | | | | | |
|---|---|---|---|---|---|---|---|---|---|
| Switching medium | Voltage [kV] | | | | | | | | |
| | <1 | 1 | 3 | 12 | 24 | 36 | 72.5 | 245 | 765 |
| Air | x | x | x | x | | | | | |
| Oil | | | x | x | x | X | x | x | |
| Compressed Air | | | | x | x | X | x | x | |
| SF6 | | | x | x | x | X | x | x | x |
| Vacuum | | x | x | x | x | | | | |

Among all these types of circuit breakers, this thesis is focused on Low Voltage Circuit Breakers (LVCBs) and their working base phenomena: the electric arc. LVCBs are understood as circuit breakers for voltage levels lower than 1 KV that use air as switching medium.

The operation of most LVCBs is based on the interruption of the electric current, establishing a long enough separation distance between the electrodes through a switching medium. During the process of contacts opening, this switching medium, generally gaseous, becomes conductive due to the high temperatures involved in the process, allowing the conduction of the electrical current through it. This process is known as electric arc. Thus, the basic technology for the current interruption in most LVCBs is characterized by the electric arc, which is a complex phenomenon where lots of physic interactions take place in a very short time.

The analysis of this electric arc has developed an increasing interest among the research community in the last years, due to its application not only in circuit breakers but also in welding arcs and fault arcs. Experimental results, new simulation models, and discussions and comparisons between simulation results and experiments are mainly being published [2].

## 1.2   AIM OF THE DOCTORAL THESIS

Due to the importance of LVCBs in the Power System, it is necessary they are reliable enough to prevent harmful conditions in the network. The main task and feature expected from a LVCB is the capability to commutate from a conductive state to an insulating one, as fast as possible, so that the possible harm in the network is minimized.

The ideal situation would be that the commutation happens instantaneously, but this does not occur in any real circuit. The time from the opening of the contacts to the extinction of the electric arc is crucial in this commutation process. In order that this commutation occurs as fast as possible, the disappearance of the electric arc must be fast. To achieve a fast disappearance, the arc voltage has to be increased in DC cases, or advantage of the zero current in AC cases must be taken. Thus, the operation optimization of LVCBs makes necessary a deep understanding of the electric arc phenomena itself and of its behaviour due to the design of the LVCB.

This knowledge can be achieved by means of either modelization and simulation tools or experimental tests. The advantage of simulation option is that it allows obtaining the evolution of physical magnitudes, which would be difficult to measure in laboratory tests. Also, with this option, it is cheaper and easier to change and test new cases, without the necessity of manufacturing new prototypes for each new arrangement.

The aim of this doctoral thesis has been to develop a new model for analysing the electric arc. This simulation model has been designed using ANSYS CFX, a Finite Volume Modelization (FVM) commercial software. The defined model is applied to simulate the behaviour of a LVCB under different conditions, simulating changes that can lead to its optimization and better understanding. This way, this new model is useful to analyze the effect of several simplifications or hypothesis in the arc phenomenon that have to be taken into account in the design process of LVCBs.

Finally, for the model's verification, real experimental tests have been carried out at Technical University of Ilmenau in Germany.

## 1.3   STRUCTURE OF THE DOCTORAL THESIS

This thesis is structured in 7 chapters. This first chapter introduces the background and aims of the thesis as well as the structure of the document.

The second chapter is focused on the electric arc phenomena. The full processes of the arc formation and maintenance are described. Also, properties during the interruption and extinction processes for DC and AC currents, in air, are analyzed.

In the third chapter, a description of the main characteristics of LVCBs is developed. This way, the existing types are shown, as well as the most relevant elements for their design and definition.

Before the new model developed in this thesis is presented, the fourth chapter includes a state-of-the-art of the electric arc modelization in LVCBs. Three main modelization groups are described: black box models, models based on graphics and diagrams, and physical models.

After that, the new model is explained in chapter 5, which does not include all possible aspects included in the real electric arc, as the work ahead in this research field is still long, but it does include some improvements regarding the reference model taken [3], such as: no simplifications due to unreal symmetry planes, finer mesh definition, full magnetic field calculation with vector potential formulation, more realistic approach for radiation with the application of the P1 model, etc. Besides, different input currents, number of splitter plates, arc ignition positions, or geometry changes have been considered in the optimization analysis. The necessary steps, parameters and considerations for its implementation in the software tool are described.

Once the new model has been presented, the sixth chapter describes the validation and verification processes used to justify the reliability of the presented model. The verification has been accomplished to study discretization errors and selecting the most appropriate mesh density and timestep for the correct operation of the computational model. Besides, discretization errors have been used to carry out a comparative analysis between three radiation models. Out of that, the most appropriate one has been selected for the presented simulation model. The validation has been achieved by an experimental setup carried out in collaboration with Technical University of Ilmenau (Germany) in its laboratory. In the experiments, an electric arc has been ignited in a prototype of a simplified LVCB chamber, for different input currents and geometries. The results have been used to prove the validity of the new proposed model.

Finally, the seventh chapter gathers the conclusions drawn from the research work developed in this thesis and proposes future research areas that could be explored to continue the work initiated in this thesis.

The thesis is completed with a list of references of previous works, upon which the research effort has been based, as well as an Annex containing additional data from the study cases and their results.

# CHAPTER 2
## ELECTRIC ARC PHENOMENON

# 2 ELECTRIC ARC PHENOMENON

## 2.1 INTRODUCTION

Electric arc phenomenon is an increasing trending topic in the research community due to its wide application in the industrial field. Circuit breakers, welding, arc furnace and several industrial applications are based on it. Regarding LVCBs, the scope of this thesis, although some non-conventional interruption techniques have been also developed, most of the manufacturers still base their interruption devices on the electric arc operation. Therefore, it is necessary to study this phenomenon in order to achieve improvements in the design of the LVCBs.

The electric arc is a complex phenomenon. A high number of physical phenomena interact during its formation, maintenance and interruption, in a very short time. Fluid dynamics, electromagnetic and thermal problems have to be taken into account. In LVCBs, where the interruption medium is air, the electric arc is formed once the air has been ionized and converted into plasma, becoming this way conductive. Thus, the electric arc has its own electrical, magnetic and thermal characteristics that no other electrical conductors have.

This chapter describes the processes leading to the appearance of the electric arc and the processes originated in circuit breakers when the separation of the electrical contacts is initiated, which allows the flow of electric current through the circuit. Likewise, it describes the structure of the electric arc, as well as its properties. In addition, aspects affecting the maintenance and arc extinction are introduced.

## 2.2 GENERAL ASPECTS OF THE ELECTRIC ARC

### 2.2.1 FORMATION AND MAINTENANCE OF THE ELECTRIC ARC

Formation of the electric arc depends mainly on the separation of the circuit breaker contacts, the applied current and the ionization of the insulating medium. When the separation of the contacts starts, the electric arc appears and maintains if the temperature in the circuit breaker chamber is high enough to ionize the isolating medium, if the current is enough to melt and volatilize the metal and if the distance between the electrodes is high enough to hold the arc.

The value of the current is important at the beginning of the circuit breaker contacts' separation. If the current is low, the rise in temperature is not enough to provoke the melting and volatilization of the metal and only a spark is originated. However, beyond a certain limit, the temperature reached exceeds the melting and volatilization limit of the metal, determining that the spark becomes conductive and an electric arc appears.

During the opening process of the electrical contacts, the insulating medium (air, vacuum or SF6) becomes conductive, allowing the circulation of electric current through an electric arc. Gases at ambient temperature behave as insulating mediums because atoms and molecules are electrically neutral. It is necessary the presence of ions and free electrons in the gas to behave as conductor, i.e., it must be at ionized state. The ionization degree depends on several factors, such as temperature, pressure and gas ionization potential. At ambient temperature, the kinetic energy of gas molecules is insufficient to produce their dissociation by colliding with each other. However, raising the gas temperature, and hence the kinetic energy of molecules, they can acquire sufficient energy to cause their dissociation and even provoke the gas ionization. This way, the gas evolves to the plasma state.

Plasma is another state of aggregation for material, like solid, liquid and gas. By increasing the temperature of a solid, the kinetic energy of molecules exceeds the energy required to maintain the solid state, turning to liquid. If temperature continues rising and sufficient energy is communicated to molecules in the liquid, to overcome Van der Waals forces, the liquid becomes a gas. A subsequent increase in temperature provides sufficient energy to individual molecules to dissociate into their constituent atoms and produce their ionization, appearing electrons and positive ions, reaching what is known as plasma or fourth state of aggregation of the material [4, 5].

As an example, nitrogen dissociates into its constituent atoms (N2→2N) about 5000 K and ionizes (N→N++e-) above 8000 K. Similarly, SF6 is approximately dissociated at 1800 K and ionized at temperatures between 5000 and 6000 K [6, 7].

By increasing the temperature, as shown in Figure 2-1, the degree of dissociation and ionization of the medium increases and thereby the number of charge carriers and the conductivity of the electric arc.
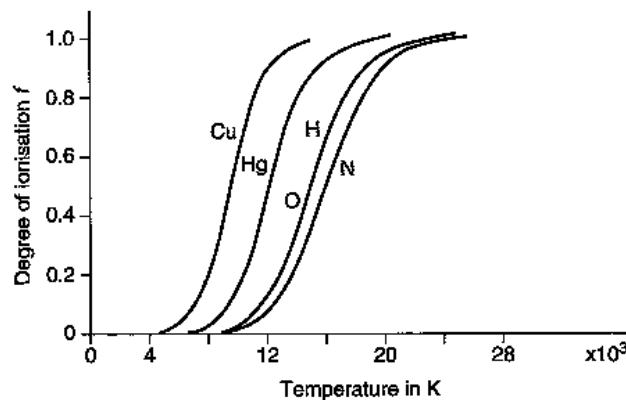


Figure 2-1 Thermal ionization degree of several metal vapour and atomic gases [7]

The thermal ionization described above must be distinguished from the ionization by collision. In this case, the ionization is caused by electrons accelerated by an electric field, acquiring much higher speeds than from thermal agitation, corresponding to thermal equilibrium state of the medium and oriented in the electric field direction. In a circuit breaker both ionization processes occur.

With the beginning of the arc between electrodes, sufficient electrons are released from the cathode. The movement of these electrons from the cathode to the anode causes the ionization of the medium. This ionization causes a quick appearance of additional electrons that enables the arc maintenance. Thus, each electron emitted is multiplied in number, deriving energy from the environment to the arc. The electrons are accelerated and the energy acquired in this way is transferred to the gas, when colliding with its atoms and molecules. Thus, in the arc, the gas is not heated from the outside but by the power released in the arc itself.

Due to the strong ionization, the arc behaves as a conductor, being the electrical conductivity of the plasma column in the range of 10-100 S/cm, depending on the temperature. Figure 2-2 shows that for main gases used in circuit breakers, such as hydrogen, nitrogen or SF6, the electrical conductivity clearly increases with the temperature.
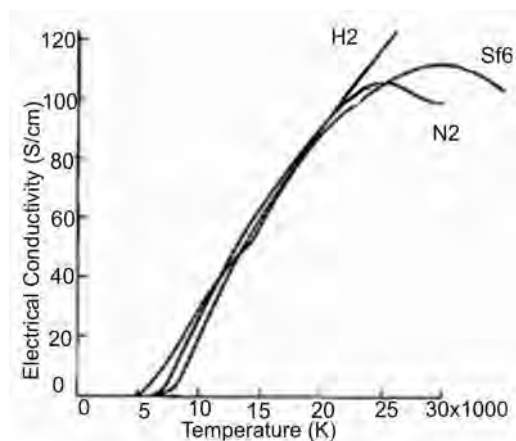
Figure 2-2 Influence of the temperature on the electric conductivity [4]

This way, the electric arc is formed by a plasma column consisting of ions and electrons from the inter-contact medium and metal vapours from the electrodes. Physically, the arc appears as an incandescent gas column with an approximately rectilinear trajectory between electrodes, whose core reaches temperatures between 6000 and 10000K.

Three different regions may be distinguished in the electric arc: the central arc column and the anode and cathode regions, at both ends (Figure 2-3). The regions adjacent to the contacts are transition areas between the gaseous conductor constituted by the arc column, which has a variable conductivity, and the solid conductor with an essentially constant conductivity.
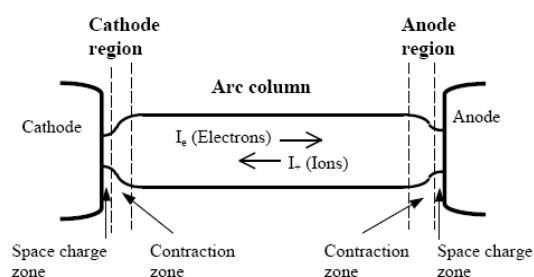


Figure 2-3 Electric arc structure [7]

The plasma is considered to be very close to thermal equilibrium when the speed of energy transmission from the environment to the plasma is reduced, compared to the energy exchange that takes place between the particles themselves. Then, all molecules, ions and electrons have the same temperature. By contrast, at the beginning of the arc and when it is about to extinguish, the energy exchange between the arc and the environment becomes comparable to the internal energy exchange. Thus, the thermal equilibrium is broken for those instants.

Parallel to ionization, recombination of oppositely charged particles occurs leading to neutral particles. The ionization by collision which takes place throughout the permanence of the arc is balanced by recombination of ions and electrons produced continuously, along and inside the ionic-electronic plasma. For possible recombination of these particles, they must remain close to each other enough time. Therefore, recombination occurs more easily at low temperatures, for which speeds are also reduced.

Finally, at thermal equilibrium, the ionization ratio equals the recombination ratio, so that the number of charge carriers is constant and the arc can be self-maintained. Accordingly,

one way to achieve the arc extinction is to produce the cooling of the plasma, since this action promotes recombination of particles and reduces the degree of ionization and the conductivity of the arc plasma.

## 2.2.2  CHARACTERISTICS OF THE ELECTRIC ARC

Probably the main characteristic of the electric arc is a decreasing voltage-current property, totally different from the one presented by metallic conductors. In a metallic conductor, voltage is proportional to current, being the V-I characteristic a straight curve. In contrast, voltage between arc electrodes decreases when current increases up to a limit value. This behaviour is explained by the increase of the temperature with the arc current, which intensifies ionization. This way, the conductivity of the medium increases and consequently the arc voltage decreases.

Thus, for small currents the arc voltage has a decreasing V-I characteristic with constant power. However, as the current increases the arc voltage adopts a substantially constant value, independent of temperature. For high values of current, the maximum temperature of the arc, about 20000K, tends to be limited by radiation heat transfer, so the electrical conductivity has an approximately constant value and the column responds to the change in the current only by varying the cross section.

As an example, Figure 2-4 shows the current-voltage characteristic of a DC arc for a given arc length and copper electrodes. According to this curve, the gradual increase of the current leads to a very sharp decrease of the arc voltage at first and a slower after, getting almost a constant arc voltage value for further increases of the current.
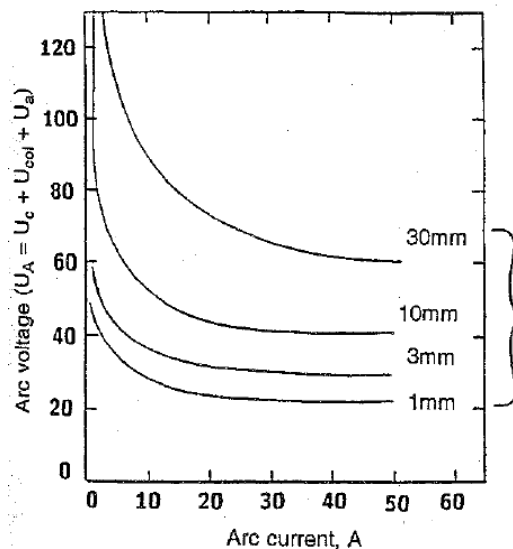


Figure 2-4 Current-voltage characteristic for a DC arc between copper contacts [8]

If the change of the current over time is reduced, the current-voltage characteristic is called static characteristic. On the other hand, when the current changes quickly over time, it is called dynamic characteristic. If the current flowing through the arc changes suddenly, the arc voltage does not take the value corresponding to the new current value according to the static characteristic, but according to the dynamic characteristic (Figure 2-5).
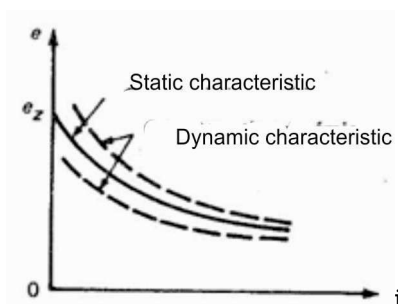
Figure 2-5 Static and dynamic characteristic [4]

This behaviour is due to the thermal inertia of the arc, as the arc conductance cannot respond instantaneously to changes in current but experiences a delay together with the arc voltage. This delay also depends on the frequency of the current. This effect is observed in Figure 2-6, which shows the variation of the arc voltage with current, for different values of frequency. At low frequencies (f1), the static characteristic of the arc is obtained.

In this situation, the speed of the current variation is very small and the arc voltage is able to adjust to the new instantaneous value of current. On the contrary, for high frequencies (f4), the arc behaves as a linear resistor and the arc can adapt to the new current value. Frequencies f2 and f3 correspond to intermediate situations. In the case of the industrial frequency (50 or 60 Hz), as the time constant of the arc is much smaller than the duration of a half cycle, the arc voltage tends to remain constant during each half cycle, with an increase of the arc voltage only near the zero current.
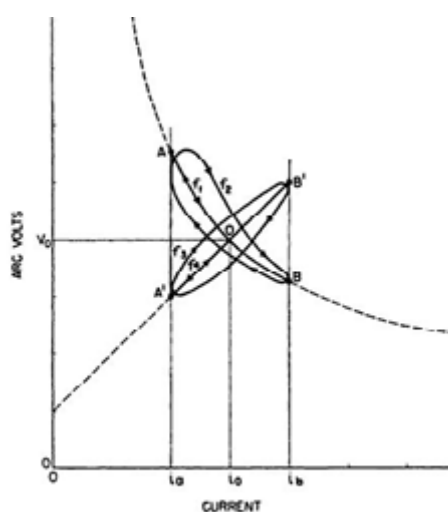


Figure 2-6 Dynamic characteristic of the arc with frequency (f1 < f2 < f3 < f4) [8]

For AC cases, the voltage-current characteristic and voltage and current curves of the arc, corresponding to copper and carbon electrodes in air, are shown in Figure 2-7 and Figure 2-8. As noted, there are different curves for the increasing current and the decreasing one. This difference is due to the thermal capacity of the electrodes and the arc gas. At points "a" and "d" the arc is ignited and at points "c" and "f" the arc is extinguished. Furthermore, the higher heat carrying capacity of metal electrodes causes the difference between the two branches to be smaller in the case of copper electrodes.

(a)                                          (b)
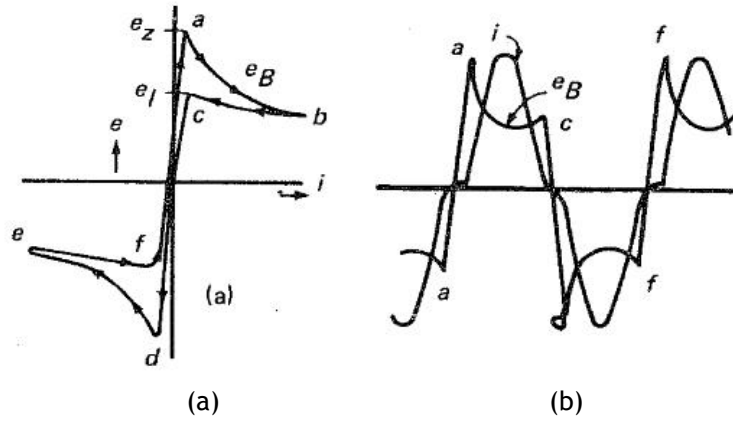
Figure 2-7 (a) Voltage-current characteristic and (b) current and voltage waveforms of an AC arc between carbon electrodes in air [4]



(a)                                          (b)
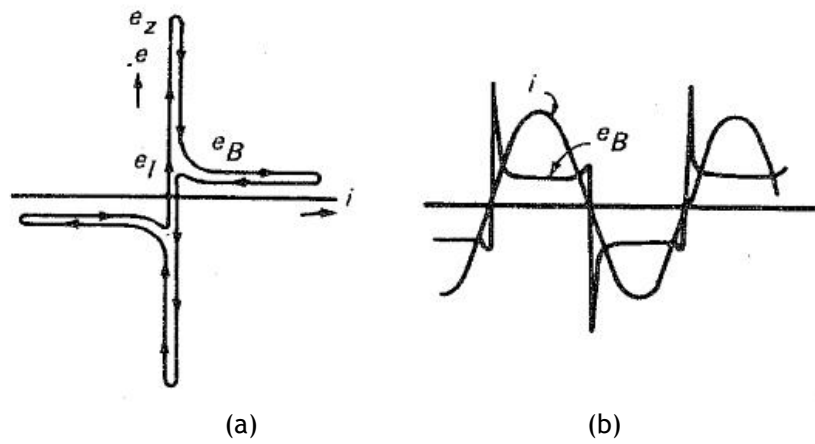
Figure 2-8 (a) Voltage-current characteristic and (b) current and voltage waveforms of an AC arc between copper electrodes in air[4].

Another important characteristic of the electric arc is the arc voltage. The distribution of the voltage drop along the arc is not linear, but in the proximity of the electrodes there is a significant voltage drop (8 to 20 V at the cathode and 1 to 12 V at the anode) [8], being considerably smaller and proportional to the length in the central area, corresponding to the arc column (Figure 2-9).
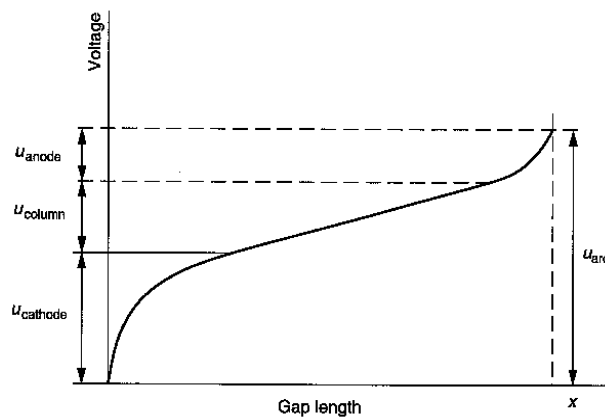


Figure 2-9 Arc voltage drop [7]

These three regions, cathode, arc column and anode, have different characteristics. Thus, the voltage drop behaves also in a different way on them:

- The cathode region is full of metal vapours from cathode, with a lot of positive ions and a small number of electrons. Thus, this region is characterized by the existence of high electric field (108-109 V/m [8]) and temperature values, as well as by a higher current density than in the arc column, due to the smaller section. Therefore, cathode provides electrons from the material, which are accelerated by the high electric field existing in the cathode region, reaching enough energy to ionize other neutral particles.

  Depending on the material, refractory and non-refractory cathodes can be distinguished. In the case of refractory materials with high boiling point (carbon, tungsten, molybdenum and zirconium), electron emission is produced by heating the material below the evaporation temperature (thermionic emission). The current densities obtained with this type of cathodes are around $10^4 A/cm^2$. The use of refractory materials in combination with good conductors, such as copper or silver, shows reduced erosion characteristic when the arc happens.

  In contrast, non-refractory materials cathodes with low boiling points, such as copper, experiment a significant evaporation of the material. Electron emission in these materials occurs by the effect of the high electric field in the proximity of the electrode surface (field emission). In this case, the range of typical values for current density is around $10^6$-$10^8 A/cm^2$.

- In the arc column, the current flow is mainly due to the displacement of electrons, resembling to the metallic conduction phenomena. This zone contains an excess of positive ions which neutralize the charge of electrons and allows high currents under small voltage drops. Ions are directed towards the opposite electrode, accumulating in the nearest zones and causing the voltage drop observed in Figure 2-9. These voltage drops correspond to the appearance of intense fields capable of giving sufficient energy to the ions to keep the electrodes incandescent and cause the release of new ions.

  The voltage drop along the arc column is characterized by a uniform longitudinal voltage gradient, with voltage values from few V/cm to several hundreds of V/cm. The voltage gradient in the arc column depends on the arc current and the energy exchange with the environment. The increase in the arc current leads generally to an increase in the diameter so that the section of the arc tends to be automatically adjusted.

- Finally, in the vicinity of the anode, as a result of the rejection of positive ions and the attraction of electrons, there is a negative space charge that causes a sharp voltage drop, called anodic drop. Anode may be passive or active, depending on whether it acts as collector of electrons coming from cathode or provides ions to the arc column due to the evaporation of contact material. In general, the current density is significantly lower than the one in the cathode area and, similarly, a constriction occurs in this region of the arc.

Therefore, the total voltage drop in the arc, $U_{arc}$, can be expressed as (2-1).

$$U_{arc} = U_{anode} + U_{column} + U_{cathode} \tag{2-1}$$

Likewise, the energy absorbed by the arc column is given by (2-2).

$$W = I_a \cdot U_{column} \cdot t \tag{2-2}$$

where:

$I_a$:    arc current

$U_{column}$: voltage drop in the arc column
t:        time

This energy is converted into heat and dissipated to the atmosphere by conduction, convection and radiation, and if the arc is developed in oil, SF6, etc, the dissociation of the fluid surrounding the arc will be also produced. This heat is transmitted to the environment being achieved temperatures in the arc between 7000K and 25000K, depending on the medium and the configuration of the circuit breaker. If the energy developed by the arc is not dissipated properly, the temperature of the medium will increase. This way, in a confined medium the inner pressure will rise, which may lead to new phenomena of decomposition and cause the explosion of the arc chamber.

The molecular dissociation level of the medium, diffusion of ions and molecules, conductivity and thermal capacity of electrodes, as well as the type and physical conditions of the environment surrounding the arc, have a great influence on the heat dissipation intensity, and on the temperature and pressure of the arc column. For example, a high thermal conductivity and an improvement in the cooling conditions of the arc area will decrease the voltage drop for a constant current [4].

Other characteristic properties of the electric arc that also vary with temperature are viscosity and thermal conductivity, as can be seen in Figure 2-10 and Figure 2-11. Figure 2-10 shows that viscosity increases for the three gases shown, $H_2$, $N_2$ and SF6 between 0 and 15000K, while from 15000K it decreases. It can be also appreciated that the highest values are obtained for $N_2$ and SF6, while $H_2$ shows the lowest ones.
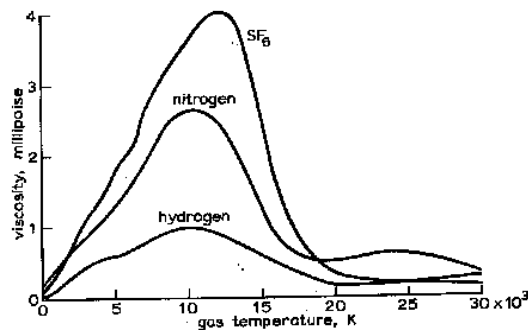


Figure 2-10 Influence of the temperature on viscosity [6]

Regarding the variation of thermal conductivity, Figure 2-11 shows the behaviour of different gases, being $H_2$ the most conductive one.
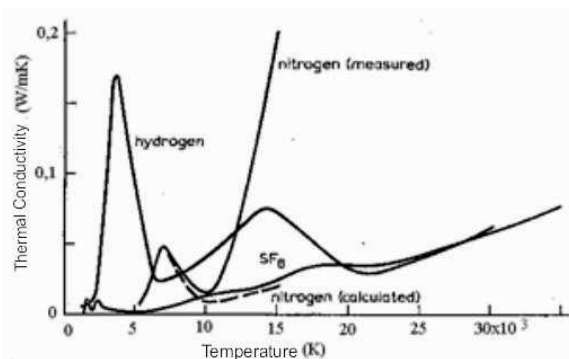


Figure 2-11 Influence of the temperature on thermal conductivity [4]

## 2.3    INTERRUPTION OF THE ELECTRIC ARC

Operation of circuit breakers is generally based on the modification of the arc plasma conductivity, mainly by means of temperature control. Thus, interruption of the circulating current is based on arc cooling. However, there is one important difference between the interruption of DC and AC currents. In case of AC, the current passes through zero every half cycle, so the aim is to modify quickly the arc conductivity in the vicinity of the zero current. In contrast, DC current does not change its polarity, so it must be forced to zero. In the analysis developed in this thesis, DC current has been considered.

### 2.3.1    DC INTERRUPTION

When the contacts start to separate, the current does not disappear instantaneously but it keeps flowing through the arc established between contacts. As it has been said, DC current interruption has the disadvantage that there is no natural zero current, so it has to be forced to zero. It is also necessary to provide a mean to dissipate the magnetic energy stored in the circuit, whose value is $(1/2)LI^2$.

The behaviour of a DC circuit, with inductive nature, can be represented in a simplified way by equation (2-3).

$$E = L\frac{dI}{dt} + RI + U_A \tag{2-3}$$

where:
E:       source voltage
R:       resistance
L:       inductance
$U_A$:    voltage through the CB contacts

Rearranging this equation, (2-4) is obtained.

$$\frac{dI}{dt} = \frac{1}{L}[(E - RI) - U_A] \tag{2-4}$$

Additionally, before opening the contacts, the conditions shown in (2-5) exist.

$$E = RI \ \rightarrow \ I = \frac{E}{R}$$

$$U_A = 0 \tag{2-5}$$

At the beginning of the arc (t=0), the term dI/dt takes the value –$U_A$/L, which indicates that current initially decreases. However, if at any time the term (E-RI) is equal to $U_A$, the value dI/dt is zero and the decrease in current stops, reaching the arc a steady state (Figure 2-12).
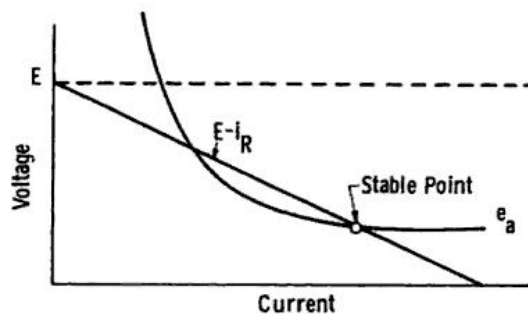


Figure 2-12 Establishing a stationary arc in a DC circuit [4]

To interrupt the circuit, the value of $U_A$ has to be greater than (E-RI), so that the current can decrease with time. Therefore, the arc voltage has to be greater than the voltage of the power supply, to force the current to zero. This is possible because the arc voltage does not depend on the system voltage, but on the characteristics of the arc. Figure 2-13 shows the general behaviour of DC circuits, where two curves are differentiated:

- $U_{A1}$ curve cuts the line E-RI at two points, so there are two points where a stationary arc can be established.
- $U_{A2}$ curve corresponds to a continuous decrease of the current up to its extinction as it is all the time above the curve E-RI.
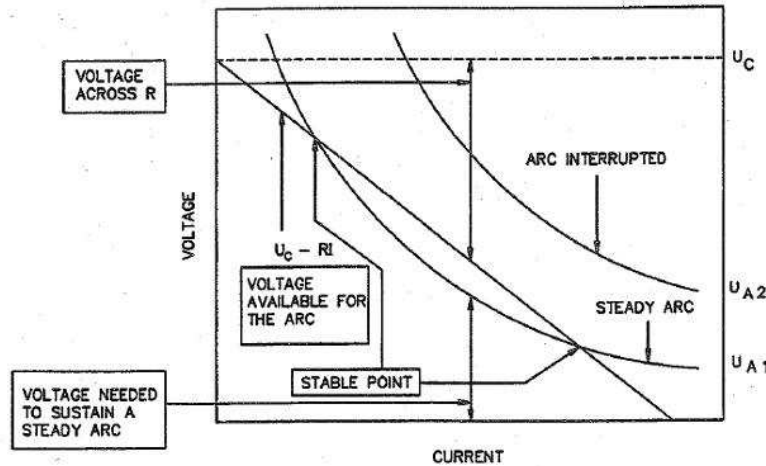


Figure 2-13 DC circuits interruption [8]

The increase of the arc voltage can be achieved by several ways such as: lengthening the arc, increasing the pressure in the medium or cooling the arc.

## 2.3.2   AC INTERRUPTION

The interruption of AC currents is facilitated by their zero crossing, twice per cycle, being only necessary to prevent the reignition of the arc after the zero crossing of the current.

If the circuit breaker is able to separate the contacts at the moment of zero current and does it with such a high speed that voltage between contacts cannot bridge the gap between them, the circuit is interrupted. Besides, as the electromagnetic energy is zero when current passes through zero, there is not any overvoltage between contacts.

However, circuit breakers currently available have an opening time at least higher than 0.02s (one cycle). Therefore, except in the case of very weak currents or very low voltages, the interruption of the current always takes place through an arc [9].

## 2.4   INTERRUPTION OF THE ELECTRIC ARC IN AIR

As exposed in Table 1-1, there are different interruption technologies based on the interruption medium. The main interruption techniques currently used are [10]: Interruption in air (LV), in vacuum (MV) and in $SF_6$ (MV and HV).

This section is focused on the interruption technique in air, because it is the technique used in LVCBs (analyzed in this thesis).

The use of air as an insulating medium has the following advantages: there is a constant renewal, it maintains its dielectric properties and the cost is zero. As a drawback, the slow speed of recombination of electrons and ions after the zero current may be mentioned.

Figure 2-14 shows some arrangements of interrupting devices used in LV. These devices cause an increase of the arc voltage and facilitate its cooling, being suitable for interrupting DC and AC currents. Thus, the increase of the arc voltage is obtained by lengthening the arc, using guiding elements in divergent arrangement (a), insulating plates (b), confinating and elongating the arc (c), or enhancing the cooling action by using materials with high thermal capacity that decompose into gases due to the temperatures reached during the arc (d). Finally, a method widely used in low voltage applications is illustrated in Figure 2-14(e), in which the arc is directed to a set of ferromagnetic plates (splitter plates or deion plates) whose purpose is to divide the arc into an amount of arcs in series. The formation of new anodic and cathodic regions, with its corresponding minimum arc voltage, allows increasing the arc voltage at higher rates than other methods and leads to achieve a voltage around 30 V in each partial arc, depending on the current and geometry.
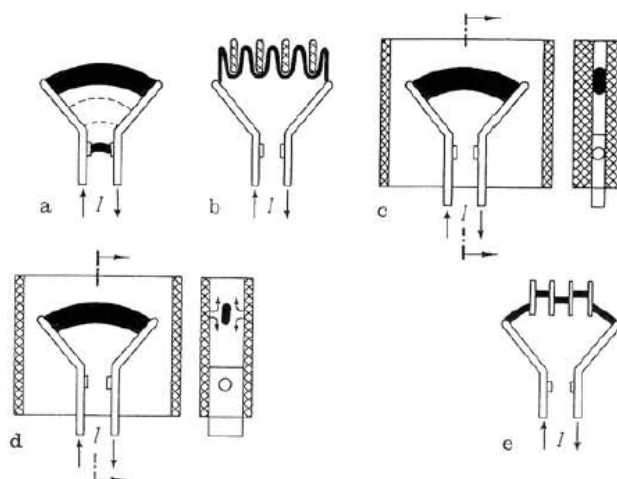
Figure 2-14 LV interrupting arrangements used in air: (a) lengthening of the arc, (b) arc lengthening using insulating plates, (c) confination and lengthening of the arc, (d) high thermal capacity materials and (e) arc division by splitter plates [8]

The mentioned options will be explained in the next chapter, where characteristics of low voltage circuit breakers are exposed.

## 2.5   CONCLUSIONS

Electric arc is the basis of many industrial applications. Thus, it is important to understand the behaviour of this complex physical phenomenon in order to improve the performance of the devices where the phenomenon is involved.

The formation of the electric arc in a circuit breaker is due to the conduction of the electrical current through the interruption medium, air for low voltage. This conduction starts when the contacts of the circuit breaker separate and it must be extinguised to interrupt the electric current effectively.

An important factor in the appearance and maintenance of the electric arc is the temperature of the medium, as the conduction itself is under the influence of the temperature, due to the ionization of the gas. When the temperature of the medium is high enough, the dissociation of the gas is achieved and the switching medium becomes into

plasma, i.e., a conductive medium. Also, other properties of the arc, as electrical conductivity, thermal conductivity and viscosity, are strongly dependant on the temperature.

Among the characteristics of the electric arc, the static and dynamic current-voltage properties for DC and AC and the arc voltage drop have to be highlighted.

Regarding the current-voltage characteristic, the voltage decreases as long as the current increases. Therefore, the behaviour is opposite to the metal conductors' current-voltage characteristic. Besides, the electric arc has a remarkable thermal inertia, so it may be differentiated between static and dynamic characteristics, depending on the current change ratio. In the case of slow change of current, the voltage drop will follow the change and we can talk about static characteristics, but if the change is fast, the voltage drop will have a delay due to the thermal inertia of the arc and so dynamic characteristics must be taken into account.

The voltage drop in the arc is another very important feature, as it is directly related to its extinction. This arc voltage is divided in three zones: anode, cathode and arc column. The highest voltage drop appears at cathodic and anodic zones.

Additionally, in a DC circuit, the extinction is achieved when the arc voltage is greater than the source voltage. In contrast, for AC currents, the natural zero current helps for interruption but reignition must be prevented for effective extinction.

Considering the special characteristics of the electric arc with DC currents, LVCBs that work with DC are analyzed in this thesis. However, not only a deep understanding of the phenomenon itself is necessary but also a good knowledge of the devices.

# CHAPTER 3
## LOW VOLTAGE CIRCUIT BREAKERS

# 3   LOW VOLTAGE CIRCUIT BREAKERS

## 3.1   INTRODUCTION

Circuit breakers are important devices in the Power System for safety and security of the system and human beings as well as for grids reconfiguration. In this sense, for a faster and more reliable current interruption when faults or other undesirable situations occur, it is important to have reliable devices. Among those devices, LVCBs are used in multiple applications.

For the improvement of these devices, modelling is a useful technique in order to analyze the most influential parameters in the current interruption. This option allows to optimize their performance, without the necessity of building and testing numerous and costly prototypes. However, considering this option, a deep knowledge of the devices, their components, working principle and influence of each part and parameter is necessary.

Thus, this chapter describes the existing CBs for current interruption in LV, explaining their principle of operation, interruption technologies and physical description of their components. Furthermore, the most relevant aspects of the influencing factors in the behaviour of LVCBs are shown, for several of their components, such as the arc chamber or electrical contacts. In particular, the geometry of the splitter plates used in the arc chamber, the number and arrangement of those plates inside the chamber, as well as the material used for its manufacturing have been identified as relevant in the behaviour of the arc chamber. In the case of electrical contacts, the material used in their manufacture is identified as an important factor in their performance.

However, it should be noted that the high specificity of the subject and the confidentiality of company data due to competition between companies cause that very limited published literature exists for LVCBs design details [11].

## 3.2   INTERRUPTION TECHNOLOGIES IN LVCBs

Different current interruption techniques exist for LVCBs that in general are based on the formation and extinction of an electric arc. The circuit breakers that follow this interruption technique have a similar layout in the design and structure, even though some differences exist. This way, the general layout of a conventional LVCB can be seen in Figure 3-1, including the following components:

- Fixed and movable conductors: part of the circuit breaker that keeps the circuit open or closed.
- Fixed and movable contacts: where the electric arc is formed when these contacts separate physically.
- Arc chamber and splitter plates stack: it is constituted by several plates, arranged in parallel between them. The aim is to split the arc in smaller arcs, in order to lengthen and extinguish it. In some references, the arc chamber is also known as arc chute.
- Terminals: to connect the circuit breaker with the electrical circuit.

Even though all circuit breakers have in common the above presented characteristics, some details vary substantially depending on the nominal voltage or current. In the following section, further differences and components of those LVCBs are exposed, as well as different interruption technologies. A review of the interruption technologies for LVCBs leads to a

coarse classification into three groups: conventional CBs, current limiter developments by static-rupture and a third group of new configurations of switches still under research [12].
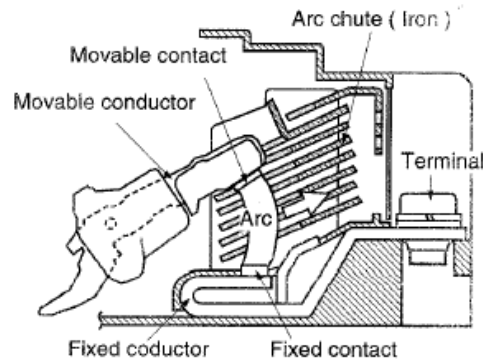


Figure 3-1 LVCB and main components [13]

### 3.2.1 CONVENTIONAL LVCB

Among conventional LVCBs, Miniature Circuit Breaker (MCB), Molded Case Circuit Breaker (MCCB) and Low Voltage Power Circuit Breaker (LVPCB) types can be found. Conventional CBs generally use air for current interruption. Though they differ in some details and components, the general construction of these CBs (Figure 3-2) includes: the main contacts designed to carry the current under normal operating conditions, the arcing contacts (also called rails) and the arc chamber. In many cases, the geometry of the current carrying parts produces a magnetic force that moves the arc into the chamber. This way, some designs use coils for increasing the magnetic force, while others help the arc by blowing air.
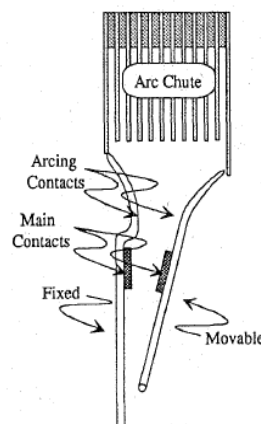


Figure 3-2 LV magnetic air switch [12]

The typical sequence in a LV conventional air circuit breaker is the following:

- The main contacts open while the arc contacts remain closed.
- The arcing contacts open and the arc starts to move along their length.
- The magnetic force produced by the arc current or by blowing coils moves the arc to the arc chamber.
- The arc is divided into several small arcs in series, by the plates of the arc chamber.
- The arc chamber allows cooling the arc, lengthening and narrowing its section until the current is interrupted.
- The arc chamber enables the ionization products to be dissipated or absorbed, restoring the dielectric strength in the air space between the contacts.

The conventional LVCBs described establish the arc in the interrupting medium, air in most LV switches, and maintain it until the next natural zero current for AC cases or until the voltage drop of the arc rises above circuit's voltage for DC cases. Then, the arc is extinguished.

Once the general aspects of LVCBs have been presented, each type of LVCB is analyzed in detail in the following subsections: MCB, MCCB and LVPCB. Although all of them have the previously described characteristics, there are differences between them regarding their design and operation.

### 3.2.1.1  Miniature Circuit Breaker (MCB)

Miniature Circuit Breakers (MCB), Figure 3-3, are widely used for domestic, commercial and small industrial installations, with voltage supply between 200 and 500V. The current to interrupt cannot be higher than 100A and the interruption characteristics are not usually adjustable. Generally, they are provided with thermal or magnetothermal devices and the housing cannot be opened to develop any maintenance of the device.



(a)                              (b)
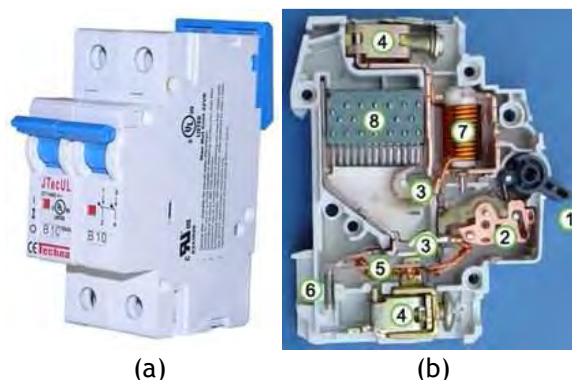
Figure 3-3 (a) MCB general view and (b) MCB components

The MCB is connected to the circuit by the terminals (4) (Figure 3-3) (b). These terminals are connected to the contacts (3). In normal operation conditions, the current enters from one of the terminals and flows through the closed contacts (3) to exit through the other terminal. In case of overload, the bimetallic strip (5) is heated, and converting that thermal change into a mechanical displacement the actuator mechanism (2) which forces the contacts (3) to pull apart is unlatched. In case of a fault, this separation of the contacts is also helped by the solenoid (7) that increases the pulling force as the current increases, causing instantaneous opening of the circuit. After that, the electric arc that appears after the separation of the contacts, moves to the splitter plates stack (8) for its lengthening and extinction. The opening of the contacts is visualized externally by the handle (1) whose position indicates the status of the circuit breaker (On/Off). Finally, after the circuit breaker is assembled, the manufacturer is able to adjust the trip current of the device by the calibration screw (6).

### 3.2.1.2  Molded Case Circuit Breaker (MCCB)

Molded Case Circuit Breakers (MCCB) can interrupt currents up to 2000A, so they are bigger than MCBs. Additionally, this device allows to adjust the interruption current (Figure 3-4). The operation principle is also thermal or magnetothermal and the components are located inside an insulating molded case. These devices are designed in order not to be opened for maintenance, so the contacts cannot be replaced.
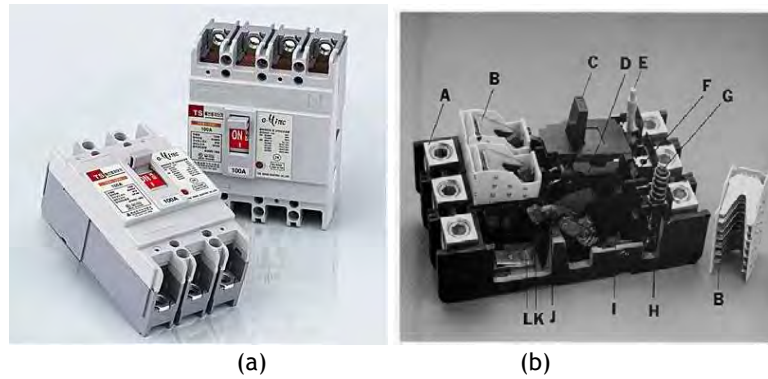
(a)                                    (b)
Figure 3-4 (a) MCCB general view and (b) MCCB-components [14]

The MCCB is connected to the circuit by the terminals (A), shown in Figure 3-4 (b). At normal operation conditions the moving contact (K) and the fixed contact (L) are closed and the current flows through them. Once the current of the circuit is higher than the adjusted trip current level (G, E), the bimetallic strip (I) is heated and pushes the operating mechanism (D) which forces the moving arm (J) and moving contact (K) to open. The order to interrupt all live conductors is given by the common trip bar (F), when any pole trips. Helped by the electromagnetic coil (H), the arc travels to the splitter plates (B). The handle (C) is used to manually trip and reset the circuit breaker and it also indicates the status of the circuit breaker (On/Off).

### 3.2.1.3  Low Voltage Power Circuit Breaker (LVPCB)

Low Voltage Power Circuit Breakers (LVPCB) have a bigger size than the previously exposed ones and their admissible short-circuit current range is around 6000A, higher than in the other types. So, the complexity of the device also increases. The interrupter itself is removable from its outer shell and the current carrying parts are accessible for inspection, maintenance and replacement (Figure 3-5 (a)). They use electronic devices for the current interruption.
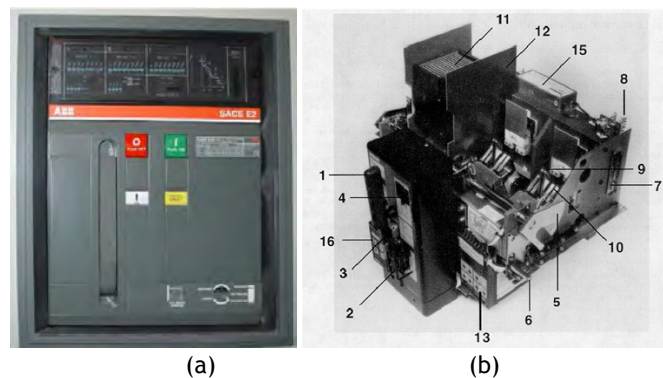


(a)                                    (b)
Figure 3-5 (a) LVPCB general view and (b) LVPCB components [14]

LVPCBs have several components to close and open the housing (2, 3 and 4) and extract the interrupter from it (5, 6 and 7). The handle (1) shows the status of the circuit breaker (On/Off) and allows tripping and resetting the circuit breaker manually. In case of overcurrent, first the principal contacts (9) are opened, helped by the disconnection set (8) and after the arcing contacts separate (10). The current is measured by an electronic component (13) and a current sensor (14), as the voltage is measured by a voltage sensor (15). The current flows to the splitter plates stack (11) physically separated by a barrier (12).

## 3.2.2  STATIC RUPTURE

Advances in power electronics have allowed the development of static rupture circuit breakers in the last years. This rupture technique, based on semiconductors properties, could present an option for the future of the electric arc as interrupting method.

Properties of semiconductors are much closer to the ideal circuit breaker than the electric arc. The value of the electrical resistance in a semiconductor material depends on the current direction. When the current flows in the conventional direction, from anode to cathode, the resistance value is very small, while in the opposite direction resistance is infinite. In an AC circuit, a change in the current polarity appears every half cycle; therefore a change in the resistance value of the semiconductor material is produced. In [12], the developments in this field are shown. It can be highlighted the simultaneous use of vacuum interrupters and thyristors GTO (Gate Turn-Off) for applications in 400V networks (Figure 3-6). The operating principle is based on the simultaneous opening signal sent by the overcurrent relay to the vacuum breakers and excitation of the GTO devices. The electric arc between the contacts of the vacuum breaker creates an arc voltage that commutates the current in the GTO, which up to this moment was ON. Thus, the vacuum interrupters recover their dielectric strength and the GTOs change to OFF state.
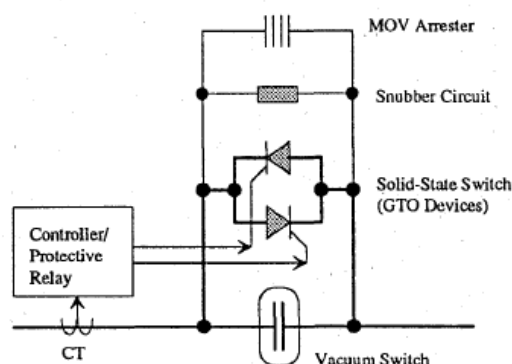


Figure 3-6 Vacuum and GTO thyristors breaker scheme [12]

The main advantages of this interruption technique include:

- Ideal ruptures without switching overvoltages
- No wear out
- Possibility to predetermine the characteristics of the circuit breaker
- Small power consumption in the current interruption

The big disadvantage is the very low thermal inertia of semiconductors. Due to this low thermal inertia, this application must be accompanied by a temperature control system of the GTOs. Besides, higher ohmic losses in normal operation, need of cooling of solid state devices and no galvanic disconnection are also disadvantages of these electronic interruption techniques. Moreover, a rated current of approximately 100A can only be used, due to the high induced voltage peak obtained due to the short interruption time. However, it can be an interesting option due to their performance at high load density and the possibility of replacement of multiple current-limiting fuses.

A key for the success of this interrupting technology, still under research, lies in the total interruption time, which is around 0.5ms.

### 3.2.3   OTHER CONFIGURATIONS

Other interruption techniques, not including the static rupture or electric arc, have been also developed.

One of those approaches consists on including polymeric current limiters in the LVCBs. Figure 3-7 presents a possible configuration, based on the previously presented static rupture with GTOs, where a PTC thermistor made from conductor polymeric material is included. This configuration avoids the need for a temperature control in the GTOs.
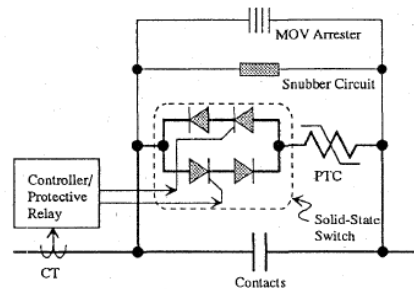


Figure 3-7 GTO and PTC based technique [12].

Another approach is presented in [13], where a current limiting technique called ISTAC (Impulsive Slot Type Accelerator) developed for MCCBs is presented. It consists of a new arc chamber designed with a J-shaped fixed conductor, composed by an organic polymer, which gets a higher magnetic flux density. This design produces a higher magnetic force that pushes the arc into the chamber, getting a bigger free space in the arc chamber so that control devices can be included. The fixed contact has a slot where the movable contact moves.
Figure 3-8 (a) shows the characteristics of the chamber and Figure 3-8 (b) shows the movement of the current during the interruption process.
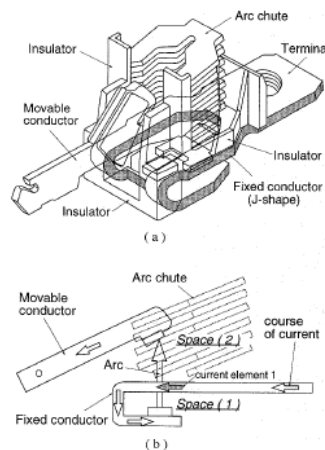


Figure 3-8 (a) ISTAC arc chamber characteristics and (b) movement of the current during the interruption process [13].

### 3.3   INFLUENCE OF THE LVCBs' COMPONENTS IN THE INTERRUPTION PROCESS

The aim of this section is to expose the most influential components of the circuit breakers in the development and extinction of the electric arc. The components analyzed have been the arc chamber and the electrical contacts, due to their influence in the movement and final extinction of the arc. These components have been taken into account in the new model developed in this thesis.

## 3.3.1  ARC CHAMBER

Regarding the arc chamber, the most influential factors are the geometry, quantity and arrangement of splitter plates, as well as the material they are made of. In general terms, [15] provides a guidance for the characteristics required by the set of splitter plates.

First, to facilitate the formation of the main arc enough separation should be provided between the contacts and the plates (3.2 to 4.7mm). Furthermore, the thickness of the plates cannot be very small to avoid melting, as a result of heat generated by the arc (1.4 to 2.4mm). Neither must be they placed very close to each other, to prevent welding of adjacent plates (1.3 to 1.6mm). Additionally, different thicknesses can be used for the plates, although the thicker plate should be located next to the opening contact.

As for the appropriate number of plates, this aspect varies with the space available and depends on the application. For circuit breakers with voltages up to 600V it is recommended to use at least 10 to 12 plates (for a contact separation of 25.4mm), while for circuit breakers or contactors with interruption capacity of 20kA at 4800V, around 50 to 60 plates should be used.

Finally, the metal coating used in the plates has to be considered, being nickel the most effective according to literature [15].

### 3.3.1.1 Geometry of the splitter plates

This subsection presents the results of several researches that analyze the effect of the splitter plates' geometry in the electric arc extinction. As previously exposed, the use of metal plates, located inside the arc chamber, has the aim of dividing the arc into smaller arcs. This allows increasing the arc voltage and facilitating its extinction, while a cooling effect is also developed by the plates.

In general, the use of a ferromagnetic material in the manufacturing of the plates distorts the magnetic field generated by the arc, producing the appearance of a magnetic force that attracts the arc toward the region of the plates. Figure 3-9 shows the operating principle.
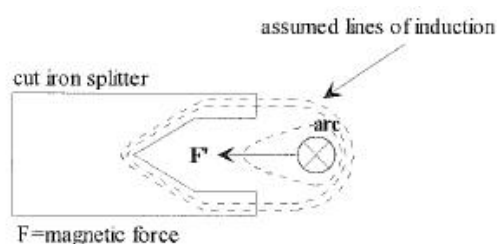


Figure 3-9 Operating principle of ferromagnetic plates used in arc chambers [8]

The distribution of the magnetic flux density and magnetic force that appear on the arc varies depending on the position of the arc. As an example, Figure 3-10 shows the magnetic field distribution obtained for different positions of the arc, regarding the plates.
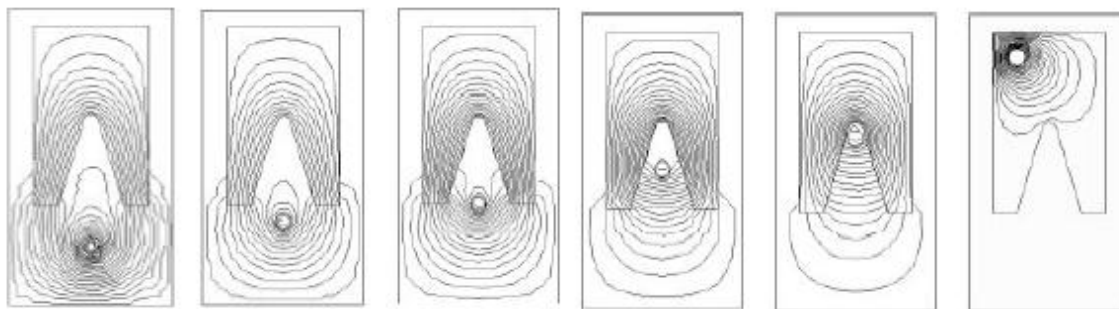
Figure 3-10 Magnetic field distribution for different positions of the arc [8]

Furthermore, the shape of the plates has also a great influence on the distribution of the magnetic flux density and on the magnitude of the force acting on the arc. Thus, the use of "V-shaped" plates (Figure 3-11) increases the attraction force on the arc by a factor of $[(360°/\alpha)$ -1], in comparison with the use of flat plates [8].
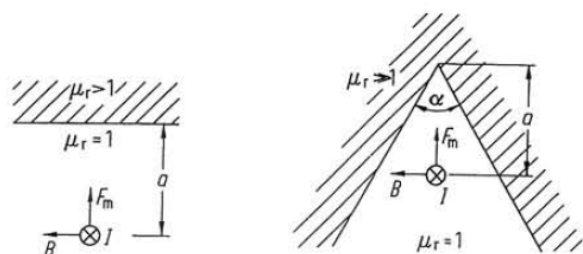


Figure 3-11 Magnetic force on the arc due to the presence of ferromagnetic material [8]

Therefore, the general practice is to use V-shaped plates or similar configurations, as shown in Figure 3-12. Typical values obtained for the magnetic field are in the range of tens of mT, by kA of arc current [8].
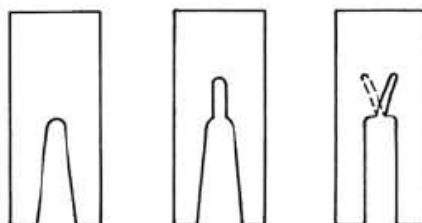


Figure 3-12 Plates for LVCBs [8]

Another example of the influence of the shape of the splitter plates on the electric arc behaviour is presented in [16], where the behaviour obtained with ferromagnetic rectangular plates (grey colour trends) and V shaped ones (black trends) is compared. In Figure 3-13 some results are provided: in (a) current and voltage are shown, in (b) the optical recordings of the movement of the arc and in (c) the distance travelled by the arc.

(a)                                    (b)                                    (c)
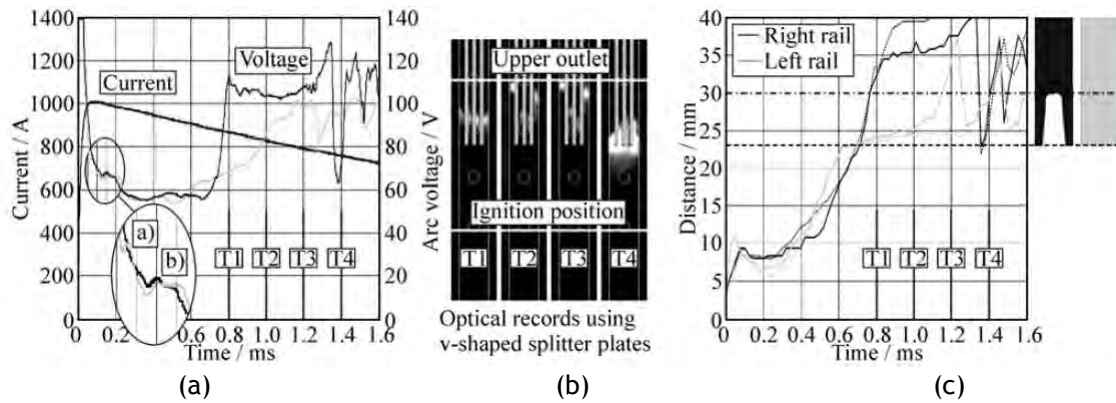
Figure 3-13 Experimental results obtained for rectangular plates (grey) and V shaped (black) [16]

Figure 3-13 (c) shows that the arc movement is slowed down at 0.6ms for rectangular plates. At that instant, the arc reaches the splitter plates and due to the intense cooling of the arc produced by the plates, together with their high flow resistance and lower magnetic field, the arc movement is slower. Also, the arc voltage increases only slightly due to the lengthening of the arc. On the other hand, when the plates are V-shaped, the arc quickly penetrates in the splitter plate stack, which causes its lengthening and a sharper increase in the arc voltage than when using rectangular plates.

This different behaviour of the two types of plates is also reflected in Figure 3-13 (a) by a sharper increase in the arc voltage in the case of V-shaped plates. For this type of plate the same figure shows an arc reignition between 1.3 and 1.4ms and a reduction of the arc voltage from 130 to 60V. Following, the arc is again subdivided moving the partial arcs towards the top.

Finally, [17] presents the behaviour of the arc chamber from a magnetic point of view, determining the magnetic force per plate acting on the arc. Thus, three types of plates are analyzed, depending on the force, Fy, acting in the direction of the central axis of the plate (Figure 3-14). For each type of plate, variation of the force depending on the distance on Y axis is shown:

- Plates with decreasing Fy (Figure 3-15)
- Plates with constant Fy (Figure 3-16)
- Plates with increasing Fy (Figure 3-17)



Metal plate with          Metal plate with          Metal plate with
decreasing force Fy        constant force Fy         increasing force Fy
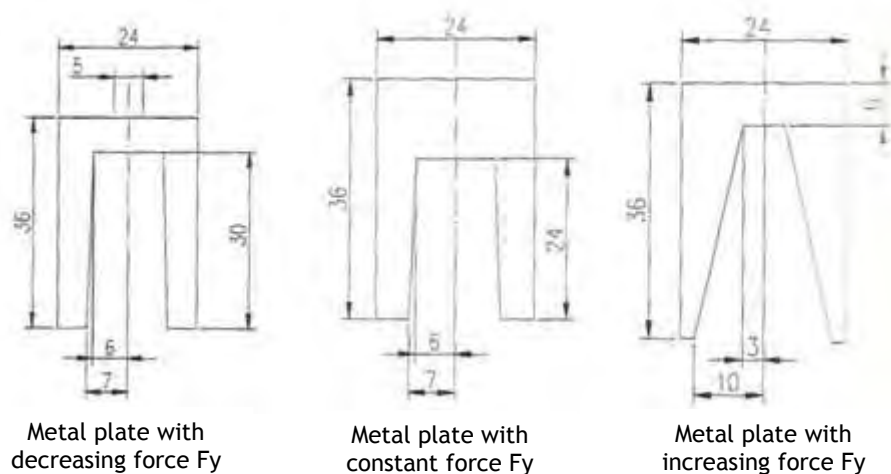
Figure 3-14 Geometry of the plates used in the arc chamber [17]
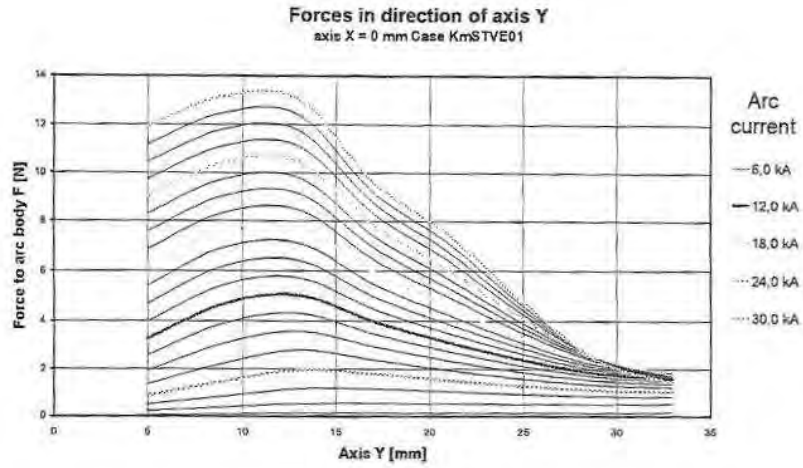
Figure 3-15 Decreasing force Fy in the plates [17]
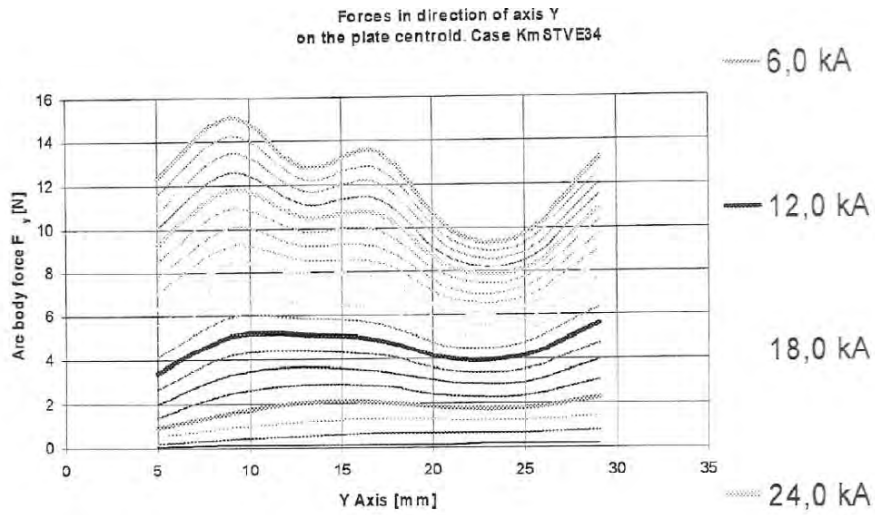


Figure 3-16 Constant force Fy in the plates [17]
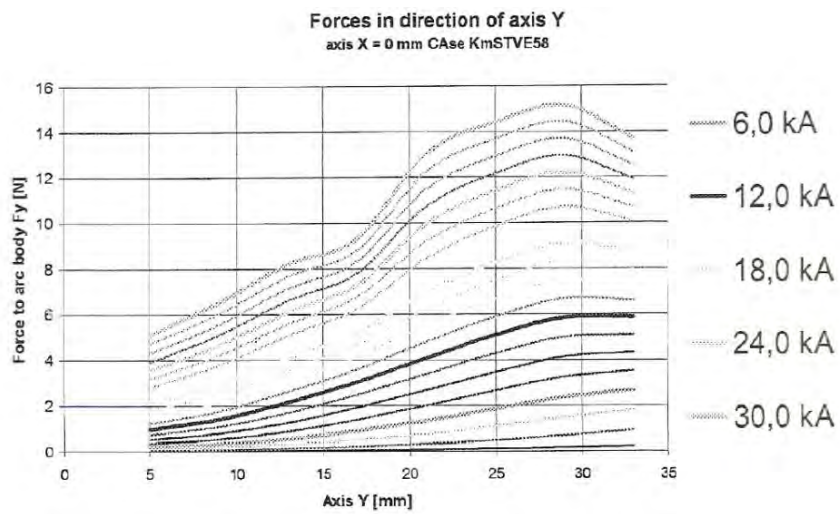


Figure 3-17 Increasing force Fy in the plates [17]

## 3.3.1.2 Arrangement and quantity of splitter plates

The behaviour of the arc may be also influenced by the arrangement of the plates [17]. The location of the plates can be classified into three groups, according to their proximity to the contacts:

- Lower group: the closest ones to the fixed contact
- Central group: the plates in the middle, not influenced by the contacts
- Upper group: the ones further away to the fixed contact and closest to the movable contact.

Thus, in the case of the lower group of plates, the magnetic field of the arc current interacts with the magnetic field caused by the fixed contact. For the central group of plates, the main effect on the plates is produced by the current of the arc column. On the contrary, the upper group of plates, close to the movable contact, is more influenced by this contact. Table 3-1 shows, qualitatively, the behaviour of the different groups of plates in the arc interruption process, taking into account the Fy force [17] (low interaction, increasing force, decreasing force and constant force) and depending on their arrangement inside the chamber (next to the fixed contact, next to the movable contact or in the central part).

Table 3-1 Behaviour, during extinction, of different combinations of plates [17]

| Effect / Group of Plates | Low interaction | Increasing force | Decreasing force | Constant force |
|---|---|---|---|---|
| Lower group (next to the fixed contact) | Bad | Excellent | Bad | Good |
| Central group | Bad | Good | Good | Excellent |
| Upper group (next to movable contact) | Poor | Excellent | Bad | Good |

The dependence of the arc voltage magnitude according to the plates of the arc chamber is analyzed in [18]. A correlation between the arc voltage and the arrangement of the plates is found. This is achieved measuring the arc voltage, arc current and the voltage between plates, for air as interrupting medium, using the arrangement shown in Figure 3-18 . In the experimental tests, the electrodes are connected by a 0.05mm diameter copper wire which melts as a result of the high circulating current, and so the arc is produced.

Figure 3-19 shows the effect of the separation between electrodes and plates on the recorded peak value of the arc voltage. The reduction of this distance, from 50 to 30mm, results in an increased value of the obtained arc voltage.

Additionally, it is observed that the voltage drop between splitter plates, as a function of the gap between splitter plates, adopts a linear evolution (Figure 3-20), with a slope of 2.3V/mm, representing the voltage drop per unit length of the arc column. The extrapolation of this line results in the voltage value of 24.5V, which is associated with the anodic and cathodic voltage drops.

(a)                                                          (b)
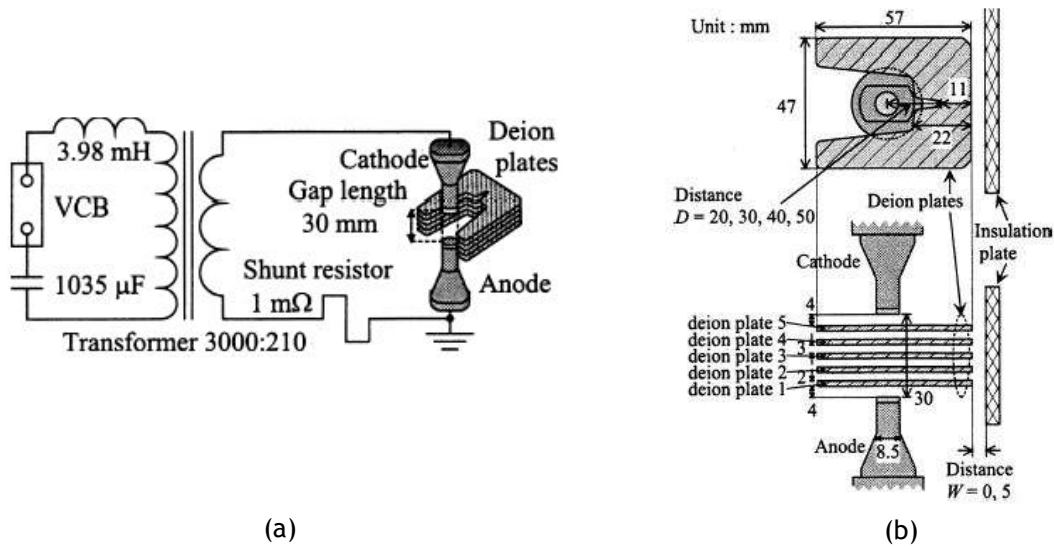
Figure 3-18 Arc set-up: (a) high current generating unit and (b) arrangement of splitter plates [18]
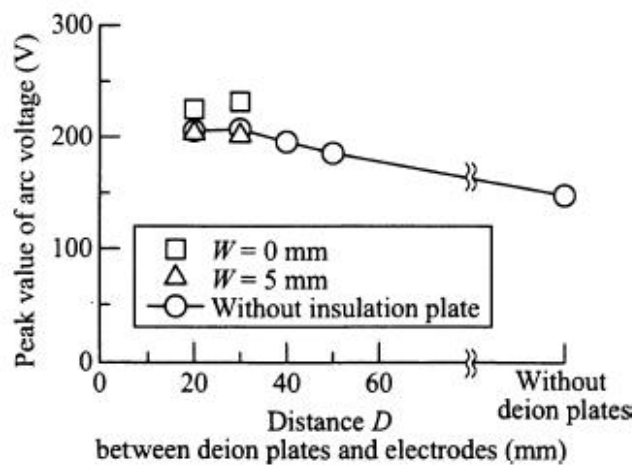


Figure 3-19 Arc voltage as a function of the distance between electrodes and plates [18]
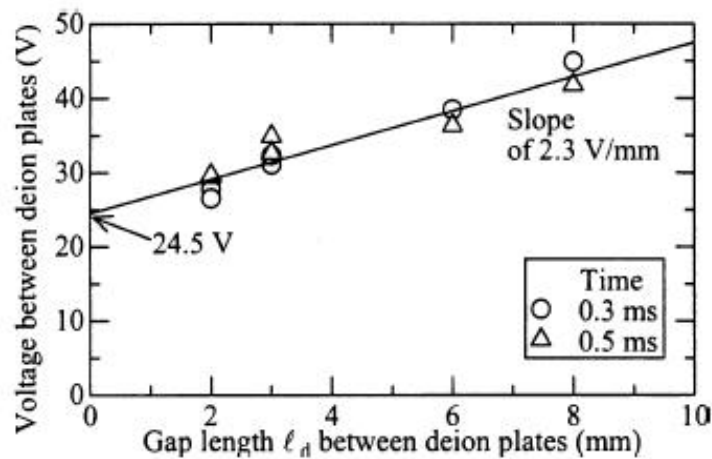


Figure 3-20 Voltage between the plates as a function of the separation distance [18]

Thus, the voltage between the first and fifth plate can be determined by the expression (3-1).

$$V_d = 2.3 \times 10^3 L_d + 24.5 N_s \tag{3-1}$$

where:

$N_s$:      number of plates on which new arc roots are originated

$L_d$:      total length of the arc between plates, obtained by the expression (3-2).

$$L_d = (N-1)l_d + (N-N_s)d \tag{3-2}$$

with:

N:        number of plates

$l_d$:      distance between plates

d:        thickness

Similarly, the arc voltage obtained without plates is analyzed as a function of the current and considering different distances between electrodes, Lg (10, 20 and 30mm) (Figure 3-21). In this case, the arc voltage obtained can be approximated by the expression (3-3).

$$v = 23 + 2.15 \times 10^3 L_g + (3.27 \times 10^{-3} + 0.130 L_g)I \tag{3-3}$$
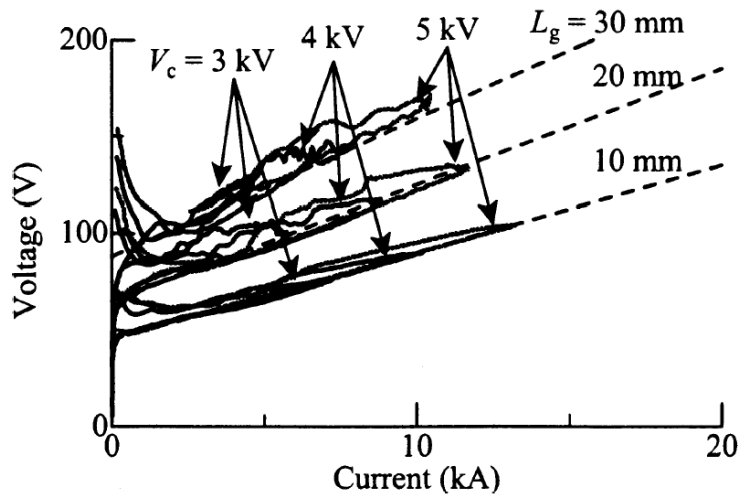


Figure 3-21 Arc voltage as a function of current (without plates) [18]

Considering the results obtained, it is proposed to calculate the arc voltage, in the presence of plates, by a combination of the previous expressions, as shown in equation (3-4).

$$v = [23 + 2.15 \times 10^3 L_{ed} + (3.27 \times 10^{-3} + 0.130 L_{ed})i] + [2.3 \times 10^3 L_d + 24.5 N_s] \tag{3-4}$$

where:

$L_{ed}$:      is the sum of the lengths of the arcs generated between the plates and electrodes.

From expression (3-4), the following conclusions about the effect of different parameters on the arc voltage can be highlighted:

- An increase of 1 mm in the separation between electrodes and splitter plates causes an increase in the arc voltage, in a magnitude of $2.15 \times 10^3 + 0,130I$.
- An increase in the current value of 1A leads to a variation of the arc voltage that can be approximated by $3.27 \times 10^{-3} + 0.130 L_{ed}$.
- An additional plate increases the arc voltage in 24.5 V.

- Increasing the separation between plates 1mm, causes an increase in the arc voltage of 2.3V.

However, it is important to observe that the algebraic expression (3-4) for calculating the arc voltage is applicable only in the case of tungsten electrodes, coated with silver and iron plates, since the use of other materials is associated with a variation of the coefficients that appear in the expression.

Finally, in [19], the influence of the plates' arrangement inside the arc chamber is also considered by analyzing the behaviour of the configurations shown in Figure 3-22. The arc currents are between 1370-6300A, with the splitter plates' geometry indicated in Figure 3-22 (c).



(a)                                 (b)                                 (c)
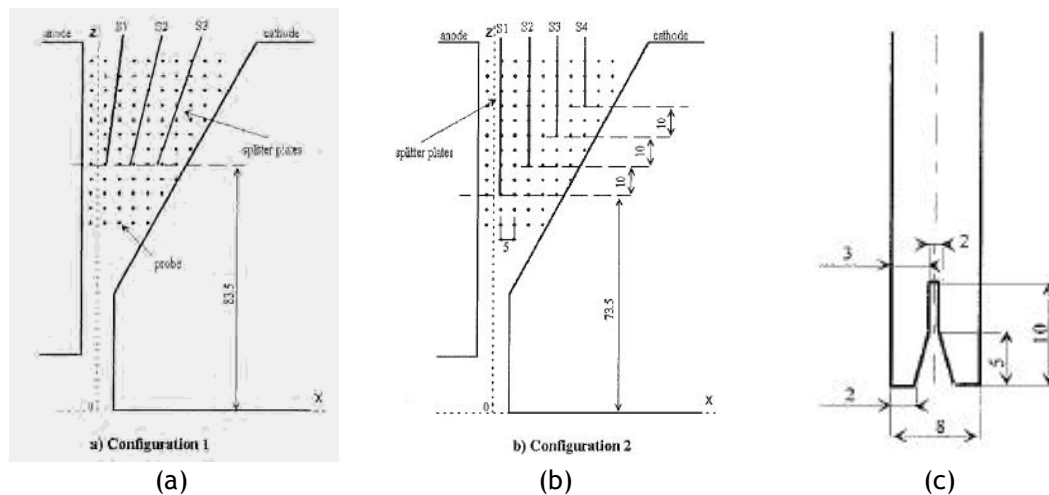
Figure 3-22 Configurations considered in the analysis [19]

The analysis of both configurations of plates is focused on the evaluation of different parameters (current-limiting effect, thermal stress, arc energy and interruption time) and the comparison of each case with the result obtained without plates (Figure 3-23).



(a)                                                          (b)

(c)                                                                  (d)
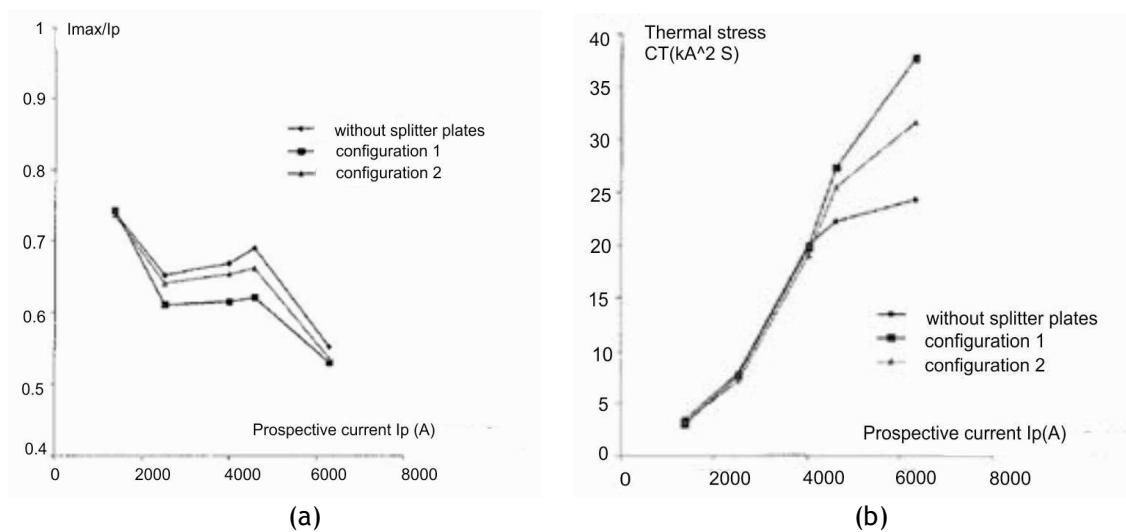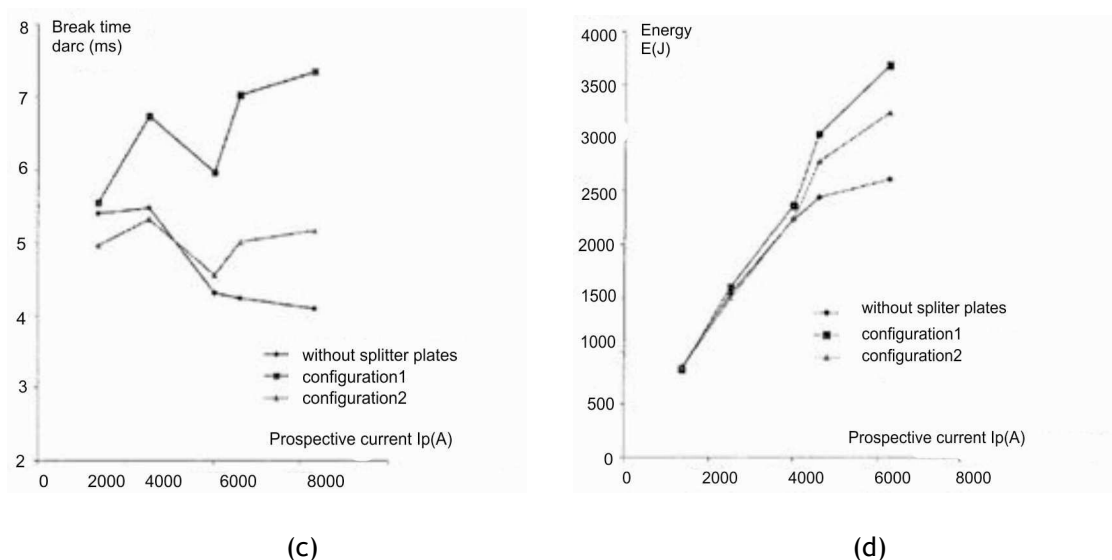
Figure 3-23 Results obtained in the analysis [19]

Regarding the current-limiting effect, there is an improvement when the plates are included in the analysis, as an increase in the arc voltage is obtained and therefore a reduction of the current. This limiting effect is more pronounced with configuration 1(Figure 3-23 (a)).

Configuration 2 (with four plates) provides a better result than configuration 1 (with three plates) regarding thermal stress (Figure 3-23 (b)).This behaviour can be justified as the arrangement of the plates used in configuration 2 allows a higher lengthening of the arc before it fully penetrates in the plates stack, which also leads to a reduction in interruption time, as shown in Figure 3-23(c).

Finally, regarding the energy released in the interruption process, there is a significant erosion of the plates for high currents, obtaining a lower arc energy value with configuration 2 (Figure 3-23 (d)).

Another experimental research for the analysis of the proper number of splitter plates needed in the arc chamber is shown in [20], where the erosion effect of the plates due to the arc current is also analyzed. It is concluded that the correct choice of the coating material, geometry and number of plates can extend the lifetime of the plates. The analysis considers a circuit breaker of 660V and 4kA and a limiting breaking capacity of 65kA. Experimental tests with 8 and 16 plates were carried out. The analysis of current and voltage oscillograms as well as high-speed filming photos showed that it is preferable the arrangement with 8 plates instead of 16. The reason is that even though a greater number of plates lead to a higher arc voltage, in the case of 8 plates an arc voltage of 500-600V is reached and for a greater number of plates a voltage only 10-20% higher is achieved.

### 3.3.1.3 Material

The material of the splitter plates has also an important influence on the arc behaviour as it is responsible for the cooling of the arc and the appearance of magnetic forces that lead to arc extinction.

In general, the splitter plates used in LVCBs arc chamber are made of ferromagnetic material, such as mild steel. They may also be made of galvanized copper or silver, in order to increase the superficial conductivity, facilitate the movement of the arc on the plates and reduce erosion [21].

Additionally, it is important to know the magnetization characteristic of the material used for a proper characterization of the magnetic behaviour of the arc chamber, due to the influence that the saturation of the material has on the distribution of magnetic induction and on the force applied on the arc (see chapter 4, section 4.3.1) [22, 23].

However, regarding this aspect, it should be noted the absence of specific information and the difficulty of obtaining this type of information for a generic material such as mild steel. Only [24] explicitly mentions the material used in the splitter plates of the arc chamber of LVCBs (silicon steel (4%) (CSN 11 340)) and its magnetization curve is provided (Figure 3-24 ).
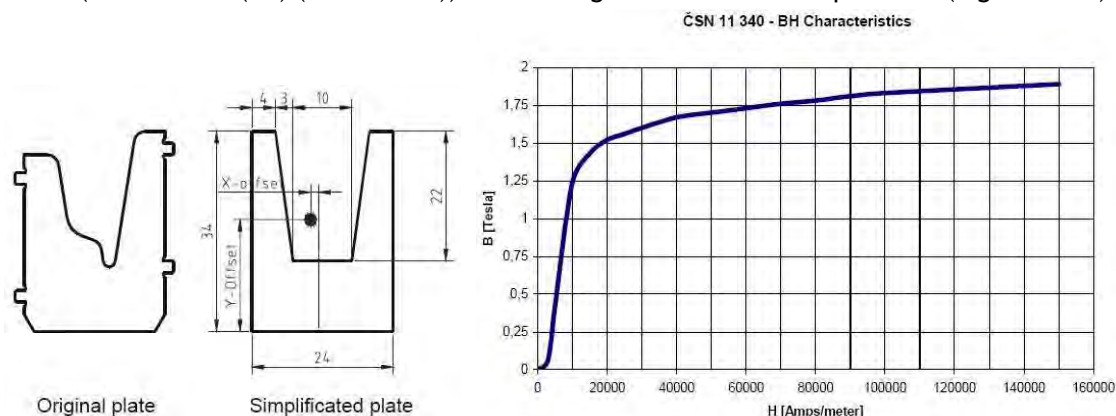


Figure 3-24 Geometry of the splitter plate and BH curve of the material [24]

In [25], the effect of using different combinations of ferromagnetic or diamagnetic materials in the plates is examined (Table 3-2), with currents from 3kA up to 30kA, and voltage of 400V. As indicated, it is proved the ability of ferromagnetic plates to extinguish the arc, but without providing information about the properties of the materials used.

Table 3-2 Combination of used splitter plates in the analysis [25]

| Case Number | Description |
|---|---|
| 1 | Full-ferrous chamber |
| 2 | ½ of bottom plates is made from non-ferrous steel |
| 3 | Bottom plates is non-ferrous |
| 4 | Bottom and middle plate is non-ferrous |
| 5 | Bottom, middle plate is non-ferrous, top ½ ferrous |
| 6 | Full non-ferrous chamber |
| 7 | Bottom and middle ½ ferrous, top has non-ferrous plates |
| 8 | Bottom and middle ferrous, top ½ non-ferrous |
| 9 | Bottom and top ferrous, middle non-ferrous |

In addition, it is important to consider other phenomena that may occur and which may have a negative effect on the interruption process. Thus, given the inherent randomness of the electric arc phenomenon, there may be situations in which the arc does not completely penetrate into the splitter plates, but surrounds them, becoming the plates an obstacle for the movement of the arc. Furthermore, the arc may also cause erosion by melting the material of the surface which, upon solidification, can short-circuit the plates and lead a lower arc voltage.

The erosion effect of the plates due to the arc current is analyzed in [20]. To analyze this effect, steel plates with two different coating are considered, oxide-coating and copper and zinc electrolytic coating. Results show that steel plates with zinc electrolytic coating are the ones experiencing minor damage due to erosion.

Finally, [21] proposes the use of ferromagnetic splitting plates with a coating of a composite material, consisting of at least two components. The first component has a melting point and conductivity not higher than a non-ferromagnetic material. The second component has higher melting point, so that it does not melt due to arc effect, preventing sprinkles produced by the melting of the first one. The high conductivity of the first component is designed to facilitate the mobility of the arc on the surface of the plates. Additionally, the vaporization of this material, by effect of the arc, allows absorbing large amounts of energy from the arc. As basic ferromagnetic materials, the following are proposed: mild steel or any soft magnetic material, constituted by nickel, cobalt or any iron, nickel or cobalt alloy. As second component, it is proposed the use of refractory metals such as tungsten, molybdenum and tantalum, as well as their carbides, nitrides and silicates.

## 3.3.2  ELECTRICAL CONTACTS

Electrical contacts are also important components in a circuit breaker as they have a great influence in the formation of the electric arc. The useful life of electrical contacts is limited by erosion, worn out and welding experienced during arc interruption. So they limit the life of the circuit breakers. MCCBs and MCBs are directly discarded when the contacts are worn out. For LVPCBs, however, the contacts can be replaced.

This section presents some aspects of interest in the design of the electrical contacts, based on the relevance that these elements have in the interrupting devices, such as the material and the adopted design.

The material used in electrical contacts must be able to withstand the stress that experiences during the operation of the circuit breaker. Among other characteristics, the contact resistance of the material and the resistance to erosion and welding must be considered. Table 3-3 classifies various materials used in the manufacturing process of electrical contacts [8].

Table 3-3 Comparison of the behaviour of materials used in electrical contacts [8]

|  | Welding of closed contacts | Welding on construction | Erosion by arcing | Dwell time | Contact resistance after arcing | Reignition voltage |
|---|---|---|---|---|---|---|
| Inferior ↕ Better | WAg,WCAg | Ag,AgCu | Ag | WAg,WCAg | WAg,WCAg | WAg,WCAg |
| | AgNi | Ag,Ni | AgCu | AgC | AgMeO | AgC |
| | AgMeO | AgMeo | AgC | AgMeO | AgNi | AgCu |
| | AgCu,Ag | AgC | AgNi | AgNi | AgCu | Ag |
| | AgC | WAg,WCAg | AgMeO | Ag,AgCu | AgC | AgNi |
| | | | WCAg,WAg | | Ag | AgMeO |

Additionally, Table 3-4 shows different materials used in LVCBs. The general trend is to use silver and its alloys for small currents, and materials with higher resistance to erosion and welding in the case of higher currents [8].

Table 3-4 Conductive materials used in LVCBs [8]

| Application | Continuous current rating | Interrupting capacity | Contact material |
|---|---|---|---|
| Relays and auxiliary contacts | ≤10A | ≤100A | Ag,AgCu(3-10%Cu)<br>AgCdO(10-15% CdO)<br>AgNi(10-20% Ni) |
| Contactors | ≤10A<br><br>>10A | ≤150A<br><br>>150A-10 kA | AgNi(10-20% Ni)<br>AgCdO(10-15% $SnO_2$)<br>$AgSnO_2$(8-12% $SnO_2$)<br>AgCdO(10-15% CdO)<br>$AgSnO_2$(8-12%$SnO_2$) |
| Residential circuit breakers, USA type | ≤125A | ≥10kA | MoAg(25-50% Ag)<br>WAg(50%Ag) |
| Switching duty residential breakers | ≤30A | ≤10kA | WAg (25-50% Ag)<br>MoAg(Ag enriched surface)<br>AgCdO (10-15% CdO)<br>AgZnO (8-10% ZnO)<br>$AgSnO_2$(8-10% $SnO_2$) |
| Residential circuit breakers, European type | ≤63A | ≤10kA<br><br>≤10kA | AgCdO(10-15%CdO)<br>$AgSnO_2$(10-15% $SnO_2$)<br>AgC(3-5%C)<br>AgC(3-5%C)<br>AgZnO(8%ZnO)<br>MoAg(25-50%Ag)<br>WAg |
| Industrial type circuit breakers, without extra arcing contacts | ≤400A<br><br>≤800A | ≤25A<br><br>≤100kA | AgC(3-5%C)+AgNi(40-50%Ni)<br>AgC(3-5%)+WAg(25-50%Ag)<br>WAg(25-50%Ag)<br>WCAg(35-50%Ag)<br>MoAg(30-50%Ag) |
| Circuit breakers with main and arcing contacts | >400A | <150kA | Main contacts:<br>AgNi (20-40%Ni)<br>AgCdO (10-15% CdO)<br>MoAg(50% Ag)<br>AgW(25-50%W)<br>WCAg(35-50% Ag)<br><br>Arcing contacts<br>WAg(20-35%Ag)<br>WCu(30-50%Cu)<br>WAg(30-40%Ag) |

In [26] the interaction of the arc with the walls of the chamber and with the electrical contacts is experimentally analyzed. Refractory materials for the electrical contacts (such as Tungsten-copper (W-Cu 80-20 Wt %)) and non-refractory (copper and silver) which cause numerous metal vapours, are compared. On the other hand, also the typical behaviour of standard contact materials, such as silver-graphite (Ag-C 95-5 Wt %), silver-tungsten (Ag-WC 60-40% Wt %), silver-nickel (Ag-Ni 60-40% Wt %) is identified. The results of the tests carried out are shown in Table 3-5, where the influence of the contact material and chamber walls is quantified in properties such as erosion of walls and contacts or dielectric strength.

Table 3-5 Behaviour of different contact materials [26]

| Insulating material | Upper contact | Lower contact | Maximum arc-voltage (V) | Maximum pressure (bar) | Upper contact erosion (mg) | Wall erosion (mg) | Superficial dielectric strength |
|---|---|---|---|---|---|---|---|
| Ceramic | Copper | Copper | 44 | 0 | -16 | +3 | <10kV |
| Ceramic | Ag-C 95-5 | Copper | 43 | 0 | -7 | +1 | <5kV |
| Ceramic | Ag-C 95-5 | Ag-Ni 60-40 | 42 | 0 | -1 | +2.5 | <5kV |
| Ceramic | W-Cu 80-20 | W-Cu 80-20 | 45 | 0 | -1 | -1 | <10kV |
| POM plastic | Copper | Copper | 61 | 3.6 | -71 | -38 | <10kV |
| POM plastic | Ag-C 95-5 | Copper | 60 | 3.8 | -45 | -45 | <10kV |
| POM plastic | Ag-C 95-5 | Ag-Ni 60-40 | 62 | 3.8 | -44 | -56 | <10kV |
| POM plastic | W-Cu 80-20 | W-Cu 80-20 | 66 | 4.2 | -2 | -46 | <10kV |

These results show that the more refractory the material is, the less the erosion is, even though being exposed to higher interaction time with the arc (Figure 3-25).
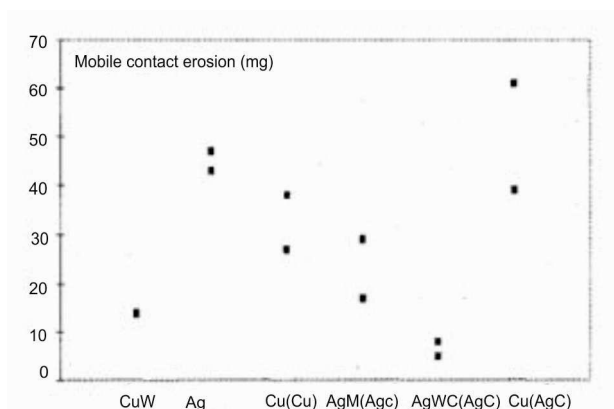


Figure 3-25 Erosion of the contacts for different materials [26]

## 3.4   CONCLUSIONS

Circuit breakers are important elements in the electrical grid, aimed to establish or interrupt the current through electric circuits, as well as for the protection of the network, equipment or human beings.

Their classification attends to different parameters, such as the interruption material inside the chamber, the interruption technique or the nominal voltage or current. For voltages lower than 1kV, circuit breakers can be classified attending to the interruption technique. The most used ones are based on the electric arc for the interruption and they are known as conventional LVCBs. Among these conventional LVCBs, three main groups can be found: MCB, MCCB and LVPCB (being the main difference their interrupting current). Each of them has different design characteristics, but several elements as electrical contacts, splitter plates of the arc chamber or the terminals are common to all of them.

Among other designs of circuit breakers for current interruption, electronic interruption devices can be mentioned. These circuit breakers are based on static rupture and the variable resistance value of semiconductors. Although the current interruption is faster than with the electric arc technique, they still cannot compete with the electric arc as interruption technology for LVCBs applications.

Regarding the most important elements of LVCBs that influence the interruption process, splitter plates and electric contacts can be mentioned.

The splitter plates of the arc chamber are important in the appearance of a magnetic force, on the lengthening, division and on the cooling of the arc. Geometry, quantity, arrangement and material of the plates are important parameters to take into account in the design. Regarding geometry, "V-shaped" plates have been proved to be more effective, increasing the magnetic force on the arc and allowing a faster penetration of the arc in the splitter plate stack. Thus, a faster lengthening and cooling of the arc is obtained with "V-shaped" plates. Regarding quantity and arrangement, an interesting result is that when a reduction in the distance between the ignition of the arc and the splitter plates stack exists, the arc voltage is increased. The addition of more splitter plates leads to an increase in the arc voltage, however, after a certain number of plates, the voltage increase becomes less significant. Finally, increasing the separation of the plates has also been proved to increase the arc voltage. But it has to be pointed out that the impact of including one more splitter plate in the chamber is 10 times bigger for the arc voltage increase, than increasing the separation of the plates 1mm.

Regarding the material, steel, cooper or silver are usually used. However, ferromagnetic material is recommended to increase the magnetic force and leading the arc into the splitter plates stack faster. Additionally, a zinc coating is recommended on the steel plates in order to reduce erosion problems.

Finally, another important element in circuit breakers is the electrical contacts. They are related to the formation of the arc due to the evaporation and melting. Also they influence on the lifetime of the circuit breaker due to their worn out. Again, silver, cooper or tungsten are recommended.

# CHAPTER 4

## MODELS FOR THE ANALYSIS OF THE ELECTRIC ARC IN LOW VOLTAGE CIRCUIT BREAKERS

# 4 MODELS FOR THE ANALYSIS OF THE ELECTRIC ARC IN LOW VOLTAGE CIRCUIT BREAKERS

## 4.1 INTRODUCTION

Despite the complexity of the arc interruption process in LVCBs, several methods to analyze its behaviour have been developed, which are fundamental for a better understanding of the device and the phenomenon itself. This way, the optimization of the LVCBs design is possible, achieving more economic and better technical options.

With the idea of LVCBs optimization, some improvements are desirable to be achieved:

- On the one hand, a fast current interruption. Thus, for DC currents an elevation of the arc voltage is needed as it has been explained in chapter 2, to increase it above the source voltage. Also an increase in the Transient Recovery Voltage (TRV) is needed to prevent dielectric breakdown. For AC current cases a faster deionization after the zero current is needed.
- On the other hand, a higher efficiency for manufacturers would be desirable. That means smaller and cheaper devices, requiring less material for the construction of the LVCB, as well as the revision of the layout of the components inside the LVCB, size, etc.

To achieve those purposes, there are two possibilities: the development of simulation models using software tools and real experimental tests. Each option has both advantages and disadvantages, briefly summarized in Table 4-1. As seen in that table, when building simulation models a good theoretical knowledge on the physical phenomenon as well as precise numerical input values for the parameters involved are required skills for the user. These requirements can be hard to achieve due to the complex nature of the electric arc phenomenon. Another important factor is the equipment needed to implement and run the simulation models. Not only the software must be selected and financially supported, but also a powerful hardware is needed. Simulation models need parallel clusters of computers to be solved. As an example, the new model developed in this thesis, being its simplicity-precision binomial in a good balance, needs almost four whole days to be solved using a four parallel clusters (see chapter 6, verification process, for further information regarding the hardware used).

But on the other hand, simulation models have several advantages. Once the model has been built and the simulation has been solved, several physical quantities, hardly available for the researcher by experimental laboratory tests, are accessible and simple to analyze. Besides, it is also easy, fast and cheap to make changes in the input parameters to prove their impact on the results. So, it can be said that simulation models are hard and relatively expensive to build, but they can be used for a long time as they are easily transformed.

Regarding laboratory tests, precise previous data are necessary to build the prototype, with exact precision on measures and layout. Furthermore, once the tests are run, it is not so easy to analyze the results as there is a strong influence of external factors in the process. Due to the volatility of real tests, the same experiment has to be repeated several times to be sure about the precision of the results. Besides, the flexibility of the experimental set-up is very low and almost no change in the configuration can be done, after the experiment has been designed, built and set up. Additionally, any change that researchers may want to make in the designs involves a new prototype and a new measurement process, and thus a high economical effort. So, it can be concluded that the main advantage of real tests compared to

simulations is that the results obtained are closer to real situations but they are harder and more expensive to obtain.

Table 4-1 Experiments vs. Simulations in LVCB electric arc

|  | Experiments | Simulation |
|---|---|---|
| **Construction requirements** | • Good prototypes<br>• Measurement precision | • Good theoretical knowledge on the phenomenon<br>• Precise numerical values of parameters |
| **Analysis of the results** | • Difficult interpretation (depending on the number of tests)<br>• Input parameters defined cannot be changed | • Simple interpretation<br>• Fast and easy change of input parameters |
| **Development** | • New designs relatively expensive<br>• New measurements necessary | • Fast changes in designs without economical cost |
| **Cost** | • High | • Relatively high initial cost<br>• Low life cycle cost |

This way, taking into account that the weakness of simulation models is that results can be far away from expected real scenarios, it is necessary to improve the simulation models existing in the research community. For this reason a new simulation model for the electric arc, explained in chapter 5, is developed in this thesis.

Previously to present the new proposed model, this chapter presents an analysis of the state of art of those existent simulation models of the electric arc in LVCBs. First of all, the different types of existing simulation models are exposed. Among those, black box models, models based on graphics and diagrams and physical models are introduced. As a result of this analysis, physical models stand out as the most complete to analyze the phenomenon of electrical arc and the behaviour of the circuit breakers. So, the state of the art of those physical models is presented, which has served as a starting point to develop the new model presented in chapter 5.

## 4.2   TYPES OF MODELS

Previously to model the electric arc or any other physical problem, some considerations and steps have to be taken into account. First of all, the problem must be clearly defined. This way, a deep analysis of the problem considering the parameters that have to be measured must be performed. After that, the mathematical model has to be developed to obtain the parameters chosen in the problem definition. Some models already exist, due to previous research works but improved models can be necessary to get a better understanding of the process. This way, optimized designs of LVCBs can be developed.

Additionally, the computer simulation has to be carried out. For that reason, assumptions and simplifications are applied in order to reduce the complexity of the real system of equations. Also, the desired boundary and initial conditions for the system must be defined.

Regarding the possible application areas and the way of application of the different tools in the development, testing and operation of circuit breakers, the electric arc simulation models can be classified in different groups [27]:

- Black box models
- Models based on diagrams and graphics
- Physical models

Although they are described more in deep in following subsections, it can be said that black box and graphics and diagrams based models consider the electric arc as a part of the grid, without analyzing its physics. Thus, a simple geometry for the electric arc is considered in these cases, without including switching elements. Besides, the only energy losses considered are conduction and convection, without any radiation. Additionally, input parameters data from previous experiments are needed.

Physical models, on the other hand, are based on the physical process involved in the arc. Therefore, the phenomenon is viewed from inside and the specific geometry of the circuit breaker is considered. The energy losses considered in these models include radiation phenomena. Also, other aspects as movement of contacts, sheath layer effects or metal vapour effects can be considered.

Table 4-2 summarizes the application field of each method. It can be seen that physical models are the best option for the design and development of devices and physical phenomena comprehension, while black box and models based on graphics and diagrams are more oriented to experimental tests and operational aspects.

Table 4-2 Scope of the different models of electric arc analysis in circuit breakers (PM: physical model, BB: "black box" model, GD: graphics and diagrams) [27]

| Type of problem | Application | | |
|---|---|---|---|
| | Design and development | Experimental tests | Operation |
| Physical problem comprehension | PM | | |
| Mechanical design | PM | GD | |
| Dielectric recovery description | PM and GD | GD | GD |
| Influence of the arc on the current | PM, GD and BB | GD and BB | BB |
| HVDC circuit breakers | PM, GD and BB | GD and BB | GD and BB |
| Small inductive currents | PM, GD and BB | GD and BB | GD and BB |
| SLF (Short Line Fault) | PM, GD and BB | GD and BB | GD and BB |
| Design and verification of tests circuits | GD | BB | |

## 4.2.1 BLACK BOX MODELS

Black box models are intended to describe the interaction between the arc and the electrical circuit during the interruption process. They can be applied in the prediction of the circuit breaker behaviour when different conditions are applied in the circuit. Thus, the most important aspect is the electrical behaviour of the arc and not the physical process that takes place. These models are built deducing a mathematical model, a partial differential equation (PDE), from voltage and current data from tests.

The following aims can be achieved:

- Finding the limiting value for current or voltage, for a given test.
- Describing the circuit influence, as parallel capacitance or amplitude of line oscillations, on limit values.
- Obtaining the statistical properties of these limits by evaluation of several tests.

- Special applications: determination of circuit interaction in the high current phase (influence of the arc on asymmetry of current), modelling of arc instabilities (current chopping, DC breaker).

Thus, black box models are constituted of one or two differential equations that relate the conductance of the arc with other electrical magnitudes, such as the arc voltage and current. Therefore, they can only be applied in the case that the situation to be analyzed is governed by the conductance. In other cases, such as in the dielectric region of the interruption process, these models are not directly applicable.

These arc models are usually written as a formula for the arc conductance $g$, as a function of circuit parameters such as: current $i$, arc voltage $u$ and some others arc parameters as time constant $T$, stationary arc voltage $U_0$, power-loss $P$. Many of these models are based on the equations proposed by Cassie and Mayr [27], where constant arc parameters are assumed.

Cassie's model is expressed by equation (4-1).

$$\frac{dg}{dt} = \frac{1}{T}\left(\frac{iu}{U_{0^2}} - g\right) \qquad (4\text{-}1)$$

where:
$U_{0^2}$:     arc voltage
$T$:       time constant

On the other hand, Mayr model is given by equation (4-2).

$$\frac{dg}{dt} = \frac{1}{T\left(\frac{i^2}{P-g}\right)} \qquad (4\text{-}2)$$

where:
$P$:       power loss
$T$:       time constant

These equations have experienced several modifications, in particular concerning to arc parameters and their dependency on other electrical quantities. Many of the published models can be represented by a first-order differential equation, as shown in equation (4-3) [27].

$$\frac{1}{g}\frac{dg}{dt} = \frac{1}{T(|i|,g)}\frac{ui}{P(i,g)} - 1 \qquad (4\text{-}3)$$

where:
g:     conductance of the arc
u:     arc voltage
i:     arc current
P:     power loss
T:     time constant

The models differ on the functional dependency of the model parameters and how they are determined. Most of these models do not have a physical justification, being the parameters P and T of the model calculated so as to obtain a good correlation between the results obtained with the model and those obtained by testing.

As it can be seen in Figure 4-1, the information to develop the model is obtained from: experimental tests, the mathematical equation (4-3), additional assumptions and the

technique of analysis itself. Several representations of this type of model have been developed in the literature.
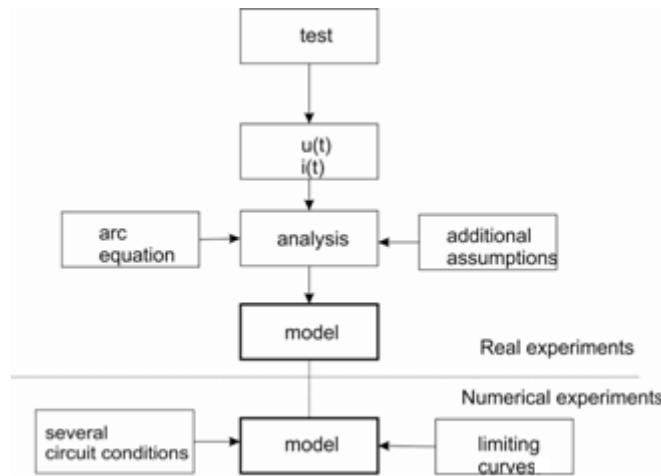


Figure 4-1 Flow chart for construction and application of black box arc models

As the model is represented by a differential equation lead by the conductance, black box models can be easily integrated into network simulation software.

In [28], a modified Mayr's equation is used in the ATP software to represent the arc through a variable resistance, represented by the type 94 from the library of the program. This component, 94, is treated as a non linear component and so, in each step of the simulation, the component receives the Thevenin equivalent of the grid (Figure 4-2).
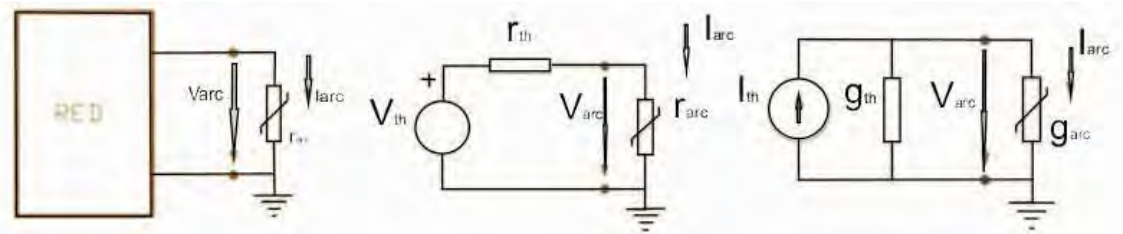


Figure 4-2 Equivalent scheme of the grid and arc black box in ATP [28]

Thus, the current of the arc is solved through an iterative process, as show in equation (4-4).

$$i_{arc}\left(g_{th} + g_{arc}\right) - v_{th}g_{th}g_{arc} = f(i_{arc}) = 0 \tag{4-4}$$

where:
$i_{arc}$:   arc current
$g_{arc}$:   arc conductance
$g_{th}$:   thevenin conductance
$v_{th}$:   thevenin voltage

According to that, $f(i_{arc})$ and $g_{arc}$ are calculated, and only when their values are lower than the minimum allowed value for the current interruption, results will be taken as satisfactory.
In [29], a black box model based on Mayr's and Cassie's differential arc equations is developed, for the software Netomac. This model is used to determine the current interruption capability of a circuit breaker and to determine whether the circuit breaker is

able to interrupting the current at a specific location in the network and under specific conditions. The model is represented as shown in Figure 4-3.
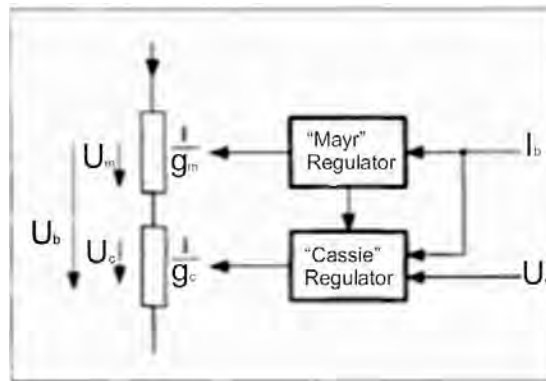


Figure 4-3 CB black box model for Netomac [29]

The part regarding the network model consists of two series-connected ohmic resistors, Mayr's and Cassie's regulators, and the arc's black box model is represented by the conductivities of Mayr and Cassie connected in series, $g_m$ and $g_c$. Thus, in the simulation, a few micro-seconds before the zero current, the model resistance is transferred to the parts modeled according to both differential equations. This resistance is calculated according to the differential equations until successful arc extinction is detected. In this case, the resistance of both parts of the circuits is very high, so an open circuit is represented.

A different example can be found in [30], where the Arc Model Blockset library, containing several arc models, to be used in combination with Matlab Power system Blockset is presented. The scheme of the black box model and its integration in an electric circuit is shown in Figure 4-4 (a) and (b). In this case, arc current and voltage are measured and, with those values, the arc resistance which has to increase from practically zero to almost infinite after the interruption.



(a)                                                    (b)
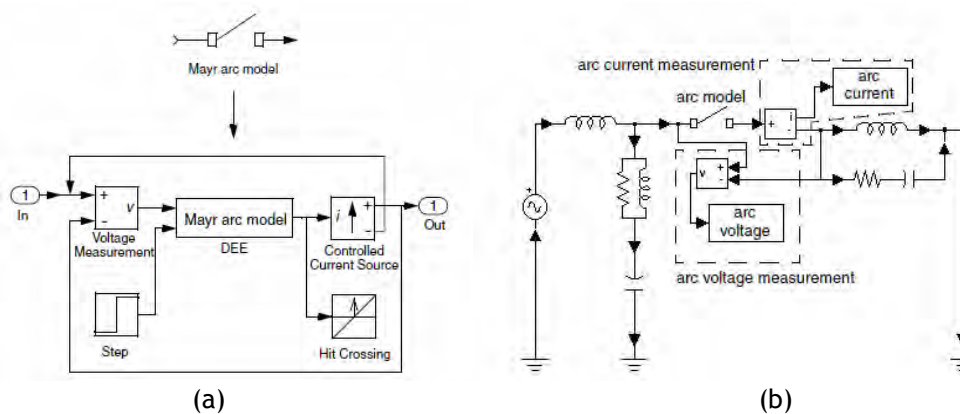
Figure 4-4 Mayr black box arc model in MATLAB and its integration in the circuit [30]

Another example of a black box model is presented in [31] where EMTP software is used. Again, Mayr's model is solved (Figure 4-5).
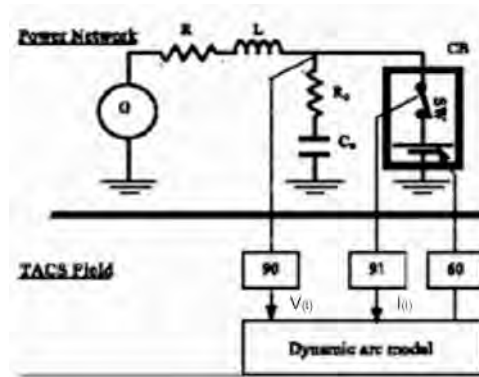
Figure 4-5 Circuit and black box model in EMTP [31]

In this case, the value of the arc voltage is computed by multiplying the computed arc resistance by the arc current measured by sensor 91. This value of the arc voltage is fed back into the power system via sensor 60. This way, arc interaction with the power system is fully considered.

Finally, [32] reviews the existing black box models to propose a new one, introducing a new non equilibrium correction for the low current regime.

To conclude, the limitations of these models can be summarized as follows. First of all, only the arc-circuit interaction is analyzed, ignoring the physics of the arc. Secondly, only processes guided by the conductance can be modelled and, besides, tests are needed for obtaining the mathematical model parameters.

## 4.2.2   MODELS BASED ON GRAPHICS AND DIAGRAMNS

Another possibility in the analysis of the interruption phenomenon and/or circuit breakers design is the use of analytical and graphical expressions, correlating circuit parameters and/or design parameters, obtained directly by testing or by applying physical or "black box" models. An example is the case of the arc voltage characteristics obtained experimentally [27].These features can be used to estimate the arc-circuit interaction. The corresponding expression is given by equation (4-5). This can be used, for example, to simulate the influence of arc voltage on asymmetry.

$$U_{arc} = K \cdot f(i, P_s, L)$$

(4-5)

where:

$U_{arc}$:   arc voltage

K:      constant characteristic of the circuit breaker and dependent on the geometry, gas type and pressure

i:      instantaneous current

$P_s$:     stagnation pressure in the arc

L:      length of arc

Another example of these models is to use graphs of dielectric recovery, after the zero current, as shown in Figure 4-6. With this data, the behaviour of a circuit breaker in a given network can be analyzed in order to determine whether it can interrupt the current effectively or dielectric failure can occur [27].
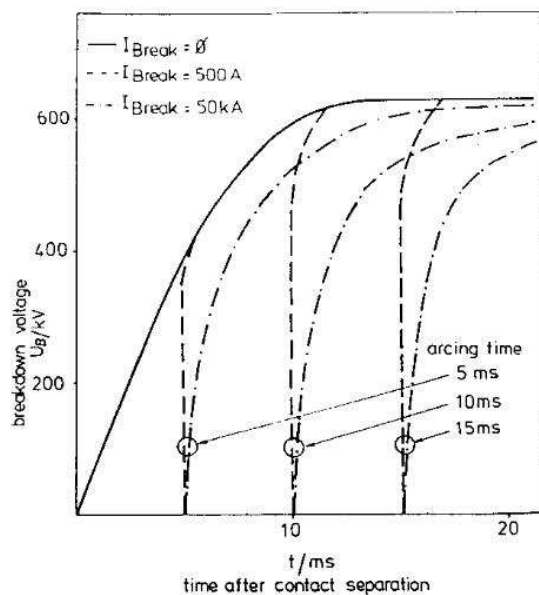
Figure 4-6 Dielectric properties of a circuit breaker without current and after the interruption of different current values, at 3 different arcing times [27].

The validity range of these tools is limited to that for which the numerical values of the parameters have been obtained experimentally. Thus, they are useful in the design of circuit breakers. Also, they are applied to compare the severity of test circuits or to analyze the validity of test circuits, as compared to the actual network conditions.

Other examples of this type of models are found in [1], where the results about the application of a circuit breaker at a specific location of the electrical network are represented in a diagram. For that aim, proper characteristics of the circuit breaker, as the type of the gas in the chamber, pressure and temperature values, as well as the characteristics of the network at the operating point, must be known. As a result, Figure 4-7 is achieved, where double logarithmic scale is used to represent the transient recovery voltage (TRV) and the current of the circuit breaker. In this figure, the thermal limit of the circuit breaker is represented by the thicker line, so the intersection point represents the maximum current that the circuit breaker is able to interrupt satisfactorily. The area under that point represents the satisfactory interruption area.
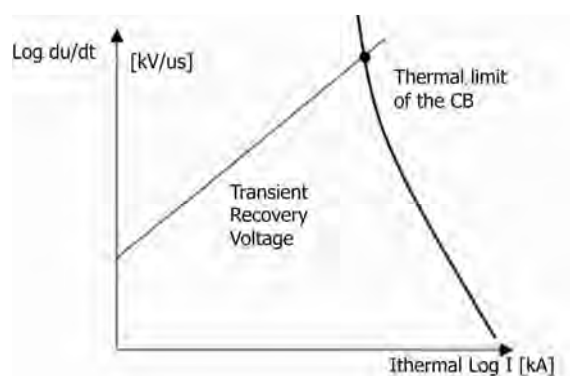


Figure 4-7 Thermal reignition limit of the CB [1]

Another reignition possibility in the circuit breakers is due to the collapse of dielectric properties, some microseconds after the zero current. So, with the dielectric characteristics of the interrupting medium and the maximum value of the voltage between electrodes (defined by the network), Figure 4-8 is obtained. In this figure, two areas are differentiated

again, the one above the dielectric limit of the circuit breaker, where reignition is produced, and the one below, where the interruption is satisfactory. The intersection point indicates the maximum current value that can be interrupted. Superimposing Figure 4-7 and Figure 4-8 the analysis for both conditions is obtained, as can be seen in Figure 4-9, where the most restrictive case and current value can be defined.
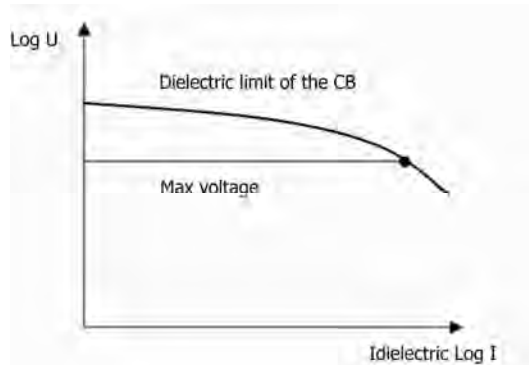


Figure 4-8 Dielectric reignition limit of the circuit breaker [1]
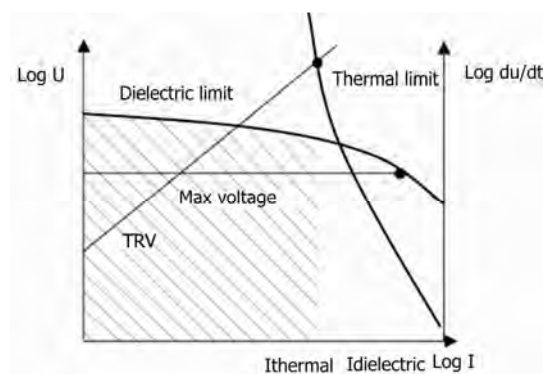


Figure 4-9 Successful operation limit for the circuit breaker [1]

In any case, this method is just a compilation of data achieved in some other analysis, as black box models or experimental setups.

### 4.2.3   PHYSICAL MODELS

Physical models receive this designation because they reproduce in detail the physical processes that take place during the electric arc phenomenon. The first attempts to represent mathematically the electric arc were those developed by Cassie and Mayr that leaded to black box models, as exposed in the previous section. However, current development of software tools enables the resolution of highly complex mathematical problems. So, physical models are able to represent in detail the physical processes taking place in the arc.

The main field of application of this type of models, given the wide range of extrapolation of results provided, is the design and improvement of circuit breakers, being possible to study not only the parameters of the circuit, but also aspects directly related to the design, such as geometry, extinguishing medium, pressure and main elements (as splitter plates or contacts) [27]. These aspects lead not only to a better understanding of the electric arc process but also to a greater reliability.

However, the major limitation of these models is, firstly, the limited accuracy in the resolution of the differential equations of the models, due to the restriction in the computation time and, on the other hand, the need of a deep knowledge about the precise physical processes involved in the phenomenon of the arc. Furthermore, the application of physical models requires knowledge of the physical properties of the extinguishing medium in a wide range of temperatures, which can reach 30000K. Also, test results from measurements of physical properties from the arc are needed to evaluate different parameters used, such as thermal conductivity, viscosity, electrical conductivity, specific heat or mass density. These aspects make the application of these type of models more difficult and determine the accuracy of the results provided by the model [1].

For the mathematical expression of the physical models, the equations of conservation of mass, momentum and energy in macroscopic elements of the arc are considered. Also, gas properties and empirical formulation to represent energy exchange mechanisms, such as turbulence and radiation, must be taken into account. However, they all require applying simplifications in relation to the geometry and physical properties of the arc plasma. In general, the following assumptions are adopted in current physical models:

- Arc plasma is electrically neutral and is represented as a mixture of gases at high temperature.

- There is a thermodynamic equation of state for each component of the plasma (electrons, ions, atoms and molecular species), but it is usually neglected in the macroscopic scale analysis.

- Physical properties of plasma (thermal conductivity, viscosity, density, specific heat, electrical conductivity) depend on its temperature and pressure conditions.

- The behaviour of the gaseous mass is described by applying the Navier Stokes' (conservation of mass, momentum and energy) and Maxwell's equations.

- Since plasma is electrically conductive, the corresponding term for the interaction with the magnetic field must be considered in the momentum equation. This magnetic field, depending on the degree of accuracy of the model, can be defined as external or self-induced by the current flowing through the arc. The second option is closer to reality.

- The magnetic field is calculated by applying Biot-Savart or by calculating the magnetic vector potential once the current distribution is known.

- The energy conservation equation is modified by considering additional terms that represent the generation of heat by Joule effect and the heat dissipation by radiation.

- In many cases, local thermal equilibrium (LTE) is assumed for the plasma, so that it is possible to set a temperature value which determines the degree of dissociation and ionization.

- The initialization of the arc is not achieved by the dynamic movement of the electrodes separation, as in reality, due to the complexity. The arc/electrode interaction is not taken into account in a microscopic way.

Given the above considerations, the equations of magnetohydrodynamic models of the electric arc (MHD) are obtained [5]. In next sections, the mathematical background of MHD

models is presented and the effects that interact in the arc, such as radiation or arc roots modelling, are also described. Then, a state of the art of the physical models is presented.

### 4.2.3.1 Magnetohydrodynamic (MHD) description

The magnetohydrodynamic definition provides information about the behaviour of the electric arc, by fluid dynamics and thermodynamic laws, at a macroscopic scale. To understand the background of the magnetohydrodynamic model (MHD), the description of the electric arc plasma, as a set of particles, has to be taken as reference. In this description, each component, electrons, ions, atoms and molecular species, has a state equation and the solution of all of them leads to a quite large mathematical problem. This requires a simplification to get something more manageable from the computational point of view.

The first approach is to consider the plasma as two fluids, where heavy particles (ions and neutrals) and light particles (electrons) are differentiated. There are certain conditions in the electric arc at low voltage, such as arc roots and reignition, which can only be properly studied assuming the plasma as two fluids, one for the arc column and another one for the nearby atoms and molecules in the electrodes, which leads to a non thermal equilibrium state.

By subdividing the plasma in two fluids, each one is characterized by its own temperature: $T_e$ (temperature of the electrons) and $T_s$ (temperature of the heavy particles) [32]. The need for different temperatures for electrons and heavy particles is seen in the relations given at the instant of starting the electric arc, extinction, reignition and in the arc roots. In the vicinity of the electrodes, in a very thin surface layer, temperature falls from the value of the plasma column (typically around 25000K) to the value of the electrode (typically around 3000K). With that temperature of the electrode, the electrical conductivity value is close to zero, so that no current should flow, but the electrode is the main supplier of current to the plasma. This contradiction is solved taking into account that in unbalanced plasmas or without thermal equilibrium, the two previously mentioned temperatures appear. While the temperature of the heavy particles falls, the temperature of electrons is maintained at a high value, so that the plasma keeps being conductor in the situations described.

However, if extinction and reignition are not considered in the analysis, and the arc roots are macroscopically solved, it is possible to simulate the evolution of the arc at a macroscopic scale, by the approach called magnetohydrodynamics. This method considers the plasma as a single fluid. The aim of this type of simulation is to reproduce the influence of macroscopic characteristics of the arc behaviour in circuit breakers, such as: general geometry, venting holes, position, quantity and shape of plates, influence of ferromagnetic materials or Lorentz force.

This way, the MHD method is used for plasmas in equilibrium. According to [33], it can be said that plasma is in LTE, when the following assumptions are fulfilled:

- Thermal equilibrium: the electrons temperature $T_e$ is equal to (or very similar) the heavy particles temperature $T_a$.

- Ionization equilibrium: the electron density, $n_e$, is equal or very similar to the density of electrons that would exist in the plasma, with a unique temperature defined by Saha, $n_{eSaha}$ in [18]. This author describes the degree of ionization of the plasma depending on the temperature, density and ionization energy of the atoms.
- Quasi-neutrality: the plasma is electrically neutral, both globally and locally.

In LV arcs, the three above assumptions are not fulfilled in the arc roots, neither in the zero current when the arc is extinguished. Although these conditions are obviously important, it can be assumed that the LTE assumption is valid for the simulation of the overall behaviour of the arc. However, although arc roots are not going to be analyzed deeply, because of the mentioned reasons, it is advisable to model those arc roots in the electric arc simulation, at least macroscopically. Thus, adopting the LTE hypothesis and, therefore, adopting a single temperature field, "T", and a single average velocity field for the fluid" $\boldsymbol{u}$", for the whole plasma, that plasma can be reduced to a single fluid, simplifying the state equations of each particle.

Thus, the particle density for the whole plasma, $n$, is defined as shown in equation (4-6).

$$n = n_a + n_e \tag{4-6}$$

The density of the plasma, $\rho$, is defined by (4-7).

$$\rho = \rho_a + \rho_e \tag{4-7}$$

The fluid velocity, $\boldsymbol{u}$, is given by equation (4-8).

$$\boldsymbol{u} = \frac{\boldsymbol{u}_a \rho_a + \boldsymbol{u}_e \rho_e}{\rho_a + \rho_e} \tag{4-8}$$

And the current density of the plasma is given by (4-9).

$$\boldsymbol{j} = \boldsymbol{j}_e + \boldsymbol{j}_i + \boldsymbol{j}_{ext} \tag{4-9}$$

Where the subscript "a" refers to heavy particles, the subscript "e" to electrons, "i" to ions and "ext" to external sources to the plasma.

Given the foregoing considerations, transport equations for the conservation of mass, momentum and energy of the plasma as a single fluid are defined, which are known as the modified Navier-Stokes equations, (4-10), (4-11) and (4-12), and describe the relation between the velocity, pressure, temperature and density of a moving fluid. These aspects are developed more in deep below:

- Conservation of mass: within some problem domain, the amount of mass remains constant as mass is neither created nor destroyed. For a fluid (liquid or gas) density, volume and shape can all change in time. Besides, mass can move through the domain, but there is no accumulation or destruction of mass through the domain; the same amount of mass that leaves the domain enters the domain. Thus, conservation of mass equation (4-10), means that the mass flow rate through a domain, or control volume, for computational problems, is constant.

  Adopting the vector notation of the equation, the first term indicates the variation of the density at a point of the space (computational point for simulations) and thesecond term indicates the variation of the same property, i.e. density, related to the change of position, i.e. entering and leaving the control volume.

$$\frac{\partial \rho}{\partial t} + \vec{\nabla}\,(\rho\vec{v}) = 0 \qquad\qquad (4\text{-}10)$$

| Change rate of density in control volume |
|---|

| Difference between the incoming and outgoing mass flow in the control volume |
|---|

- Conservation of momentum: momentum is defined as the product of mass and velocity. The conservation of momentum states that, within some problem domain, the amount of momentum remains constant; as momentum is neither created nor destroyed, but only changes through the action of forces as described by Newton's laws of motion ($F = m.a$). Dealing with momentum is more difficult than dealing with mass and energy, because momentum is a vector quantity having both magnitude and direction. Momentum is conserved in all three physical directions at the same time. It is even more difficult when dealing with a gas because forces in one direction can affect the momentum in another direction due to collisions between molecules.

Thus, in the modified momentum equation of Navier Stokes for the electric arc, (4-11), the first term indicates the local change in the computational point of the control volume of the momentum; the second term expresses the difference of momentum relating to the input and output of the control volume; the third ones indicates the accelerating force by pressure distribution; the fourth one represents the surface forces acting on control volume, composed by two terms (the first one is important for compressible fluid flow, and the second one is important when strong velocity gradients are present); the fifth term, representing the Lorentz force, is the term that relates the electric and magnetic field with the fluid dynamics law (representing the acceleration due to the magnetic field) and finally the sixth term, which represents the gravity's force. It has to be said that this sixth term is usually neglected in LVCB arcs, as it has only importance for superimposed flows, e.g. Free Burning Arcs.

$$\rho\frac{\partial \vec{v}}{\partial t} + \rho(\vec{v}\nabla)\vec{v} = -\vec{\nabla}p + \frac{4}{3}\vec{\nabla}\mu(\vec{\nabla}.\vec{v}) - \vec{\nabla}\times\mu(\vec{\nabla}\times\vec{v}) + \vec{j}\times\vec{B} + \rho.\vec{g} \qquad (4\text{-}11)$$

| Change rate of momentum in the volume control |
|---|

| Pressure gradient |
|---|

| Lorentz force. Interaction term with the magnetic field. |
|---|

| Momentum difference in the incoming and outgoing flow in the control volumen |
|---|

| Surface forces on the control volume |
|---|

| Accelerating gravity force |
|---|

- Conservation of energy: within some problem domain, the amount of energy remains constant, as energy is neither created nor destroyed. Energy can be converted from one form to another (potential energy can be converted to kinetic energy) but the total energy within the domain remains fixed.

So, the third equation of Navier-Stokes (4-12) defines, in the first term the local change rate of the energy in the control volume; the second one the enthalpy difference of fluid entering and leaving the control volume; the third one the work produced by the pressure change and pressure gradient, usually small compared to the enthalpy exchange. On the right side of the equation, the fourth term of the equation shows the heat loss by conduction; the fifth one the heat loss by radiation (highly important in electric arc

formulation and fully explained later in this section); the sixth one the viscous dissipation term; and the seventh one the electric energy dissipation in the control volume due to ohmic heating, additional term relating the fluid dynamics once again with the electric field.

$$\rho \frac{\partial H}{\partial t} + \rho(\vec{v}.\vec{\nabla})H - \frac{\partial p}{\partial t} - (\vec{v}.\vec{\nabla}p) = \vec{\nabla}.\frac{\lambda}{c_p}\vec{\nabla}H - \vec{\nabla}.\vec{q}_R + \Phi + \vec{j}.\vec{E} \qquad (4\text{-}12)$$

| | |
|---|---|
| Variation rate of enthalpy in the control volume | Work produced by the pressure change and pressure gradient |
| | Conductive heat loss |
| | Ohmic heating input in the CV |
| | Viscous dissipation term |

Enthalpy difference in the incoming and outgoing flow in the control volume

Radiative heat loss

being Φ the viscous dissipation factor (usually neglected), expressed as (4-13.)

$$\Phi = \Sigma \left[ \mu \left( \frac{\partial v_i}{\partial x_j} + \frac{\partial v_j}{\partial x_i} \right) - \frac{2}{3}\mu \frac{\partial v_k}{\partial x_k} \delta_{ij} \right] \frac{\partial v_i}{\partial x_j} \qquad (4\text{-}13)$$

where:

| | |
|---|---|
| $\rho$: | gas density |
| $\vec{v}$ : | gas velocity |
| $t$: | time |
| $p$: | pressure |
| $\mu$: | viscosity |
| $\vec{j}$ : | current density |
| $\vec{B}$ : | magnetic flux density |
| $\vec{g}$ : | gravity acceleration |
| $H$: | gas enthalpy |
| $\lambda$: | thermal conductivity |
| $c_p$: | specific heat at constant pressure |
| $\vec{E}$ : | electric field |

This way, when applying Navier-stokes modified equations to arc plasma, specifically in momentum equation (4-11) and energy equation (4-12), electromagnetic terms must be specified representing ohmic heating and Lorentz force interaction with fluid dynamics. Therefore, Maxwell's laws have to be solved at the same computational time of Navier-Stokes and thus, equations (4-14) to (4-20) must be added to the problem solution.

Electric potential:

$$\vec{E} = -grad\phi \qquad (4\text{-}14)$$

Maxwell equations:

$$rot\vec{H} = \vec{J} + \frac{\partial \vec{D}}{\partial t} \tag{4-15}$$

$$rot\vec{E} = -\frac{\partial \vec{B}}{\partial t} \tag{4-16}$$

$$div\vec{B} = 0 \tag{4-17}$$

$$div\vec{D} = \rho_e \tag{4-18}$$

Besides, the magnetic field can be calculated with the vector potential formulation (4-19) or following Biot-Savart (4-20).

$$\vec{B} = rot\ \vec{A} \tag{4-19}$$

$$\vec{B} = \frac{\mu_0}{4\pi} \iiint \frac{(JdV)xr}{r^3} \tag{4-20}$$

where:
$\vec{H}$:      magnetizing field
$\vec{D}$:      displacement field
$\rho_e$:      charge density

Most of the time, the choice between one of those two formulations for the magnetic field calculation is determined by the characteristics of the software. In any case, it is important to mention that the computational cost of Biot-Savart formulation is higher. In the case of simplified models, there is the possibility of neglecting the calculation of the magnetic field and consider it external and constant.

Figure 4-10 shows the physical processes, fluid dynamics and electromagnetism interaction that takes place in the electric arc.
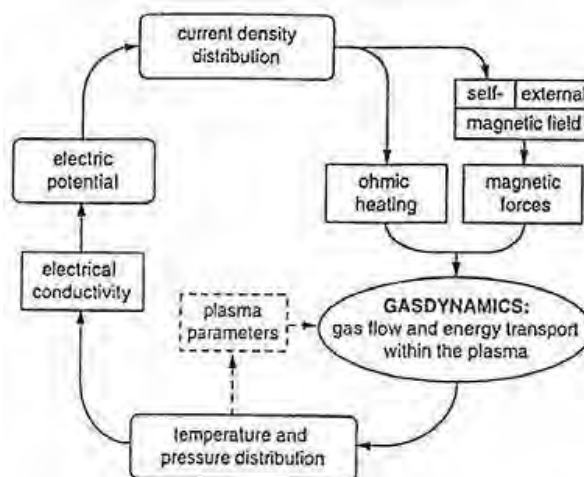


Figure 4-10 Interaction of physical processes in the arc column [34]

The electric arc current from the arc causes ohmic heating by Joule effect and the appearance of magnetic forces. Due to self inducted or/and external magnetic fields, the movement of gas and energy transport in and out of the plasma is produced. These aspects modify the distribution of temperature and pressure inside the chamber. As a result, the

value of electrical conductivity and other physical properties of the plasma, such as thermal conductivity, viscosity, density and specific heat are also modified. Meanwhile, the distribution of electric conductivity determines the distribution of voltage and current density in the chamber.

Finally, an important phenomenon in the magnetohydrodynamic description, that deserves to be treated deeper, is the radiation heat transfer from the arc, represented by the radiative loss term in the energy equation.

### 4.2.3.2 Radiation

As seen, conservation of energy equation (4-12) includes heat transfer terms due to conduction, convection and radiation. But radiation is the most powerful mechanism for heat transfer in plasma due to its temperature dependence and the high temperature values in the electric arc phenomena, which ranges from 10000K to 30000K [32]. Thus, an additional radiation contribution to the heat term, $\nabla q_R$, in the energy conservation equation is added, as shown in equation (4-12).

Radiative transfer is defined as the physical phenomenon of energy transfer in the form of electromagnetic radiation. The propagation of radiation through a medium is affected by absorption, emission and scattering. In order to represent mathematically this phenomenon in LVCB electric arcs three different models are usually used: P1, NEC and NECS. But, to be able to understand the background of this phenomenon, it is necessary to start from the most general radiation approach known as Radiative Transfer Equation (RTE). RTE models the energy transfer as an integrodifferential equation. In this case, the conservation of the radiative energy along a ray path of direction $\hat{s}$ is given by equation (4-21) [35] [36].

$$\left.\frac{dI_v}{ds}\right|_{\hat{s}} = \nabla I_v|_{\hat{s}} \cdot \hat{s} = k_v I_{bv} - \beta_v I_v + \frac{\sigma_{sv}}{4\pi}\int_{4\pi} I_v\left(\widehat{s_\iota}\right)\Phi(\widehat{s_\iota},\hat{s})d\Omega_i \tag{4-21}$$

where:

| | |
|---|---|
| $I_v$: | spectral radiative intensity, intensity of radiation at a certain point in a direction $\hat{s}$ at a frequency $v$. |
| $k_v$: | absorption coefficient |
| $I_{bv}$: | emission of the fluid at a certain point, at a frequency $v$, for a black body defined by Plank's law |
| $\sigma_{sv}$: | scattering coefficient. |
| $\beta_v = k_v + \sigma_{sv}$: | extinction coefficient |
| $\Phi(\widehat{s_\iota},\hat{s})$ : | phase function |
| $d\Omega_i$: | solid angle |

The equation above represents the net balance of the spectral radiative intensity $I_v$ along a propagation direction $\hat{s}$. In the left side term, the increment of $I_v$ is represented by its gradient, while in the right side of the equation the contributions which produce such a net increment are summed up. There, the first term represents the absorbed part of the ideal black body emitted radiation. The second one the power losses represented by the absorbed and scattered spectral radiative intensity. Finally the third term represents the scattering from other directions than $\hat{s}$ over the solid angle.

The difficulty in obtaining numerical solutions for equation (4-21) is the large number of variables for the radiative intensity. Thus, $I_v$ needs three variables for space r, two for direction $\hat{s}$ and one for the frequency $v$. So, a high computational time is needed. However, applying the following simplifications, a more manageable model, $P_N$, is obtained:

- Scattering can be neglected because the size of the particles is much smaller than the wave lengths present. Following [37], $\sigma_{sv} = 0$, so the last term of equation (4-21) is neglected and $\beta_v$ is replaced by $k_v$, resulting equation (4-22).

$$\left.\frac{dI_v}{ds}\right|_{\hat{s}} = \nabla I_v|_{\hat{s}}.\hat{s} = k_v(I_{bv} - I_v) \tag{4-22}$$

- The frequency dependence is handled by splitting the radiative spectrum into grey bands (usually five or six).

- The radiative intensity can be expressed as a Fourier series which separates the radiative intensity variable in two: one depending on coordinates and the other one depending on the direction, as shown in equation (4-23).

$$I_v(r,\widehat{s}) = \sum_{l=0}^{\infty}\sum_{m=-l}^{l} I_l^m(r)Y_l^m(\hat{s}) \tag{4-23}$$

where:

$I_l^m(r)$:         position coefficients
$Y_l^m(\hat{s})$:         spherical harmonics.
$l \, and \, m$:         coordinates $\in S^2$

- Taking only the first term of this Fourier series, N=1 [35], the radiative intensity $I_v$ can be related to the incident radiation $G_v$ (radiation at a specific surface), which leads to the P1 model for the incident radiation $G_v$, as shown in equation (4-24).

$$\nabla\left(\frac{1}{k_v}\nabla G_v\right) = 3 \, k_v(G_v - 4\pi I_{bv}) \tag{4-24}$$

This Helmholtz type governing equation is solved by a finite volume discretization. Thus, P1 is the more precise, stable and realistic radiation model among the three methods used. That radiation model has been used in this thesis for the new model presented in chapter 5.

A second way to calculate the radiation, less expensive from a computational point of view, is to represent radiation with the so called Net Emission Coefficient (NEC) method [38]. This method is characterized by converting radiated power in a function of local properties of the fluid, as temperature and pressure. This means that the radiation model is completely local, where any point or node of the fluid irradiates energy, although the reabsortion of the irradiated energy is completely neglected. This is the limit of the optically thin plasma. Due to its great simplicity and extremely reduced computational cost, the NEC can be used in arc simulations. A NEC ($\varepsilon_N$) corresponds with the difference between the energy emitted in the centre of an isothermal sphere of radius $R_p$ and the energy emitted by all the other points of the sphere and absorbed by the central point. Thus, it is defined as shown in equation (4-25).

$$\varepsilon_N = \int_0^{\infty} B_V K_p' \exp\left(-K_p' R_p\right) dv \tag{4-25}$$

where:

$v$:      frequency
$B_V$:      Plank's function
$K_p'$:      monochromatic absorption coefficient

NEC models have been considered by several researchers and references can be found for their values in plasma air, as a function of temperature and pressure for different values of $R_p$. For the ideal case of optically thin plasma $R_p = 0$ can be considered [37-41]. However,

this model is generally considered inadequate because, in the real context, the heat radiated interacts with other fluid spots encountered along the radiation direction, before being dissipated of the computational domain. This is known as radiation with participating media and needs a much more complex, non local, model.

A third approach for the radiation definition, based on a simplification of the exposed NEC is the Net Emission Coefficient Simplified (NECS) method [3]. The computational cost is lower, but the precision of the calculation is also lower as NECS represents a linearization of the previously presented NEC (Figure 4-11). The simplified emission coefficients (ε) are calculated as shown in equation (4-26).

$$\varepsilon = A(e^{BT} - e^{BT_r}) \tag{4-26}$$

where:

$A$:       constant coefficient, 300 [W/m^3]
$B$:       constant coefficient, 0,0011 [1/K]
$T_r$:     room temperature, 300 [K]
$T$:       temperature

Thus, a negative source term including the NECS from equation (4-26) is defined in the energy conservation equation (4-12), as exposed in equation (4-27).

$$S_{rad} = -\varepsilon \tag{4-27}$$
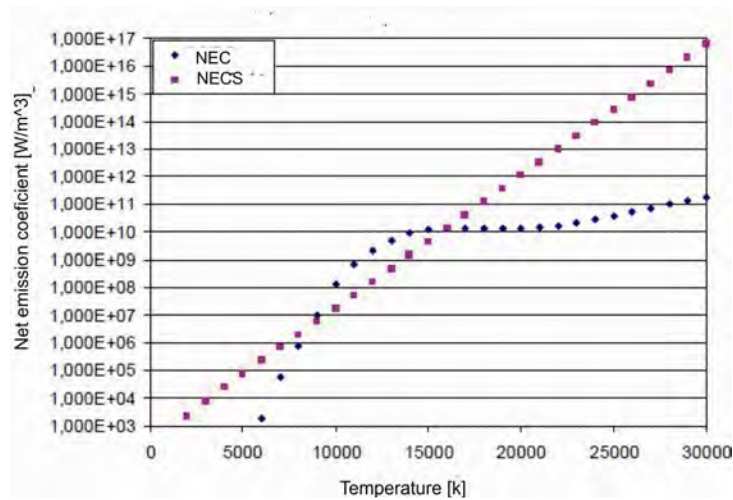


Figure 4-11 Value of the Net Emission Coefficients (NEC) and Simplified Net Emission Coefficients (NECS) [3]

The main weakness of NEC, and consequently of NECS, is that the absorption of energy is not taken into account but only the emission. For that reason, they are very efficient methods numerically, that is, computational time is low, but not very accurate. They do not provide the mechanism for the interaction between the arc and the surrounding medium and boundaries.

This way, looking for the best precision in the model presented in this thesis, P1 radiation model has been chosen for the radiation approach of the new electric arc model developed [42].

## *4.2.3.3 Arc roots*

The arc roots phenomenon is also important, due to its complexity and its influence on the arc process. The arc roots are produced on the interface of the electrodes or the splitter plates with the plasma. The importance of the roots in the arc behaviour is due to their influence on the formation, maintenance and extinction of the arc, as they provide the necessary metal vapours and charge carriers to initiate and sustain the electric arc. Additionally, the arc roots on the splitter plates and plasma interface influence the extinction of the arc helping to increase the arc voltage.

The physical behaviour, at a micro-scale, of the interface between the electric arc and metallic conductors is very different to the behaviour of the arc plasma column. Figure 4-12 shows the processes that cause the movement of the arc roots along the electrodes. Basically, the metallic conductor is heated by the current flowing through it and by the plasma flow, thus a displacement of the roots happens in the direction of the flow.
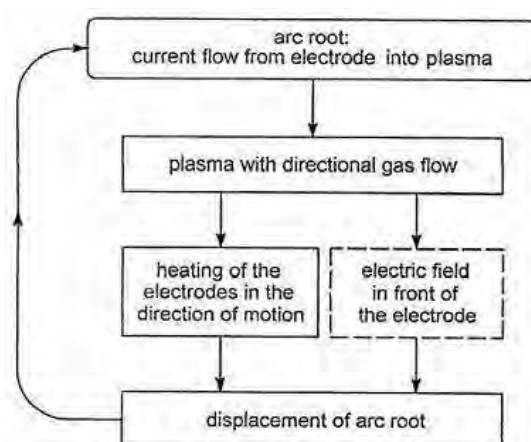


Figure 4-12 Movement of the arc roots along the electrodes [34]

The behaviour of the electric arc on the electrodes, rails or splitter plates, where arc roots are formed, has to be described by means of the non equilibrium theory. Thus, LTE cannot be applied if the process is analyzed at micro-scale. However, the outcome from a macro-scale arc root model is a localized voltage drop at each arc root spot and so it does affect the total arc voltage. As seen in Figure 2-9, the total arc voltage is the result of the sum of the voltage drops in the arc column, anode and cathode. Thus, as the arc voltage has to be greater than the electric circuit voltage, in order that the interruption is successful, the current technology employed to produce current limiting circuit breakers and to extinguish LV arcs is based on the exploitation of localized voltage drops at the arc roots. This situation is obtained by increasing the arc voltage with the creation of new anodes and cathodes, and so their associated voltage drops, at the surface of the splitter plates.

The cross-section of the arc-electrode attachment zone is considerably smaller than the typical one of the arc column. Between the arc column and the electrode surface, i.e. in the arc root, a constriction zone is identified. So, a stratified structure can be defined, with different physics models for each layer, as shown in Table 4-3.

Inside the constriction zone, current density increases close to the electrode, due to the narrowing of the arc cross section, and finally, in the constricted plasma (CP) layer it becomes comparable to the typical values found at the electrode surface. Heat produced by Joule heating ($jE$) is mainly removed by means of radiation $\nabla q_r$. Other forms of heat transfer,

such as conduction, convection and enthalpy transport by diffusion of species, play a minor role.

Table 4-3 Layers in the arc roots [32]

|  | $n_e = Z_i n_i$ | $n_e = n_{Saha}$ | $T_e = T_h$ | $j.E = \nabla.q_r$ |
|---|---|---|---|---|
| Arc column Constricted zone Constricted plasma (CP) | LTE | | | yes |
| Layer of thermal perturbation | yes | yes | yes | no |
| Layer of thermal non-equilibrium (TN) Ionization layer (IL) Space-charge sheath (SH) | yes yes no | yes no no | no no no | no no no |
| Electrode | not applicable | | | |

Closer to the electrode, the effect of heat removal by means of conduction inside the metallic body begins to be non-negligible, and the radiation is no longer the dominating heat transfer mechanism. Thus, the LTE hypothesis must be discarded when dealing with the layers next to the electrode surface. Looking closer to the electrode, a first layer of thermal non-equilibrium is present, with electron temperature $T_e$ different from heavy particle temperature $T_h$. Then, ionization layer is formed, where the electron density $n_e$ differs from that predicted by means of the Saha equation.

Finally, a space charge sheath appears and the plasma is no longer quasi neutral. The cathode and the anode have a space charge sheet of opposite sign. Each electrode with its own space charge sheath behaves like a capacitor.

It can be said that the two electrodes do not behave symmetrically. First, due to the mass difference between electrons and ions, with the consequent difference in their mobility. Secondly, because the electrons that leave the cathode, run through the arc plasma, later on are reabsorbed by the anode and finally are available for flowing as current into the connected network, while ions only move from the anode to the cathode.

The strong electric field present in the sheat layer is responsible for accelerating both, electrons emitted from the cathode and ions coming from the ionization layer. Electrons are repelled from the electrode, while ions are attracted. It is the kinetic energy gained by electrons from the electric field in the sheat layer that enables them to ionize neutral molecules when they are in the ionization layer, providing the required ionization energy. Since light and heavy charged particles, i.e. electrons and ions, behave different in an electric field, the relevant species exhibit different properties and the LTE hypothesis is no longer applicable.

## 4.3   STATE OF THE ART OF PHYSICAL MODELS FOR LVCBS

Modelling the electric arc behaviour is a highly complex task due to the difficulty of obtaining a model that accurately represents all the characteristics of the real phenomenon. However, given the difficulty of obtaining values for some physical magnitudes of the arc experimentally, modelling their behaviour by a software tool is of great interest. It can provide more complete, easy, manageable and economical information. Various proposals exist, even though no one provides all the physical aspects involved in the electric arc yet.

Thus, this section presents the state of the art of previous research work about modelling and simulation of the behaviour of LVCBs. References have been classified in two different groups:

- Arc modelling to calculate the magnetic field and the magnetic forces acting on the arc.
- Detailed developments of arc models using magnetohydrodynamics.

### 4.3.1   MAGNETIC FIELD AND MAGNETIC FORCES CALCULATION ON THE ARC

The complexity of the detailed modelling of the electric current interruption physical phenomena has lead to some proposed models to adopt a simplified approach. In these models, only the magnetic field distribution in a stationary position is calculated, with the aim of evaluating the magnetic forces acting on the electric arc and analyzing the influence of factors, such as the magnitude of the current or the arrangement of plates in the arc chamber. But unlike MHD models, the movement of the plasma flow is not taken into account.

Among the advantages of these models, their simplicity compared to MHD models can be pointed out. As fluid dynamics is not considered, the definition of the problem, as well as the computational resolution, is much easier. On the other hand, leaving aside the fluid mechanics phenomenon causes that the model is not a true reflection of a real scenario.

A first example is presented in [43] and [44], where an iterative process to calculate the evolution of the electric arc in a magnetic air circuit breaker, by a 2D FEM model, is proposed. As a result, the magnetic field generated by the current is obtained. From that parameter, the magnetic force acting on the arc is evaluated, together with the aerodynamic force that causes its displacement (aerodynamic model). In every iteration, the current is calculated from the cross section of the arc, which is obtained by computing the energy balance of the arc column (electro thermal model) and defined by the heat of the arc column. Figure 4-13 shows the result obtained for the evolution of the arc, for different time instants. It is perceived the translation of the arc along the electrodes and the corresponding elongation.
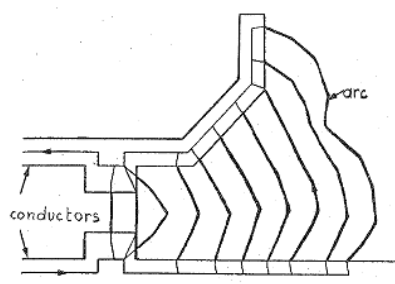


Figure 4-13 Evolution of the arc inside the chamber [43, 44]

Additionally, in [45-47], by a 3D FEM application, repulsive forces between contacts and magnetic blow forces acting on the arc during the interruption of fault current are discussed, for a MCCB (Figure 4-14). The arc is modelled as a homogeneous conductor with a conductivity of $10^{-4}\sigma_c$ (where $\sigma_c$ is the conductivity of the conductors) and with different diameters, depending on the magnitude of the current (Table 4-4). Figure 4-14 and Figure 4-15 show an example of the models developed.

Table 4-4 Relation between current and arc diameter [45-47]

| Current (A) | Arc diameter (mm) |
|---|---|
| 100 | 5 |
| 600 | 8 |
| 900 | 9 |
| 1200÷2400 | 10 |
| 5000 | 16 |
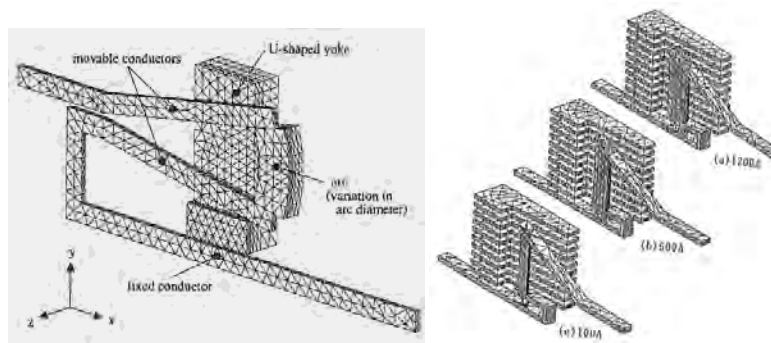


Figure 4-14 Models developed for the study of magnetic forces [45-47]
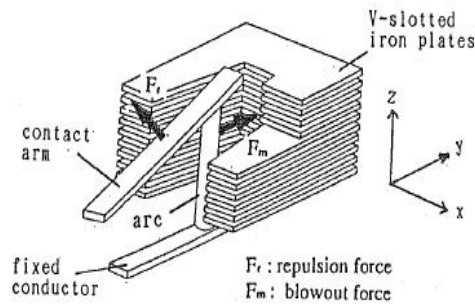


Figure 4-15 Contact system in a modelled circuit breaker [45-47]

Figure 4-16 and Figure 4-17 show the results obtained in the simulation of the model explained above, regarding distribution of flux density B and magnetic force, respectively.
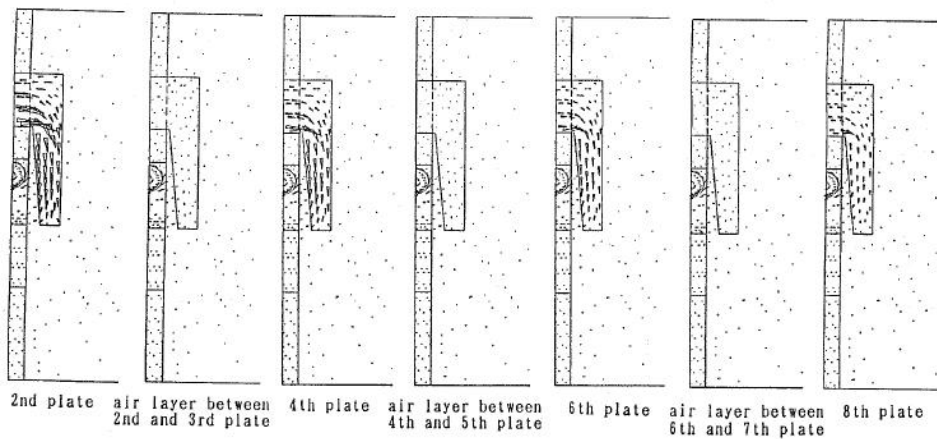


Figure 4-16 Distribution of flux density in the splitter plates of the arc chamber [45-47]
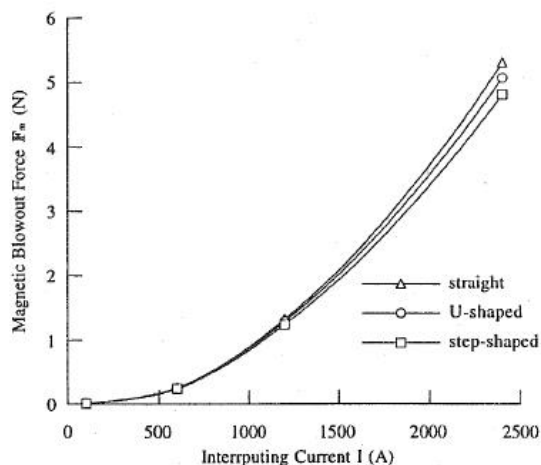
Figure 4-17 Magnetic force applied on the electric arc as a function of current and contacts configuration [45-47]

Another example of the application of the FEM for the study of the magnetic forces on the arc is proposed in [48] for a MCB. The arc is modelled as a section of a rectangular prism, considering the reduction in the cross sections at both ends of the arc (Figure 4-18). In this model, the current is assumed to be homogeneously distributed in the arc column. For the arc chamber, two parallel arc rails with no plates are only considered. The value of the arc current is obtained by applying a voltage difference in the circuit and executing a static analysis, using the values of Table 4-5. Finally, the calculated current is used to obtain the magnetic flux density, the magnetic field distribution and the force acting on the arc.

Table 4-5 Values used in the analysis [48]

| Magnitude | Numeric value |
|---|---|
| Conductivity copper | $6 \times 10^7$ S/m |
| Conductivity steel | $10^7$ S/m |
| Conductivity arc roots | $25 \times 10^3$ S/m |
| Conductivity arc column | $14 \times 10^3$ S/m |
| Applied voltage | 60 V |
| Calculated current | 400 A |
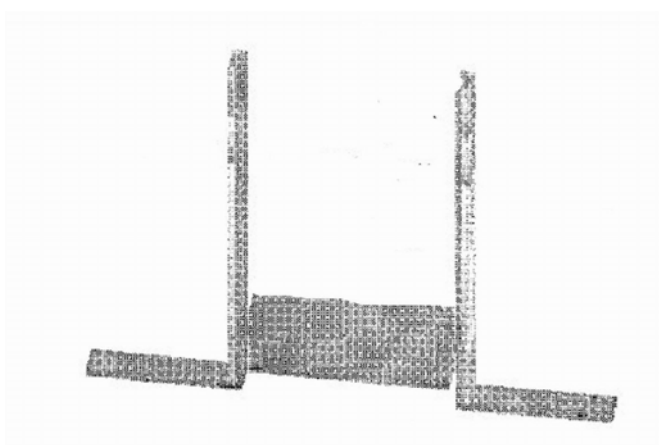


Figure 4-18 Modelled geometry of the arc in a MCB [48]

Moreover, in [49] the analysis is focused on the influence of the splitting plates located inside the extinction chamber in the trajectory described by the arc. The arc, in this case, is considered as a current filament of infinite length, being analyzed its motion in a transverse plane. Besides, the plates are substituted by planes of infinite thickness. After the arc

penetrates in the area of the plates, where division occurs, it is considered that the arc consists of multiple arcs of reduced length, arranged between the plates on a common shaft.

The problem of the arc movement is treated different in the case it is located outside or inside the plate, by defining the appropriate boundary conditions for the magnetic vector potential in each case. Figure 4-19 shows an example of the arc trajectory that is obtained by applying the proposed model to one of the geometries analyzed, depending on the ignition point of the arc.
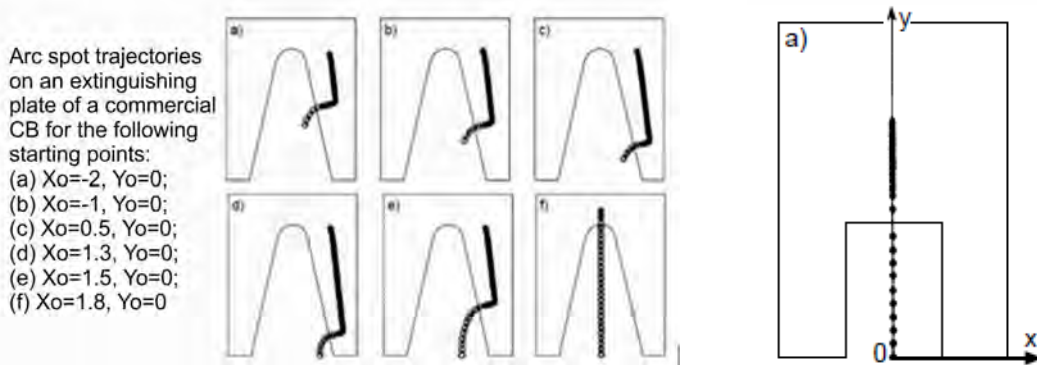


Figure 4-19 Trajectory of the arc root on the extinction plates, for different locations of the ignition point [49]

Another analysis using the FEM, regarding the magnetic force acting on the arc inside the arc chamber of a MCCB, is presented in [22]. In this paper, it is proved that magnetic blowout forces and the distribution of the magnetic field induced by arc current depend on the shape, arrangement and material used in the chamber. Different thicknesses and angles of inclination of the plates (Figure 4-20 and Table 4-6), and different currents (3kA, 15kA and 9kA) have been considered for the model. Also, four different splitter plate combinations have been considered and the arc is modelled as a conductor of 10mm diameter, as shown in Figure 4-20 and Table 4-6.
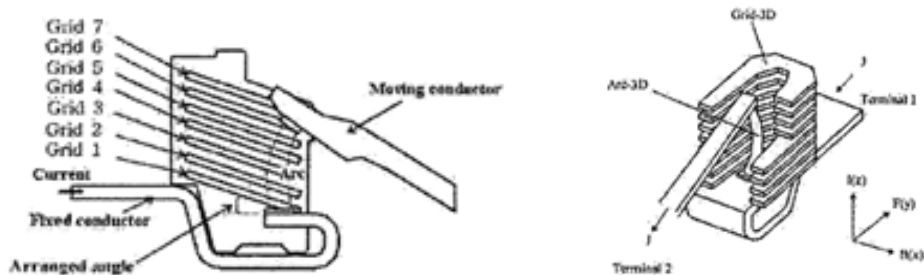


Figure 4-20 Arc chamber on MCCB [22]

Figure 4-21 shows an example of the flux density distribution obtained in the simulation. From the results obtained, the magnetic force acting on the arc is determined for each plate configuration. The highest value obtained for configuration 3 determines its superiority over the other configurations, which is confirmed qualitatively by experimental tests as a shorter interruption time is obtained with this configuration. It is also worth to be noticed the influence of the different thicknesses, angles and arrangements of the plates in the chamber in the results, as shown in Table 4-7, where it can be seen that the magnetic force is higher when the thickness of splitter plates 2 to 7 is reduced.

Table 4-6 Arrangement of the arc plates considered in the analysis [22]

| | Feature | Conditions |
|---|---|---|
| **Model 1** | | Grid 1- Grid 6: Thickness (2mm)<br>Angle of distribution: 20 degree |
| **Model 2** | | Grid 1- Grid 6: Thickness (2mm)<br>Angle of distribution: 20 degree |
| **Model 3** | | (a) Grid 1: Thickness (2mm)<br>(b) Grid2-Grid7: Thickness (1.6mm)<br>Angle of distribution: 20 degree |
| **Model 4** | | (a) Grid 1: Thickness (2mm)<br>(b) Grid2-Grid7: Thickness (1.6mm)<br>Angle of distribution: 15 degree |
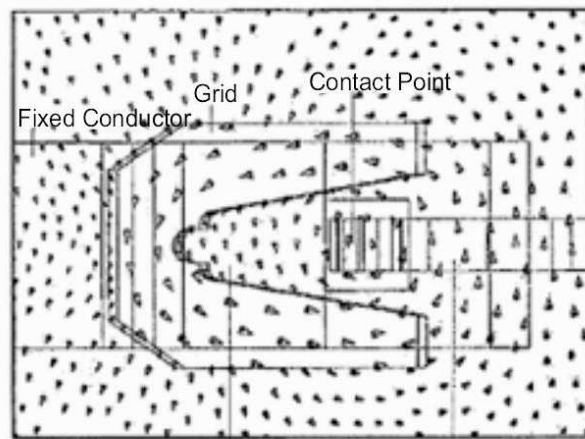


Figure 4-21 Magnetic flux density distribution on a splitter plate [22]

Table 4-7 Magnetic blowout force for different splitter configurations [22]

| Magnetic blowout force [N] | |
|---|---|
| Model 1 | 42.3 |
| Model 2 | 54.7 |
| Model 3 | 105.2 |
| Model 4 | 70.8 |

Finally, the electrodynamic forces acting on the electric contacts at the opening instant are analyzed, also by FEM in [23] for a commercial LVCB model (Figure 4-22). The result of the study shows that there is a significant magnetic force component in the "x" direction (Figure 4-23). Besides, Figure 4-24 shows the variation in the intensity of the force calculated. As shown, in absence of permeable material the strength value varies with the square of the current. However, when considering plates of ferromagnetic material, the material reaches saturation at a certain current value, reducing the magnitude of the acting force.
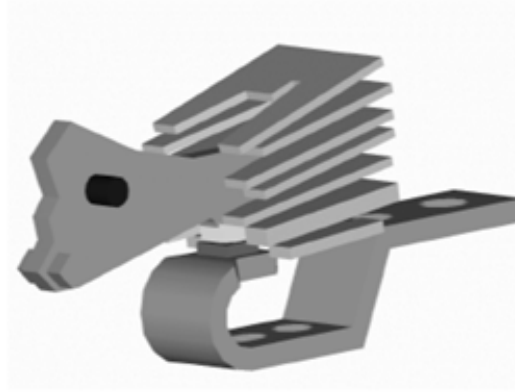
Figure 4-22 Geometry of the analyzed LVCB [23]
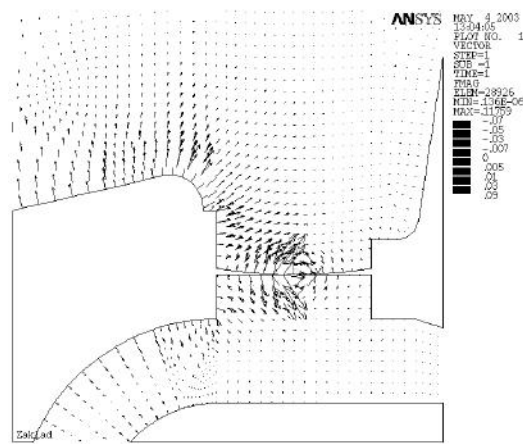


Figure 4-23 Magnetic force distribution [23]
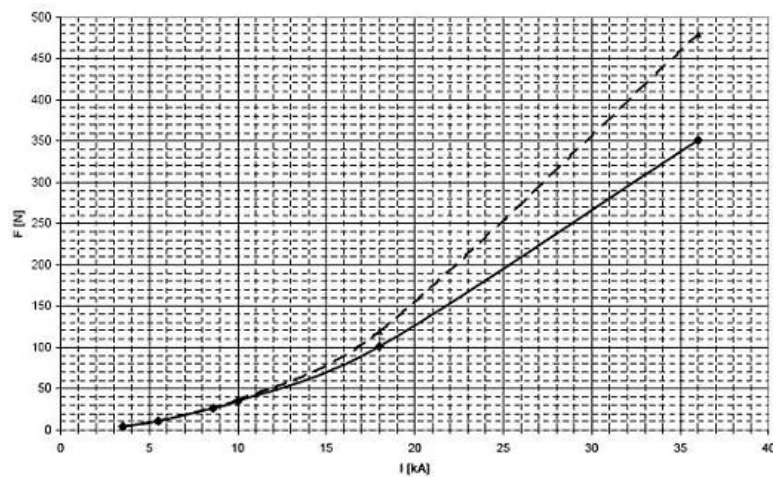


Figure 4-24 Saturation effect on the calculated force [23]

Summarizing, Table 4-8 shows the main characteristics of the electromagnetic models exposed above. As it can be seen, they do have some common characteristics, as most of them use a FEM software tool for the analysis. Also, they compute the electromagnetic field and model the electric arc applying simplified approaches. The magnetic force appearing on the arc is calculated as well as the trajectory of this arc along the arc chamber in some of them.

Table 4-8 Magnetic and electric physical models review

| Reference | Software | Geometry | Models | Computed | Result analyzed |
|---|---|---|---|---|---|
| [43, 44] | FEM | 2D | Arc= cylindrical wire with cross section as a function of the heat of arc column | Magnetic field (Biot-Savart) Current and field distribution | Prediction of movement of the arc under electromagnetic forces |
| [45-47] | FEM | 3D, ½ symmetry | Arc= cylindrical wire with diameter given by current value | Electromagnetic field | Electromagnetic forces on the contacts 3D current and flux distribution |
| [48] | FEM | 3D | Arc= solid rectangular prism with homogeneous current distribution | Electromagnetic field | Magnetic forces on the arc Prediction of the position of the arc |
| [49] | Boundary element method | 3D | Arc=current filament of infinite length Plates=steel, infinite thickness | Magnetic field by magnetic force potential | Arc spot trajectories across and field potential distribution on rectangular ferromagnetic plates |
| [22] | FEM | 3D | Four splitter plates arrangements Arc= 10mm diameter cylinder | Electromagnetic field by vector potential | Magnetic force Flux density Comparison between different splitter plates arrangements |
| [23] | FEM Ansys | 3D, No symmetry | Ferromagnetic plates | Electromagnetic field by vector potential | Magnetic force |

But, as it has been pointed out, these models are incomplete as they only consider half problem, i.e., the electromagnetic part, but no fluid flow model is considered. Thus, the existent magnetohydrodynamic models are exposed below.

## 4.3.2  MAGNETOHYDRODYNAMIC MODELS

As explained in section 4.2.3.1, MHD models take into account both electromagnetic field and fluid flow description and their interaction, being much more complete than those described in the previous section. However, the development of this type of models is a difficult task. First of all, a good knowledge of the phenomena is necessary, a precise use of the software tool where the model is going to be implemented is also required and finally, obtaining verification for the model can be also hard, as specific laboratory material is needed.

Additionally, the research in this field is specially developed by manufacturers such as Siemens and Schneider electric, which are usually reluctant to share the results obtained, and so little research work on this topic is published. On the other hand, considering the academic groups researching on electric arc MHD models, the knowledge is mainly

concentrated in: TU Braunschweig (Germany), Xian University (China), Paul Sabatier University (France) and TU Ilmenau (Germany).

The references found in this field reflect general characteristics for the models proposed and also the results and conclusions are set out in broad outline.

### 4.3.2.1 Academic models

#### A) Technical University of Braunschweig (Germany)

The group of Technical University of Braunschweig has been identified as the one with the longest experience on the field. Their research field is focused on MHD simulations with parallel and divergent rails, analyzing the arc splitting process in the splitter plates and verifying the results by real experimental tests. Their first publication dates from 1998 by Karetta [50]. In this paper, the geometry shown in Figure 4-25 with parallel arc runners is considered.
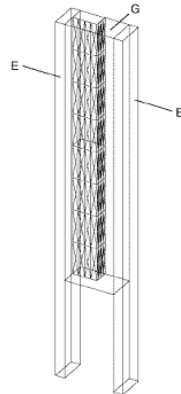


Figure 4-25 Geometry for the LVCB with parallel electrode rails, and 1/4 symmetry applied [50]

This first model was developed with FLOW3D software to implement the fluid flow conservation equations, but the modified terms due to the electromagnetic interaction had to be implemented by the user through a coupling with a FEM software. Meshing data are not provided. The magnetic field has been calculated with the Biot-Savart law, due to the software's needs. Finally, for the radiation heat term presented in energy equation (4-12), a simplified approach defined by the user is applied, as shown in equation (4-28).

$$Sr = 4\alpha k \Delta T^4 \qquad (4\text{-}28)$$

where:
$Sr$:     radiative source added in the energy equation
$\propto$:     Stefan-Boltzmann constant
$k$:     absorption coefficient
$\Delta T$:     difference between arc and room temperature

For the arc ignition, the model is started by a steady-state calculation to obtain the initial distribution of temperature and current flow, without considering the effect of magnetic forces in the simulation. Then, with the results from the steady state the magnetic field is also considered and for the first time, time evolution of the arc position, arc voltage and pressure level, temperature distribution and flow velocity are analyzed.

As an example of the results, Figure 4-26 shows the temperature distribution obtained in the simulation, where the movement of the arc along the proposed geometry over time can be

seen. The arc is represented by temperature, as it is known that only in the gas flow over 10000K there will be current carriers, so that is the location where the arc plasma is.
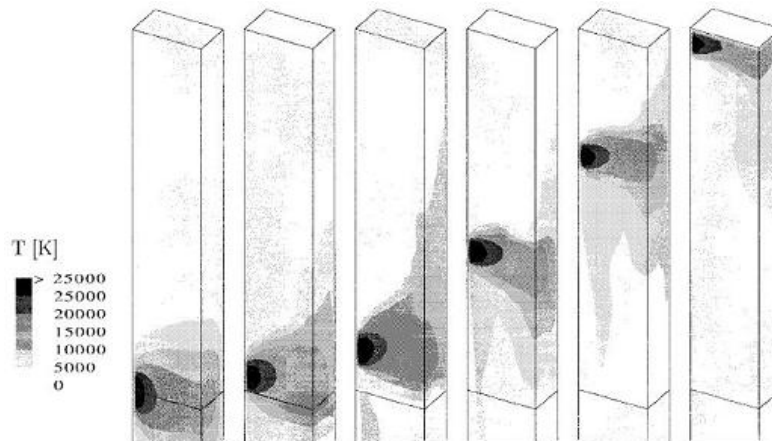


Figure 4-26 Temperature distribution obtained in the simulation [50]

All the simplifications exposed, plus the ¼ symmetry applied for its resolution, make the model quite simple and no real tests were done to validate it. However, it is important to highlight this reference as an early attempt to simulate the arc movement where gasdynamic and electromagnetic processes are coupled.

A new model developed by the same researchers is presented in [34]. The arc movement between two diverging elements is simulated (Figure 4-27), in order to evaluate the effect of the arrangement of different types of barriers at the end of the arc chamber (open, closed, vent). Similar assumptions to those adopted in the previously exposed reference [50] are considered, but in [34] also experimental tests are developed for comparison with simulation results.
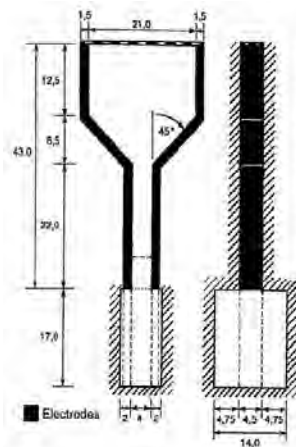


Figure 4-27 Model with divergent electrodes [34]

Figure 4-28 shows an example of the temperature distribution for a 40% opened chamber and Figure 4-29 the influence of ventilation on the movement of the arc. It can be concluded that an opened chamber is more effective, as the movement of the arc is faster. That means that the arc arrives sooner to the splitter plate stack, and so, the arc division, the arc voltage rise and finally the extinction are obtained in a shorter time.
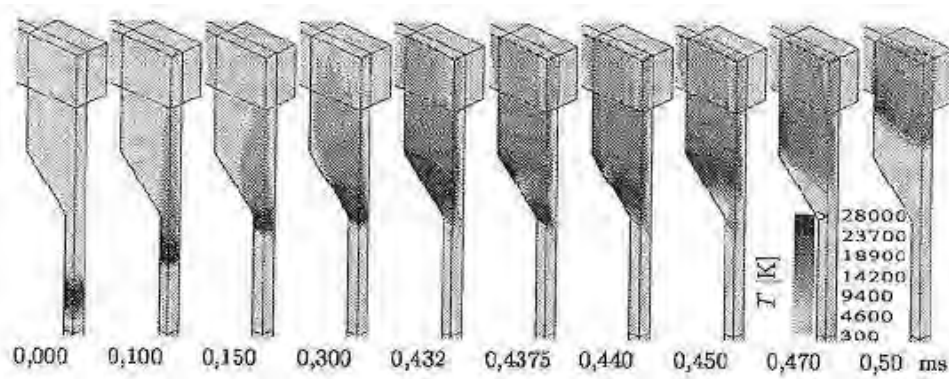
Figure 4-28 Time evolution of temperature distribution with 40% opened chamber [34]
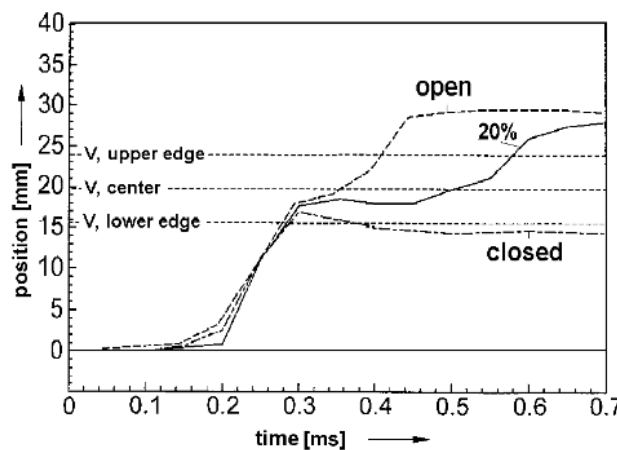


Figure 4-29 Simulated arc position in chambers with different cross-sections of the vents [34]

Reference [51] introduces a change in the software used to implement the model, from FLOW3D used in the previous two cases to CFX5. However, this software CFX5 still needs the coupling with a FEM software for the electromagnetic implementation. Regarding the magnetic field, due to the software requirements, the calculation method is changed from Biot-Savart to Vector potential formulation. The other assumptions and settings are maintained as in [50] and [34], but with experimental results for both geometries.

An example of the temperature distribution obtained for a quarter of geometry is shown in Figure 4-30. However, results are not in good correspondence with the experimental results (Figure 4-31), so the model still needs to be improved.
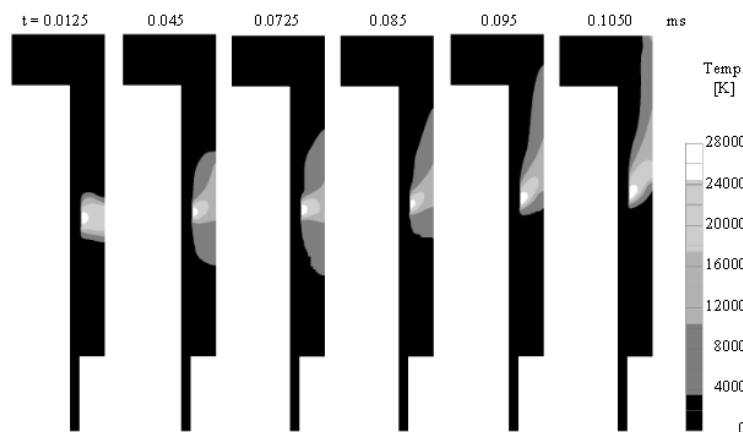


Figure 4-30 Temperature distribution over time [51]
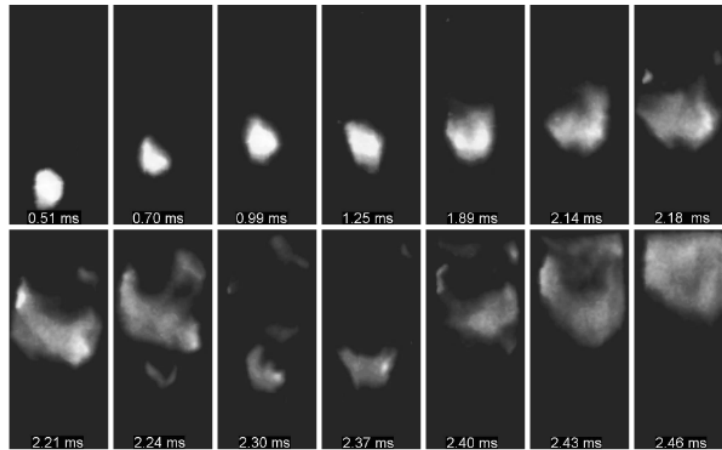
Figure 4-31 High-speed film of arc, ignition by wire at 500 A [51]

The influence of ferromagnetic material is analyzed in [52]. The geometry, presented in Figure 4-32 includes U-shaped profiles of ferromagnetic material on the parallel electrodes to assess the effect of intensification of the magnetic field.
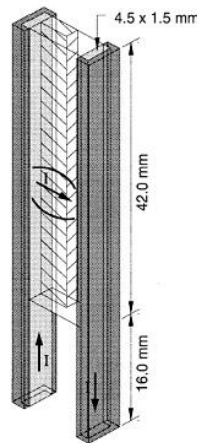


Figure 4-32 Model with parallel ferromagnetic electrodes [50-52]

The boundary conditions considered include that the heat flow at the interface electrode/plasma remains invariable, limiting the value of the temperature during the calculation process to 3.000 K, which is the boiling point of copper. The current imposed in the simulation is distributed on the boundary electrode/plasma by considering a weight factor. This factor represents the temperature dependence of thermionic emission mechanism, so only high temperature areas contribute to the emission intensity, constituting the roots of the arc. In this case, flow equations have been solved with an old version CFX software that allows ferromagnetic analysis. Double symmetry planes are applied, so only one quarter of the geometry is modelled. The results, showing the arc position for different ferromagnetic arrangements, display that the arc movement is faster, the higher the ferromagnetic presence (curve C in Figure 4-33).

Also, the arc development is recorded with a high speed camera (Figure 4-34), showing its real movement in a simplified chamber, where the chaotic and no symmetric shape of the arc can be highlighted.
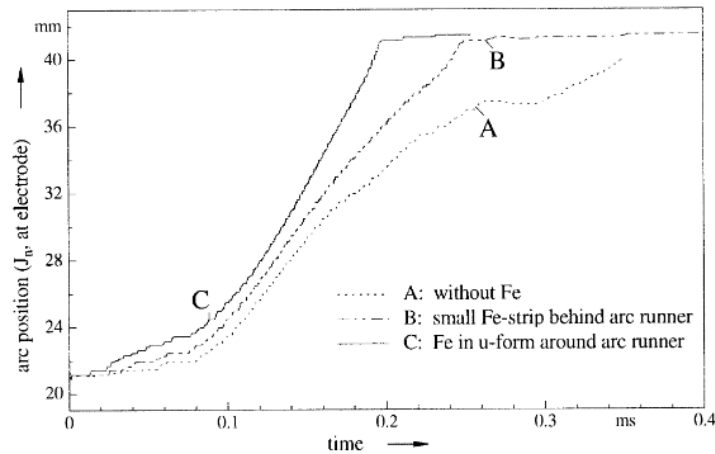
Figure 4-33 Simulated arc position versus time for different ferromagnetic arrangements [52]
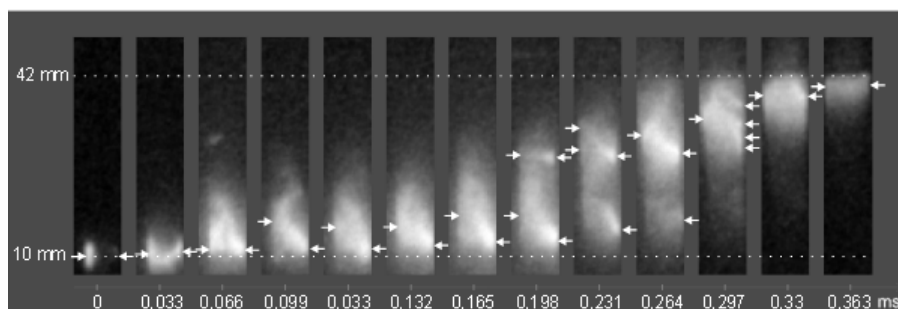


Figure 4-34 High-speed movie (33.000 frames / second) of arc movement in a chamber with U-shaped iron lining [51]

Later references analyze the splitting process of the electric arc in the splitter plates and the creation of arc roots on the plates started to be analyzed [53]. The authors propose to build a thin sheath layer of meshing elements around the plate, where the electrical conductivity is not the electrical conductivity of the plasma. Instead, it is nonlinear and according to the current-density voltage characteristic of Figure 4-35. No information about the numerical data used is given, but the asymptotic value of the voltage which is 10V. This means that when the voltage difference between a splitter plate and the adjacent plasma is small, only a small current flows through the plate. However, when it approaches $U_0$, the value necessary for the spot formation, an almost unlimited current can flow through the plate, but also residual current remains in the flow due to this voltage difference and the electrical plasma conductivity. This phenomenon is shown in Figure 4-36.



Figure 4-35 Voltage-Current density principle for an electrical conductivity in the splitter plate shell [53]
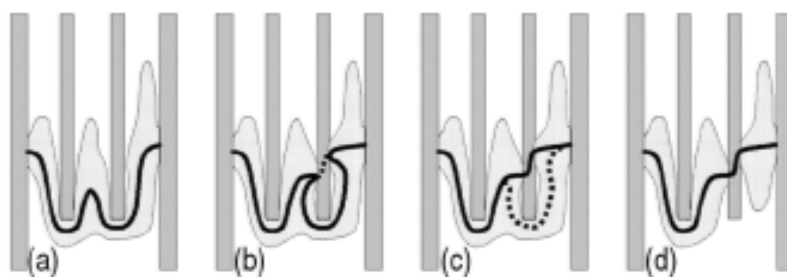
Figure 4-36 Principle of arc splitting by metal plates [54]

Here, a 20mm long splitter plate (SP) is considered in the arc chamber geometry as shown in Figure 4-37.



Rails 4.5x1.5, 58 long
Rail distance inside 8
Side walls 4.5 apart adjacent to rails
Barrier 1.6 thick, 20(15) long
Venting holes in upper wall 25% of cross-section

All dimensions in mm

(a)                                                                  (b)
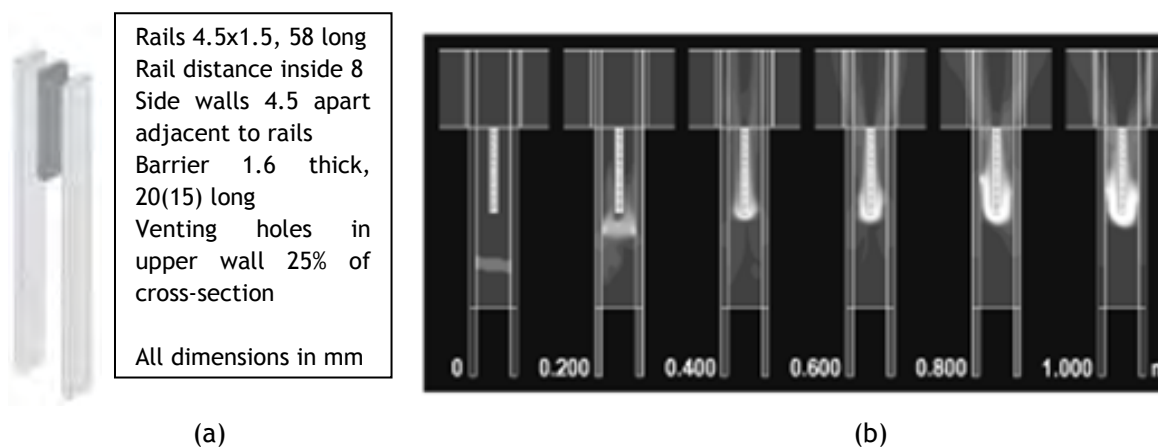
Figure 4-37 (a) Geometry for the model with 1 SP and (b) simulation results for 5kA rms and 20mm splitter plate [53]

In this case, the arc has been ignited asymmetrically, for a closer similarity with a real scenario, and an expansion volume has been modelled in the upper side of the chamber (Figure 4-37 (b)). The lengthening of the electric arc, which bends around the plate, according to an U-shaped trajectory can be seen. The splitter plate has been designed to be 20mm long. Additionally, the simulation is repeated considering a 15mm SP (Figure 4-38). The results are the same up to 0.675ms but after that instant, the plasma blows in the expansion volume in the second case (Figure 4-38).
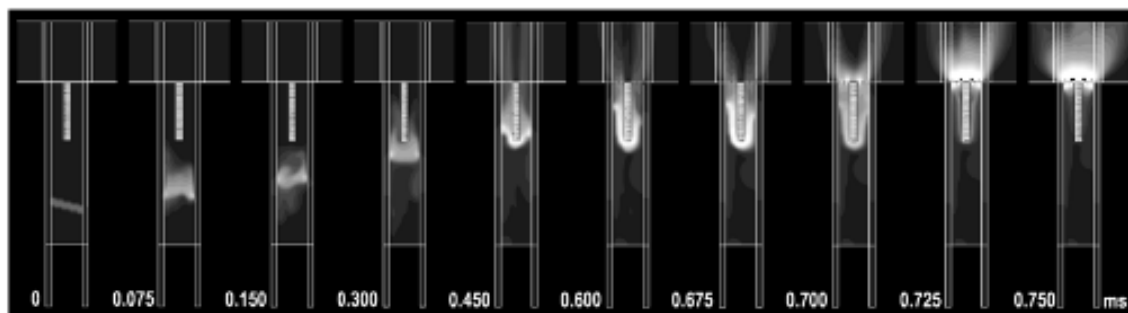


Figure 4-38 Simulation results for 5kA rms, 15mm splitter plate [53]

In this paper, the same arc root model has been applied to other geometry, shown in Figure 4-39, where the bending of the arc around the plate is also achieved.

Rails 4.5x1.5, 16 long
Rail distance inside 8
Side walls directly adjacent to rails
Copper plate 2 thick, 7 long
Upper side open (exhaust volume)

All dimensions in mm

(a)



(b)
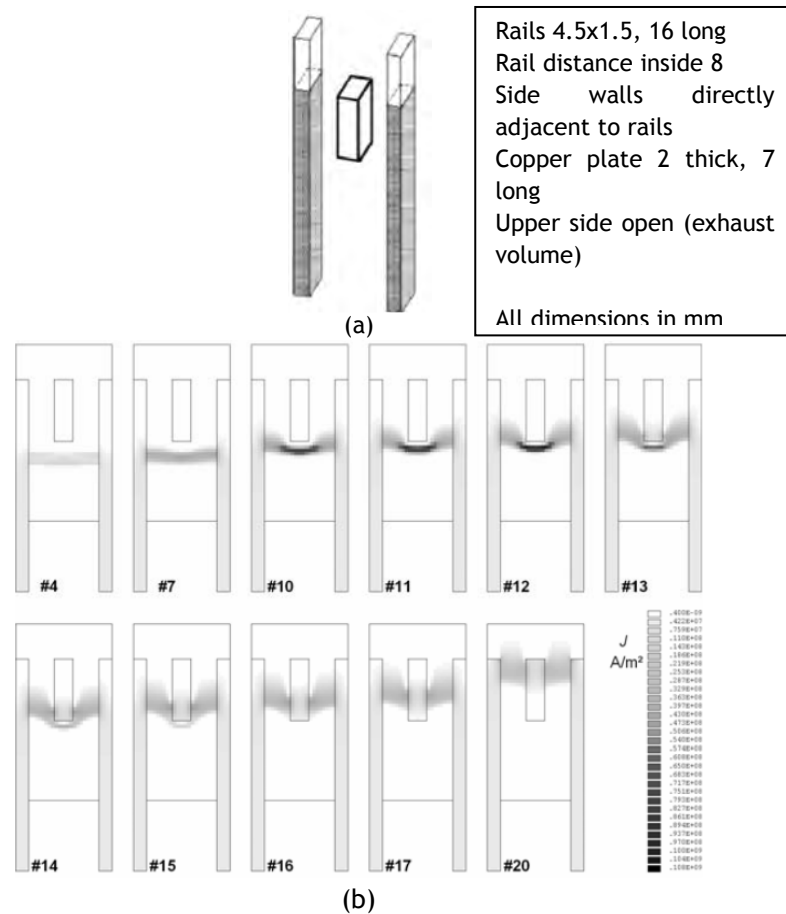
Figure 4-39 (a) Model considered in the analysis of the arc splitting process and (b) simulation results for 25A DC [53]

Also, the movement of the arc along a chamber with one splitter plate is recorded (Figure 4-40), which allowed observing a similar behaviour. But, as different current values have been used in experiments and simulations, it is only possible to compare the results qualitatively.
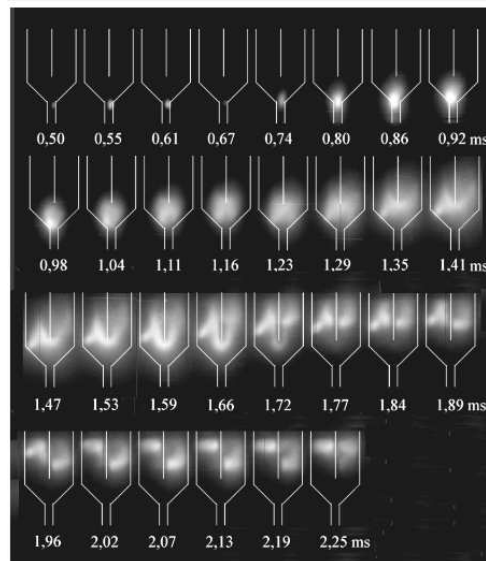


Figure 4-40 High speed images from experiments of electric arc at 1kA rms [53]

The same model shown in Figure 4-39 (a) is applied in [54], for 100A DC, showing the results in Figure 4-41.
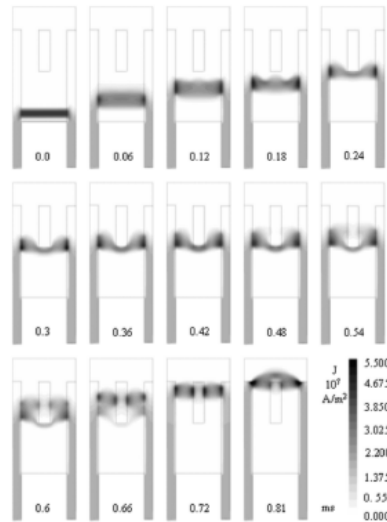
Figure 4-41 Simulated process of arc splitting on a metal plate, between two parallel arc runners, for 100A DC [54]

Once again, smaller current is used in the simulation than in the real experiments, so only general qualitative behaviour of the arc, upper movement and bending can be compared. Besides, the magnetic field calculation has been neglected, with the aim of simplification and an external constant magnetic field of 0.01T has been imposed.

Another step further is taken in [55], where the radiation model used in the simulation differs from the one used up to now. In the previous exposed references a $T^4$ dependent model has been applied (equation (4-28)). This model only takes into account the emission of radiation, but no absorption, leading to higher arc voltage values in comparison with real experiments. Thus, the results of three radiation approaches are analyzed in this model:

- The simple $T^4$ model from [34, 50-54, 56], without absorption
- Net Emission Coefficients (NEC), with a defined reabsorption wavelength
- Radiation heat conductivity to represent diffusion

Simple $T^4$ model from [34, 50-54, 56] without absorption is represented in Figure 4-42 by a thick black line, while in the same figure also the NEC cases for several Rp self-reabsortion radius lengths are shown. Besides, the radiation heat conductivity as a function of temperature is shown in Figure 4-43.
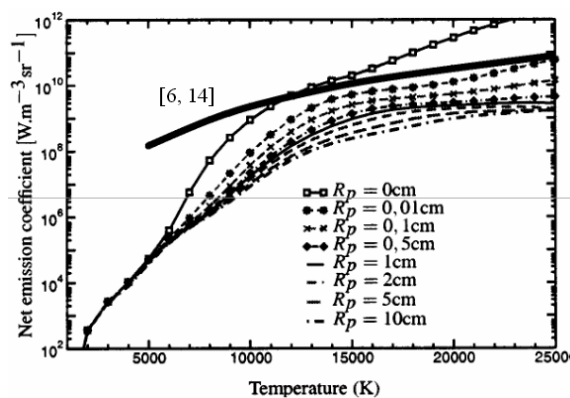


Figure 4-42 Simple $T^4$ model from [34, 50-54, 56] in thick black line without absorption and NEC cases for different Rp reabsortion lengths [55]
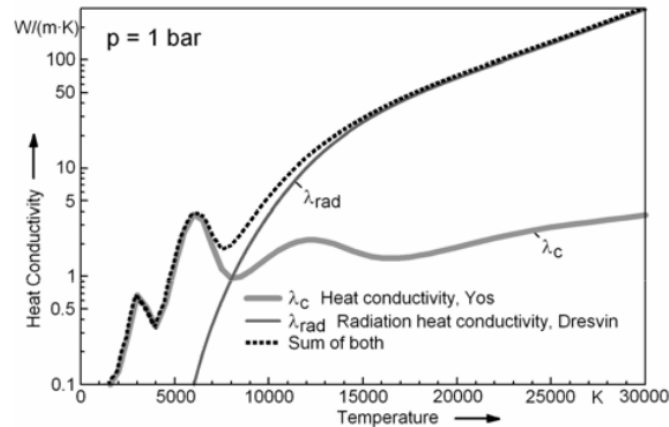
Figure 4-43 Classical heat conductivity (air), radiation heat conductivity ($N_2$) and sum of both [55]

With these three approaches, four radiation models are tested; #0, #1, #2 and #3:

- #0 is the model with only $T^4$ simple approach
- #1 is a contribution between radiative heat conduction and NEC, with a higher portion of radiative heat conduction
- #2 lies in between #1 and #3
- #3 is a contribution between radiative heat conduction and NEC, with a lower portion of radiative heat conduction

For these four radiation models, the arc voltage has been calculated (Figure 4-44). It is noticed that cases #1, #2 and #3 yield more realistic lower voltages.
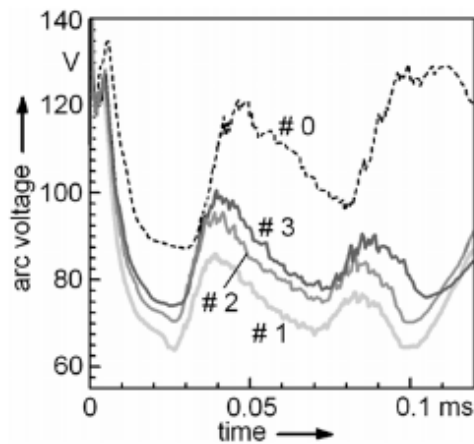


Figure 4-44 Arc voltages for 5kA rms [55]

The arc movement obtained in the simulation is shown in Figure 4-45, presenting that the current flows at certain instants through the plate and the surrounding medium.

Once again, comparison between simulation and experimental results can only be qualitative as the input current does not have the same magnitude. The arc voltage and current obtained in the experiments are presented in Figure 4-46 and the arc movement images have already been presented in Figure 4-40. The shape of the arc voltage in the simulation corresponds to the one from experiments.
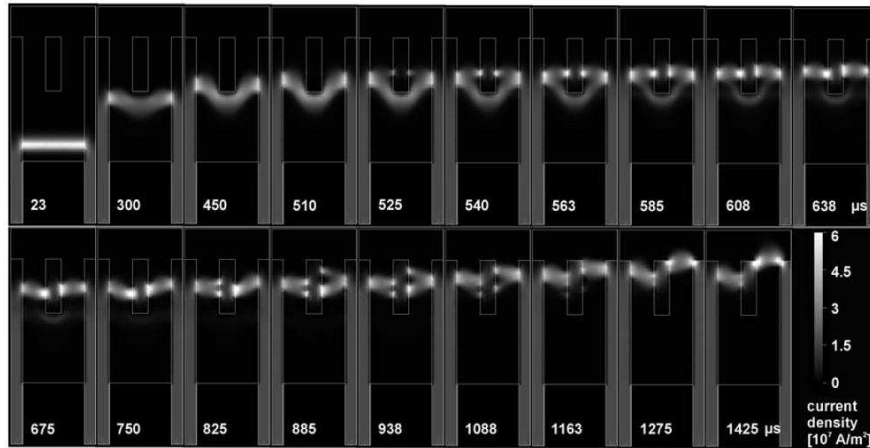
Figure 4-45 Simulation of the arc splitting process for 100A DC [55]
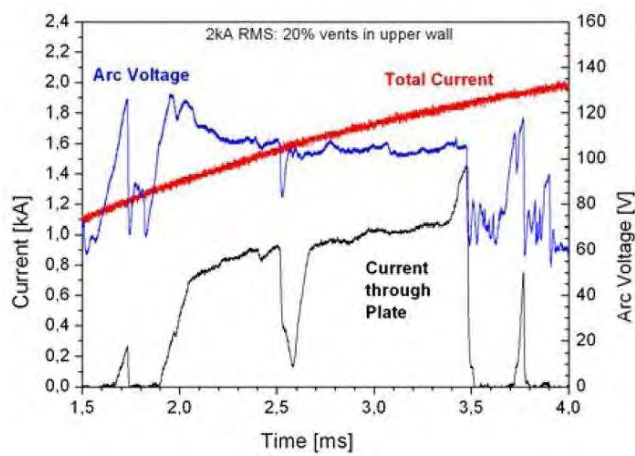


Figure 4-46 Oscilloscopes measurements of the total arc current, current through the plate and arc voltage (2 kA rms) [55]

A similar analysis is developed in [57], but this time the vector potential formulation is considered for the magnetic field and so, less computational cost is required. The obtained results are the same as those presented in [55].

New voltage-current density curves for electrical conductivity calculation around the splitter plate are introduced in [58], as shown in Figure 4-47.
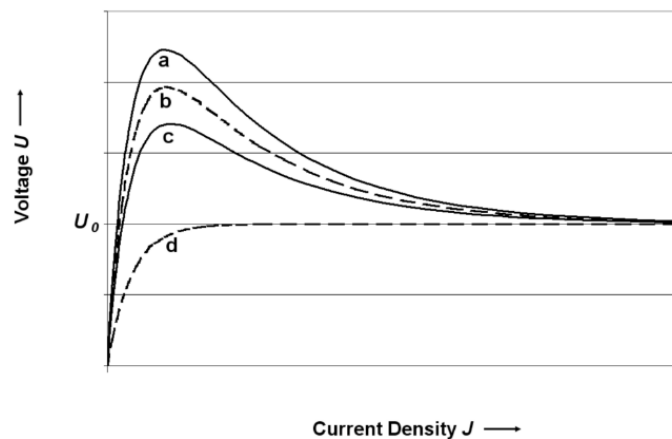


Figure 4-47 Voltage-Current Density characteristic for arc roots modelling in the splitter plate [58]

The curves from Figure 4-47 are based on the equation and the experimental data presented in [59]. The voltage current relation is expressed by equation (4-29).

$$U(J) = \frac{aJ + bJ^d}{c + J^d} \qquad\qquad (4\text{-}29)$$

where:
U:      voltage
J:      current
"a", "b", "c" and "d" are coefficients extracted experimentally (Table 4-9).

Table 4-9 Coefficient for Voltage-Current relation in the arc root of the splitter plates [59]

| Coefficient | Anode | Cathode |
|---|---|---|
| a | $3.0 \times 10^8$ | $3.0 \times 10^8$ |
| b | 5.0 | $1.0 \times 10$ |
| c | $1.1 \times 10^{14}$ | $1.1 \times 10^{14}$ |
| d | 2.0 | 2.0 |

When the geometries used before are applied to simulate the movement of the arc, several differences are found between the curves proposed (Table 4-10). It is noticed that the higher the ignition voltage, the higher the voltage increase, and the later the division of the arc begins. The reason for this behaviour is a longer arc bending around the plate. Thus, the location of first arc roots is further from the lower edge of the plate, for a higher voltage peak.

Table 4-10 Comparison between different arc root models [58]

| | Arc root model | | | | |
|---|---|---|---|---|---|
| | Curve a | Curve b | Curve c | Curve d | without arc root model |
| Voltage increase before subdivision | No sub-division of arc | 8.7 V | 6.7 V | 1.6 V | 0 V |
| Time first arc root formation | | 450 µs | 390 µs | 300 µs | 210 µs |
| Location of first arc roots above edge of plate | | 3.9 mm | 2.5 mm | 0.8 mm | 0 mm |
| Max. arc root current density | | $1.5 \cdot 10^8$ A/m² | $1.1 \cdot 10^8$ A/m² | $5 \cdot 10^7$ A/m² | $5 \cdot 10^7$ A/m² |
| Parallel arc roots | | yes | yes | no | no |

In [60] and [61], the curves presented above in Figure 4-47 are used. However, in this case, experiments and simulation are analyzed for the same current value, 1kA rms, so that a direct comparison can be made (Figure 4-48 and Table 4-11). Regarding the arc movement, the general behaviour is similar, but some differences can be noticed. For example: in the real case the arc bending takes longer, and in the simulation the current goes through the SP faster.

Looking to Table 4-11, some similarities and differences are found. The arc voltage rises in both cases before splitting starts and then continues rising to a local maximum. The arc roots appear at a certain distance from the lower edge of the plate and have a considerably higher current density than the arc column.

Besides, comparing them quantitatively, the voltage increase before subdivision is equal in experiment and simulation. But, in the experiments the subdivision starts later because the arc bending around the plate takes longer, as Figure 4-48 shows.

Table 4-11 Comparison of measured and simulated arc splitting process [61]

| | Experiment | Simulation |
|---|---|---|
| Voltage increase before subdivision (V) | 18-20 | 19 |
| Time of beginning of subdivision after arc ignition (µs) | 1020 | 620 |
| Location of first arc roots (mm above lower edge of plate) | 3-4 | 6.8-7.8 |
| Maximum arc voltage (V) | 89 | 72 |
| Arc root current density (A/m$^2$) | 0.5-6x10$^5$ | 2.2x10$^5$ |



(a)                              (b)
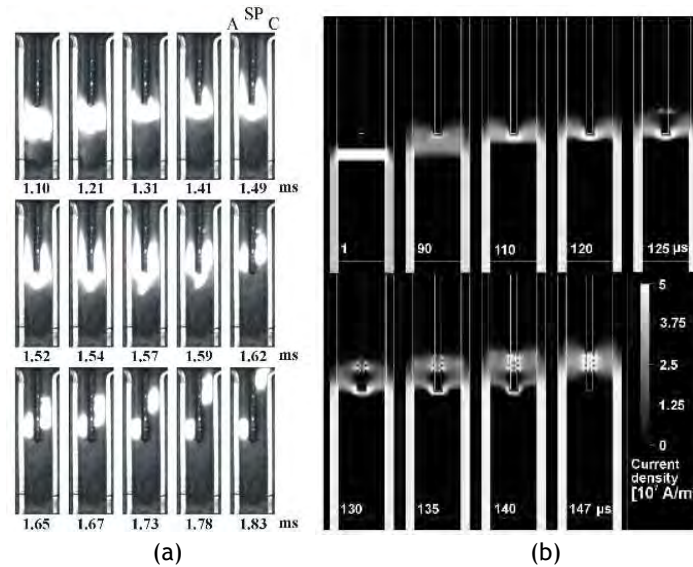
Figure 4-48 (a) Experimental results and (b) simulation results of electric arc movement for 1kA rms [60]

Finally, the last contributions of this research team for the arc simulation are focused on a simplification of the splitter plates stack. So, in the approaches developed by Riss [62, 63], the splitter plates stack is assumed to be a porous medium. Figure 4-49 shows the original geometry model with the splitter plates stack (on the left) and the geometry with the porous media (on the right). As the number of splitter plates in the original model is high, 7, and the simulation would take long to be solved, double symmetry has been applied, simulating a quarter of the model. In contrast, for the model with the porous assumption, MHD equations are solved but they have to be averaged taking into account the porosity of the material. Figure 4-50 shows the time evolution of the current density for both cases.
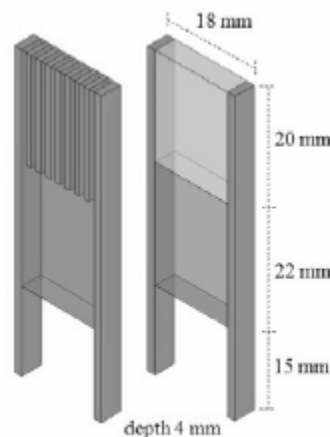


Figure 4-49 Model with splitter plates stack and porous medium [63]

<center>(a)                                                                          (b)</center>
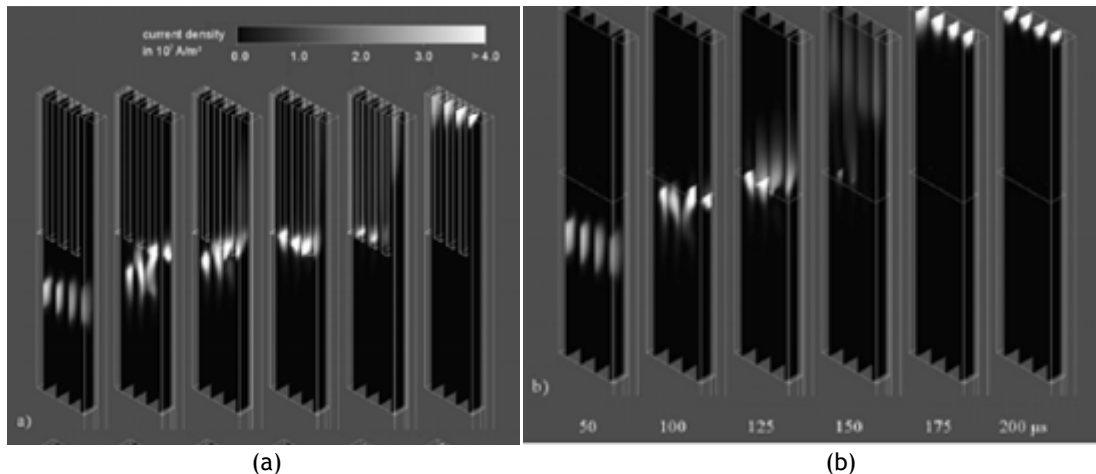
Figure 4-50 Current density evolution for (a) original geometry with splitter plates stack and double symmetry and (b) for the supposition of porous medium [63]

The aim of this new approach is to reduce the computational time, in order to facilitate the simulation. However, although not explicitly published in the corresponding reference, it was mentioned at the conference that the improvement in computational time was small. So, only the achievements up to [61] will be taken into account in this thesis.

*B) Xi'an University (China)*

The second research group with the largest number of contributions is Xi'an University of China. Most of their publications show simpler geometries than the previously exposed ones. The electrodes in these contributions are no rails but rectangular elements. Thus, no fluid displacement is generally shown in the results. Instead, effects of the arc ignition position, gassing material, venting size or splitter plates size are analyzed.

The first paper [64], applies several physical approaches of the previously exposed analysis from Lindmayer et al. [34, 50, 54, 65], but to a different geometry. So, comparison between results of both research groups is difficult, but partial conclusions can be obtained. The geometry considered (Figure 4-51) consists on a 50x8x8mm physical domain. In the middle of those 50mm length, a small anode and cathode are defined, 4x4mm, but not rails as in the previous cases. Between the electrodes the arc column is ignited.
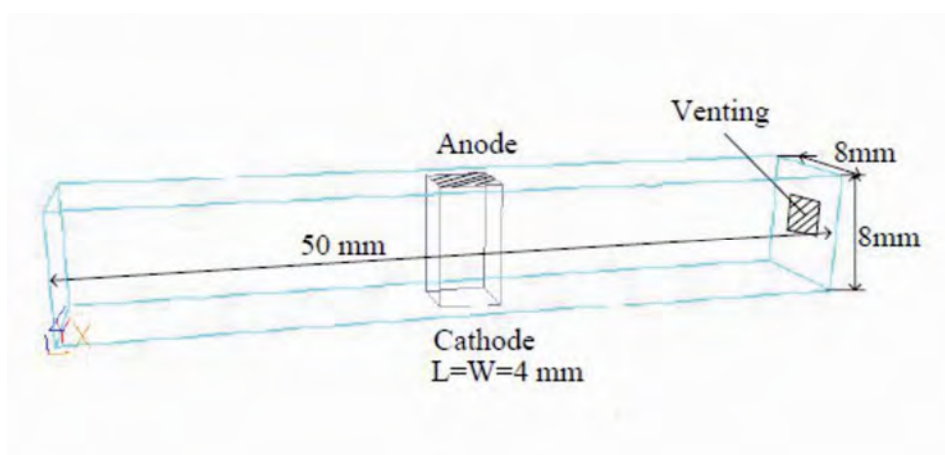


Figure 4-51 Geometry considered for the LVCB arc chamber [64]

The simulation model is defined for 100A, not specified if DC or AC. The plasma is assumed to be in LTE and no arc root or arc-electrode interaction is modelled. Even though the magnetic induction is calculated with Biot-Savart equation, an external field of 0.001 T is defined. For the heat exchange, no conduction is assumed between the outside and the arc chamber, except on the right end, where the chamber is modelled with ambient temperature and pressure due to the venting hole. The radiation model for the arc is modelled as in most of previously exposed paper using a simplified emission equation (4-28), even though it has been already proved not to be satisfactory.

A good approach presented in this paper is the treatment of plasma as a gas mixture, with thermodynamic and transport properties obtained from [66]. Thus, the physical properties, thermal conductivity, viscosity, density, specific heat and electrical conductivity, are expressed as functions of temperature and pressure.

Regarding the results, three aspects are analyzed: the effect of arc ignition location, of venting size and of gassing material. Besides, to analyze the arc ignition, three locations for arc ignition have been considered:

a)   In the middle of the model (electrodes location in Figure 4-51)
b)   10mm closer to the venting end (right side in Figure 4-51)
c)   10mm further from the venting end (right side in Figure 4-51)

For case a), the temperature distribution obtained in the simulation, for three different time instants, is exposed in Figure 4-52. It can be noticed the diffusion of the arc towards the venting end, but not a real movement. That performance can be explained due to the lack of rails in the geometry of the model.
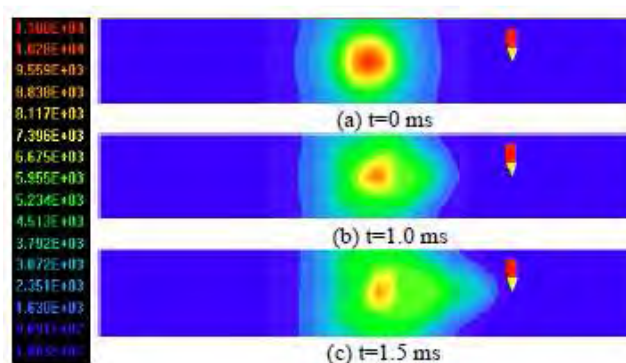


Figure 4-52 Temperature distribution for 3 timestep [64]

As a result of the three ignition positions proposed, Figure 4-53 is obtained, where the ratio of the velocity of the fluid flow is represented as a function of time. Case a) has been taken as reference, with 1 as value, and the two other cases have been referred to it. Case b), in a line marked as 1, is more elevated than the reference. Thus, igniting the arc closer to the venting end implies higher velocity values, and the opposite for case c). So, the further the distance from the venting end to the arc ignition, the slower the arc moves, which is not a desirable effect. This is mainly related to the pressure distribution in the chamber and should be further investigated.
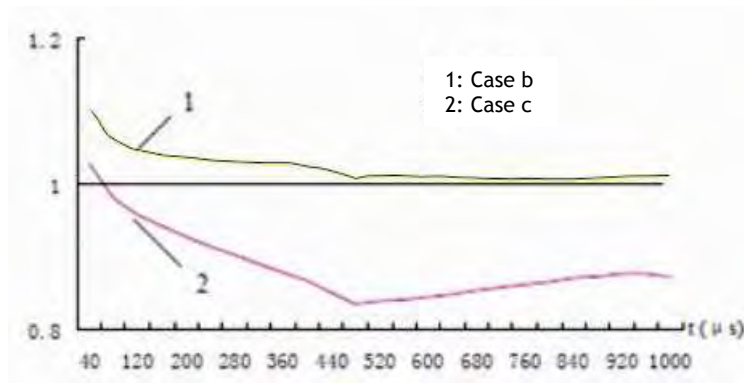
Figure 4-53 Arc velocity ratio of different arc initial locations [64]

Regarding the venting size analysis, the previously exposed case a) has been taken as reference for ignition and two different venting sizes have been analyzed: full opening and 1/9 of the entire area. Taking once more case a) with full opening as reference, the arc velocity (curve 1) and electric potential (curve 2) corresponding to partial opening, are shown in Figure 4-54. It can be concluded that when reducing the venting size, the arc motion and velocity are also reduced. The effect of the opening zone has already been analyzed in [34] and shown in Figure 4-29, where it was concluded that a bigger opening lead to a faster arc movement. So both results agree.
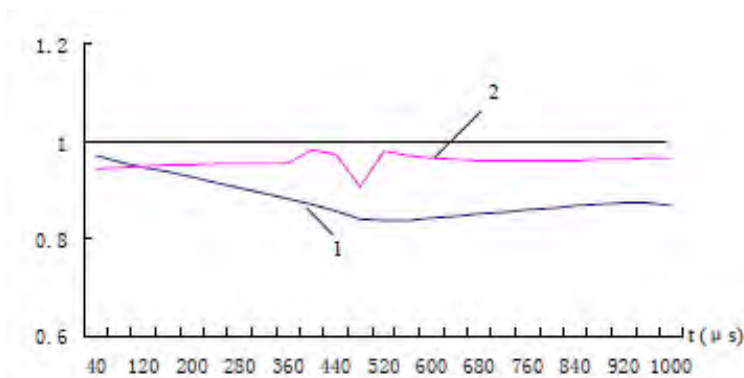


Figure 4-54 Arc velocity and electric potential ratios of different venting sizes [64]

Finally, to evaluate the influence of the presence of a gassing material, the arc chamber with air or with 90%Air-10%PA6 gas mixture is considered, being concluded that in the second case electric potential (1) increases and the temperature (2) drops, but mainly in the initial stage.
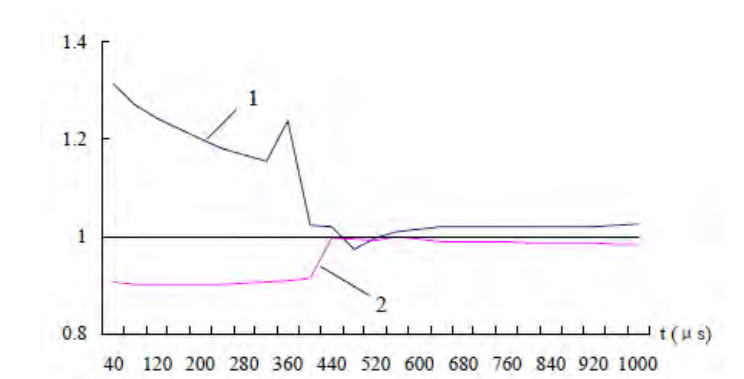


Figure 4-55 Electric potential and arc temperature ratios with gassing materials [64]

Even though the results extracted from this reference, regarding the three aspects explained are very interesting, no results of arc motion are shown.

Moreover, in [67], a ferromagnetic material is introduced, in order to analyze its effect. So, the venting from the previous geometry is substituted for a ferromagnetic closure, as shown in Figure 4-56.
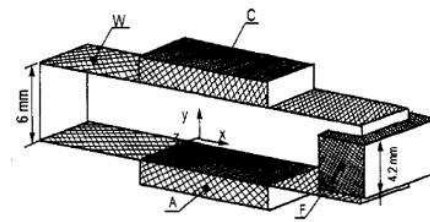


Figure 4-56 Model of the considered arc chamber (A: anode, C: cathode, W: walls, F: ferromagnetic material) [67]

There are also some changes in the physical set up, as the radiation model applied in this case is the NEC model and vector potential formulation is considered for calculation of the magnetic field. The external surface of the chamber is maintained at 300K and the temperature attained by the electrodes is limited to the melting temperature (2500K). Firstly, a simulation is performed without considering the ferromagnetic material. The result is used as initial state in the simulation of arc motion due to the magnetic force that appears considering the ferromagnetic material at the end of the chamber. The arc movement along the chamber towards the ferromagnetic material can be seen in Figure 4-57. Authors say that the arc motion is raised with the arc column located closer to the ferromagnetic materials, even though no results are exposed.
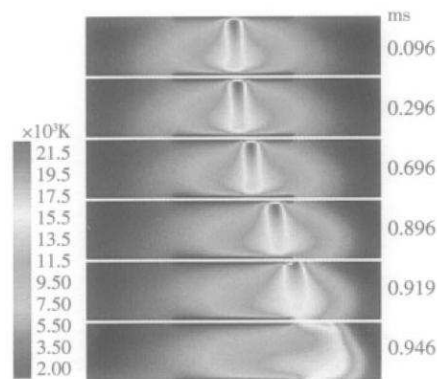


Figure 4-57 Evolution of the arc position by temperature variation [67]

With the same approach, but using two ferromagnetic splitter plates, the magnetic flux density and the Lorentz force under the effect of the ferromagnetic splitter plates are obtained in [68]. The geometry has cathode and anode as rails and two splitter plates (Figure 4-58).

Half symmetry is applied to develop the model and a hexahedral mesh type and a time step of 1μs have been considered in the transient simulation. The problem is solved using the software FLUENT, for a current of 200A, first as a stationary problem and after as a transient. Besides, the arc is ignited in the middle of the chamber. Magnetic flux density, temperature and electric potential are calculated for three different time instants, showing once again that the effect of ferromagnetic plates moves the arc to them.
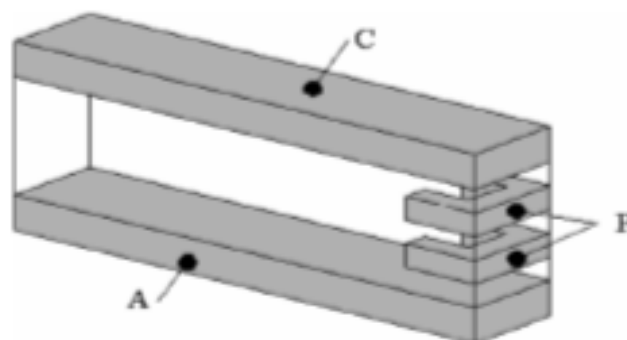
Figure 4-58 Simplified geometry of the arc chamber [68]

Another research work about the influence of the switching medium on LVCB arcs is presented in [69]. Three different composition atmospheres are considered (air, air-10% PA-polyamide- and air-10% POM-polyoxymethylene-). The arc chamber considered in the analysis is shown in Figure 4-59, where the top and bottom faces are the cathode and anode, respectively. Besides, several ceramic plates and vents are arranged at one end.
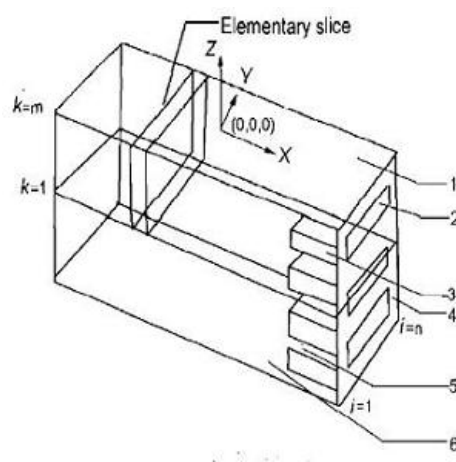


Figure 4-59 Arc chamber considered in the simulation [69]

The analysis is again carried out using FLUENT software tool, but in this case for a current value of 150A. Data from the mesh are revealed: 0.225 mm, 0.5mm and 0.5mm are the spacing along x, y and z axis, respectively. As in the previous case, 1μs is the timestep used in the transient simulation. The MHD model is solved with a simplified emission radiation model and vector potential as magnetic field resolution method. The arc root position has been modelled by calculating the position of the highest average value of electrical conductivity.

Calculating again the stationary and transient states, results show that air-10% PA and 10% air-POM configurations provide a more effective cooling and a faster acceleration of the arc motion toward the arc extinguishing zone than pure air as switching medium. Figure 4-60 shows how the arc reaches the splitter plates stack at about 1.1ms for air, while for air-10%PA and air-10%POM, the arc reaches the splitter plates at 0.86 and 0.78ms, respectively, and so a faster switching time can be achieved.
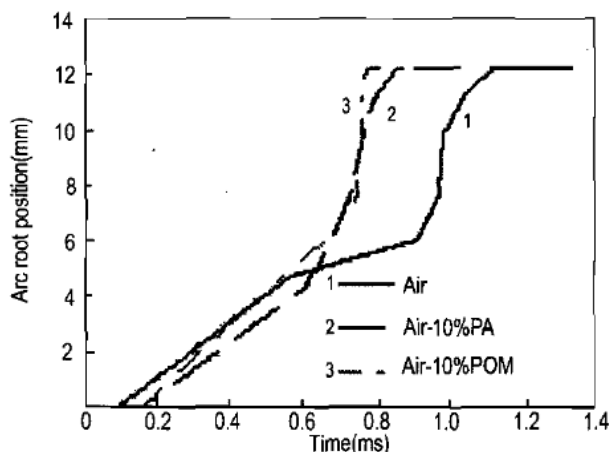
Figure 4-60 Comparison of arc root position for three different switching mediums [69]

The approach proposed in [70] is applied to determine the position of the arc roots. As in previous cases, first the stationary case is considered. Following, the movement of the arc under the action of a magnetic field of 4mT is analyzed. Figure 4-61 shows the evolution of the temperature distribution obtained, being compared with the high speed arc images from experimental tests.



(a)                                        (b)
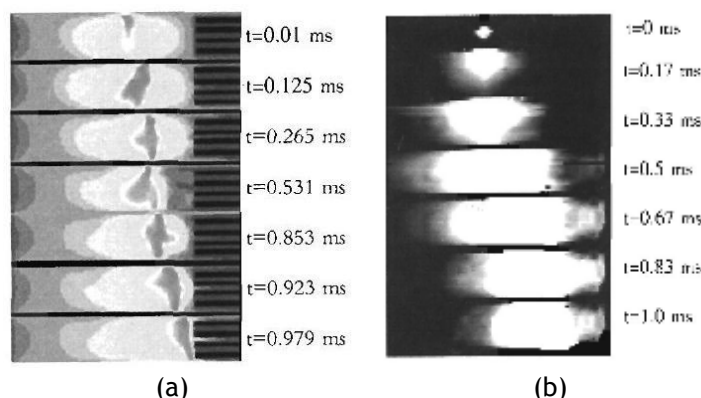
Figure 4-61 Temperature distribution obtained at different time instants (a) in the simulation and (b) arc movement images from experiments [69]

Moreover, unlike in earlier works, in [71] the lengthening and interruption process is analyzed during the opening of the contacts, but the arc ignition is not considered. The model used is shown in Figure 4-62.
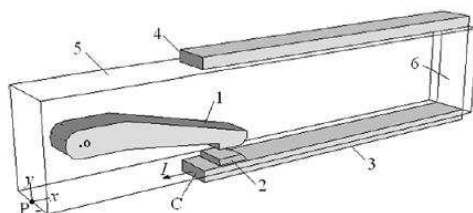


Figure 4-62 Model of the arc chamber (1: moving contact, 2: fixed contact, 3: guiding elements arc, 4: insulating walls) [71]

The analysis starts considering a small separation of the contacts (1mm) which increases with the movement of the movable contact. As initial condition (t=0), the temperature distribution corresponding to a gas velocity of 0m/s is considered. During the simulation, a magnetic field of 5.5mT in the z axis direction and a rotation speed of the movable contact of 112rad/s are considered.

The boundary conditions are similar to those considered by others authors (temperature of the outer surface of the chamber equal to 300K, imposition of a current density at the cathode, zero electrical potential at the anode, etc.). Additionally, the simulation needs to readjust the mesh corresponding to the contact area, as the simulation is running, as a consequence of the opening of the movable contact. This dynamic mesh complicates the solution significantly. In particular, hexahedral cell configuration is used to mesh the fixed region and tetrahedral for the deformed region, according to Figure 4-63, being the total number of meshing elements equal to 132850.
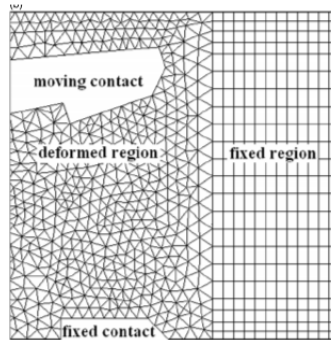


Figure 4-63 Meshing of the model [71]

Results obtained from experimental tests are compared to those obtained in the simulation (Figure 4-64). In both cases a similar behaviour is obtained, being observed that the arc travels towards the end of the chamber approximately in the same time period. For simulation results, Figure 4-64 (b), temperature distribution is shown as arc movement representative.
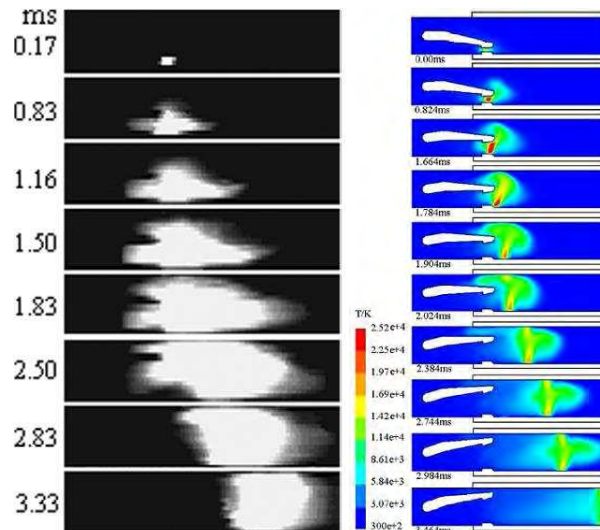


Figure 4-64 Arc movement obtained in (a) the experimental tests and (b) temperature obtained by simulation [71]

As in previous reference [64], in [72] the effect of the arc ignition location on the movement of the arc is analyzed, by comparing experimental results with those obtained in simulations. The analysis by simulation considers a very simplified 2D model (Figure 4-65) so as to eliminate the effect of other factors on the arc movement. Thus, this model considers the plane parallel to the electrodes and perpendicular to the arc column. Among the assumed boundary conditions, the outer contour is supposed to be adiabatic, except at the venting (right side end) where atmospheric pressure and temperature are considered.
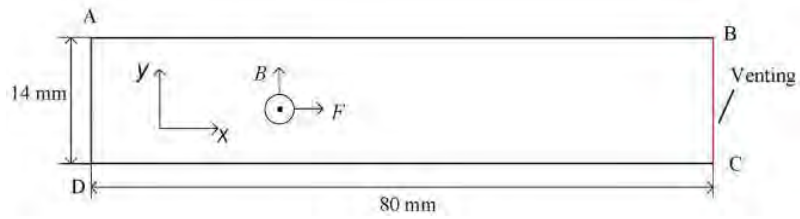
Figure 4-65 Model considered in the simulation [72]

The results obtained reveal, again, an increase in the velocity of the arc when reducing the volume between the venting and the arc ignition point, since it produces an increase in pressure. Figure 4-66 provides an example of the results obtained, showing the time evolution of the temperature in the case of the arc ignition at the midpoint of the arc chamber. Figure 4-67 validates the advantage of closer ignition points to the venting end: at the same time instant, showing that for ignition at 25mm, measured from the venting, the arc has travelled a longer distance than for ignition at 40mm.
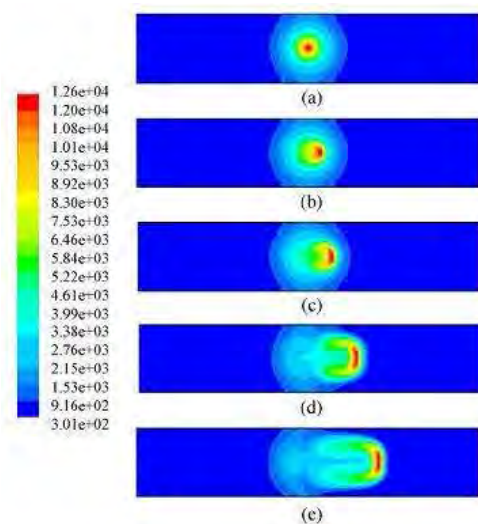


Figure 4-66 Evolution of the temperature with the ignition point at the middle plane
((a) t=0 ms, (b) t=0,1 ms, (c) t=0,2 ms, (d) t=0,5 ms, (e) t=1,0 ms) [72]
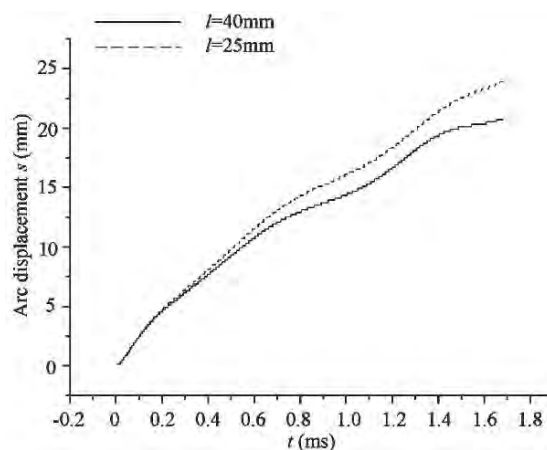


Figure 4-67 Simulation result of arc displacement at different arc ignition positions [72]

In [73], the effect of gassing material and metallic vapour are analyzed based on different gassing mixtures: air and 90%air-10%PA6 for the gassing composition and 99%air-1%Cu, 99%air-1%Ag, 99%air-1%Fe, for the possible metal vapours from the electrodes. Besides, NEC and

simplified emission radiation models are compared. The geometry is again the one exposed in Figure 4-65. Results of simulation and experimental tests are also compared. Analyzing the results, it is demonstrated that the arc motion velocity decreases when the air is contaminated with metallic vapours (Figure 4-68), obtaining the fastest arc velocity for pure air.
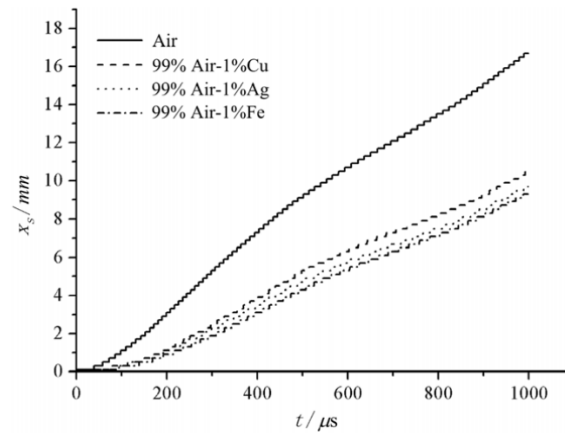


Figure 4-68 Arc displacement for pure air and air with metal vapours [73]

On the other hand, a pure air arc is slower than plasma with gassing material PA6, as Figure 4-69 shows, mainly due to the electrical conductivity increase.
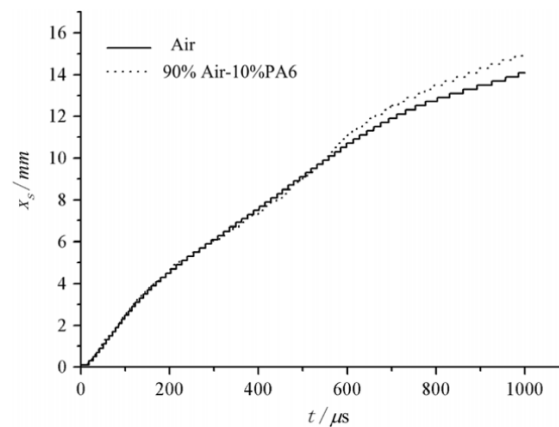


Figure 4-69 Comparison of gassing components for arc displacement [73]

Also, two radiation models are compared regarding arc displacement, concluding that the arc motion velocity is lower before 4ms with NEC model and then higher after 7ms (Figure 4-70).
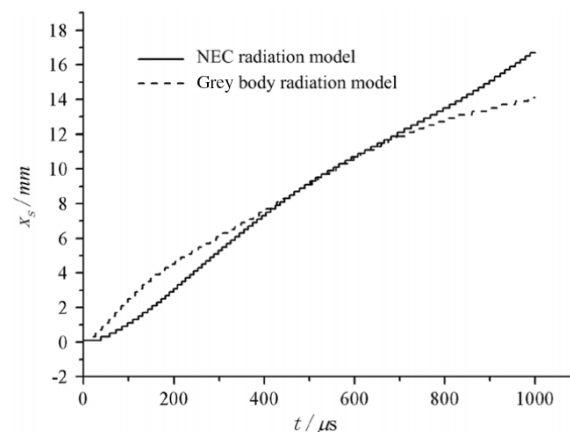


Figure 4-70 Comparison of radiation models for arc displacement [73]

For a deeper analysis of the ferromagnetic material effect, two different gassing material compositions are analyzed in [74]: 100% pure air and 99% air-1% Fe. The geometry model analyzed to evaluate the Fe influence is shown in Figure 4-65. Results (Figure 4-71 and Figure 4-72) prove that the iron vapour may cool the arc central region and decelerate the arc motion forward. So, it is not a good influence in the arc interruption process.
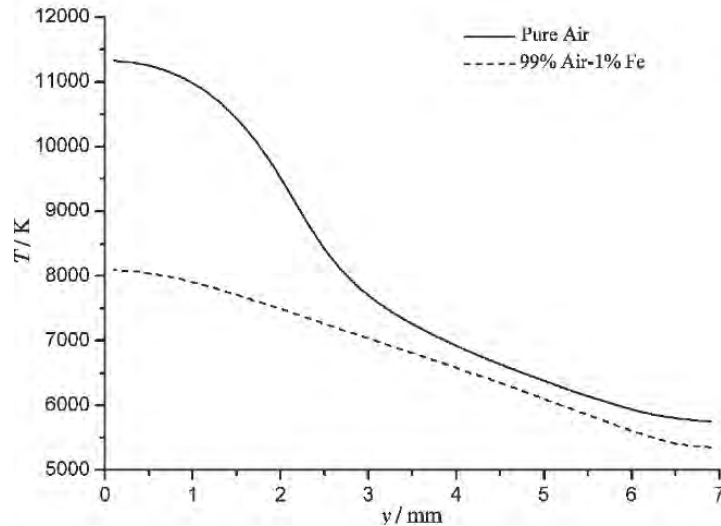
Figure 4-71 Comparison of the variation of arc temperature for pure air and 99%air- %1 Fe [74]
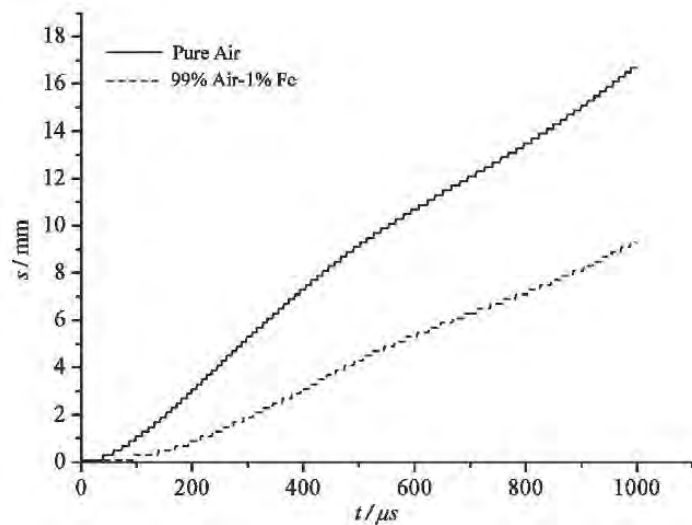
Figure 4-72 Comparison of the arc displacement of pure air and 99%air-%1 Fe [74]

To analyze the influence of the size of a ferromagnetic splitter plate on the arc motion, the geometry model presented in Figure 4-73 is used.
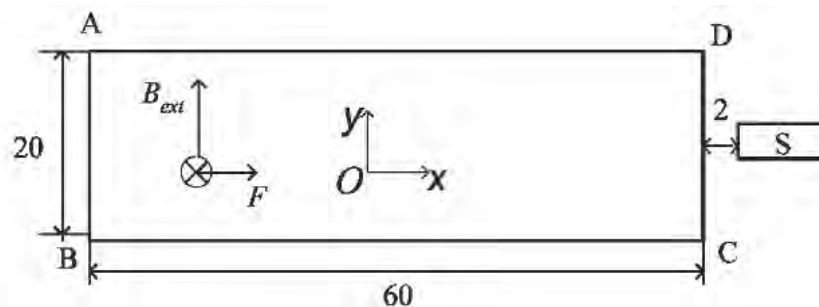
Figure 4-73 Geometry model for analyzing the size of a ferromagnetic splitter plate on arc behaviour [74]

Results (Figure 4-74) demonstrate that the arc motion can be enhanced by increasing the size of the splitter plates.
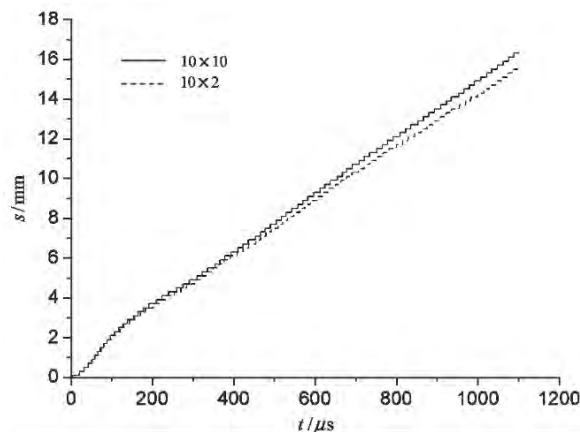


Figure 4-74 Influence of the size of the splitter plate on the arc displacement [74]

Besides, an arc root model has been defined for the analysis of arc splitting in the splitter plates [75], consisting of a thin layer of non linear electrical resistance elements to represent the voltage drop of plasma sheath and the formation of new arc roots. The geometry simulated is shown in Figure 4-75, where a very detailed model of a MCB is obtained.



(a)                                                                                 (b)
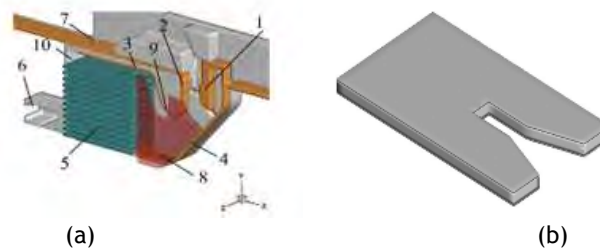
Figure 4-75 (a) Geometry of the analyzed MCB and (b) splitter plate of the chamber [75]

Half symmetry is again applied and the arc temperature distribution sequence on the symmetry plane is presented as a result of arc movement (Figure 4-77).

Voltage and current values obtained in the simulation are compared to real results, as shown in Figure 4-76, where a good compromise between simulation results and real measurements is reached.
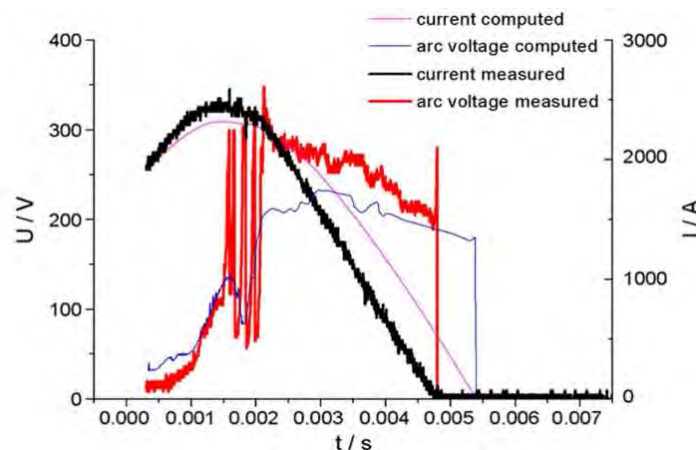


Figure 4-76 Arc current and voltage of simulation and experiment [75]
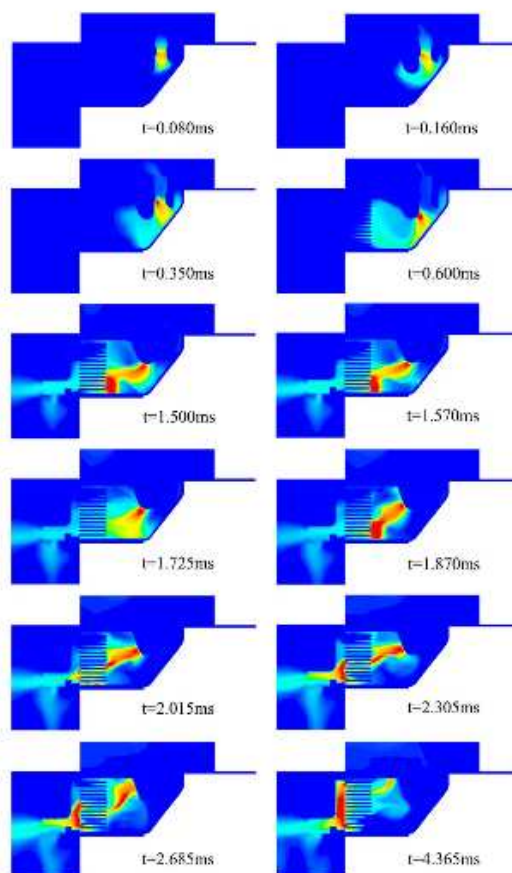
Figure 4-77 Arc temperature distribution sequence on the symmetry plane of the arc chamber comparing models with and without plastic ablation [75]

Finally, in their latest research work [42], a revision of arc commutation, motion and splitting, radiation models discussions, metal erosion, wall ablation and turbulence phenomenon is included.

For arc motion analysis, a simulation of arc motion in a simple chamber with two parallel runners is presented. The outlet is set at the centre of the endwall to connect the inner air volume with the atmosphere outside the chamber, while the rest of the arc chamber is enclosed by electrodes and sidewalls. Figure 4-78 shows the 3D plasma temperature distribution at different times during the arc motion, at a 10mm width chamber with 16% of outlet area. The arc current is 400A and the magnetic field is 5mT. The arc column's shape significantly changes due to the increasing arc moving velocity. At $t$ = 1.18 ms, there is a nose in front of the arc column in the simulation, which conforms with their experimental results.

Regarding wall ablation and metal vapours, the paper shows that iron vapour has a large influence on the arc formation. However, modelling of arc root formation and metal erosion is still rudimentary in nowadays simulations. The behaviour of microscopic particles in the arc plasma sheath layer, the liquid drop splashing and the evaporation of multimaterials with gas composition production under the arc thermal action have yet to be precisely modelled to reflect the actual process.
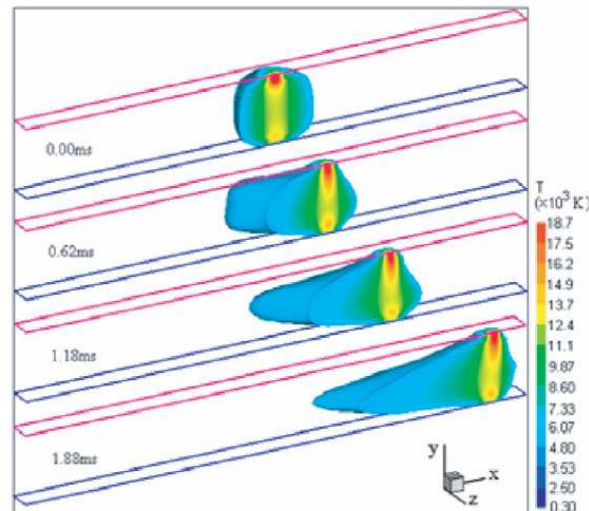
Figure 4-78 Temperature distribution in the arc chamber, T>5000K [42]

Finally, regarding turbulence, most of the previous work on turbulence verifies the validity of existing turbulence models in high-voltage switching arcs. The parameters of turbulence models seem to be related to the arc chamber volume and the arc current. But, turbulence in the arc gas flow is seldom considered for LVCBs, which may affect the simulation results for high-current air arcs in a larger arc chamber.

All these problems can explain the differences, between results of simulations and experimental results that still exist in the cases exposed.

*C) Other Universities*

Other academic research teams, with most remarkable contributions in the area of arc modelling simulations are grouped and presented in this section. Among these teams, Université Paul Sabatier in France, Technical University of Ilmenau and Technical University of Dresden in Germany are significant.

Regarding Université Paul Sabatier in France, they analyze [70] the motion of the arc under the action of an external magnetic field, using Fluent and FEM codes. The influence of the gas nature in the arc and speed of appearance of arc re-strikes, considering air as well as a mixture of air and PA6 (polyamide 6, the polymer of the housing of the LVCB) is also analyzed. The geometry considered is simplified in order to facilitate the resolution of the problem (Figure 4-79), designing a pallelepipedic volume of 30x14x23mm.
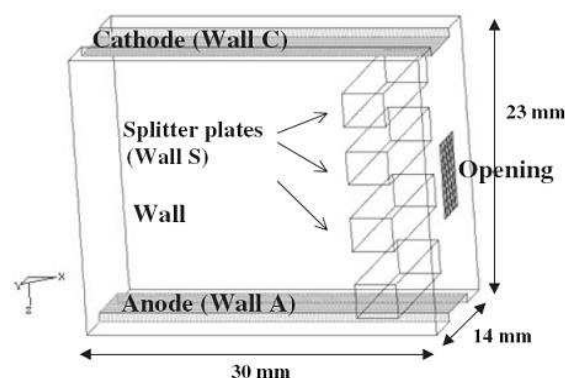


Figure 4-79 Simplified geometry of a LVCB [70]

Once again, the steady state is firstly analyzed to obtain the initial conditions for the analysis of the transient state. Figure 4-80 shows the results obtained for the distribution of temperature and voltage.

1: 20kK
2: 18kK
3: 16kK
4: 14kK
5: 12kK
6: 10kK
7: 8kK
8: 6kK
9: 4kK
10: 2kK

(a)

1: 25V
2: 23V
3: 21V
4: 19V
5: 17V
6: 15V
7: 13V
8: 1V
9: 9V
10: 7V
11: 5V
12: 3V
13: 0

(b)
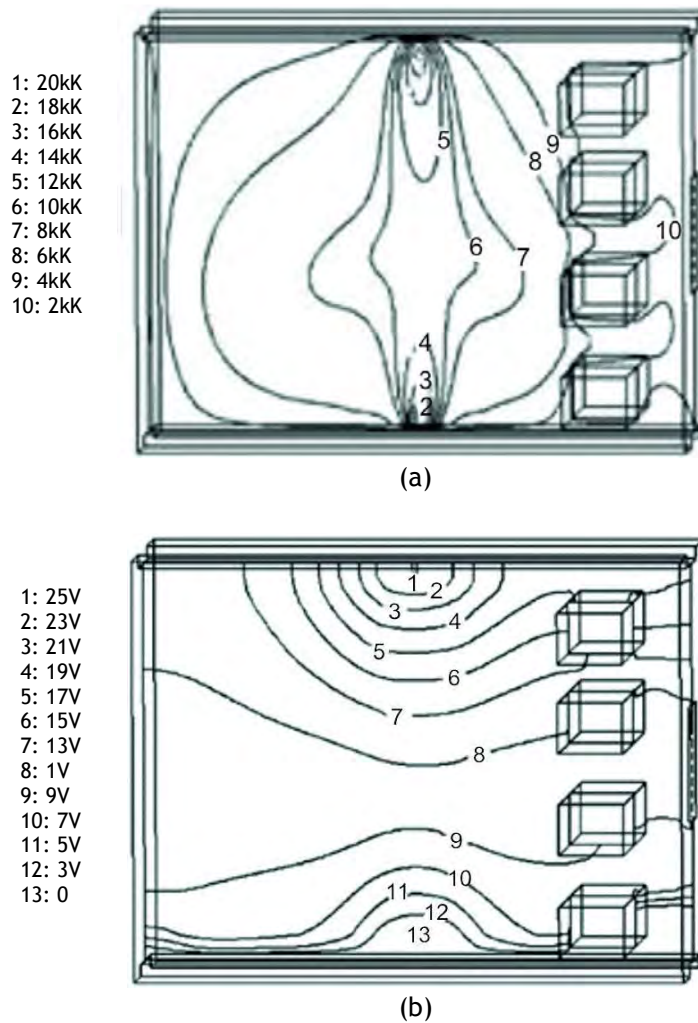
Figure 4-80 Results obtained in the steady state simulation. (a) Temperature, (b) Voltage [70]

The results of arc voltage and displacement due to the effect of the magnetic field obtained in the steady state, are shown in Table 4-12. The parameters considered in the simulation for every considered atmosphere have been a current of 100A and an externally applied magnetic field of 2 and 5mT. For those conditions, an increase of the arc voltage related to the applied field and the proportion of PA6 is observed.

Table 4-12 Effect of the externally applied magnetic field and arc curvature [70]

|          | Air | Air-5%PA6 | Air-10%PA6 |
|----------|-----|-----------|------------|
| Bc=0     | ddp=25.02 $\delta x=0$ | ddp=28.15 $\delta x=0$ | ddp=35.02 $\delta x=0$ |
| Bc=2mT   | ddp=25.25 $\delta x=4.48$ | ddp=41.6 $\delta x=4.64$ | ddp=60.93 $\delta x=6.14$ |
| Bc=5mT   | ddp=29.67 $\delta x=6.47$ | ddp=60.8 $\delta x=6.97$ | ddp=108.75 $\delta x=7.47$ |

For the simulation of the transient state, the magnetic field created by the arc itself and the contribution of the electrodes are simultaneously considered. A method to determine the position of the arc roots on the electrodes, based on the calculation of an average electrical

conductivity, is proposed. Figure 4-81 shows an example of the results obtained in the simulation.
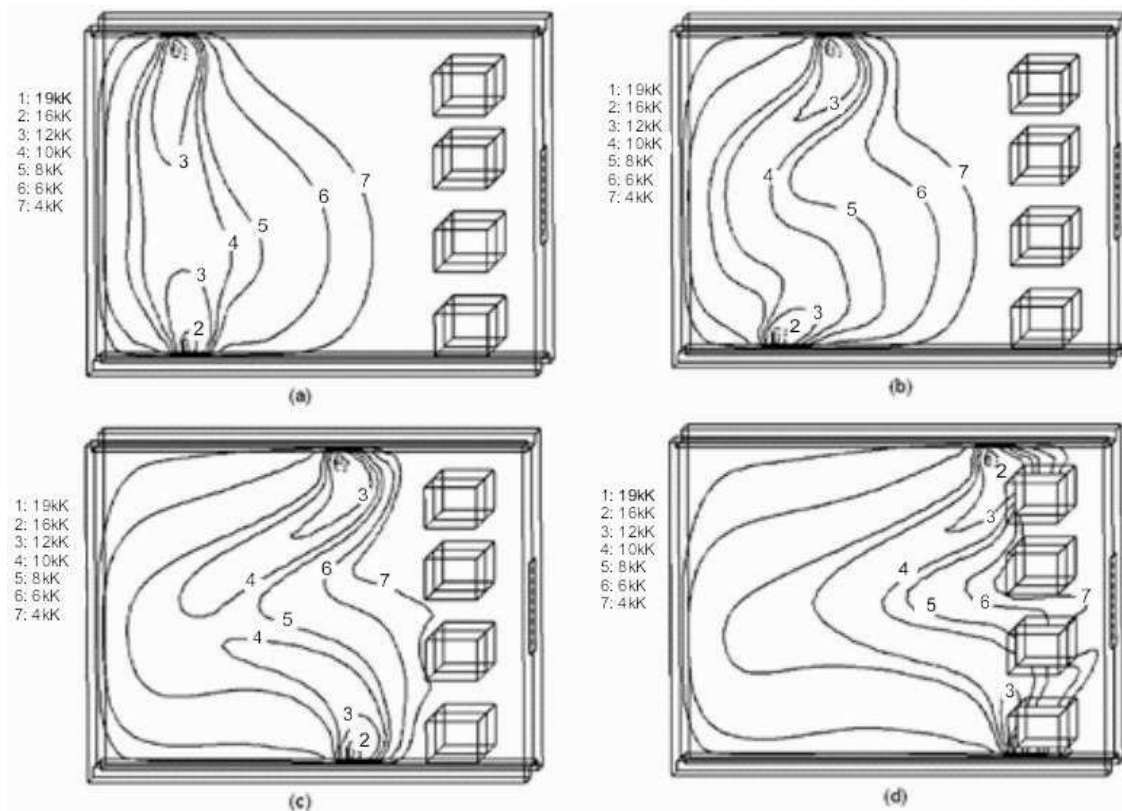


Figure 4-81 Temporal evolution of the temperature for I=100 A ((a) t=40 μs, (b) t=310 μs, (c) t=580 μs, (d) t=870 μs) [70]

Regarding the composition of the gassing material, once again it is demonstrated that presence of PA6 to the air of the chamber benefits switching characteristics, increasing the electrical potential.

Another research team, Technical University of Ilmenau, in Germany, has developed a work already exposed in section 3.3.1.1, regarding the influence of splitter plates, where the effect of different splitter plate shapes is analyzed, taking into account P1 radiation model [16]. For the arc roots model, a non-linear electrical resistance is used, with the same data that in [57].

Finally, the Technical University of Dresden in collaboration with CFX Berlin proposes a model developed with CFX 12 software (beta version) [3]. This work is based on previously presented works from Lindmayer's team [50, 54, 55, 58, 65].The geometry modelled can be seen in Figure 4-82, where three domains are defined: fluid, rails and splitter plate. The fluid has been considered as air, being its parameters function of the temperature up to 30000K, and the rail and the splitter plate have been considered made of regular copper. As for the boundary conditions, the room temperature has been defined as 300K, the pressure as 0Pa and the inlet current through the cathode as 50A. In this case, calculation of the magnetic field is neglected and an external and constant value of 0.1T has been imposed.

The radiation model has been defined with the Simplified Net Emission Coefficient (NECS) model presented in section 4.2.3.2. Finally, the arc roots have been modelled by defining a new and variable conductivity for the air, based on J/V values from experimental tests developed by Lindmayer, as seen in Figure 4-83 [58, 76].
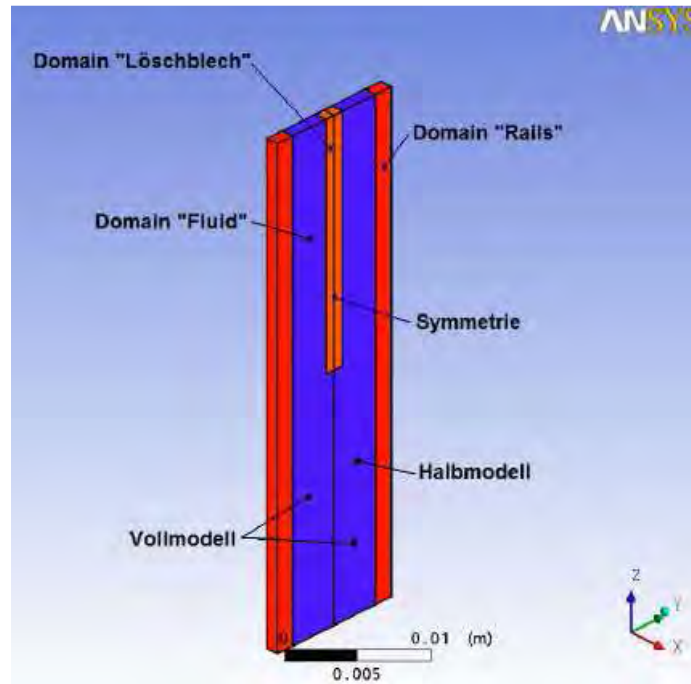
Figure 4-82 Modelled geometry with symmetry in the middle plane (y axis) [3]
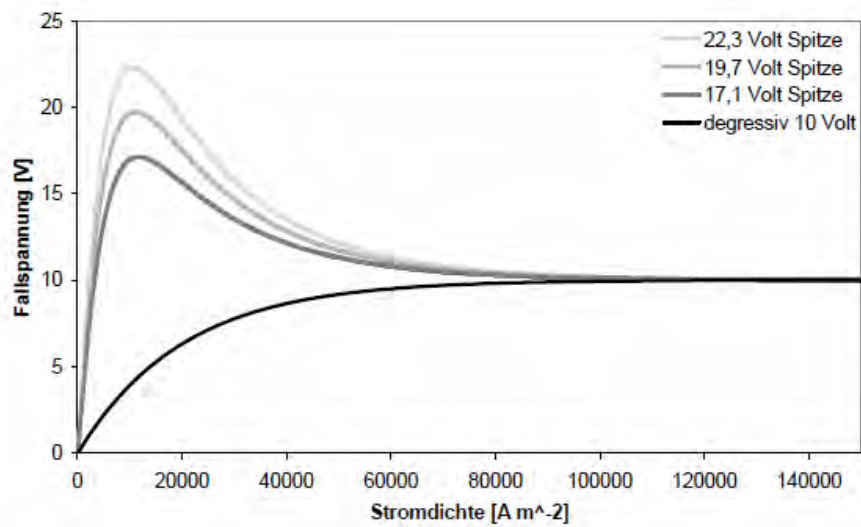


Figure 4-83 Curves for voltage drop over current density in the arc roots [3]

Evolution of the current density at different time-steps is obtained and shown in Figure 4-84. The arc is ignited at 10mm from the bottom. After that, the bending of the arc around the plate is shown at 0.575ms. Later on, current flow through the plate at 0.636ms is represented and finally at 0.735ms the arc is approaching to the top of the chamber. The results are exposed for the four V-J curves shown in Figure 4-84 to Figure 4-87.
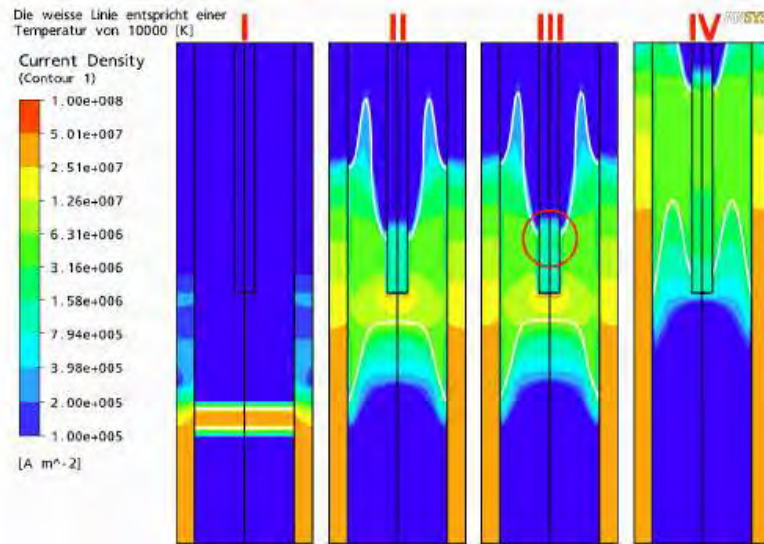
Figure 4-84 Current density evolution for 1, 575, 636 and 735 µs and for 10V peak V-J [3]
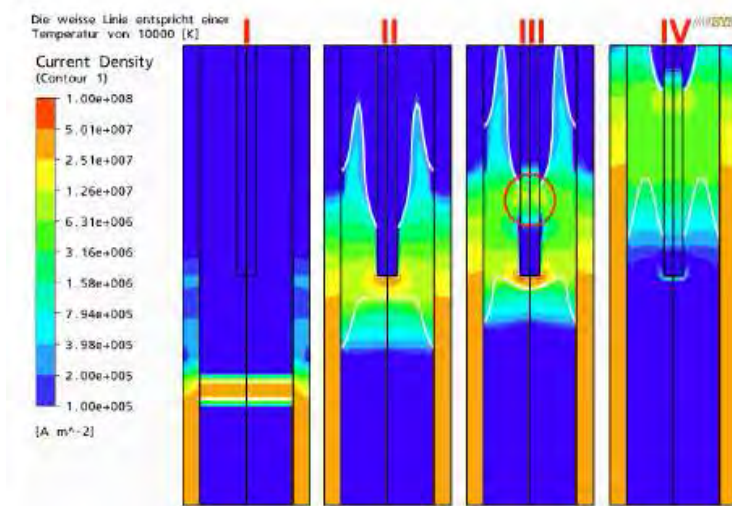


Figure 4-85 Current density evolution for 1, 575, 636 and 735 µs for and 17.1V peak V-J [3]
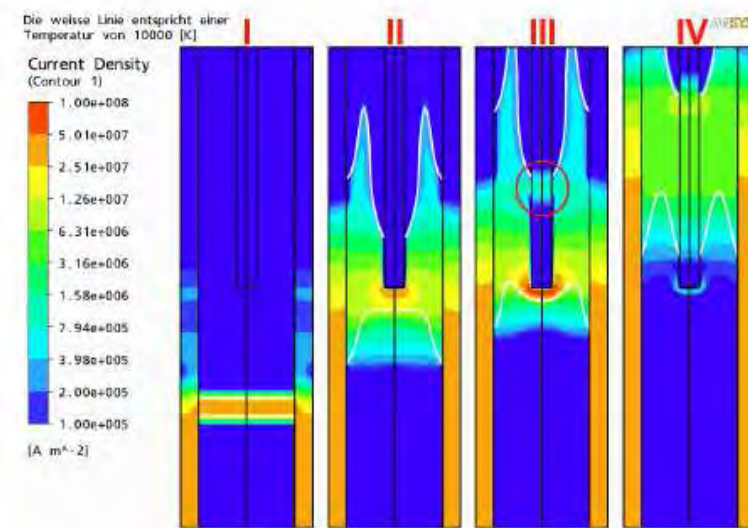


Figure 4-86 Current density evolution for 1, 575, 636 and 735 µs and for 19.7V peak V-J [3]
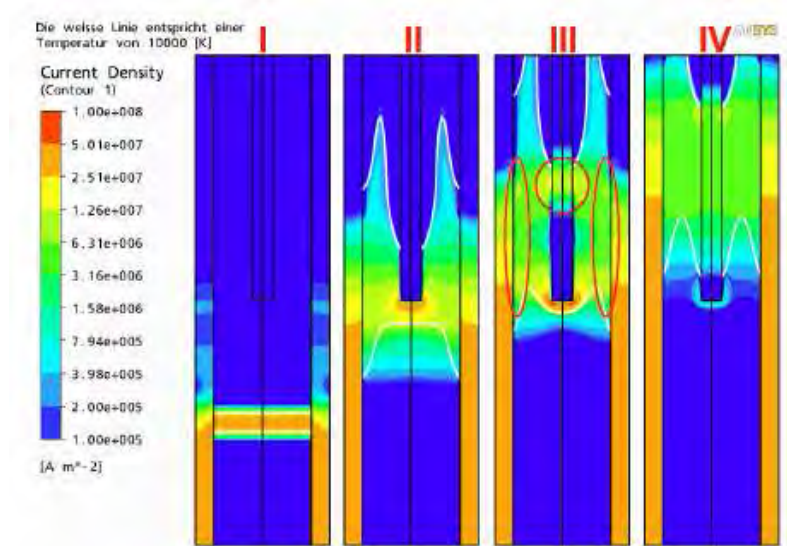
Figure 4-87 Current density evolution for 1, 575, 636 and 735 µs and for 22.3V peak V-J [3]

It can be highlighted that the higher the peak of the V-J curve, the higher the arc root is formed on the splitter plate. Overall, a diffuse arc is obtained and although the different peaks of the curves seem to lead to a little different at 0.636ms, for the current flow in the splitter plate, it does not really make a difference in the overall behaviour.

### 4.3.2.2 Manufacturers' models

Regarding LVCB manufacturers, Schneider Electric has published several papers in the area of the electric arc. Their research is mainly focused on the analysis of reignition effects and they usually also show the arc movement based on the temperature.

Figure 4-88 shows the device tested in [77], [78] and [79], where the arc re-strike and the interaction between the arc and the walls of the switching chamber of a LVCB is analyzed. In this model [79], Navier-Stokes equations are solved in the gas (MHD), along with the thermal conduction equation in the chamber walls. The model developed is 2D, analyzing the phenomena desired in a perpendicular plane to the electrodes.
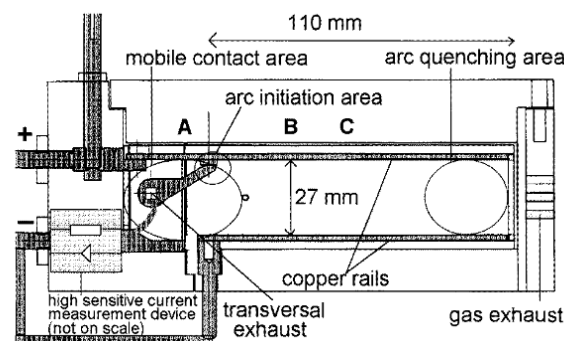


Figure 4-88 Side view of the circuit breaker model [79]

The simulation results for the arc voltage, inner pressure and the erosion rate of chamber walls are compared to experimental values (Figure 4-89). Figure 4-90 shows an example of the temperature distribution obtained in the simulation, representing the displacement of the arc during 9ms along the chamber.
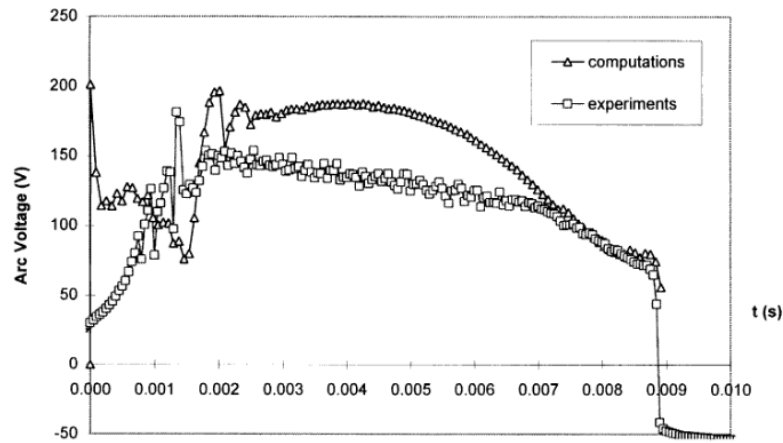
Figure 4-89 Comparison of the arc voltages [79]
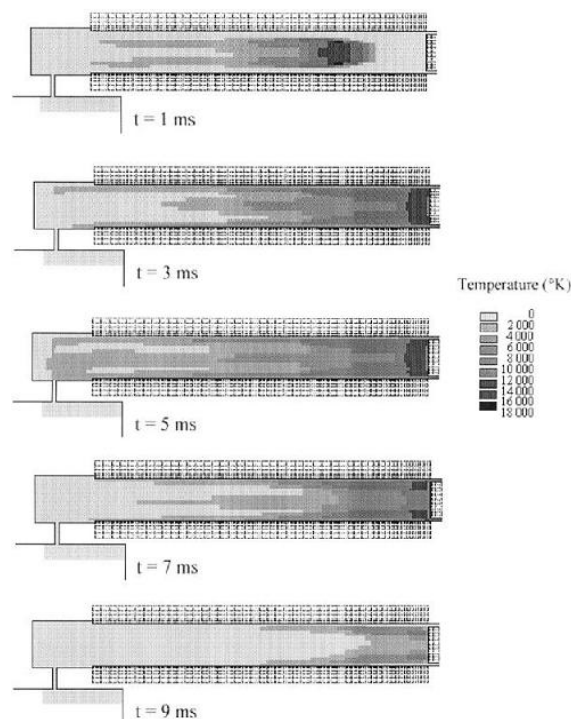


Figure 4-90 Temperature of the gas inside the chamber by simulation [79]

The same geometry is analyzed in [80], where the simulation of the arc in the 2D transverse middle plane between the electrodes of the chamber is obtained (Figure 4-91). Among the issues taken into account in the simulation, the consideration of conductive elements and the arc itself in the magnetic induction can be mentioned. The simulation considers the chamber fully closed, being the walls at 300 K. The arc ignition is produced by a local injection of energy ($2x1011W/m^3$) in front of the moving contact. When the local temperature reaches 10.000K, the fluid becomes conductive and the forced heating is interrupted, imposing the current circulation. Thus, heating by Joule effect and the electric arc appears. Figure 4-92 shows an example of the evolution of the temperature distribution with the arc motion. This time, the arc reaches the end of the chamber in just 1.5ms.
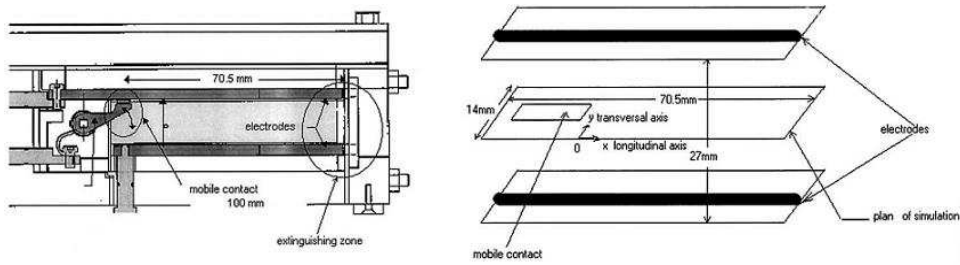
Figure 4-91 Arc chamber and plane considered for the simulation [80]
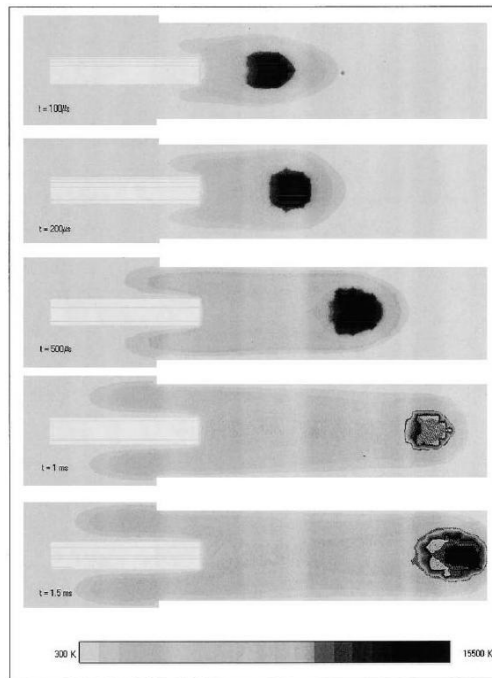


Figure 4-92 Evolution of the temperature inside the chamber obtained in the simulation [80]

A further step is presented in [81], where the interaction between the circuit breaker and the network is analyzed. In this analysis, a MHD model that includes the magnetohydrodynamic equations, radiation phenomena and contact erosion is developed using a 2D CFD code. But also the arc voltage induced on the circuit breaker is calculated and inserted into a simple electric network, constituted of a voltage source, a resistance and inductance (Figure 4-93).
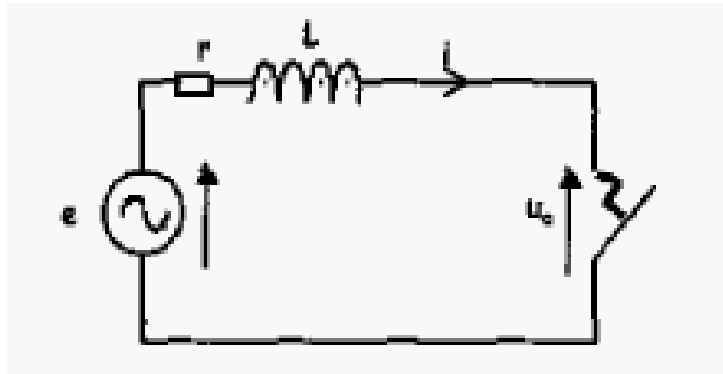


Figure 4-93 Connection of the CB to the grid through the arc voltage [81]

The LVCB model used is shown in Figure 4-94, where the electrodes, the movable contact and the arc chamber with the plates are modelled. The arc voltage obtained with the MHD simulation model acts as a second voltage source for the grid of Figure 4-93, which can be

mathematically expressed by equation (2-3). This way, it becomes possible to model and analyze the limited current of the circuit of Figure 4-93.
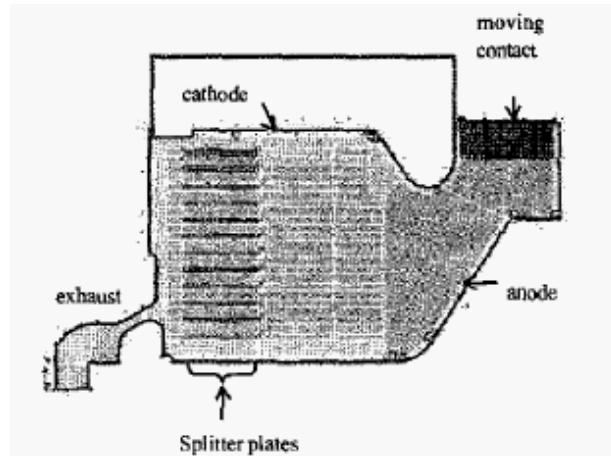


Figure 4-94 LVCB MHD model [81]

Regarding the results obtained in the MHD simulation, it is observed that the arc voltage increases when the arc enters the splitter plates in the arc chamber, mainly due to the voltage of the arc column and the voltage drop in each arc root that appear on the plates. Thus, when the arc voltage becomes higher than network voltage, the current begins to decrease achieving its interruption.

Another model from Schneider Electric is proposed in [82] where a 3D LVCB geometry model is presented (Figure 4-95), using the software N3S-NATUR.
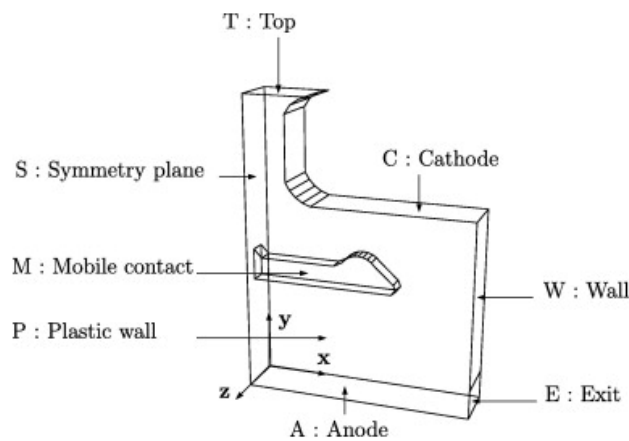


Figure 4-95 Geometry of the LVCB [82]

A half symmetry plane has been applied for simplification. A dynamic mesh defined with 118026 tetrahedral elements is considered in the analysis, where the separation of the contacts is modelled. The timestep is defined as $5.10^{-8}$ s and a total 3ms of arc movement has been simulated. As a result, once again the temperature of the arc movement is obtained (Figure 4-96).
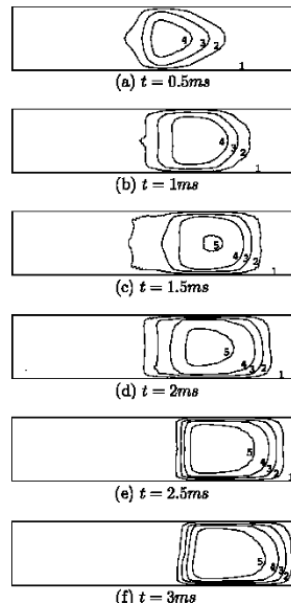
Figure 4-96 Contours of constant temperature (1:300K; 2:6000K; 3:12000K; 4:18000K; 5:24000K)

Siemens AG company has also developed different models in this area, for LVCBs. In [83], a simplified model for MCCBs is presented, composed by two volumes (Figure 4-97) at different temperatures and with different boundary conditions, where the average values for temperature and pressure are calculated for each time instant. Thus, it is a different model compared to the previously exposed ones, due to the two volumes.
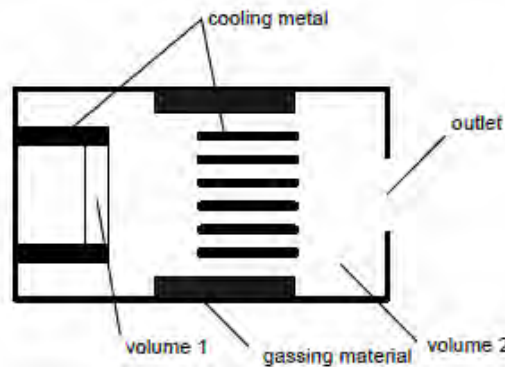


Figure 4-97 Simplified model for MCCB with two volumes [83]

Volume 1 represents the electric arc, where electric power is injected. Due to the power increase, this volume will increase and displace volume 2, with lower temperature, outside the chamber. The total volume $Vt = V_1 + V_2$ is considered constant all the time. Besides, a constant and equal pressure is assumed for the two volumes. After some time, the entire chamber will reach the same temperature. Figure 4-98 shows the expansion of volume 1 versus the contraction of volume 2.
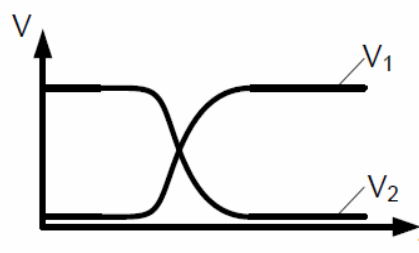


Figure 4-98 Dependence and variation of the volumes over time [83]

Experimental measurements of pressure are used to validate the model (Figure 4-99), where approximate values between real experiments and simulation can be found, with maximum pressure values around $6.10^5$ bar. A small delay over time of simulated values, regarding the real values is detected.
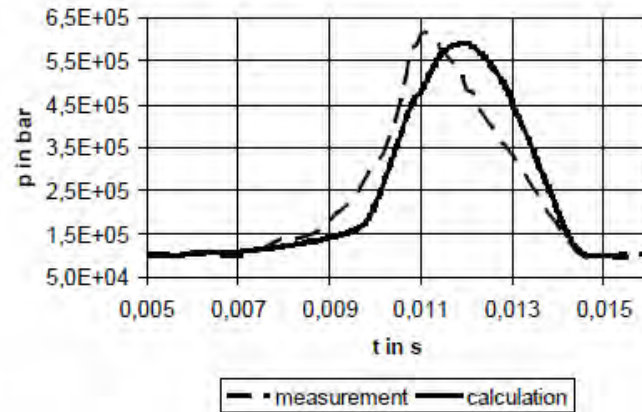


Figure 4-99 Pressure obtained experimentally and from simulation [83]

Furthermore, results of power, temperature and mass are represented in Figure 4-100. This graph shows how the arc power is transferred (negative value) by radiation and gassing material to the chamber (metal cooling). A third part of the incoming power is concentrated in the splitting plates and the rest is dissipated by the gas.
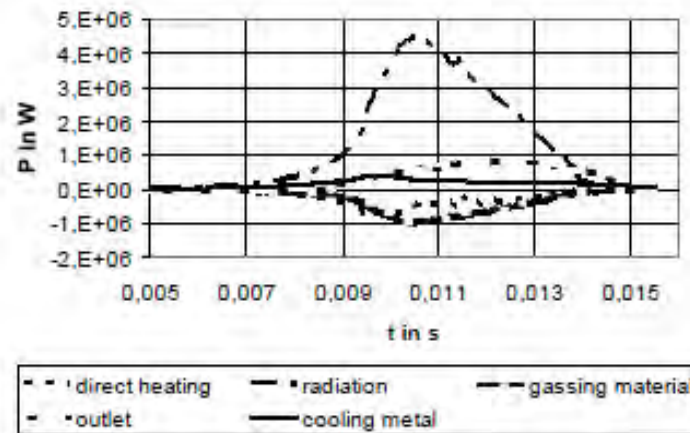


Figure 4-100 Power of different processes over time [83]

In [84], published by Siemens, a state of the art of the last 15 years of arc simulation is included. Besides, a new model of electric arc for a MCCB is presented. The influence of the mesh quality, the vaporization of copper, the geometry and models of arc roots are considered, for currents between 10000 and 15000 A. The arc chamber modelled, shown in Figure 4-101, is more approximated to real chambers than previously presented ones.

Experimentally measured current and voltage are shown in Figure 4-102. The simulation carried out between 4 and 6ms, is indicated in blue in the figure as the most interesting part.

Additionally, as seen in Figure 4-101, two types of mesh have been used in the simulation, a finer and a thicker mesh, called as "fine" and "coarse" in Table 4-13. Then, for each mesh, different features have been applied, obtaining five different cases. The special features incorporated are:

- Arc root model for the first case with fine mesh
- 15% of copper in plasma due to the evaporation of the electrode with a coarse mesh in the third model
- A closed structure, simulating the boundary condition between the arc chamber and the volume between the electrodes as a wall, for the fourth model with the coarse mesh.
- Finally, cases 2 and 5 just represent the model without any special feature, with a fine and coarse mesh, respectively.
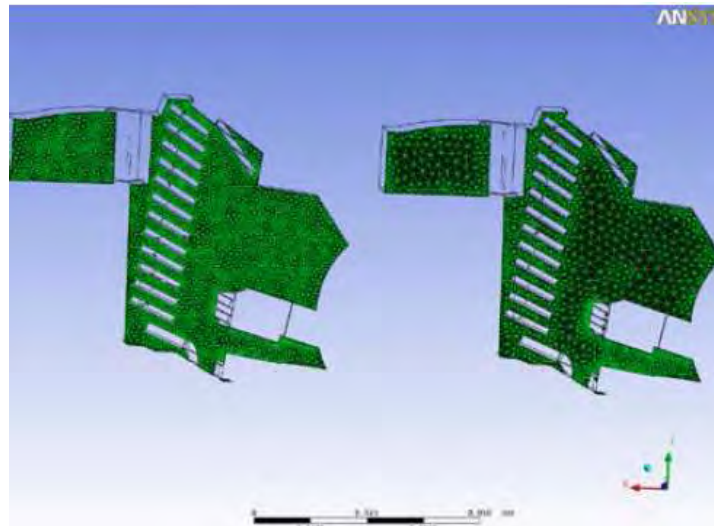


Figure 4-101 Meshing of the arc chamber model with 50000 and 100000 nodes [84]
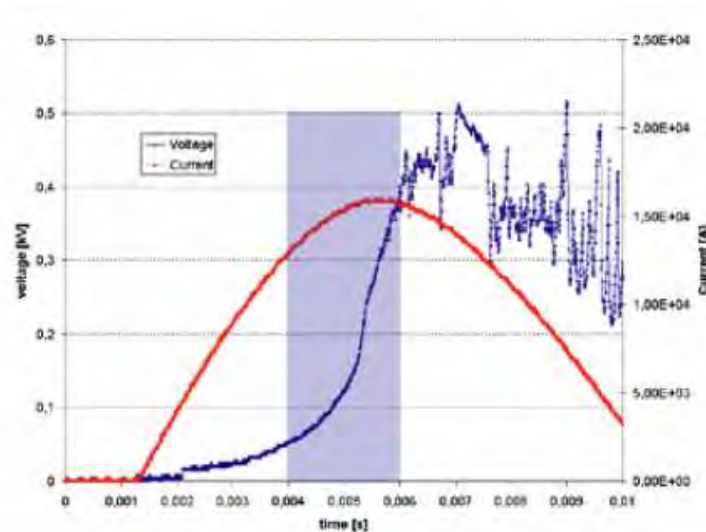


Figure 4-102 Measured voltage and current [84]

Table 4-13 Simulated models [84]

| Case | Mesh | Specific feature |
|---|---|---|
| 1 | Fine | Arc root model |
| 2 | Fine | - |
| 3 | Coarse | 15% copper |
| 4 | Coarse | Closed |
| 5 | Coarse | - |

For these cases, the voltages shown in Figure 4-103 are obtained in the simulation.
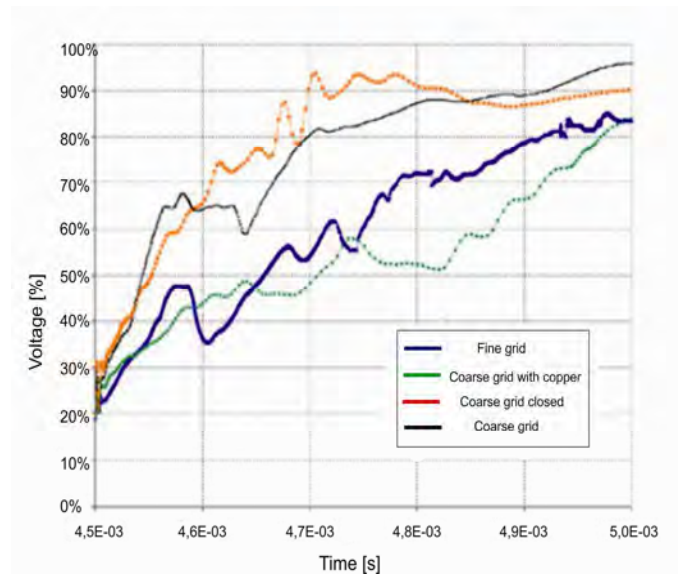
Figure 4-103 Voltage drops in the arc chamber, for various simulations [84]

Thus, the following conclusions can be extracted from the simulation:

- Coarse grid leads to higher arc voltages at the beginning of the opening process, which is not in concordance with real data (Figure 4-102). Also, it is noticed that a difference up to 20% at some points, between voltage values obtained with fine or coarse grid simulation. Therefore, it is evident the importance and influence of meshing size in the simulations.

- With the assumption of 15% copper in the air, the arc voltage value decreases. The reason is that as the gas composition is different, the parameters that define this gas, as electrical conductivity, thermal conductivity, viscosity etc., are also different, but especially electrical conductivity. In this case, electrical conductivity has greater value at lower temperature. Therefore, the arc voltage value in this case is the lowest.

- Finally, in the case of a closed chamber, the arc is accelerated with a higher pressure into the splitter plates. Therefore, the voltage curve will be larger, as shown in Figure 4-103.

Figure 4-104 shows the temperature distribution in case of "closed" or "open" wall. However, no chart legend in shown on it, so no further conclusions can be obtained.



(a)                                                      (b)
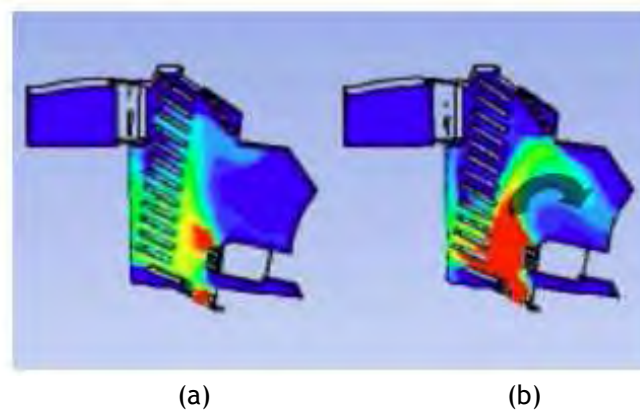
Figure 4-104 Temperature distribution for (a) closed wall, and (b) open wall [84]

To conclude with this geometry of a MCCB, moving mesh and the ablation of both electrodes and wall have been taken into account in [2]. Temperature and pressure plots results are exposed in Figure 4-105.
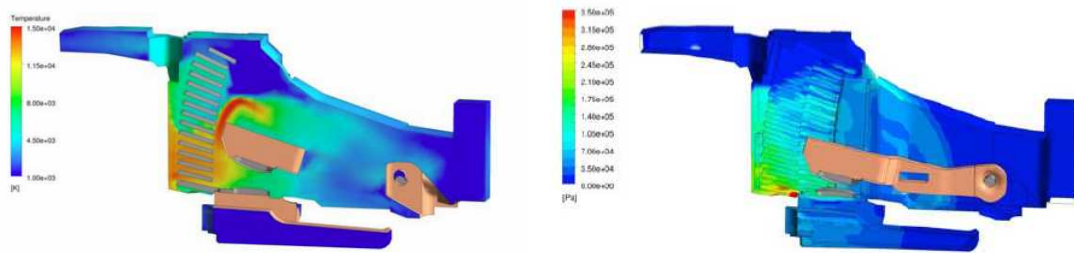


Figure 4-105 (a) Temperature plot and (b) pressure plot [2]

The pressure plot is an early snapshot with the pressure wave visible on the way to the outlet, while in the temperature plot it is noticed the colour range between 10000K (blue) and 15000K (red).

As verification of the model, the voltage values obtained in the simulation and experimental tests are compared in Figure 4-106. It can be seen that the simulated values are lower than the real measurements, even though they follow more or less the same trend.
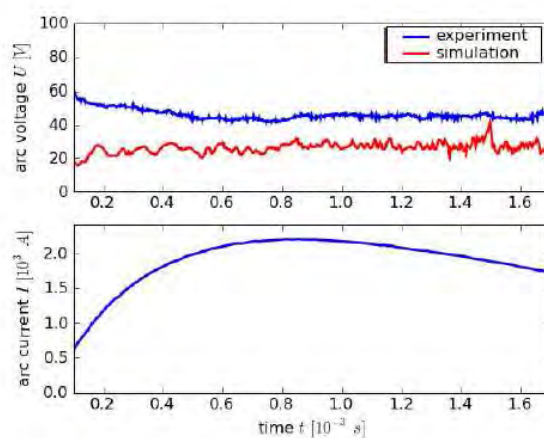


Figure 4-106 Experimental and simulated value of arc voltage and imposed arc current [2]

### 4.3.2.3 Comparison

As a summary of all the models reviewed in the literature, Table 4-14 is presented. In this Table the main characteristics of all references previously exposed are collected, making easier the comparison between them.

Table 4-14 MHD models review

| Research team | Reference | First author-Year | Software | Geometry | Symmetry | Mesh | Magnetic field | Radiation model | Splitter plates | Arc roots model | Experimental validation | Results |
|---|---|---|---|---|---|---|---|---|---|---|---|---|
| TU Braunschweig (Germany) | [50] | Karetta-1998 | Flow 3D | Parallel rails | 1/4 | No data | Biot-Savart | Simplified emission | No | No | No | Arc position Arc Voltage Pressure Temperature Flow velocity |
| | [34] | Karetta-1998 | Flow 3D | Divergent rails Opening of Chamber: Open, close, with vents. Expansion volume | 1/4 | No data | Biot-Savart | Simplified emission | No | No | Yes | Arc position Arc Voltage Pressure Temperature Flow velocity |
| | [51] | Lindmayer-2002 | CFX 4 FEM | Divergent rails Opening of Chamber: Open, close, with vents. Expansion volume | 1/4 | No data | Vector Potential | Simplified emission | No | No | Yes | As in [34] High speed camera images, flow |
| | [52] | Lindmayer-2002 | CFX 4 FEM | Parallel Ferromagnetic rails (with no Fe, total Fe, or stripped) | 1/4 | No data | Vector Potential | Simplified emission | No | No | No | Arc position Temperature Pressure |
| | [53] | Lindmayer-2003 | CFX 4 FEM | Parallel rails Splitter plate | 1/4 | No data | Vector potential | Simplified emission | Yes,1 | Yes, layer R/J | Yes | Arc position Splitting process |

| Research team | Reference | First author-Year | Software | Geometry | Symmetry | Mesh | Magnetic field | Radiation model | Splitter plates | Arc roots model | Experimental validation | Results |
|---|---|---|---|---|---|---|---|---|---|---|---|---|
| TU Braunschweig (Germany) | [54] | Lindmayer-2004 | CFX 4 FEM | Parallel rails Splitter plates of dif length | 1/4 | No data | Constant | Simplified emission | Yes, 1 | Yes, layer R/J | Yes | Arc position Splitting process |
| | [55] | Lindmayer-2005 | CFX 4 FEM | Parallel rail Splitter plate | 1/4 | No data | Constant | Emission NEC Conductivity | Yes, 1 | Yes, layer R/J | Yes | Arc position Splitting process |
| | [57] | Rüther-2006 | CFX 4 FEM | Parallel rail Splitter plate | 1/4 | No data | Vector potential | No data | Yes, 1 | Yes, layer R/J | Yes | Arc position Splitting process |
| | [58] | Mutzke-2007 | CFX FEM | Parallel rail Splitter plate | 1/4 | No data | Constant | No data | Yes, 1 | Yes, layer R/J: 4 curves | Yes | Arc position Splitting process |
| | [60] | Mutzke-2007 | CFX FEM | Parallel rail Splitter plate | 1/4 | No data | Vector potential | No data | Yes, 1 | Yes, layer R/J: 4 curves | Yes | Arc movement and experiments same I[A] |
| | [61] | Muztke-2008 | CFX FEM | Parallel rail Splitter plate | 1/4 | No data | Biot-Savart | No data | Yes, 1 | Yes, layer R/J: 4 curves | Yes | Arc movement and experiments same I(A)] |
| | [62] | Riss-2011 | CFX-beta | Parallel rails, Porous medium in the splitter plates | 1/4 | Around 100000 CFX mesh | No data | No data | Yes, porous medium | No | No | Arc movement Voltage drop |
| | [63] | Riss-2012 | CFX-beta | Parallel rails, Porous medium in the splitter plates | 1/4 | Around 100000 CFX mesh | No data | No data | Yes, porous medium | No | No | Arc movement Voltage drop |

| Research team | Reference | First author-Year | Software | Geometry | Symmetry | Mesh | Magnetic field | Radiation model | Splitter plates | Arc roots model | Experimental validation | Results |
|---|---|---|---|---|---|---|---|---|---|---|---|---|
| Xi'an University (China) | [64] | Xingwen-2005 | PHOENICS FEM | Parallel anode and cathode No rails | No data | No data | Biot-Savart | Simplified emission | No | No | No | Venting size, gassing and arc ignition effect |
| | [67] | Yi-2005 | No data | Parallel anode and cathode. No rails Ferromagnetic | No data | No data | Vector potential | NEC | No | No | No | Arc movement based on T distribution |
| | [68] | Yi-2006 | Fluent FEM | Parallel rails Splitter plates | 1/2 | Hexahedral Timestep 1us | Vector potential | No data | Yes, 2 | No | No | Magnetic flux Temperature Electric potential |
| | [69] | Qiang-2006 | Fluent FEM | Parallel rails Splitter plates | 1/2 | 0.225, 0.5, 0.5mm grid spacing (x, y, z) 1 us | Vector potential | Simplified emission | Yes, 4 | Yes | Yes | Arc position |
| | [71] | Yi-2007 | Fluent FEM | Opening contacts Parallel rails | 1/2 | Hexa and Tetrahedral 132850 cells | Vector potential | Simplified emission | No | No | Yes | Contact separation Arc movement |
| | [72] | Xingwen-2007 | Fluent FEM | 2D | No data | 0.2, 0.2 mm grid size | Biot-Savart | Simplified emission | No | No | Yes | Arc ignition influence on arc displacement |
| | [73] | Xingwen-2007 | Fluent FEM | 2D | No | 0.2, 0.2 mm grid size | Biot-Savart | NEC Simplified emission | No | No | Yes | Gassing properties and radiation model influence on arc displacement |

| Research team | Reference | First author-Year | Software | Geometry | Symmetry | Mesh | Magnetic field | Radiation model | Splitter plates | Arc roots model | Experimental validation | Results |
|---|---|---|---|---|---|---|---|---|---|---|---|---|
| Xi'an University (China) | [74] | Xingwen-2009 | Fluent Ansys | Parallel rails | 1/2 | 0.2, 0.2 mm grid size | Biot-Savart | NEC Simplified emission | Yes | Yes, nonlinear electrical resistance | Yes | Fe and splitter plate size effect |
| | [75] | Rong-2010 | No data | Splitter plates stack | 1/2 | No data | Vector potential | NEC | Yes | Yes, nonlinear electrical resistance | Yes | Temperature distribution V, I |
| | [42] | Yang-2013 | No data | Parallel rails and splitter plate stack | 1/2 | Moving mesh | Vector potential | NEC P1 | Yes | Yes, nonlinear electrical resistance | Yes | Arc commutation, motion and splitting. Radiation, erosion, ablation and turbulence discussion |
| Université Paul Sabatier (France) | [70] | Swierczynski-2004 | Fluent 4.5 FEM | Parallel rails Splitter plates | No, full | 0.16, 0.33, 0.65 grid spacing. 265000 cells | Vector potential and rectilinear equation | No data | Yes,4 | No | No | Arc root positions Temperature |
| TU Ilmenau (Germany) | [16] | Rümpler-2007 | Fluent FEM MpCCI | Parallel, V-shaped plates | No, full | No data | Biot Savart | Simplified emission and P1 | Yes, rectangular and V-shaped | Yes, non linear resistance | Yes | Arc position Arc voltage |
| CFX Berlin TU Dresden (Germany) | [3] | Lohse-2009 | CFX-beta V12 | Parallel rails 1 SP | 1/2 | No data | Constant | NECS | Yes 1 | Yes | No | Arc movement |
| Schneider Electric (France) | [77] | Fievet-1997 | Own software | 2D Parallel rails | - | No data | No data | NEC | No | No | Yes | Reignition |

| Research team | Reference | First author-Year | Software | Geometry | Symmetry | Mesh | Magnetic field | Radiation model | Splitter plates | Arc roots model | Experimental validation | Results |
|---|---|---|---|---|---|---|---|---|---|---|---|---|
| Schneider Electric (France) | [78] | Fievet-1997 | Own software | 2D Parallel rails | - | No data | No data | NEC | No | No | Yes | Reignition |
| | [79] | Domejean-1997 | Own software | 2D Parallel rails | - | No data | No data | NEC | No | No | Yes | Arc voltage Pressure Current Temperature |
| | [80] | Rachard-1998 | Own software | 2D Parallel rails | - | No data | Biot Savart | No data | No | No | No | Magnetic force and viscosity influence |
| | [81] | Wild-2004 | Own software | 2D Full chamber Splitter plates, grid | - | No data | Biot Savart | Experimental law | Yes | No | Yes | Reignition Lorentz Force |
| | [82] | Piqueras-2008 | Own software | 3D | 1/2 | 118026 cells | Biot-Savart | P1 | No | No | No | Temperature distribution |
| Siemens (Germany) | [84] | Anheuser-2009 | CFX FEM | Realistic MCCB | No data | 50000 and 100000 nodes | No data | NEC | Yes | Yes | No | Temperature |
| | [2] | Anheuser-2011 | CFX FEM | Realistic MCCB | No data | No data | No data | NEC | Yes | Yes | Yes | Temperature Voltage |

## 4.4   CONCLUSIONS

As it has been exposed along this chapter, electric arc modelling through software simulation is an important tool for better understanding the arc phenomena and the future design optimization of LVCBs. For a better approximation of simulation models to real scenarios, it is essential to have a deep knowledge of the phenomenon itself and the software tool. A good simulation model will lead research community to an improvement of these switching devices.

As a complementary aspect of the software simulations, real experimental tests arise. Firstly, these tests are essential for the validation of the developed simulation models, to know how close or far from real scenarios the results of the simulation are. Secondly, some advantages of real experiments over simulation models can be highlighted, such as precision and accuracy. But for a long research process, software simulation may allow achieving a better compromise between cost and accuracy than real tests, as the cost of real experiments is very high for any change that could be necessary in the prototype or the analysis conditions.

Thus, among the simulation models, three main groups are found:

- Black box models, treat the arc as a differential equation inside the electric grid, and focus their analysis on the effect of the arc on that electric grid, but not on the arc phenomena itself.

- Models based on graphics and diagrams, usually, are derivated from the information extracted from the other two models, black box or physical or even from real experimental data. Their aim is to collect all the limiting data for the design and operation of LVCBs.

- Physical models are the most complete ones for the understanding of the phenomena evolution and the improvement of circuit breakers designs, as they focus their attention on the inner physical processes. As the new model developed in this thesis is considered in this group, a review of the application of this type of models to LVCBs has been presented in this chapter.

Considering physical models, two main research areas can be distinguished. Researches that only concentrate their attention on the electric and magnetic field, calculating just their effects on the movement and displacement of the arc. And second, researches involved with the complete physical process of the arc, including fluid flow dynamics, electric and magnetic fields and heat transfer.

Regarding the electromagnetic models, all of them have several common features. All of them are developed with a FEM tool. Some are developed in 2D, assuming the corresponding simplifications, but most in 3D, as the accuracy and the correspondence with real scenarios is higher. The arc is modelled as cylindrical or parallelepiped conductor, which moves as a result of the magnetic Lorentz force. Thus, the arc movement and the effect of the magnetic forces on the arc motion, and also on the contacts, are analyzed.

In the second group of physical models, besides electromagnetic effects also fluid dynamics are considered, defining the arc as a conductive plasma flow. FVM and FEM software tools have been used by most researchers due to the interaction between fluid dynamics and electromagnetic fields. In the first papers, these two software tools have been coupled by

user defined scripts. Nevertheless, in newer references [3, 62, 63] CFX arise as a tool that already couples both phenomena.

Some of these models have been developed 2D and some others 3D. But, the complexity of these models makes it necessary to introduce simplifications. One possibility is the simplification in geometry taking advantage of symmetry effects and so, many researchers consider only half or quarter of the complete geometry. However, that means to assume the arc as a symmetric process which is completely unreal, as real experiments results show.

Regarding geometry, most of the existing models use very simplified chambers, with parallel rails as cathode and anode and sometimes with one or two splitter plates. This is due to the higher computational cost associated with more complex geometries that, in general, only manufacturers or important research centres can afford. However, it does not have too much sense to complicate the simulation defining complicated geometries with lot of details, when the model of the arc is still physically incomplete.

Regarding the mesh, no information is usually provided in the literature. However, simulations are very dependent of meshing data and a bad or poor mesh will lead to poor results, as it will be shown in chapter 6. In the few data revealed regarding the mesh, hexahedral or tetrahedral meshes around 100000 cells have been used, which is not actually a very accurate meshing.

For the magnetic field, three approaches are used: Biot-Savart equation, vector potential formulation or the application of a constant external magnetic field value without having into account the magnetic field induced by the arc current itself. The choice between Biot-Savart and vector potential is mainly due to the software characteristics. Even though it has to be pointed out that Biot-Savart formulation requires the highest computational time. In any case, the external field option is the less accurate one, as it is further from the real phenomenon.

Several approaches are also exposed in the literature analyzed to represent radiation heat transfer. The simplest one is a simplified emission equation, based on Stefan-Boltzmann constant, as it allows reducing computational time, but leads to incorrect arc voltages when comparing simulation results with real tests. Secondly, NEC method is also widely used in many references. This approach is more realistic and the computational time is not so high. However, this method and its simplification, NECS, have to be criticized as they do not take into account the absorption effect. Three references uses the most complete radiation model up to now, P1, approaching better the effect to real cases, as the three phenomena involved in radiation, emission, absorption and scattering are considered. This way, the thermal transfer from the arc to the switching medium is better modelled and the voltage drops obtained are lower than with NEC or NECS cases, which match better real measurements.

In the analysis of the arc root models, not many options come up. The experimental results for voltage-current density from Lindmayer are the only published data for arc root modelling. With these data, different models have been defined for its application: Sheath layer or electrical contact resistance. However, further approaches are needed in this field for electric arc modelization improvement.

Thus, taking into account these contributions and in particular [3] as a base reference, a new model is proposed in this thesis (chapter 5), where several improvements have been introduced over the base model, taking into account the above mentioned disadvantages of the reviewed models. In the new model, no simplification regarding symmetry is applied, a

deep study of the meshing influence has been achieved, the most real approach for the radiation has been defined, P1, and a non linear contact resistance for the arc root models have been applied. Finally, real experiments have been developed for the validation of the new proposed model and a better understanding of the phenomena.

# CHAPTER 5

## NEW MODEL FOR ANALYSING THE ELECTRIC ARC

# 5   NEW MODEL FOR ANALYSING THE ELECTRIC ARC

## 5.1   INTRODUCTION

As it is well known, the good performance of LVCBs in the electric network is fundamental for the safety and reliability of the grid. Thus, the improvement of the LVCBs design is an important task. Throughout chapter 3, the existing LVCBs have been exposed. Mainly three groups can be distinguished, MCB, MCCB and LVPCB, according to the current limit they can interrupt. But in the three cases common elements, pieces and characteristics exist, such as: arc chamber, arc contacts, splitter plate stack, inlet and opening, etc, all of them important in the design and optimization of LVCBs.

Inside the arc chamber, electric current interruption occurs mainly by means of electric arc phenomenon. Thus, when defining and improving LVCBs, it is essential to analyze the electric arc phenomenon itself. Moreover, it has to be taken into account that as well as the arc has direct effects on the lifetime of LVCBs components, the components have also direct influence on the interruption process and electric arc extinction. Two alternatives are available to analyze this interaction: software simulation and real experimental tests. Both of them have advantages and disadvantages.

Experiments lead to a more realistic approach, but they are very expensive and difficult to carry out. The construction of the chamber prototype and the test bench takes a lot of effort. Besides, any change that has to be tested requires a new investment, which means a lot of time and money, i.e. the flexibility of experiments is low.

Software simulation models also require an economic investment, but are very flexible tools that allow testing changes in the design, reducing the need of new prototypes. In contrast, it should be pointed out the difficulty of modelling such a complex phenomena as the electric arc, due to the deep knowledge required about the electric arc phenomenon and the software tool used to represent the phenomenon adequately and obtain accurate results. Additionally, after the simulation model has been built and tested, validation of the model should be developed to check the reliability of the results. But it is easier to prove the reliability of the results than achieve the whole research work by experiments in laboratory.

Among simulation models, two alternatives can be again distinguished for physical analysis of the electric arc in LVCBs. Models where just magnetic and electric effects are considered, or full MHD models where the whole physic process of the arc is considered. Analyzed in chapter 4, it has been proved that MHD models are more complicated but also provide a more complete behaviour of the electric arc.

Thus, in this thesis a new MHD model for the analysis of the electric arc in LVCBs has been developed. The proposed model, defined using ANSYS CFX, considers a simplified geometry, following the tendency of simplified geometries exposed in chapter 4 for other authors, but it reproduces the behaviour of the electric arc with better accuracy. Later on, the proposed model has been applied to evaluate the effect of changes in the geometry of the chamber, quantity of splitter plates, position of the arc ignition, different input currents and arc roots definition.

In the following sections, first of all general aspects of the proposed model are introduced. Thus, characteristics of the software tool selected for the simulation are related, emphasizing the advantage of a single software, which already couples the whole MHD itself, and not two

as many authors had used, as exposed in chapter 4. Also, the necessary steps to define the simulation model are defined.

Afterwards, the new proposed model is presented. A first model, named "base model", is defined taking as reference the model proposed in reference [3], but including several improvements in the geometry, mesh, material parameters, radiation and magnetic field calculation. The results obtained are compared to the bibliography and with the results obtained in real tests developed in the laboratory of the Technical University of Ilmenau (Germany), as presented in chapter 6.

## 5.2   SOFTWARE TOOL

As it has been explained in chapter 4, electric arc physics is defined by fluid dynamics and electromagnetic. Thus for the magnetohydrodynamic resolution, a software coupling both equation systems is necessary. To solve Navier Stokes equations, a Computational Fluids Dynamics (CFD) code is needed. This code employs a discretization method that approximates a system of differential equations to a system of algebraic equations, which can be solved to obtain an approximation to the exact solution. The discretization allows translating a continuous set of equations into a finite set of values that can be numerically evaluated (Figure 5-1). Thus, the numerical solution will be represented by a set of discrete values given by $u_1, ..., u_{i-1}, u_i, u_{i+1}, ..., u_n$.
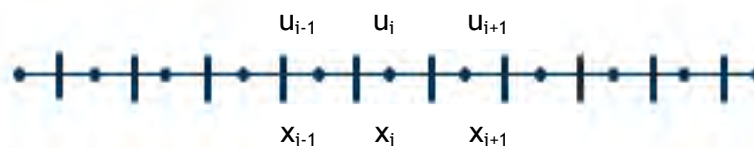


Figure 5-1 Discretization effect

For that purpose, three numerical methods can be used: Finite Differences (FD), Finite Element Method (FEM) and Finite Volume Method (FVM)

For those three methods, the most relevant aspect to be taken into account is the type of mesh used. A general classification allows separating the meshes into three types: structured, unstructured and hybrid meshes. Following the most relevant characteristics are presented:

- A structured mesh is characterized by regular connectivity that can be expressed as a two or three dimensional array. In structured meshes, all nodes have the same number of nodes around it (Figure 5-2 (a)) and can be applied to simple domains. This restricts the type of elements to quadrilaterals in 2D or hexahedral in 3D. Table 5-1 presents its advantages and disadvantages.



|         (a)          |          (b)          |          (c)          |
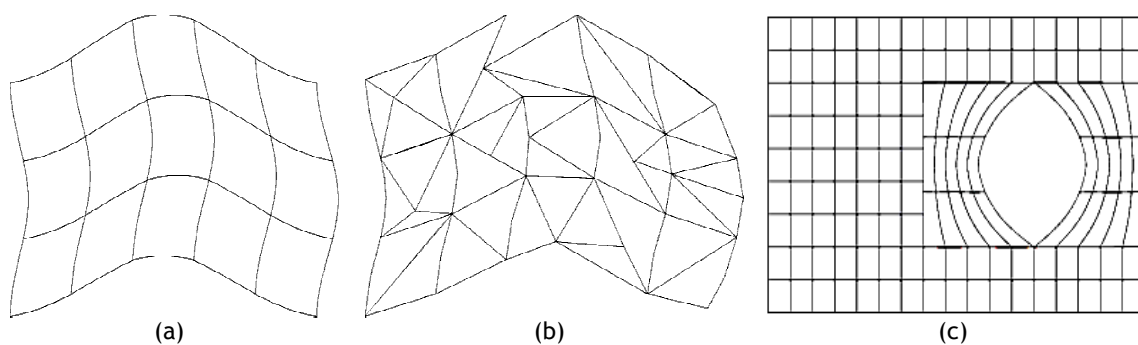
Figure 5-2 Meshing types: (a) structured grids, (b) unstructured grids and (c) hybrid mesh

Table 5-1 Advantages and disadvantages of the structure mesh

| Structured mesh | |
| --- | --- |
| Advantages | Disadvantages |
| • High control degree by the user. Mesh can be accurately designed to user requirements<br>• Hexahedral cells are very efficient at filling space, support a high amount of skewness and stretching before affecting solution<br>• Grid is flow aligned which helps the solver to converge<br>• Post-processing is easy as the logical grid spacing act as excellent reference points for examining the flow field | • Longer time is required to produce the mesh compared to an unstructured mesh<br><br>• Some geometry does not allow structured topology due to the high skewness angles and stretch of cells that are required |

- An unstructured mesh is characterized by irregular connectivity, which is not readily expressed as a two or three dimensional array in computer memory. The unstructured grid, shown in Figure 5-2 (b), is used for all kind of geometries and has an irregular data structure. Compared to structured meshes, the storage requirements for an unstructured mesh can be substantially larger since the neighbourhood connectivity must be explicitly stored. Advantages and disadvantages are presented in Table 5-2.

Table 5-2 Advantages and disadvantages of the unstructured mesh

| Unstructured mesh | |
| --- | --- |
| Advantages | Disadvantages |
| • Automated grid generation allows less effort to define mesh<br>• Well suited to inexperienced users<br>• Valid for most geometries<br>• Users are able to get results for relatively large mesh size quickly | • Lack of user control – mesh may not be defined as well as the user may desire in certain areas<br>• Tetrahedral elements do not twist or stretch well, which will severely impact on the accuracy<br>• Require excellent CAD surfaces. Small mistakes in the geometry can lead to large meshing problems<br>• Post processing software requires larger computer power |

- Finally, the block-structured grid or hybrid mesh, shown in Figure 5-2 (c), is a mesh that contains structured portions and unstructured portions.

Besides meshing type, other important parameters when defining a numerical method are: consistency, stability and convergence. Consistency relies on the truncation error, which is the difference between the discrete equation and the exact one. Stability has to do with the magnitude of the errors. Finally, convergence is the sum of consistency and stability.

Another aspect that has to be taken into account when choosing the discretization method is the way the discretization is achieved. It will be different for the conservation laws (mass, energy and momentum) whether the integral form or weak form (equation (5-1)), or the differential or strong form (equation (5-2)) is adopted as a base. As shown below, they are just two different expressions of the same equation.

$$\frac{\partial}{\partial t}\int_V u(x,t)dV + \int_A f(u)n\,dA = \int_V S(u,x,t)\,dV \tag{5-1}$$

$$\frac{\partial u(x,t)}{\partial t} + \nabla f(u) - S(u,x,t) = 0 \tag{5-2}$$

where:

$S(u,x,t)$:       source term
$u(x,t)$:        state variable
$f(u)$:        flow

Thus, attending to those parameters (mesh type, stability, convergence, consistency and conservation laws form) characteristics of the discretization methods (FD, FEM and FVM) can be explained:

- Finite Differences method (FD): the domain is discretized into a series of grid points and a structured mesh is required. The governing equations in differential or strong form are discretized and converted to algebraic form. First and second derivatives are approximated by truncated Taylor series expansions. The resulting set of linear algebraic equations is solved either iteratively or simultaneously.

  Depending if the used FD method is forward (equation (5-3)), backward (equation (5-4)) or centred (equation (5-5)), the approximated solution of the strong form, can be calculated, as shown in equations (5-3) to (5-5).

$$u_{x_i} = \frac{u_{i+1}-u_i}{\Delta x} \tag{5-3}$$

$$u_{x_i} = \frac{u_i-u_{i-1}}{\Delta x} \tag{5-4}$$

$$u_{x_i} = \frac{u_{i+1}-u_{i-1}}{\Delta x} \tag{5-5}$$

  The discrete form of the integral equation applying FD, on the other hand, is shown in equation (5-6).

$$\frac{(u_{i+1}-2u_i+u_{i-1})}{\Delta x^2} = s_i \tag{5-6}$$

Where: $u_{xx} = s(x)$ in the region $\Omega = \{x: 0 \le x \le 1\}$

  The main advantage of this method is that it is easy to implement. However, the main disadvantages are that it is restricted to simple grids and does not conserve momentum, energy and mass on coarse grids. Thus, it is not valid for the aim proposed in this thesis.

- Finite Element Method (FEM): In this case, an unstructured or mixed grid can be used. As it can be seen in Figure 5-3, the continuous domain $\Omega = \{x: 0 < x < 1\}$ is discretized in N-1 subdomains, where $\Omega_i = \{x: x_{i-1} \le x \le x_i\}$. Therefore, the approximate solution for the integral form is calculated as shown in equation (5-7).

$$u^\delta(x,t) = \sum_{i=1}^n u_i(t)N_i(x) \tag{5-7}$$
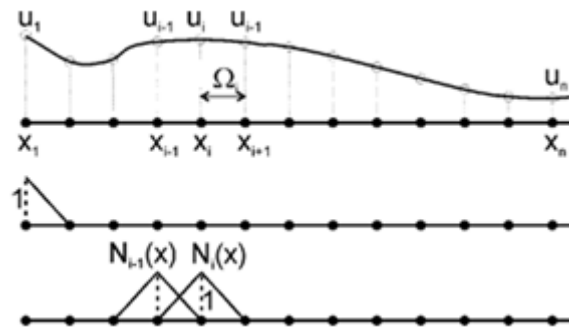
Figure 5-3 Discretization method in the FEM

And for the differential form, the discretization solution is shown in equation (5-8).

$$\frac{(u_{i+1} - 2u_i + u_{i-1})}{\Delta x} = \Delta x s_i \qquad (5\text{-}8)$$

where:

$u$:        value of the function

$x$:        discretization points

Among the advantages, higher accuracy on coarse grids can be mentioned, as well as good approaches for diffusion dominated problems, viscous flow or free surface problems. Regarding disadvantages, it can be mentioned that it is a slow method for large problems and not well suited for turbulent flow.

- Finite Volume Method (FVM): the solution domain is subdivided in a finite number of small control volumes, or cells, as shown in Figure 5-4. The differential equations which define the system are integrated over the control volume and the divergence theorem is applied. The grid defines the boundaries of control volumes while the computational node lies in the centre of the control volume.

To evaluate derivative terms, the values at the control volume faces are needed, thus an assumption have to be made about how the value rise. The result is a set of linear algebraic equations: one for each control volume. Then, they have to be solved iteratively or simultaneously.
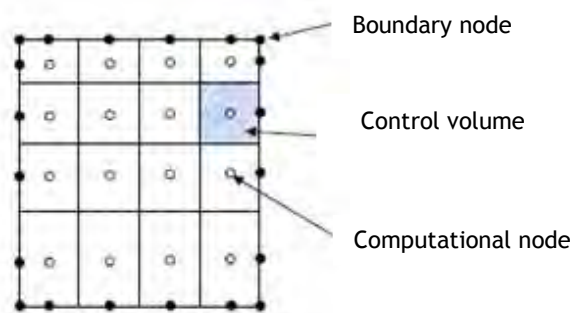


Figure 5-4 FVM grid

The total flux through the control volume boundary is calculated by the sum of integrals over the six control volume faces (in 3D).

In this case, the strong form of the conservation equations is solved as shown in equation (5-9).

$$\frac{(u_{i+1} - 2u_i + u_{i-1})}{\Delta x} = \Delta x s_i \tag{5-9}$$

So, the difference between the three methods relies in the spatial points where the evaluation of the equations to be solved is done, as well as the type of mesh that can be used or the accuracy of results. Figure 5-5 shows a comparison of the three numerical methods regarding flexibility and precision. It is noticed that the best compromise is obtained by FVM method. Thus, the most common numerical methods included in the main commercial CFD software tools are FVM (85%) and FEM (15%).
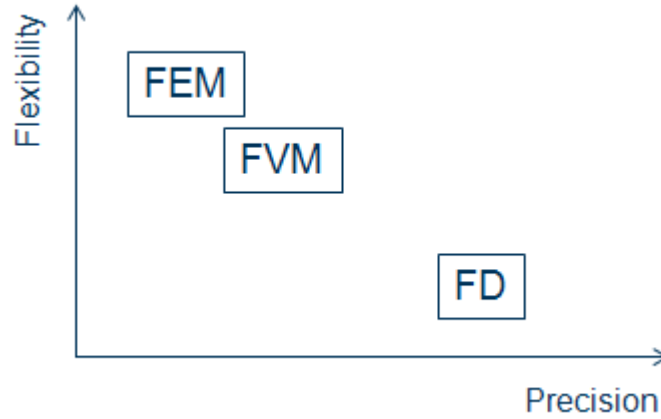


Figure 5-5 Flexibility vs. Precision for the numerical methods

In the FVM method, for each conservation law, the following steps are taken defining the computational variable as $\phi$:

−   Integration conservation law is satisfied in each cell (dΩ -> ΔΩ).
−   Values of the computational variables are calculated in the cell-centered computational node.

Thereby, the discretization equation (5-10) is obtained.

$$a_P \phi_P = \sum_{nb} a_{nb} \phi_{nb} + b \tag{5-10}$$

where:
$nb$:      neighbour cell of P
$\phi$  :      general variable
$a_p$:      centre coefficient
$a_{nb}$:      influence coefficient for neighbour cells
$b$  :      contribution of the constant part of the source term

Applying (5-10), at each iteration and each cell, a new value for variable $\phi$ in cell P can be calculated. But, most of the times it is common to apply an underrelaxation coefficient, U, to reduce the difference between the old and new values and help to the system stability, as shown in equation (5-11).

$$\phi_P^{new} = \phi_P^{old} + U(\phi_P^{new} - \phi_P^{old}) \tag{5-11}$$

where U can be:

- U<1: underrelaxation case. The convergence speed will be slowed down, but the stability will be increased, i.e. the possibility of divergence or oscillations in the solutions decreases.
- U=1: no relaxation case. It uses the predicted value of the variable.
- U>1: overrelaxation case. It can sometimes be used to accelerate convergence but will decrease the stability of the calculation.

For the new simulation model proposed in this thesis, an underrelaxation factor, U=0.2, has been used for the enthalpy. This value has been adjusted as a result of own experience, after different values have been tried.

On the other hand, the numerical scheme chosen to determine the value of $\phi$ is a second-order upwind scheme, obtaining the value of $\phi$ from the cell values in the two cells upstream of the face. Second-order upwind with limiters is one of the most popular numerical schemes because of its combination of accuracy and stability.

This way, the iterative process is repeated until convergence is achieved. Convergence is defined by:

- Discrete conservation equations (momentum, energy, etc.) satisfy a specified tolerance in every cell.
- The solution no longer changes with additional iterations.
- Mass, momentum, energy and scalar balances are obtained.

After that, the residuals (i.e. the differences between new and old values of computational variables) measure imbalance (or error) in conservation equations. The relatively scaled residual, at point P, is defined as shown in equation (5-12).

$$R_P = \frac{|a_P \phi_P - \sum_{nb} a_{nb} \phi_{nb} - b|}{|a_P \phi_P|}$$
(5-12)

For the new model developed, the required scaled residual has been defined as $1 \times 10^{-4}$, also adjusted from own experience.

Taking into account all these features, an analysis of existing commercial software tools has to be carried out before choosing the most appropriate for the analysis. Software tools used by other authors for plasma MHD analysis are shown in Figure 5-6.

As software tools have been improved over time, before commercial software tools have been available for the analysis of the electric arc, some authors have chosen a self written code for the definition of the model [11, 85]. Among commercial software, up to the appearance of ANSYS CFX v11 with beta version, the way to couple fluid dynamics flow and electromagnetic equations has been to use CFD and FEM software and user defined routines, or use a third commercial software (e.g. MpCCI) for the coupling.

Thus, it can be seen in Figure 5-6 that Ansys CFX v11, and higher versions, is the best option. Thereby, the software used for the new model developed in this thesis has been ANSYS CFX v13.0. This software is a high performance general purpose fluid dynamics program that has been applied to solve wide-ranging fluid problems. It uses a FVM and a coupled solver, which solves the hydrodynamic equations as a single system. As said, from version 11 and higher offers the possibility to solve the coupled set of electromagnetic equations and to define User Defined Routines, by Fortran.
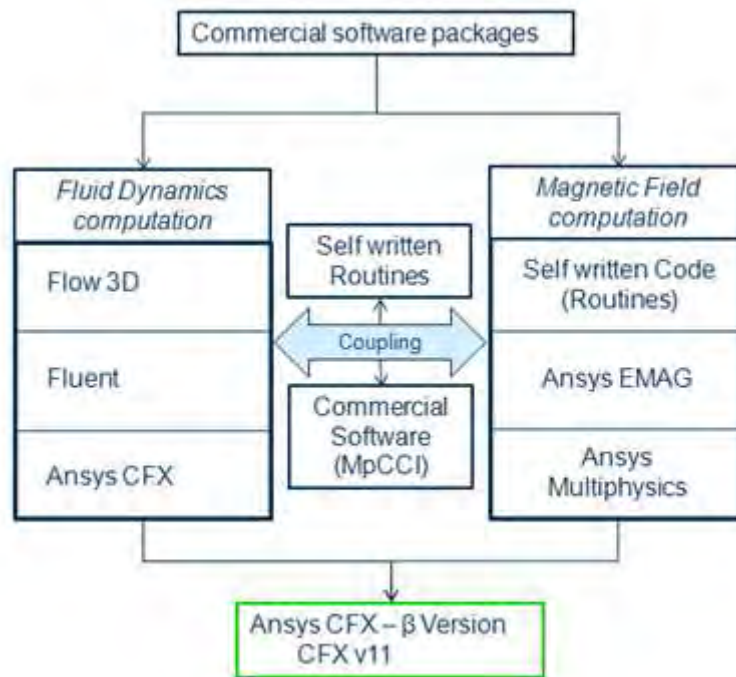
Figure 5-6 Plasma-MHD commercial software

## 5.3    DESCRIPTION OF THE NEW MODEL

In this section, the characteristics of the new proposed model, developed following the steps shown in Figure 5-7, are described. First of all, the problem must be completely defined. After, it can be solved and finally, it must be validated and verified. The aim is to develop a new simulation model of the electric arc for a LVCB with better performance than the existing ones.

The first step in the definition of the model is to define the geometry. At this step a choice between precision and flexibility must be made, due to the increase in the model complexity as more details are included. After that, geometry and meshing have to be created, modeling in CAD or dedicated programs. Design Modeler from Ansys for the geometry and ICEM CFD for the mesh have been used in the present case. Together with the meshing, domains and subdomains on the model have to be defined, specifying the boundary and initial conditions. The material used in each domain has to be selected and their physical parameters must be specified. Special care must be taken in the case of air, because it will have a direct influence on the results. Afterwards, special physical considerations have to be defined, as radiation phenomena and arc roots treatment. Finally, solver parameters have to be adjusted before running the simulation.

If the simulation converges and a solution is obtained, the results have to be post-processed and analyzed. A process of validation and verification will allow determining whethere those results are valid. Validation checks that no significant difference between the model and the real system exists. Verification ensures that the model behaves as intended, without, or with the minimum computational errors. In case of divergences, no results will be obtained. The problem of a divergence in a numerical method can be due to many reasons, sometimes a combination of factors. In those cases, it is advisable to overview the whole definition process again.
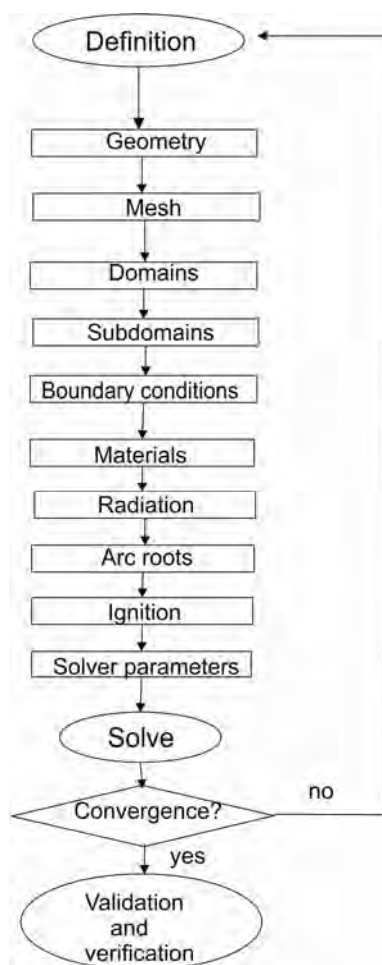
Figure 5-7 Flux diagram for definition and simulation of the electric arc

The new proposed model of the electric arc has been built taking as reference the model presented in [3] and described in chapter 4. Therefore, the results obtained with the new model are first compared to the results presented in [3]. However, several changes and improvements have been made in the new model proposed:

- Geometry:
    – Symmetry effect has not been considered, as it is proved that is not a good assumption.
    – A 3D approach has been applied, instead 2D [3].

- Mesh: the mesh has been improved, developing a structured hexahedral mesh and increasing the number of cells and its accuracy.

- Material: air properties have been updated with [39].

- Radiation: an improved radiation model, P1, has been applied, after analyzing the effect of NEC, NECS and P1 models.

- Magnetic field: magnetic vector potential calculation is adopted for the resolution.

On the other hand, the following assumptions applied to the reference model have been still maintained for the new proposed model:

- No gravity effects have been taken into account, neglecting the last term in equation (4-11), acceleration of gravity. This term is generally neglected in all the references exposed for MHD models in chapter 4 (see Table 4-14).

- Local Thermodynamic Equilibrium (LTE) is considered, introduced in chapter 4 and also presented in every MHD reference model analyzed (see Table 4-14).

- No metal vapours or plastic ablation have been considered.

- No turbulence flow has been considered, as usually neglected in MHD models (see Table 4-14)

### 5.3.1 GEOMETRY

The geometry of the proposed new model is shown in Figure 5-8 [3]. It constitutes a simplification of the LVCB geometry, while being composed of the main elements of these devices: anode, cathode and splitter plate. The dimensions have been maintained as in the reference model described in [3], so that a comparison of results can be made. Dimensions for the model proposed in this thesis are shown in Figure 5-8:

- Height: 40mm
- Width: 11mm
- Depth: 2.5mm
- Dimensions of the anode and the cathode: 40x1.5x2.5 (hxwxd) mm
- Splitter plate dimensions: 20x2x2.5 (hxwxd) mm
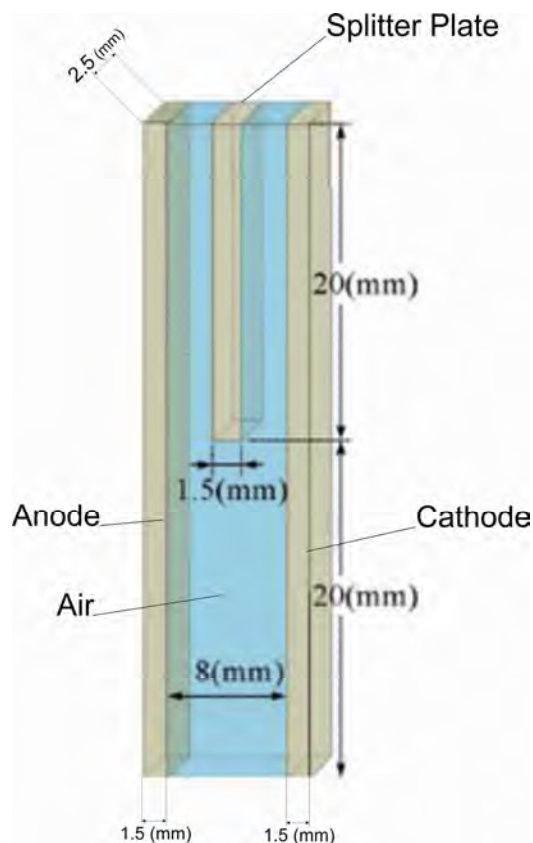


Figure 5-8 Proposed model geometry with dimensions

However, there is a main difference between the model proposed in this thesis (Figure 5-8) and the one presented in [3], related to the symmetry treatment. In [3], a 2D model is adopted by means of considering deepness dimension of 1 mm, with just one cell in the mesh in that direction and a symmetry effect for the middle plane is proposed (Figure 4-82). This is proposed in order to reduce the calculation time and the approach is related to the ¼ symmetry plane that all references from Lindmayer propose [34, 50-58, 60-63].

Nevertheless, it is well known that the electric arc is not an ordered phenomenon, but a chaotic process. Therefore, one dimension cannot be neglected if the aim is to have a realistic approach. That is why a 3D approach has been adopted for the model developed in this thesis, by increasing the depth of the model to 2.5 mm.

Due to the same reason, the half symmetry plane proposed in [3] has not been considered (Figure 5-9). On the one hand, some references remark the benefits of no symmetry application (chapter 4 [16, 70]) and, on the other, references exposed in chapter 4 show images of the arc movement from experimental results clearly show that in no case the arc is a symmetric phenomena (Figure 4-34 from [51], Figure 4-48 from [58, 60], Figure 4-61 from [69] and Figure 4-64 from [71]).

Thus, in order to get a model closer to a real scenario, a new analysis has been made in this thesis, regarding the influence of the symmetry plane with the models already exposed: Figure 5-8 for the whole geometry without any symmetry plane and Figure 5-9 with a half symmetry plane and only 2D as proposed in [3]. All the characteristics of the model, apart from the symmetry restrictions in the geometry, have been kept constant, with the exception of some boundary conditions that were forced to be changed due to the geometry. In that case, the conditions for the reference model from [3] have been taken.
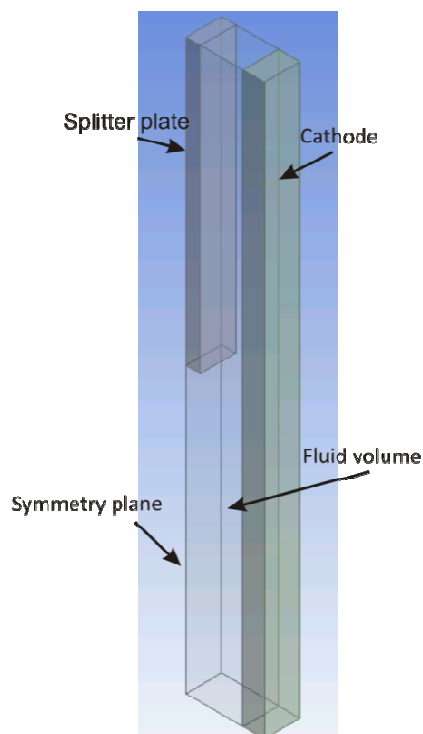


Figure 5-9 Proposed model with the half symmetry plane

Analyzing the results obtained in both cases, represented by temperature and current density vectors, it is observed that they present different results and so, a different behaviour for the arc displacement (Figure 5-10). The results for the symmetry case have been obtained

applying mirror effect. The complete sequence of graphs for the arc behaviour is included in the Annex, Figure A-1. When symmetry is considered the bending process of the arc around the plate is not produced. So, by the timestep 0.3ms, when the arc in the model without symmetry starts to bend, the one with symmetry is already splitted, which does not match real cases. After, by timestep 0.6ms, when the arc without symmetry splits in the plate, the arc has already disappeared in the model with symmetry. Finally, by 0.9ms, when the arc has disappeared in the model without symmetry, in the symmetric model the arc is already reignited.

Therefore, there is clearly a time gap between the two models, where the model with symmetry is faster and the splitting process is missed (it has to be reminded that the settings for that physical phenomenon are the same in both models, and only the symmetry options have been changed). Besides, even if symmetry can be appreciated in both results, due to the symmetrical geometry and arc ignition, the arc does not behave symmetrically in a real test, as it has been previously justify in various references (Figure 4-34 from [51], Figure 4-48 from [58, 60], Figure 4-61 from [69] and Figure 4-64 from [71]). Therefore, the assumption of symmetry leads the model further from real scenarios although the computation time decreases to a half. For that reason, in this thesis a model without symmetry has been chosen.
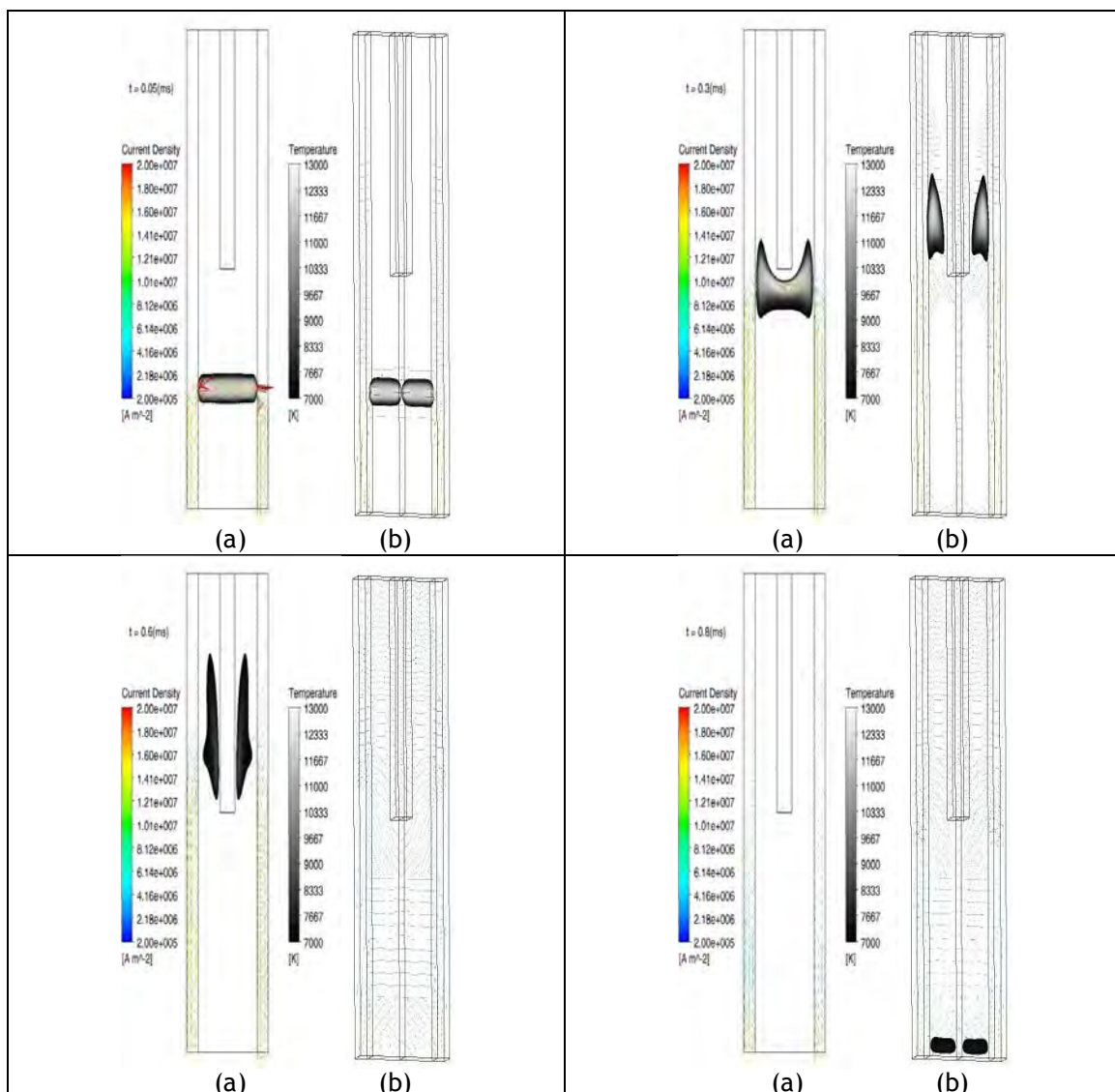


Figure 5-10 Arc movement comparison for (a) model without symmetry and (b) with symmetry

## 5.3.2 MESH

Meshing the geometry consists on dividing the model into a number of small elements where the equations of the model are solved. It is a necessary step in numerical methods that allows its discretization and resolution. The chosen mesh has a great influence on the results. This way, the same model, with same physics and boundary conditions, can produce different results when different meshes are considered or even not converge at all.

Meshing information is not usually provided in literature, not type, parameters or size. In order to evaluate its influence on the electric arc, a detailed analysis with three different meshes applied to the proposed model has been developed as validation process and it is fully explained in chapter 6. As a result of that analysis, the most appropriated mesh for the new proposed model has been adopted.

The software tool chosen for meshing the model is also an important decision; precision, flexibility and user-friendliness are important characteristics in order to choose the most appropriate. The mesh developed for this model has been designed with the ICEM CFD commercial software, belonging to ANSYS. The characteristics defining the hexahedral mesh created are shown in Figure 5-11, Table 5-3 and Table 5-4.
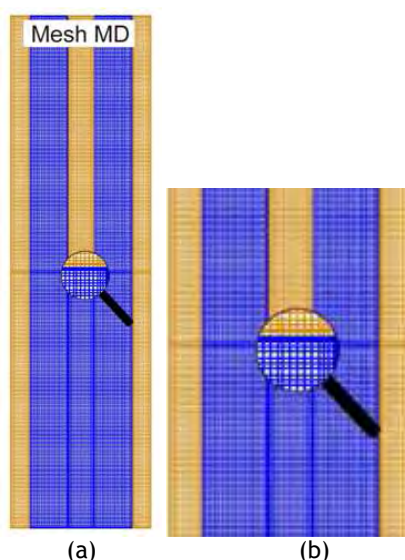


(a)                              (b)
Figure 5-11 Overview of the (a) full mesh and (b) detailed

As shown in Figure 5-11, structural hexahedral mesh has been adopted defining a finer mesh at interfaces and edges, where the change of the parameters value could make the system unstable and divergent. The mesh selected is defined by the following characteristics (Table 5-3):

- Edge length: length of the edge that is divided in nodes.
- Number of nodes per edge: number of nodes by which the edge is divided. In this case, after analysing multiple cases for this geometry, a constant value of 10 times the edge length has been chosen for the number of nodes in each length. Thus, a homogeneous fine mesh has been obtained.
- Spacing: distance for nodes definition at the beginning and end of each edge.
- Ratio: factor by which the spacing is increased in the following nodes. Spacing and Ratio design the finer mesh that is applied at interfaces and complicated edges intersection.
- Total number of elements: total number of elements in the whole mesh.
- Total number of nodes: total number of nodes in the whole mesh.

Table 5-3 Description of the mesh

| Edge length (mm) | Number of nodes | Spacing | Ratio | Total number of elements | Total number of nodes |
|---|---|---|---|---|---|
| 20 | 200 | | | | |
| 3 | 30 | | | | |
| 2.5 | 25 | 0.05 | 1.3 | 1144546 | 1057350 |
| 2 | 20 | | | | |
| 1.5 | 15 | | | | |
| 1 | 10 | | | | |

Once the mesh is defined, its quality parameters have to be checked. For that, the following parameters are used:

- Aspect ratio: the concept of the mesh aspect ratio relates to the degree that mesh elements are stretched, i.e., shows the difference between the length and height of the same element. The most relevant measure of aspect ratio for the CFX-Solver is illustrated in Figure 5-12. It involves the ratio of the maximum to minimum integration point surface areas in every element. As it can be seen in Table 5-4, values can range from 1 to 1000 but the higher the value of the aspect ratio, the more irregular and imprecise is the mesh. Therefore, values close to 1 are desirable and in the model presented in this thesis minimum and maximum values are 1 and 2.98.
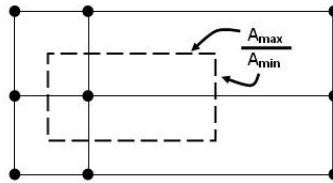


Figure 5-12 Element length and height for aspect ratio calculation [86]

- Volume change: this parameter describes the ratio of a cell volume to the volume of its largest neighbour. A value of 1 indicates that a cell has a volume equal to its neighbours. Large jumps in volume from cell to cell cause instability in the solver. Thus, a value close to 1 is desirable. The values can range between 1 and 20 and for the mesh proposed 1 and 1.69 are obtained as minimum and maximum values, respectively.
- Angle: it shows the angle in the inner part of the elements, between adjacent element faces or adjacent element edges. It gives a measure of the orthogonality of the mesh and for a hexahedral mesh it takes the value of 90°.
- Determinant 2x2x2: it shows the difference between the biggest and the smallest element in the mesh. The determinant is found dividing the smallest determinant of the Jacobian matrix, by the largest determinant of the Jacobian matrix at each corner of the hexahedron. A determinant value of unity indicates a perfectly regular mesh element. Zero would indicate that the element has 1 or more degenerate edges, and a negative determinant indicates an inverted element. As seen in Table 5-4, the determinant for the mesh proposed is equal to 1, so the best approach is obtained.

Table 5-4 Mesh quality

| Parameter | Imposed minimum | Minimum value | Maximum value | Imposed maximum |
|---|---|---|---|---|
| Aspect Ratio | 1 | 1 | 2.98 | 1000 |
| Volume Change | 1 | 1 | 1.69 | 20 |
| Angle | 25˚ | 90° | 90° | - |
| Determinant | 0.2 | 1 | 1 | - |

## 5.3.3 DEFINITION OF DOMAINS AND BOUNDARY CONDITIONS

In the proposed model the following domains have been defined: fluid volume or air, splitter plate, cathode and anode (Figure 5-8). For the domains definition, the values for the material parameters have been adopted taken into account reference [3].

The material used in solid domains (cathode, anode and splitter plates) is copper, with constant physical properties and no dependency with T or P.

The material used in the fluid volume has been specified as a User Defined Material, i.e. a material defined by the user parameterization, including in the program all the data for its definition. The fluid in the case of the electric arc in LVCBs is not just air, as it has been explained in chapter 2. Therefore, the data used in [3] for air properties have been substituted for updated data obtained from reference [39]. The updated values for the air, mass density, specific heat, electrical conductivity, viscosity, and thermal conductivity included in [39], are shown in Figure 5-13 to Figure 5-17.
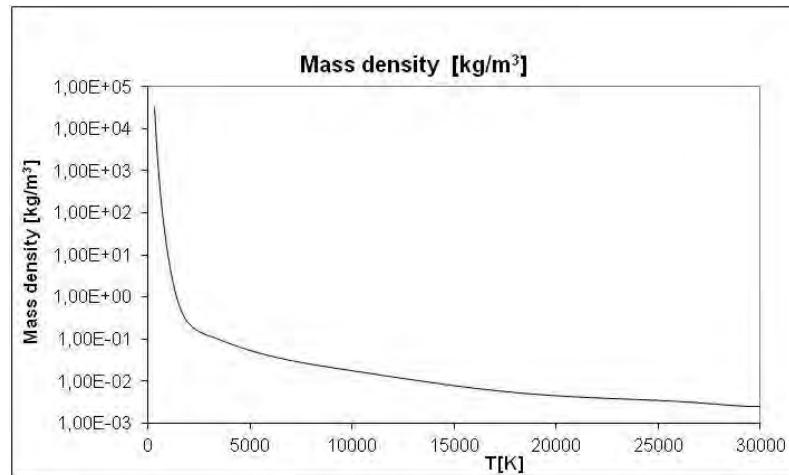


Figure 5-13 Mass density for high temperature air [39]
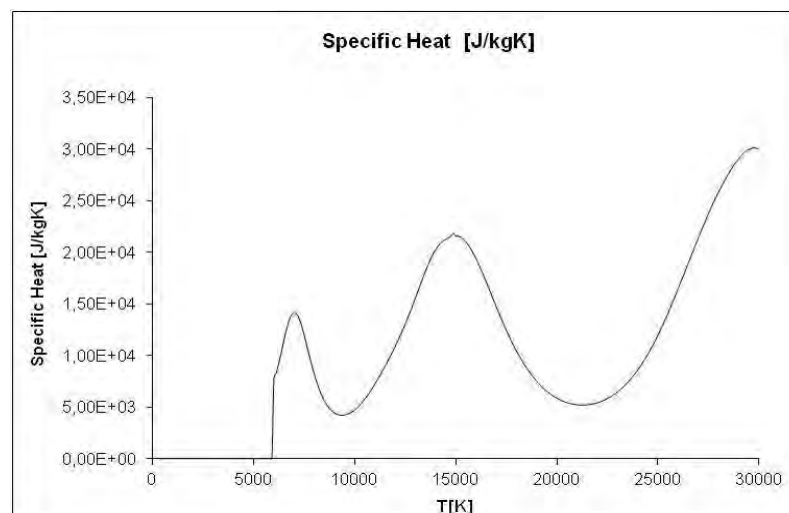


Figure 5-14 Specific heat for high temperature air [39]
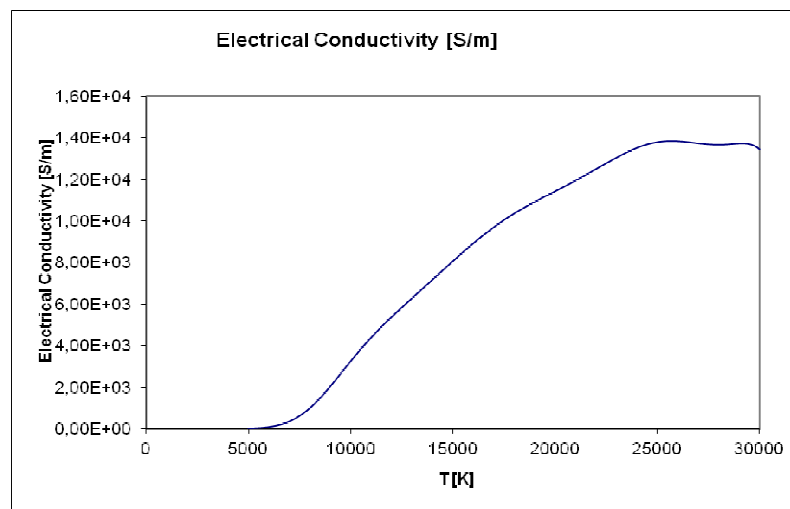
Figure 5-15 Electrical conductivity for high temperature air [39]
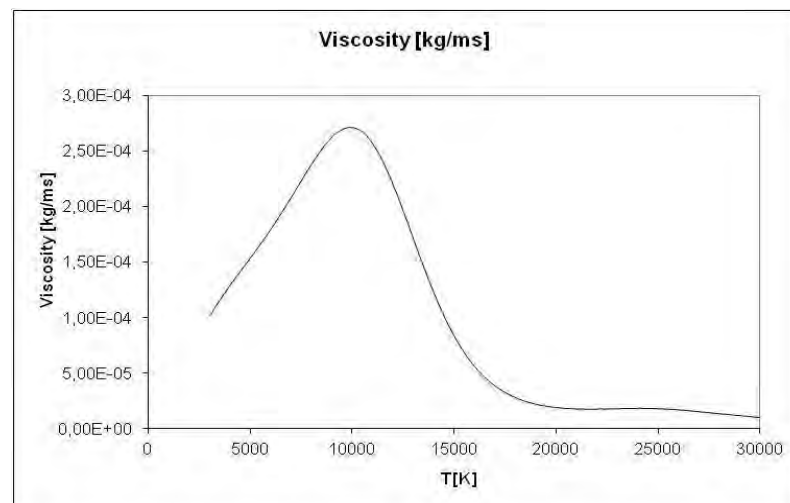


Figure 5-16 Viscosity for high temperature air [39]
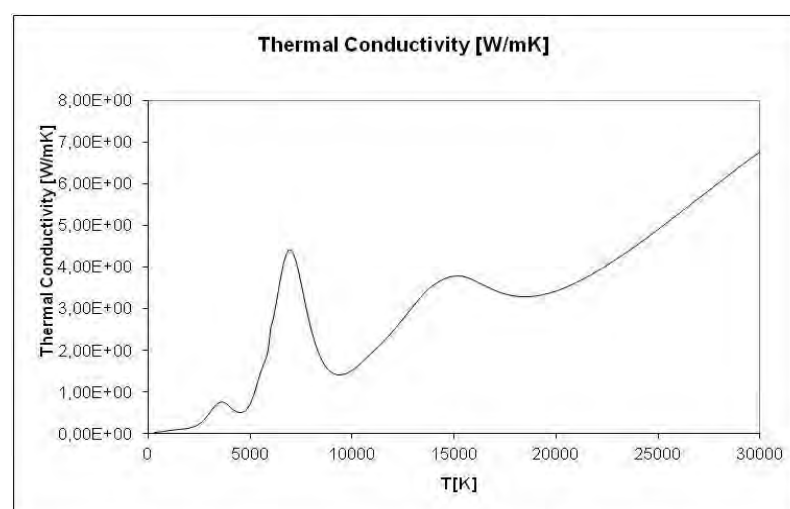


Figure 5-17 Thermal conductivity for high temperature air [39]

As can be seen, physical properties of the air vary in a wide range of temperature. It has to be reminded that inside the chamber the air temperature varies from ambient temperature, around 300K, up to around 25000K when plasma state is achieved. Thus, it is important to take into account the variation of the air properties with temperature, as the accuracy of the model is directly affected by the correct definition of these values.

Once the domains have been defined, the behaviour of interfaces and outside boundaries of the model have to be also defined. The interfaces are the common surfaces between different domains, air and solid parts. The boundary conditions applied in these common surfaces of the model are described in Table 5-5 and Figure 5-18. The values adopted have been chosen taking into account those applied in the reference model [3].

Table 5-5 Boundary conditions applied in the model

| Boundary | T [K] | P[Pa] | Electric field | Magnetic field | Type of boundary |
|---|---|---|---|---|---|
| Front and back walls of air, splitter plate and electrodes. Air_Wall_Down | Adiabatic | - | Zero flux | Zero flux | No slip wall |
| Interfaces | Adiabatic | - | CIF | CIF | No slip wall |
| Openings | 300 | 0[Pa] | Zero Flux | $A_i$=0[Tm] | Opening |
| Anode_Down | 500 | - | Flux In I=50[A] | Zero Flux | Wall |
| Cathode_Down | 500 | - | 0[V] | Zero Flux | Wall |
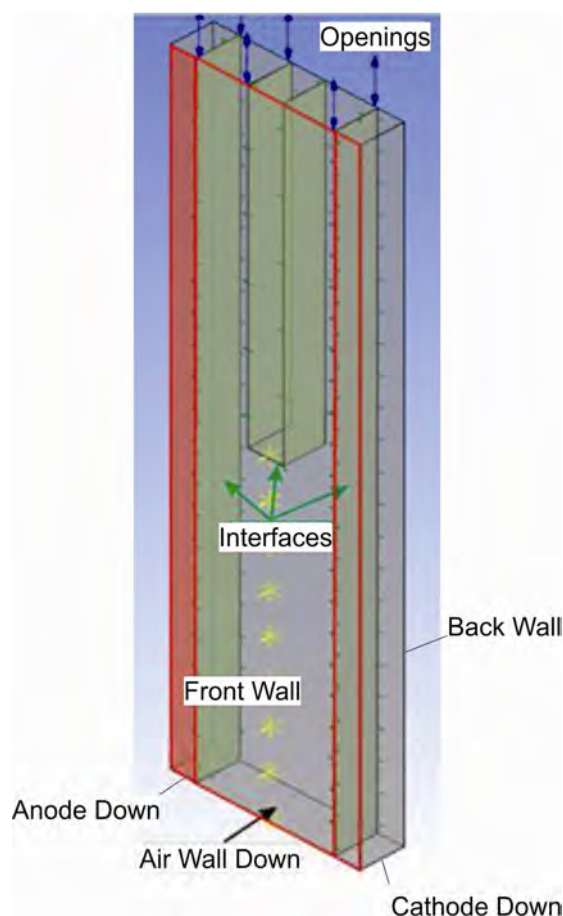


Figure 5-18 Boundary conditions on the model

At the boundaries between the model and the outside, i.e. at the front and back walls of the air, splitter plate and electrodes, plus the down part of the air (named as Air_Wall_Down in Figure 5-18), no external interaction has been defined, considering the temperature exchange as adiabatic. Neither exists an interaction of the electric and magnetic field with the outside. The solid walls have been defined with non slippery condition, which means that the fluid velocity is zero at the walls in contact with the fluid.

At the interfaces air-electrodes and air-splitter plate, the temperature exchange has also been defined as adiabatic. Although this is not a real condition, it is necessary for the software selected in this thesis. Considering all the references exposed in chapter 4, none of them clarify this detail, but this option is used to obtain the arc running. Otherwise, the electrical conductivity of the copper is much higher than the corresponding to the air, so the electric current introduced from the anode would never be transferred to the air if adiabatic condition is not imposed.

Regarding electric and magnetic field Conservative Interface Flux (CIF) is applied at the interfaces. It implies that the variables will flow between both sides of the interface. Once again, the wall is defined non slippery.

At the top face, the opening of the air volume (see Figure 5-18) is at atmospheric conditions, thus the temperature is set to be 300K and the pressure is equal to 0Pa. No interaction is defined for the electric field. For the magnetic field, this is the point where the magnetic vector potential is set to 0. This boundary condition is necessary to be as far as possible from the electric current of the arc, to impose the decrease of the magnetic field along distance.

Finally, some small changes have been made regarding the reference model [3]. Temperature of the lower face of anode and cathode has been changed from 300K to 500K, in order to improve the stability and avoid divergence errors due to the high difference of temperatures imposed in the initialization stage on the solid part and air volume. In the down face of the anode, an incoming current of 50A has been imposed, and in the down face of the cathode 0V or grounding has been considered, in order to define the direction of the arc between electrodes. Besides, no interaction for the magnetic field has been defined in those boundaries as they have been defined as wall.

## 5.3.4 PARAMETERIZATION

After geometry, mesh, domains and boundary conditions have been defined, parameterization of the rest physical conditions is necessary:

- ELECTRIC AND MAGNETIC FIELDS: regarding the electric field, Maxwell equations, as exposed in chapter 4, are solved by the software. With the idea of improving the model presented in [3] (where an external magnetic field with a constant value of 0,1T is considered) the magnetic field is calculated in the new model proposed with the vector potential formulation, taking into account the induced magnetic field due to the electric arc current at every simulation timestep of the simulation. As explained in the boundary conditions, to apply this method, it is necessary to specify a boundary where $\vec{A} = 0$, to impose the field decrease with the distance, at the furthest point from the current injection.

- RADIATION: as it has been exposed in chapter 4, radiation takes into account the thermal exchange due to the elevated temperatures appearing in the electric arc. Thus, it is an important term in the energy conservation equation.

Among the radiation models described in section 4.2, NECS, NEC and P1 have been tested in the new model. Each model has been built in this thesis with the formulation exposed in chapter 4 and different references as base data: [3] for NECS, [38, 40] for NEC and [41, 87] for P1. As it is explained in the verification process, chapter 6, the most realistic and best option is P1 radiation model. In this case, radiation spectrum, to emit and absorb the energy, is divided into six spectral bands, for different frecuencies. Within these frequency bands, the spectral absorption coefficients of the plasma are set as a function of temperature and pressure. Therefore, for the model developed in this thesis, the solver solves six extra differential equations in order to describe the energy transport in each band. This fact leads undoubtedly to an increased computational time, but the precision of the results is higher.

- ARC ROOTS: the voltage-current density curve characteristics for modelling arc roots presented in [3, 58, 61] and described in chapter 4 have been adopted. It is known that the voltage drop at the arc roots is around 5-10V each, depending on the electrode material, the arc current and its polarity. During the division of the arc in a splitter plate, an additional cathode and anode fall is created on each side of the plate and, modelling this process, the additional voltage drop of the arc roots is taken into account in the total arc voltage.

In the new model developed, the local nonlinear resistance is implemented by the nonlinear resistance option available in CFX v13 for interfaces. The value for this nonlinear resistance is chosen according to a specific voltage-current density characteristic shown in Figure 5-19 and Figure 5-20, being the scale for current density extended in Figure 5-20, to $1 \times 10^7 A/m^2$. So, before a new arc root is formed, an ignition voltage has to be exceeded. Different values of ignition voltage are compared: 22.3V, 19.7V, 17.1V and 10V peaks. Those values have been obtained from experimental results. Dividing the values from Figure 5-19, the resultant ohmic resistance shown in Figure 5-21 is obtained ($R[Omh.m^{-2}] = V[V]/J[A.m^{-2}]$).
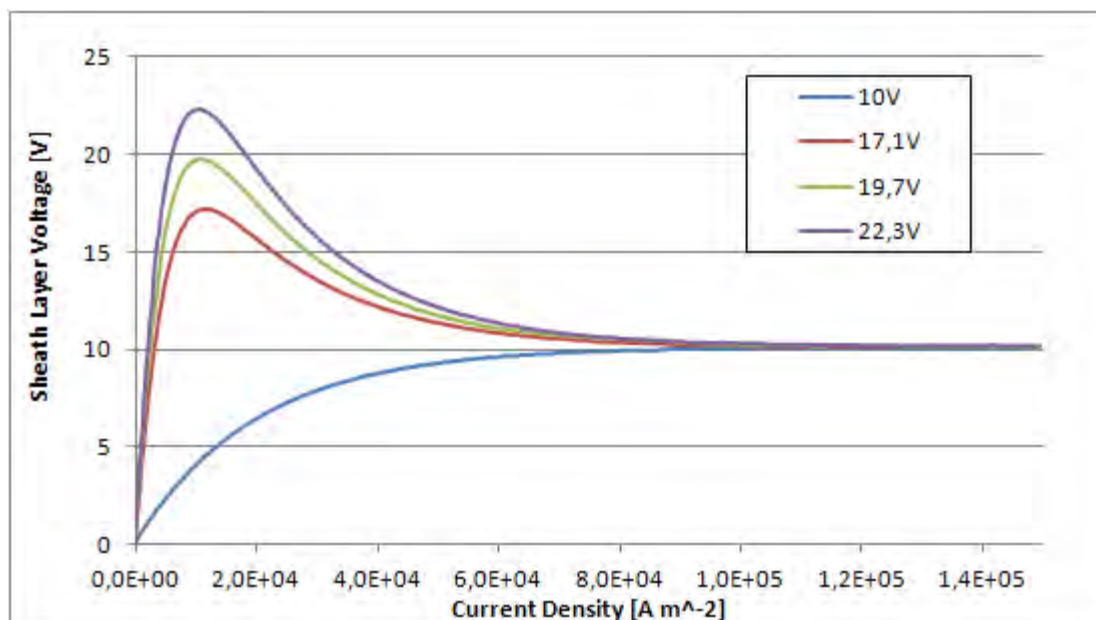


Figure 5-19 Voltage drop-current density curve for new arc roots, up to $1 \times 10^5 A/m^2$
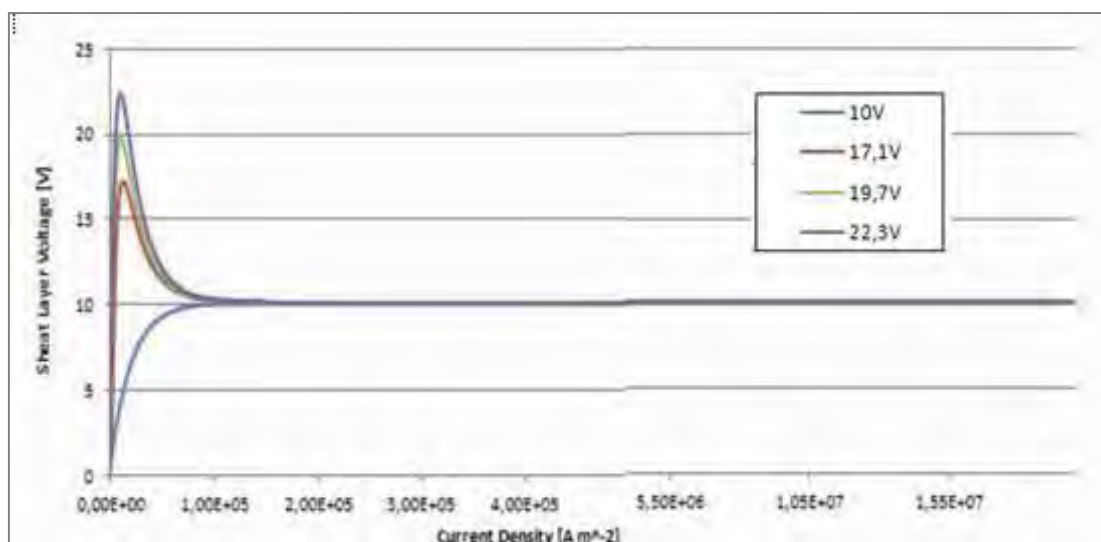
Figure 5-20 Voltage drop-current density curve for new arc roots, up to $1 \times 10^7$ A/m$^2$
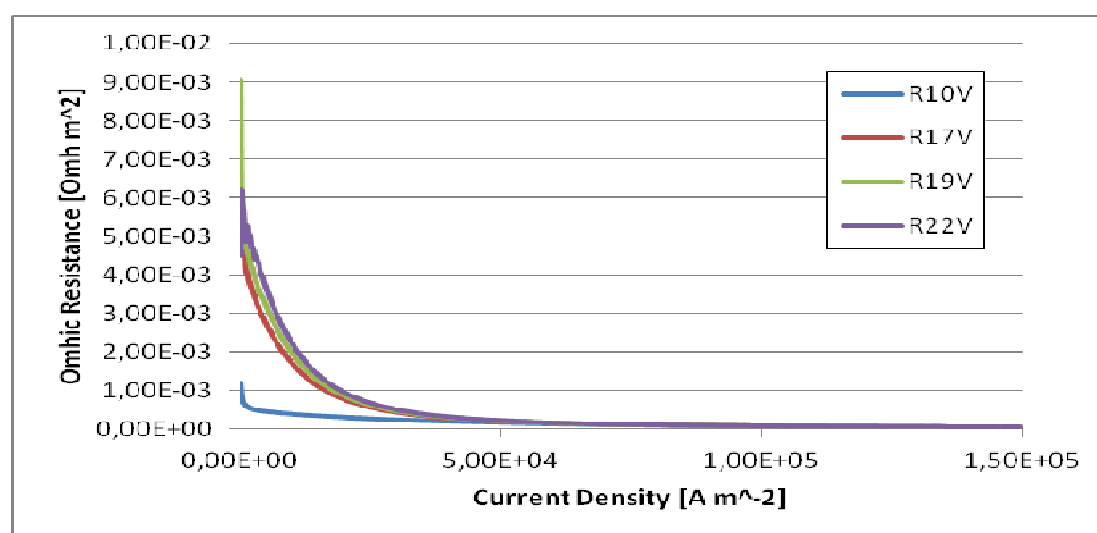


Figure 5-21 Ohmic resistance

- ARC INITIALIZATION: the ignition of the arc has been modelled initializing a hot cylindrical channel of 10000K between the rails. With the purpose of evaluating the effect of the initial position of the arc, two cases have been considered:

  - Position 1 (Upper Ignition): The arc has been initiated at 10 mm high from the lower face (Air_wall_down), as in [3] for comparison of results.
  - Position 2 (Lower Ignition): The arc has been initiated at 1mm high from the lower face (Air_wall_down), as in the real experiments presented in chapter 6 for validation of the model.

- SOLVER DATA: finally, the simulation time has been set-up to 1ms as in [3], with a timestep of $2,5 \times 10^{-6}$s, whose selection is justified in chapter 6, after having developed an analysis of the influence of different timestep values.

## 5.4  SIMULATION RESULTS

Once the settings of the new proposed model have been described in the previous sections, the different tests and results obtained with the new proposed model are presented along this section.

All the cases analyzed and tested are summarized in Table 5-6. Those cases have been classified in 5 groups: A, B, C, D and E. At the same time, each group has been subdivided for different tests.

Table 5-6 Cases analyzed with the new proposed model

| Case | Effects | Tests analyzed | | Purpose |
|---|---|---|---|---|
| A | Base model | A.1 | 10V peak V-J arc root | Compare the new proposed model with the reference model [3], simulating the four V-J for arc roots |
| | | A.2 | 17,1V peak V-J arc root | |
| | | A.3 | 19,7V peak V-J arc root | |
| | | A.4 | 22,3V peak V-J arc root | |
| | | | Comparative | |
| B | Splitter Plates | B.1 | 0SP | Analysis of the effect of the splitter plates |
| | | B.2 | 2SP | |
| | | | Comparative | |
| C | Arc Ignition location and input currents | C.1 | 50A, 0SP | Analysis of location of the arc ignition and different input currents, for comparison with the real experimental results of chapter 6 and verification of the proposed model |
| | | C.2 | 50A, 1SP | |
| | | C.3 | 100A, 0SP | |
| | | C.4 | 100A, 1SP | |
| | | C.5 | 200A, 0SP | |
| | | C.6 | 200A, 1SP | |
| | | | Comparative | |
| D | Expansion volume | D.1 | Expansion volume (EV) | Analysis of geometry changes and its effects on the arc movement |
| | | D.2 | EV and down wall up | |
| | | D.3 | EV and longer electrodes | |
| | | | Comparative | |
| E | Arc Roots | E.1 | Constant R | Analysis of the effect of the arc root models. |
| | | | Comparative | |

First of all, in group A, the model has been defined as explained in the previous section. This model has been implemented taking into account the model presented in [3] and the modifications commented to improve it: radiation model changed to P1, full 3D geometry without symmetry simplification, fine mesh, vector magnetic potential calculation and updated data for air. Regarding the arc roots model, as explained in section 5.3.4, the four curves for voltage-current density characteristics have been applied to implement the Ohmic non linear-resistance between the splitter plate and the fluid volume. The fourth curves have been modelled and compared.

This case A constitutes the base model that is compared to the reference [3]. The results confirm the validity and improvement of the proposed model compared to that reference [3]. This A model, named from now as the base model, will be the starting point for subsequent changes and analysis (cases B, C, D and E).

Secondly, in case B, the effect of different number of splitter plates has been analyzed. As a starting point to obtain new B models, the A.3 model with one splitter plate (1SP) and 19,7V peak for the V-J curve of arc root definition has been chosen. That model, A.3, has been modified changing the number of splitter plates that are included in the chamber, from one (1SP) to zero (0SP) in case B.1 and two in case B.2 (2SP).

Thirdly, the position of the arc ignition has been analyzed in case C. The ignition used in models A and B, as explained in the section before, is located 10mm high from the down face of the air. In case C it is ignited at 1mm high, considering zero and one splitter plates, as well as different current values equal to 50A, 100A and 200A. So, a total of six subcases have been simulated: C.1 for 50A input current with zero splitter plates and C.2 for 50A input current but with one splitter plate; C.3 for 100A input current with zero splitter plates and C.4 for 100A input current but with one splitter plate; C.5 for 200A input current with zero splitter plates and C.6 also for 200A input current but with one splitter plate. These simulations will be used for the verification process of chapter 6.

In the fourth case, D, geometry analysis has been developed, changing the shape of the chamber. Three options have been tested. First of all, case D.1, applying an expansion volume in the upper part of the chamber for comparison with literature [55, 57, 58, 60, 61, 65] already presented in chapter 4 (Table 4-14). Secondly, case D.2, lengthening the electrodes, and finally, case D.3, defining the air wall down higher, shortening the distance between the splitter plate and the bottom of the chamber.

Finally, as the results for the ohmic resistance obtained for the voltage-current density for new arc roots are not satisfactory enough (Figure 5-31 to Figure 5-35), another comparison with constant ohmic resistance has been carried out in case E.1.

For each simulation case the images of the fluid flow movement are presented, as a temperature distribution in black and white, and current density in colour vectors. The images have been extracted for the middle plane of z axis (depth) at different timesteps. Besides, graphics for the evolution of maximum voltage drop, current density in the air and in the splitter plate, temperature and pressure of the fluid flow are shown.

All the simulation models have been run on a queuing system of four clusters, of approximately 2,3GHz each, and the simulation model of 1ms proposed in this thesis took around four days to be solved (Table 6-5).

### 5.4.1   CASE A: BASE MODEL

In base case A, a replica of the reference model [3] with the proposed improvements has been built. This way, a 40x11x2.5mm chamber, with anode, cathode, splitter plate and air, has been designed, where MHD formulation has been solved, including a full geometry without symmetry and with 3D. The arc ignition has been defined by a hot channel of 10000[K] at 10mm from the lower face of the air and 50A are injected from anode to cathode. Radiation model has been updated to P1, magnetic vector potential formulation has been adopted and hot air characteristics published in [39] have been applied.

This base model A is tested for four different V-J curves, as shown in Figure 5-19, to model the arc roots effect on the splitter plate. These V-J curves have been presented by Lindmayer in [58] and followed up to now for arc root implementation. The curves differ in the peak values. The lowest one has a peak value of 10V, the second one of 17.1V the third one of 19.7V and the last one of 22.3V. Those four cases are presented in tests A.1, A.2, A.3 and A.4.

### 5.4.1.1  Case A.1: V-J arc root curve for 10V Peak

In this first case, A.1, the reference model [3] is tested with the changes explained above plus the V-J arc root curve with 10V peak. Figure 5-22 shows the arc movement expressed by temperature and current density evolution for some timesteps. The timesteps chosen for this representation have been 0, 0.3, 0.5, 0.6, 0.7 and 0.8. These timesteps have been chosen to compare the results with the arc movement obtained in the reference model [3] (Figure 4-84). In this case, two more timesteps have been presented (0.3 and 0.8ms), which have been considered interesting. The whole evolution can be seen in Figure A-2 (Annex), from 0 to 1ms, every 0.05ms.

Therefore, looking at Figure 5-22, it can be seen that the arc is ignited at 0ms, at 10mm from the lower part of the chamber. After, the bending around the splitter plate starts at 0.3ms, continues at 0.5ms and is completely splitted in two arcs, at both sides of the plate, at 0.6ms. It continues its way up through the opening and disappears at 0.8ms. If these results are compared to the reference model presented in Figure 4-84, it can be said that a better approach has been achieved for the arc evolution with the new model, as the arc is less diffuse.

Between the similarities of both models, the rise of the arc upwards the top of the chamber can be highlighted. Starting, bending around the splitter plate and finally splitting at similar timesteps. It is hard to make a further analysis because no more data are provided in the reference model [3], but as said, the general upwards movement is fulfilled and also the magnitudes of the current density obtained are of the same order ($10^5$ to $10^7$ A/m$^{-2}$). Temperature results are not shown in the reference model, but it has been extracted for the proposed model, because temperatures above 10000K are obtained in the current carrying plasma. That is another characteristic that can be seen in Figure 5-22 and Figure A-2 with temperature and current density vectors correlation.

Among the differences, the diffusion of the arc can be highlighted. In the new model developed, the arc is more concentrated than in reference model [3] (Figure 4-84). This can be attributed to the mesh refinement carried out in the new model, as well as to the more precise radiation or/and magnetic field modelling.

In addition to the arc movement behaviour of Figure 5-22, arc voltage drop, temperature, pressure and current density results are included in Figure 5-23 to Figure 5-27.

The voltage drop obtained between electrodes, represents the total arc voltage, which has to rise in order to achieve a satisfactory current interruption in a circuit breaker. Figure 5-23 shows the voltage drop obtained for this test A.1, where significant characteristics reflected in Figure 5-22 can be emphasized: the voltage drop starts to increase at timestep 0.3ms that is when the arc starts to bend around the splitter plate. It continues increasing up to 0.6ms, where the arc is divided into paths and starts to decrease. At 0.8ms the arc in the chamber is just residual in the simulation.

Figure 5-22 Arc movement behaviour, expressed by temperature and current density for case A.1, 50A, 1SP and V-J arc root curve for 10V peak, at 0, 0.3, 0.55, 0.6, 0.7 and 0.8 ms
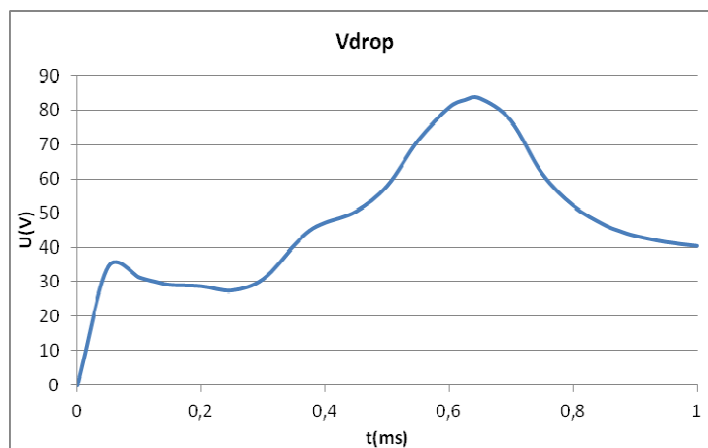


Figure 5-23 Arc voltage for 50A 1SP model, V-J 10V Peak for case A.1

Other characteristics that have been analyzed and represented, directly related with the results of Figure 5-22, are the temperature and current density in the air. As they vary in a very wide range the maximum values of both parameters have been chosen.

This way, the correspondence with the values from Figure 5-22 is not quantitatively, but a qualitative idea can be extracted. In the first place, it has to be cleared that the maximum

expressions of those variables are taken from the cell in the domain that presents the maximum value for these parameters. In Figure 5-24 and Figure 5-25 maximum values of air temperature and current density in air are represented, respectively. A general correspondence between them and with Figure 5-22 is observed. The temperature increases from 0 to around 0.6ms and then starts decreasing, where it can be seen that the temperature drops from 10000K. For the current density, even if Figure 5-25 looks very bouncing, it has to be taken into account that the scale from "y" axis (vertical) ranges from 0 to $7 \times 10^7$ in the highest point, which is a big step. So it is better to focus on the big scale changes that are determined at the beginning, from 0.3ms to 0.6ms, in coincidence with the bending of the arc and the disappearance at 0.7ms.
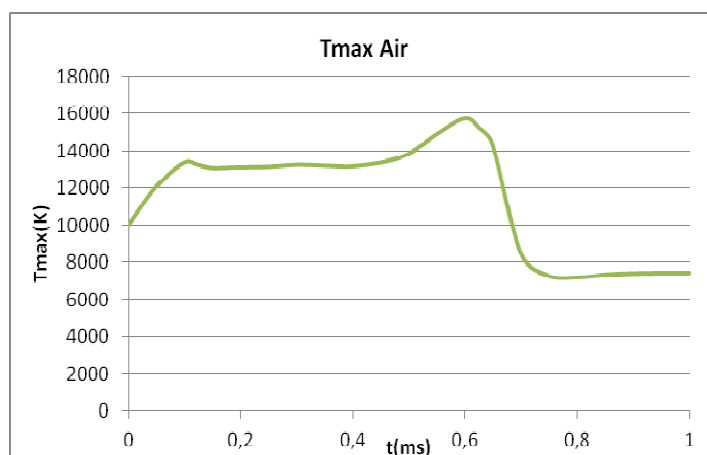


Figure 5-24 Maximum temperature in air, for 50A 1SP model, V-J 10V Peak, for case A.1
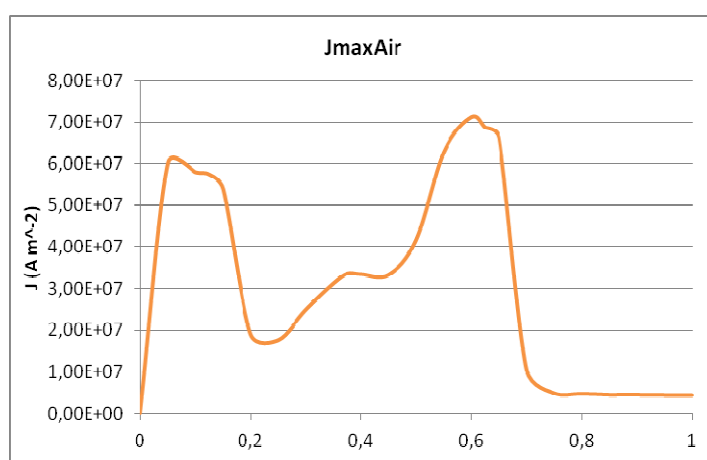


Figure 5-25 Maximum current density in air, for 50A 1SP model, V-J 10V Peak, for case A.1

The maximum current density through the splitter plate is shown in Figure 5-26. It can be seen that the current starts travelling through the plate at 0.3ms, when the arc reaches that area of the splitter plate, and increases up to 0.6-0.7ms. The small value reached by this magnitude, compared to the electric current in air, is in correspondence with Figure 5-23 where current ranges from $2 \times 10^5$ to $2 \times 10^7$ A/m². Figure 5-26 shows that maximum current density value through plate barely reaches $5.0 \times 10^5$ A/m², being 2 orders smaller comparing to the current in the air. In the reference model [3], it is also shown that the current density through the plate is around $5.0 \times 10^5$ A/m² (Figure 4-84).
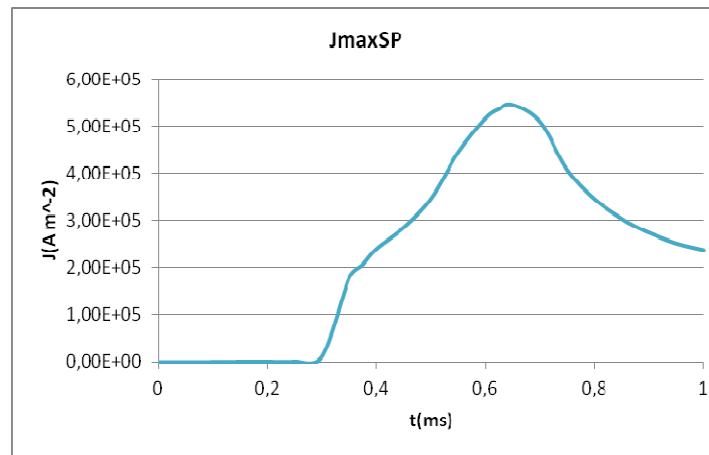
Figure 5-26 Maximum current density in splitter plate for 50A 1SP model, V-J 10V Peak, for case A.1

Regarding the results for pressure (Figure 5-27), an interesting phenomenon is also observed that allows a better understanding of the electric arc behaviour. The maximum pressure peak obtained in the arc chamber is achieved by 0.1ms which, looking at Figure A-2, is the instant when the arc starts its way up along the rails. That performance is due to the heating up of the air between the arc and the lower face of the chamber, as a result of the ignition channel. As soon as the air is heated, it tries to expand, creating the gradient pressure expressed in MHD formulation.
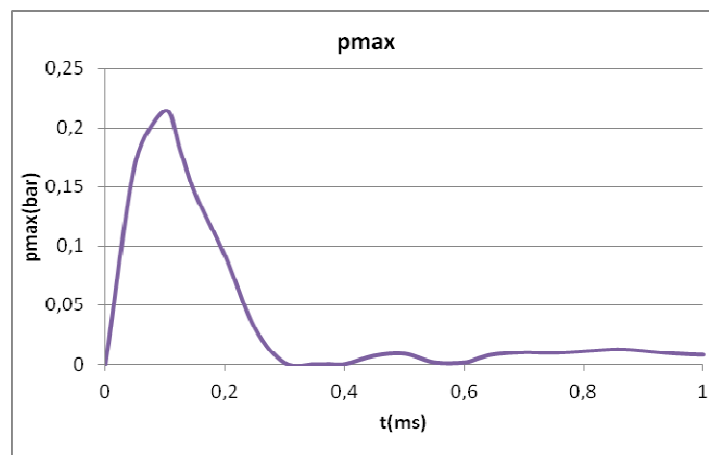


Figure 5-27 Maximum pressure for 50A 1SP model, V-J 10V Peak, for case A.1

## 5.4.1.2  Case A.2: V-J arc root curve for 17.1V peak

Following the tests at [3] the next curve of V-J for arc roots with 17.1V peak (Figure 5-19) is tested in the new model, A.2, for a comparison with the reference model. Results for temperature and current density are shown in Figure 5-28, being very similar to previously analyzed case A.1.

The whole arc movement images are shown in Figure A-3 and the characteristics of arc voltage drop, temperature, pressure, current density in the air and maximum current density in the splitter plate are shown in Annex from Figure A-4 to Figure A-8, respectively. None of them represents a great difference regarding case A.1, as it will be explain in the comparative analysis, so explanations from case A.1 are still valid for the analysis of the results of case A.2.
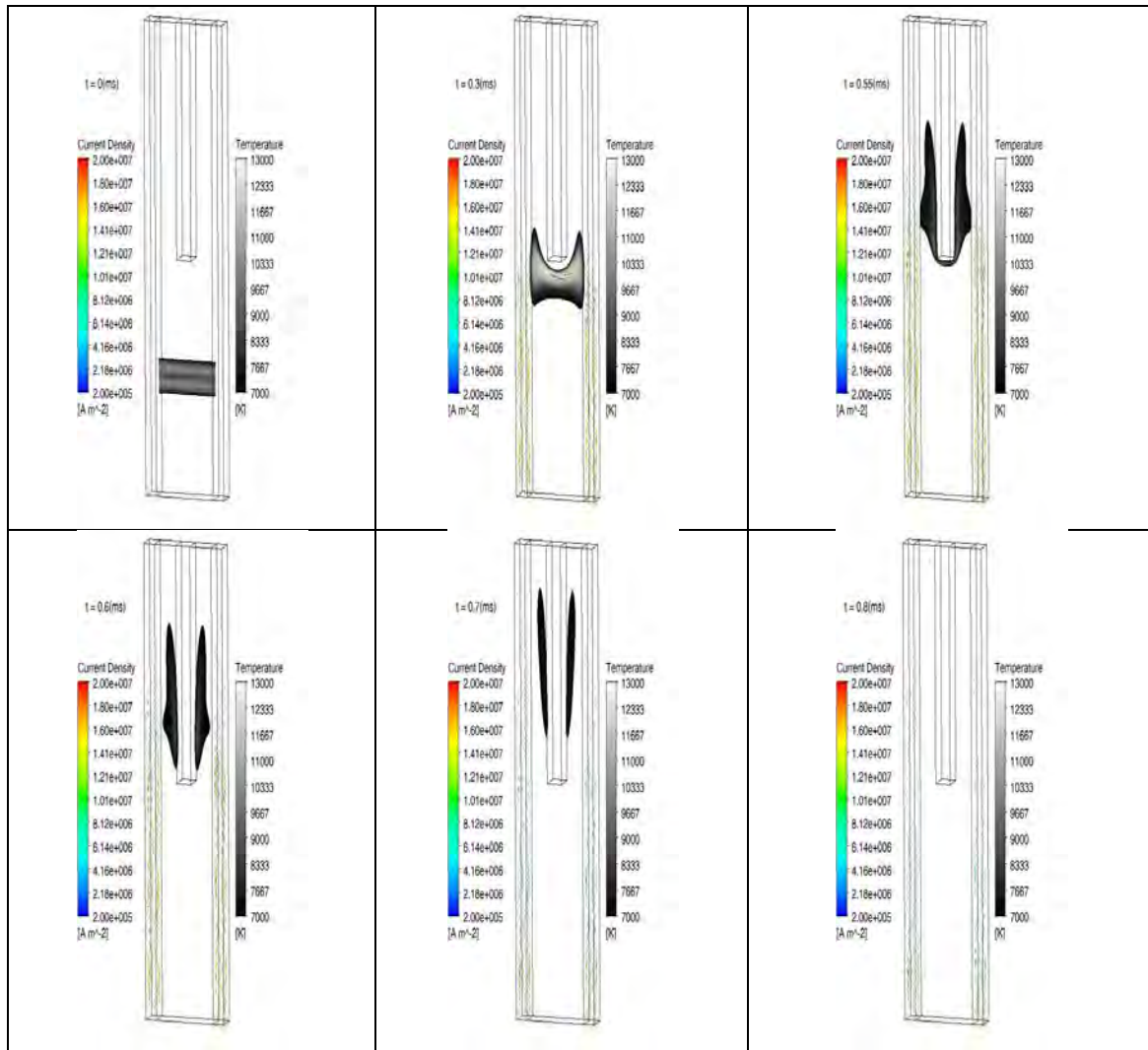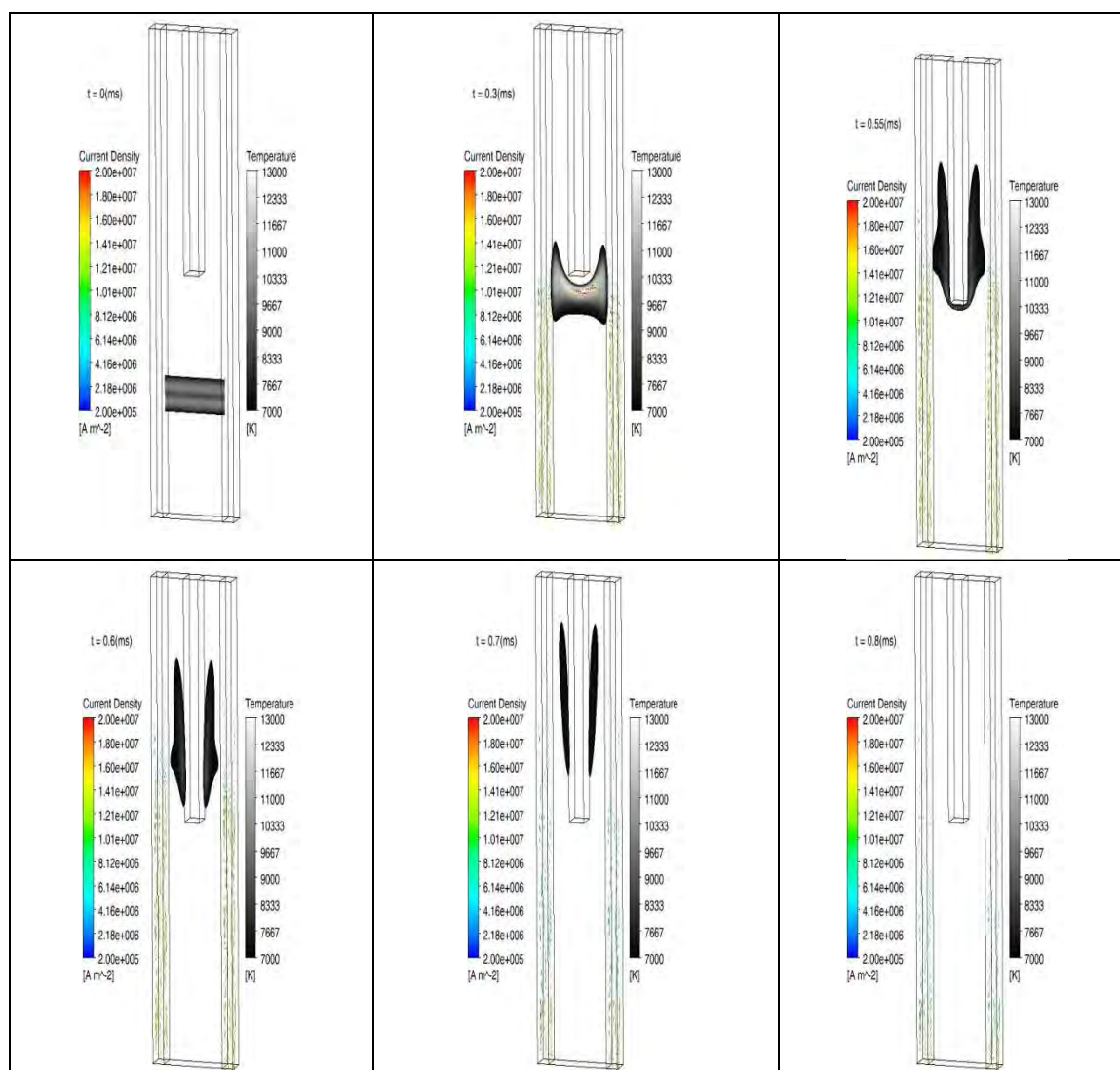
Figure 5-28 Arc movement behaviour, expressed by temperature and current density, for case A.2, 50A, 1SP and V-J arc root curve for 17,1V peak at 0, 0.3, 0.55, 0.6, 0.7 and 0.8 ms

### 5.4.1.3  Case A.3: V-J arc root curve for 19.7V peak

Testing the next V-J curve, from Figure 5-19, of 19.7V peak for the ohmic resistance calculation, the results for temperature and current density are shown in Figure 5-29, which are apparently the same as in cases A.1 and A.2, previously analyzed.

The whole arc movement images are shown in Figure A-9 and the characteristics of arc voltage drop, temperature, pressure, current density in the air and maximum current density in the splitter plate are shown in Annex from Figure A-10 to Figure A-14, respectively. Again, no great differences regarding case A.1 or case A.2 appear.
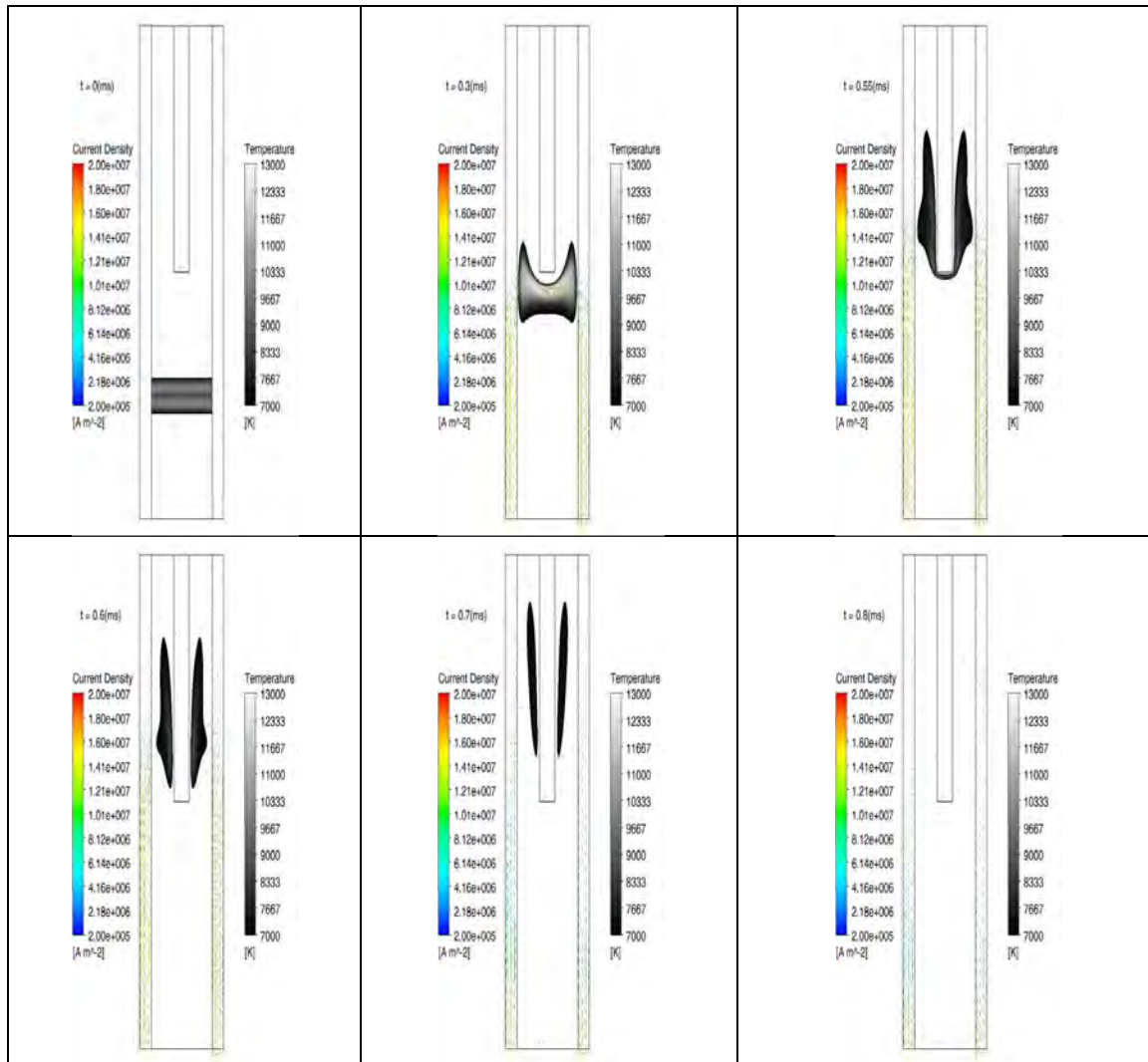
Figure 5-29 Arc movement behaviour, expressed by temperature and current density for case A.3, 50A, 1SP and V-J arc root curve for 19.7V peak at 0, 0.3, 0.55, 0.6, 0.7 and 0.8 ms

### 5.4.1.4  Case A.4: V-J arc root curve for 22.3V peak

Finally, the last V-J curve, from Figure 5-19, with 22.3V peak is tested for the ohmic resistance calculation. Results for temperature and current density defining the movement of the arc are shown in Figure 5-30, being again very similar to cases A.1, A.2 and A.3.

The whole arc movement image is shown in Figure A-15 and the characteristics of arc voltage drop, temperature, pressure, current density in the air and maximum current density in the splitter plate are shown in Annex, from Figure A-16 to Figure A-20, respectively. None of them differs again greatly from case A.1, A.2 or A.3 as it will be analyzed in the comparative analysis.
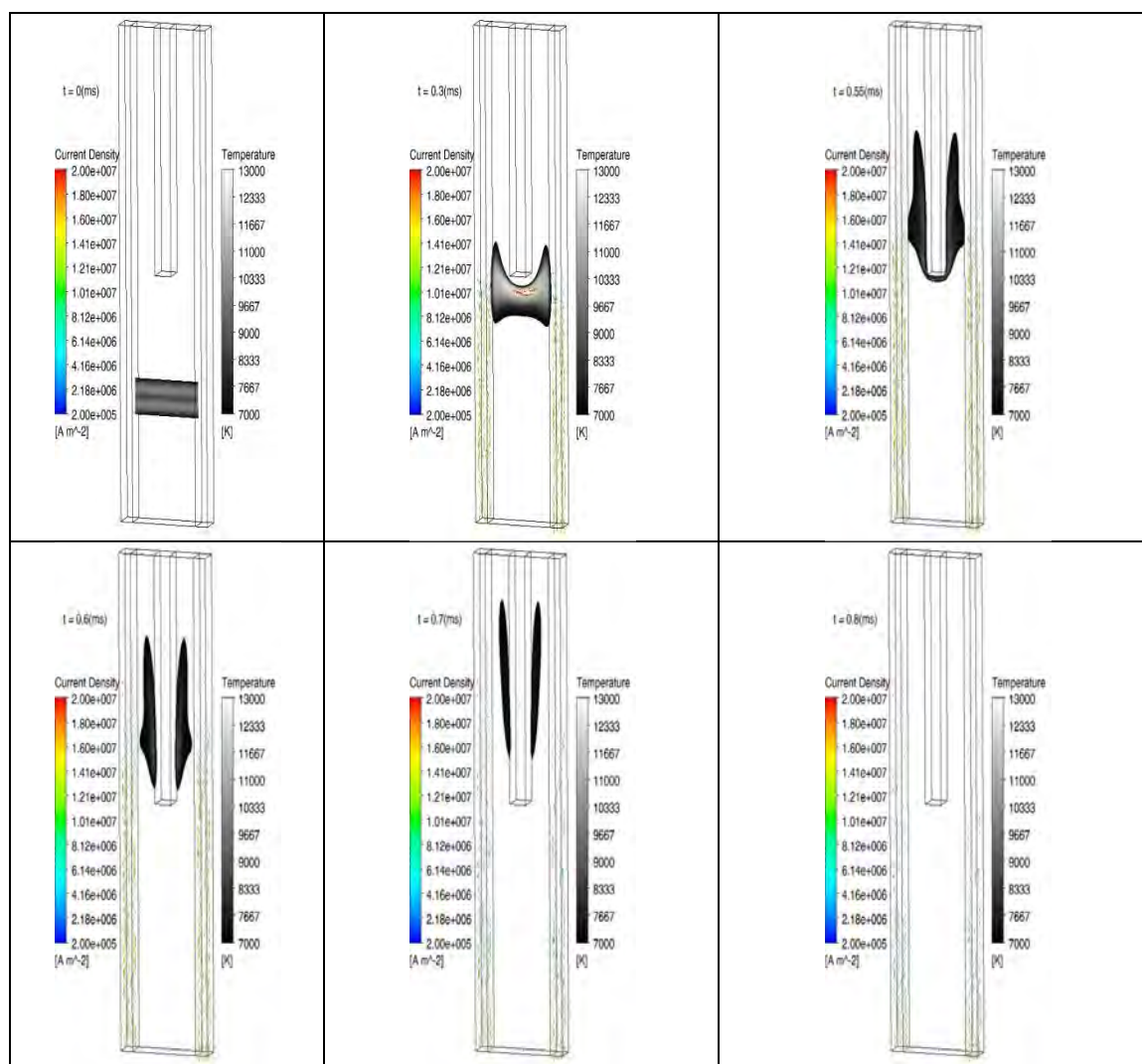
Figure 5-30 Arc movement behaviour, expressed by temperature and current density for case A.4, 50A, 1SP and V-J arc root curve for 22.3V peak at 0, 0.3, 0.55, 0.6, 0.7 and 0.8 ms

### 5.4.1.5 Comparative analysis

Comparing cases A.1 to A.4 with the reference model [3], (Figure 4-84 to Figure 4-87 and Figure 5-22, Figure 5-28, Figure 5-29 and Figure 5-30, respectively), it can be said that the new model ensures the arc movement upward along the chamber, as in the reference model, and that this process is achieved in the correct timesteps, reaching the splitter plate at 0.3ms, bending at 0.5ms and splitting at 0.7ms. Also, correct orders of magnitude for the analyzed parameters are achieved. Besides, as an advantage of the new model, the arc is more constricted compared [3], which was a problem for Lindmayer [58, 60, 61]. This aspect is achieved in the new model due to the effect of the improvements in the geometry, meshing and radiation effects.

The duration of the bending and the arc voltage increase is an interesting factor to analyze, as a satisfactory arc interruption directly depends on it. However, the duration of the bending cannot be compared to [3], as in the reference model the data published are limited (the total duration of the arc and its extinction time is missing). That is why data obtained with the new model will have to be compared to real experimental results developed for this thesis and presented in chapter 6. As it will be explained in that chapter, a good agreement is shown, which reinforces the validity of the new model proposed.

Additionally, the duration of the arc movement and the magnitudes of the evaluated parameters, T, p, V and J from the results of the new model cannot be compared to the rest of references analyzed in chapter 4 (Table 4-14), due to differences in geometrical dimensions of the chamber and differences in the input currents for the arc. However, the overall qualitative movement is supported by all those references, where the arc moves towards the opening of the chamber.

Regarding the arc roots modelling [3], the same tests have been carried out with the new model in cases A.1, A.2, A.3 and A.4. The results obtained for the four different cases analyzed for arc voltage drop, maximum temperature in air, maximum pressure, maximum current density in the air and splitter plate are shown from Figure 5-31 to Figure 5-35.
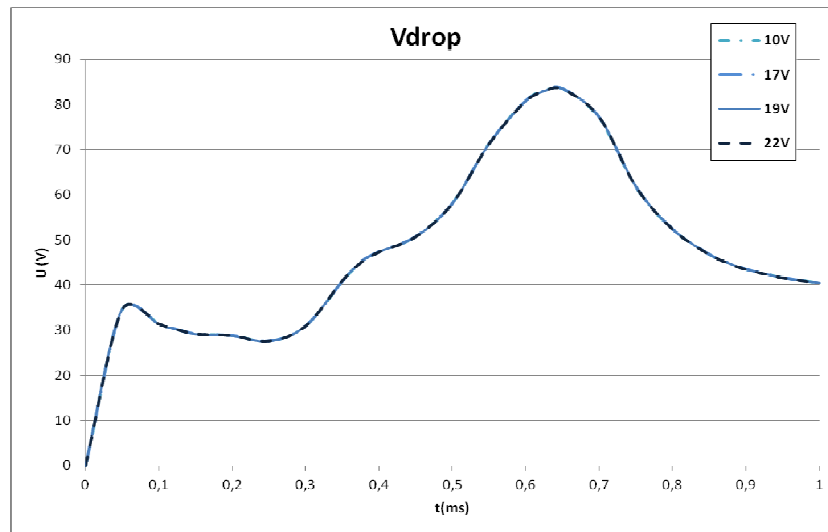


Figure 5-31 Voltage drop for 50A 1SP model, V-J arc root curve comparison, for case A



Figure 5-32 Maximum temperature in air for 50A 1SP model, V-J arc root curve comparison, for case A

Figure 5-33 Maximum pressure for 50A 1SP model, V-J arc root curve comparison, for case A



Figure 5-34 Maximum current density in air for 50A 1SP model, V-J arc root curve comparison, for case A



Figure 5-35 Maximum current density in splitter plate for 50A 1SP model, V-J arc root curve comparison, for case A

Analyzing these results, the four curves for arc roots modelling introduced by Lindmayer and followed in the reference model by Lohse [3] (Figure 5-19 and Figure 5-20), leads to th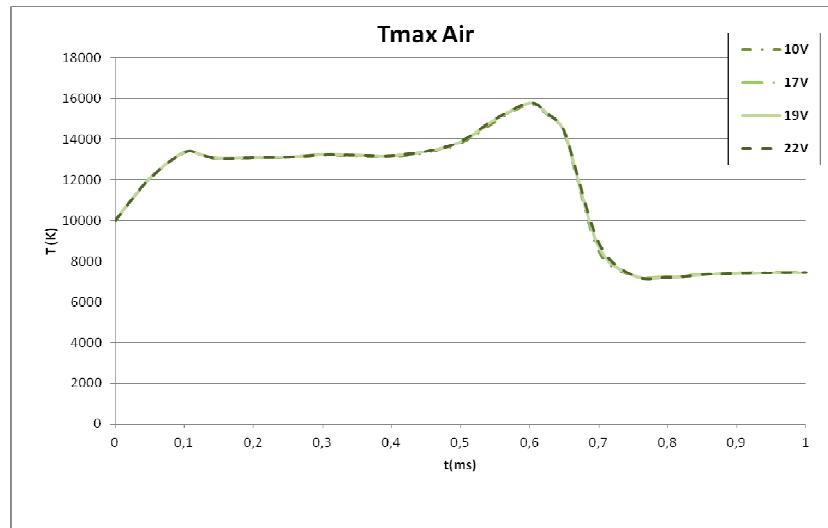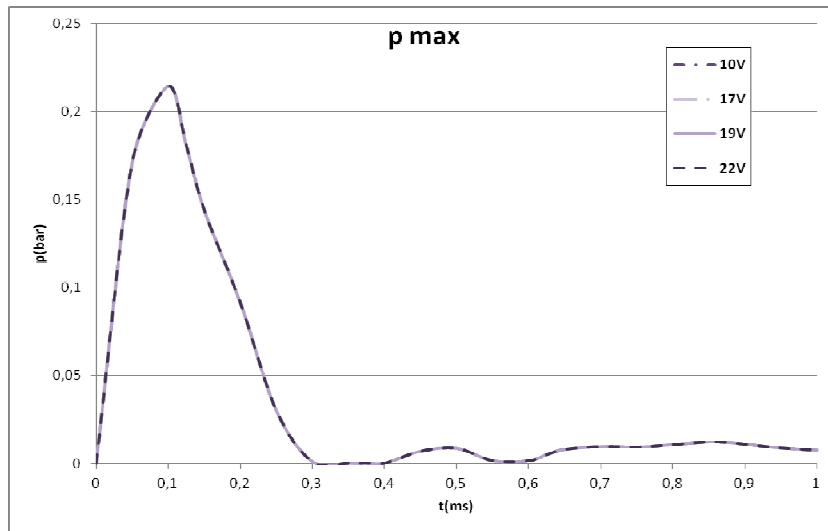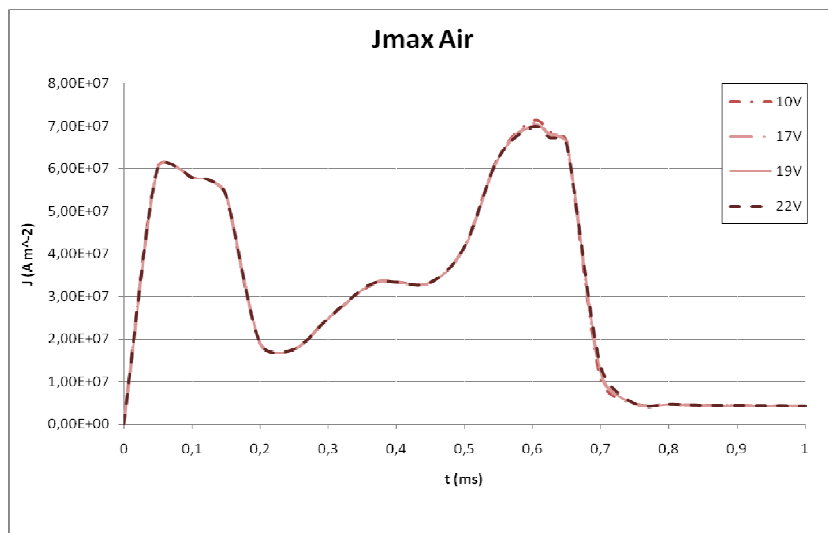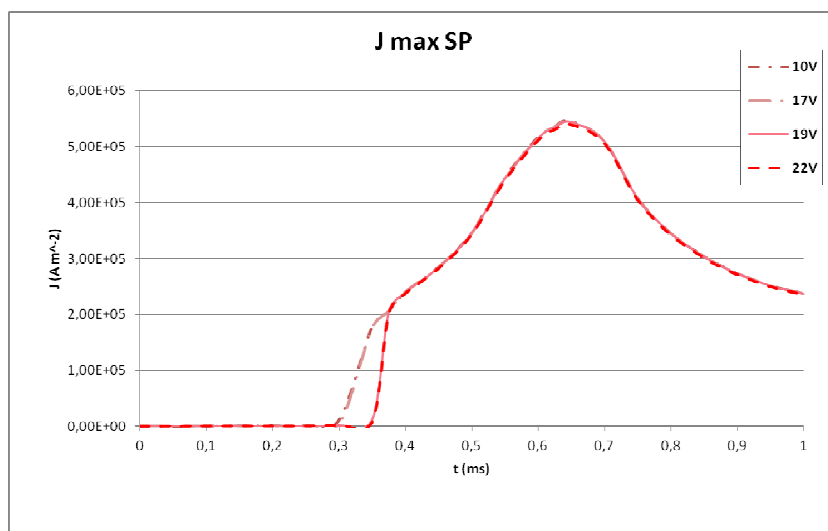e same behaviour in the new model proposed. This is explained by the values achieved by the current density in the air and its association with the ohmic resistance calculation (Figure 5-20). In the whole simulation, the value of the current density in the air is around $10^7$ A/m$^2$. Looking at the data of the proposed V-J curves (Figure 5-19 and Figure 5-20), it can be seen that for a current density value equal to $10^7$ A/m$^2$ there is no difference between the four curves, achieving a voltage drop of 10V. Thus, the ohmic resistance calculated for the four cases with those values is just the same. Therefore, it makes sense that the four simulations are equal in the new model proposed.

This achievement is not only in disagreement with the reference model but also with references [55, 57, 58, 60, 61, 65]. Taking notice of the current value results, also the operating point for those models is around $10^7$, so the values of Ohmic resistance in these cases should also be the same ones for every V-J curve.

Also the symmetry effect, applied in these models, where the V-J curves lead to four different results [3] and [55, 57, 58, 60, 61, 65], can be the responsible for a negative impact in the symmetry plane, due to the inaccuracies proved in Figure 5-10. Thus, being the operating point for the current density around $10^7$ A/m$^2$, these four curves are the same. So, from now on, only one of those four curves will be used for the next tests.

## 5.4.2   CASE B: SPLITTER PLATES

In this case, the effect of including different number of splitter plates in the arc chamber is presented. The reference model is the previously presented new model in case A, with 50A of input current in the anode, one splitter plate (1SP) in the chamber and the rest of the characteristics as explained (Figure 5-22 to Figure 5-30). Case A model has been geometrically modified in case B, for two different situations.

The first one corresponds to zero splitter plate in the chamber (0SP) and is analyzed in case B.1. The second one, with two splitter plates in the chamber (2SP), is analyzed in case B.2. The thickness of the splitter plates is 1mm each for the 2SP case, while for the base model A is 1.5mm (Figure 5-8). Obviously, if the chamber general dimensions are maintained, the thickness of the splitter plates has to decrease while increasing the total amount of them.

The aim of this case B is to verify that the new model presented in Case A is robust, good and precise enough to fulfil arcing theory presented in chapter 2. It has to be reminded that the greater the lengthening of the arc, the greater the increase in arc voltage. Thus, the most satisfactory the current interruption is. This arc lengthening is generated in LVCBs with an increase in the number of splitter plates in the chamber, as presented in chapter 3.

### 5.4.2.1   Case B.1: Zero splitter plates (0SP)

Results obtained for the arc movement behaviour, expressed by current density and temperature, are shown in Figure 5-36 for the most significant timesteps and for the whole simulation time in Figure A-21. The timesteps chosen for Figure 5-36 are 0, 0.3, 0.55, 0.625, 0.7 and 0.9ms.

A clarification has to be made regarding the geometry of the chamber shown in Figure 5-36. In this case B.1 no splitter plate is taken into account, but looking at the geometry presented Figure 5-36 it might be misunderstood that the splitter plate is there, as its contour is still shown in the drawing. This is because the domain of the splitter plate has been changed to

air, integrating it in the already existing air domain, with the same physical characteristics and without any geometric limitation. Thus, case B.1 is obtained from case A, modifying the material used in the domain of the splitter plate that is changed to air.

Regarding the arc movement behaviour obtained for 0SP, Figure 5-36 shows that the arc travels constant and uniformly along the arc rails, until the top of the chamber is reached, but no splitting or disappearing happens.

As it is noticed, by 0.3ms the arc has already travelled more than half of the length of the chamber and by 0.7ms is almost at three quarter of the chamber, but at 0.9ms it is still running in the chamber. So, comparing to case A with one splitter plate (Figure 5-22), it can be said that without splitter plate, there is no bending, no arc voltage increase and no extinction.
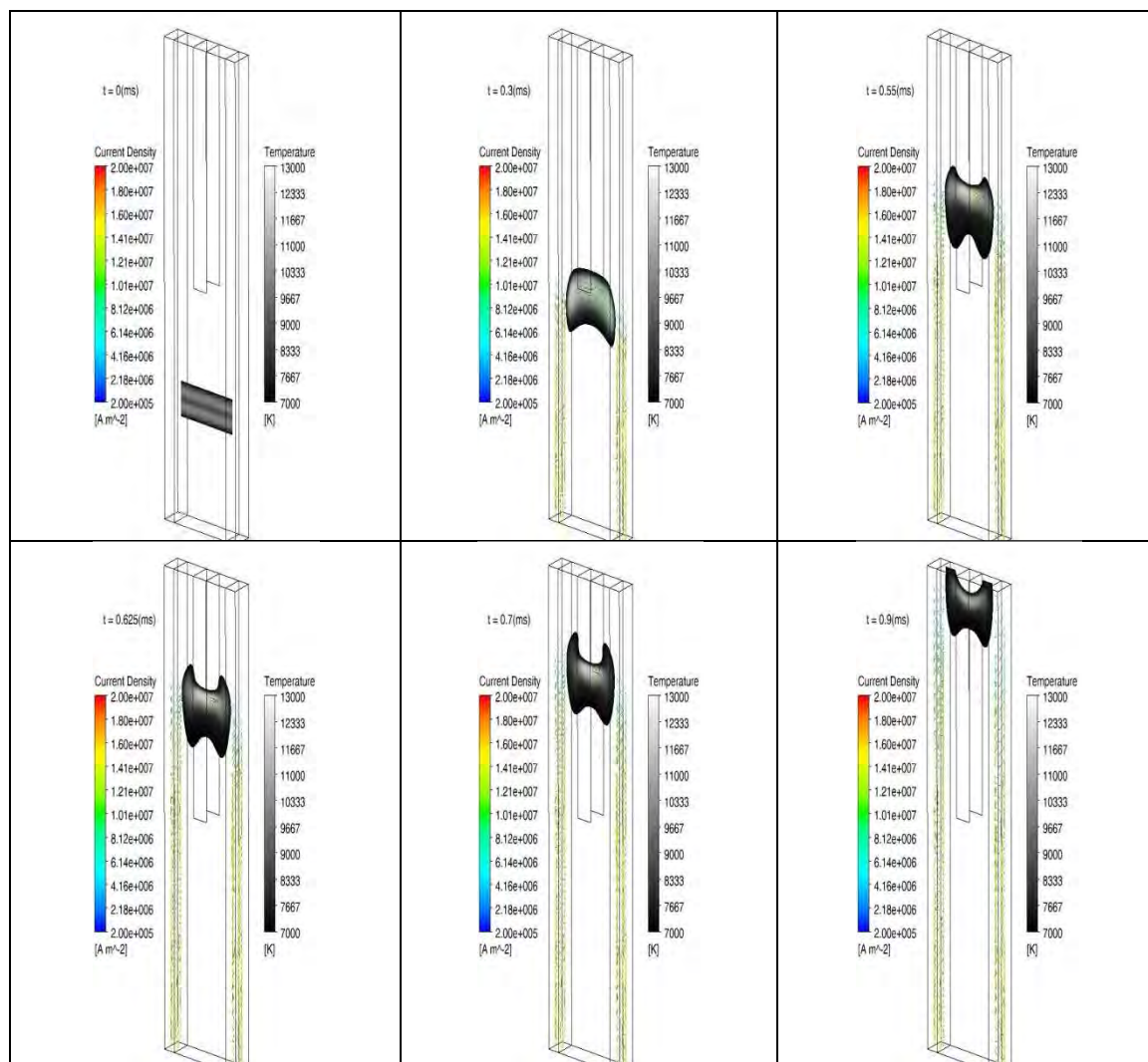


Figure 5-36 Arc movement expressed by current density and temperature for 50A and zero splitter plate (0SP), case B.1

### 5.4.2.2 Case B.2: Two splitter plates (2SP)

In case B.2 two splitter plates have been modeled in the previously exposed arc chamber, (Figure 5-8). Thus, the thickness of each splitter plate has been reduced to 1mm. Results obtained for the arc movement behaviour expressed by current density and temperature are

shown in Figure 5-37 and Figure A-22. The timesteps chosen for Figure 5-37 are 0, 0.3, 0.45, 0.55, 0.6 and 0.7ms.

Regarding the arc movement behaviour obtained in case B.2, Figure 5-37 shows that the arc reaches the splitter plates at around 0.3 ms, as in the 1SP case (case A, Figure 5-22), but the splitting is in three segments this time, due to the bending on the two splitter plates. The total splitting of the arc in three partial arcs happens at 0.5ms, while in the case A with 1SP at 0.6ms. Additionally, the total extinction of the arc for the 2SP case is achieved by 0.7ms, while in the 1SP case is at 0.8ms. So, it can be said that the arc splitting and extinction is faster with 2SP design.
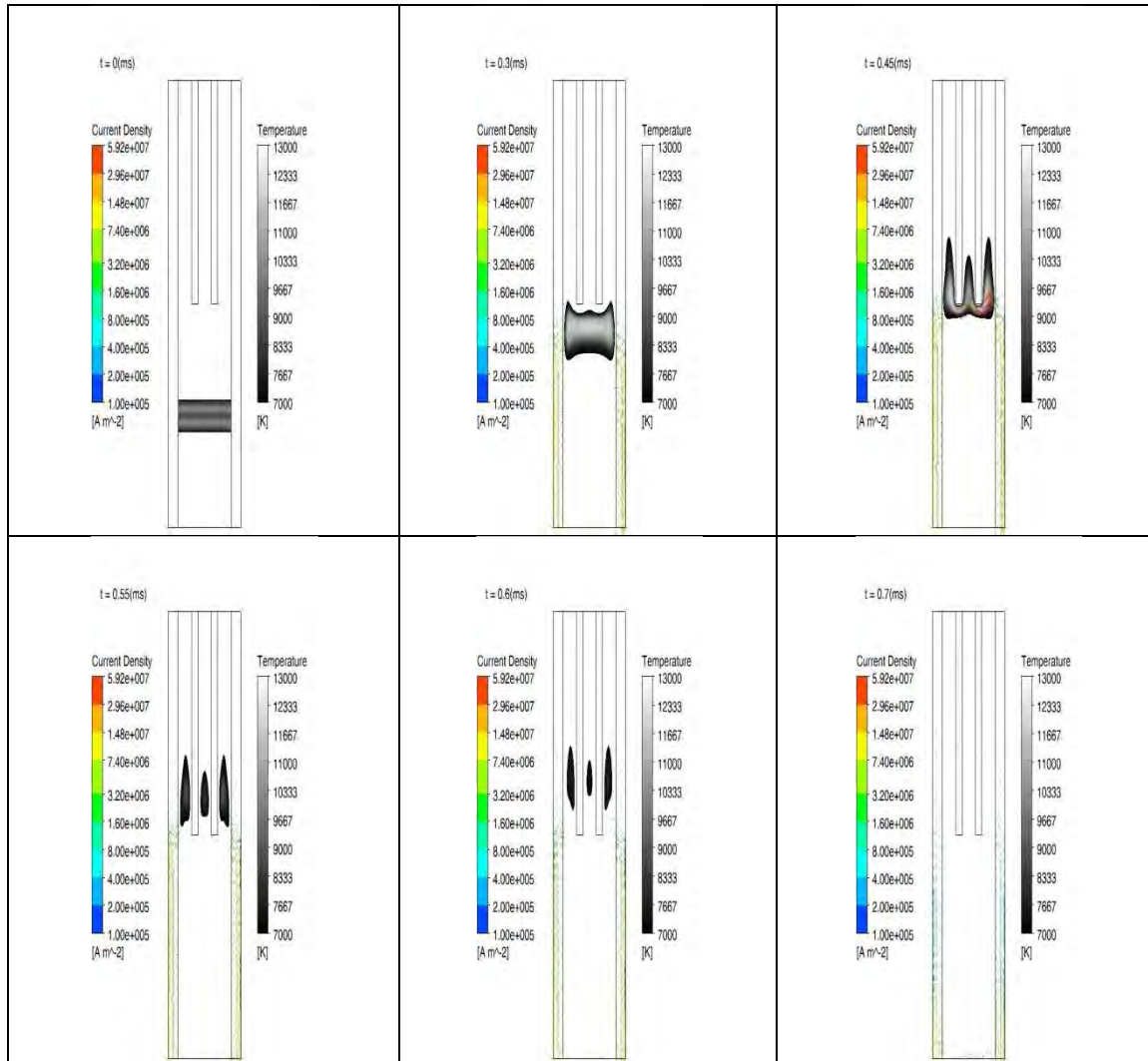


Figure 5-37 Arc movement expressed by current density and temperature for 50A and two splitter plate (2SP), case B.2

### 5.4.2.3  Comparative analysis

Besides, comparing the arc movement behaviour for case A with 1SP, and cases B.1 and B.2 of 0SP and 2SP, respectively (Figure 5-22, Figure 5-36 and Figure 5-37), additional data from those three cases is compared in this section. Arcing voltage drop, maximum temperature in the air, maximum pressure in the air, maximum current density in the air and maximum current density in the splitter plates, are shown in Figure 5-38 to Figure 5-41.

Regarding the arc voltage, Figure 5-38, the difference between the three cases is clear. In the case of 0SP, the arc voltage is almost constant during the whole arc movement, as it is

expected to happen, no bending, no lengthening of the arc and therefore no new anode and cathode are obtained. In 1SP and 2SP cases, the arc voltage increases around 40V during the bending, but in the case of 2SP the arc voltage increase is faster. For example, by timestep 0.45ms, the arc voltage for 1SP model is 50V while for 2SP is 55V, and for 0.5ms the values of the arc voltage are 55V and 60V, respectively. These are the instants when the greatest curvature of the arc around the splitter plate is obtained. That is why the arc extinction is faster with 2SP. The correlation of this phenomenon is clearly seen in the arc movement images in Figure 5-37. According to the arcing theory of chapter 2, it is expected that the arc voltage increases with the number of splitter plates and so does the model. Therefore, it can be stated that the new model proposed is a good and robust one.
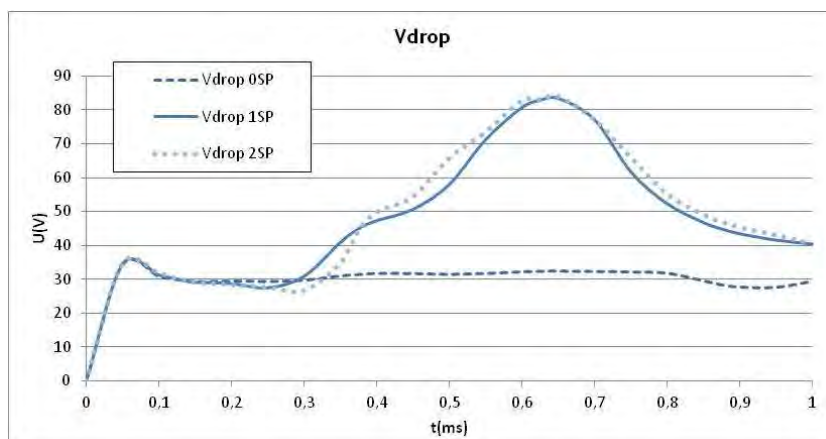


Figure 5-38 Voltage drop for 50A model, SP comparison, case B

Reasonable temperature results are also obtained for 0SP case, as the temperature almost remains constant. On the contrary, for 1SP and 2SP cases the temperature starts rising as the arc starts bending and around 0.6-0.7ms it goes down, below 10000K, so the plasma state disappears. This decrease in the temperature is produces together with the decrease in the arc voltage and current density (Figure 5-38 and Figure 5-41).
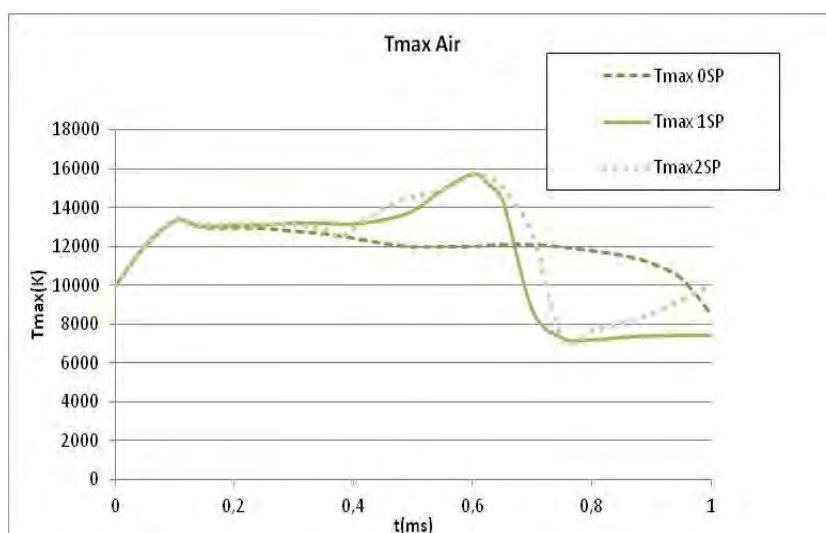


Figure 5-39 Maximum temperature in air for 50A model, SP comparison, case B

Air pressure shows also the expected behaviour (Figure 5-40). Value of pressure is higher the smaller is the space for the air inside the chamber so, the higher the number of splitter plates, the smaller the space for the air inside the chamber and so, the higher the pressure.

These results allow verifying again that the model performance is correct, even though the increase is much notorious in the 0SP-1SP comparison than in the 1SP-2SP.
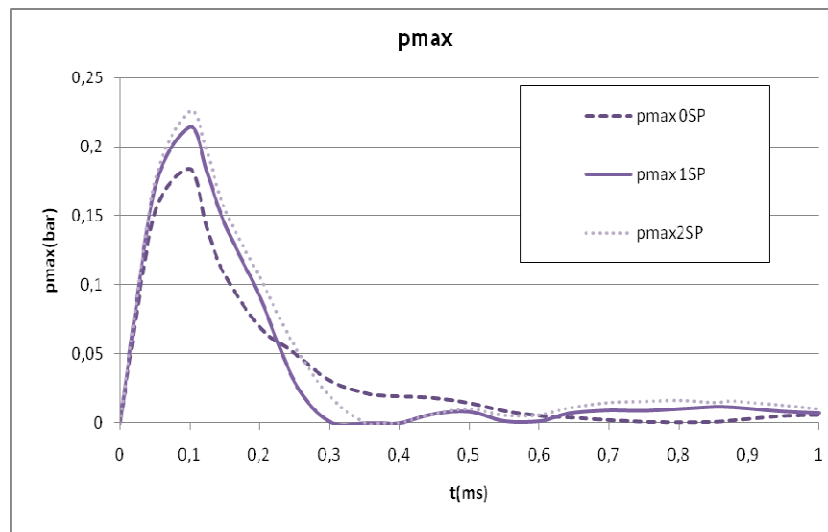


Figure 5-40 Maximum pressure for 50A model, SP comparison, case B

Finally, it is again remarkable the difference between the current density in the air without splitter plates, or with one or two splitter plates. In the 1SP and 2SP cases, the current density rises from 0.3 ms to 0.6-0.7 ms, depending on the model, when it goes down again because cooling process starts.
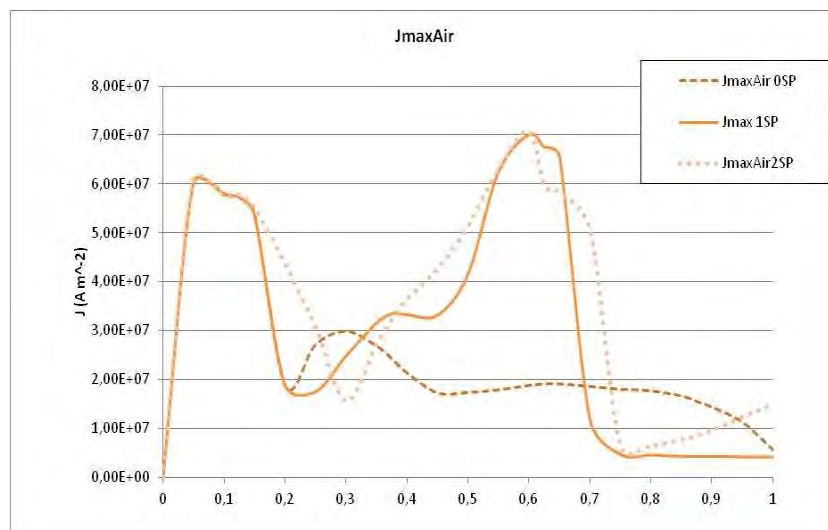


Figure 5-41 Maximum current density in air for 50A model, SP comparison, case B

Also, information for the current density in the splitter plate is shown in Figure A-23, for 1SP and 2SP cases. The 0SP case has been removed from the chart as it has no sense to talk about current density in splitter plates for that case.

Summarizing, along this case B two aims have been fulfilled. On the one hand, the reinforcement that the new model proposed and presented in case A is adequate, as it has fulfilled arcing theory physics. On the other hand, it has been proved, once again, that the increment of splitter plates in the arc chamber is beneficial for the arc interruption process. Zero, one and two splitter plates in the arc chamber have been compared. It has been proved that the 2SP model leads to a bigger bending and lengthening of the arc around the splitter plates, and to a bigger voltage drop and faster extinction. When comparing 1SP and 2SP

cases, an improvement of just 0.1ms in the extinction process is obtained (Figure 5-22 and Figure 5-37), which represents the 10% of the total simulation time of this case, 1ms.

### 5.4.3 CASE C: LOWER ARC IGNITION AND DIFFERENT INPUT CURRENTS

In case C, the position of the arc ignition and the input currents have been changed. This way, lower ignition for different current values (50A, 100A and 200A) has been tested, with 0SP and 1SP.

For comparison purposes, model from case B.1 has been taken as reference, with 50A and 0SP. The arc ignition position has been changed from 10mm above the lower face of the chamber to 1mm, leading to case C.1. After that, model from case A has been taken as reference again, with 50A and 1SP and the arc ignition position has been also modified, leading to case C.2

Following, changing arc input currents of case C.1 to 100A and 200A, case C.3 for lower arc ignition 100A and 0SP, and case C.5 for lower arc ignition 200A and 0SP are obtained.

Finally, in the same way, changing arc input current values in case C.2 to 100A and 200A, case C.4 for 100A, 1SP and lower arc ignition, and case C.6 for lower arc ignition 200A and 1SP are also obtained.

#### 5.4.3.1 Case C.1: Lower arc ignition, 50A input current and 0SP

Results for the arc movement behaviour, expressed by current density and temperature, are shown in Figure 5-42. The images for the whole simulation time are, as in the previous cases, shown in the Annex (Figure A-24).

The most remarkable characteristic of case C.1 is that the upwards movement of the arc along the electrodes is very slow in comparison with case B.1. As seen in Figure 5-42, for 1ms simulation time the arc has only moved around 1mm in case C.1, while in Case B.1, where the arc is ignited 10mm above the down wall (Figure 5-36), the arc has reached the top of the chamber.

This effect can be explained by analyzing the momentum equation of Navier–Stokes where a term corresponding to the pressure gradient is included. The pressure due to the air volume below the arc, that is between the lower face of the chamber and the arc, is smaller for case C.1 than for case B.1, as the air volume heated up in case C.1 is only $1x11x2.5mm^3$ while for case B.1 is $10x11x2.5mm^3$.

The behaviour exposed in Figure 5-42 is in correspondence with experimental results, as will be exposed in chapter 6.

Figure 5-42 Arc movement expressed by current density and temperature, for lower arc ignition, 50A input current and 0SP model, case C.1

### 5.4.3.2 Case C.2: Lower arc ignition, 50A input current and 1SP

In case C.2, lower ignition, an input current of 50A and 1SP have been considered and the reference model for comparison is the case A (Figure 5-22).

Looking at the results shown in Figure 5-43, it can be said that there is no difference in the simulations between case C.1 (lower ignition, input current of 50A and 0SP) and case C.2 (lower ignition, input current of 50A and 1SP).This is due to the effect of the slow upwards movement in these cases of lower ignition, as the simulation time of 1ms is not enough for the arc to arrive to the splitter plate area.

This result is confirmed in chapter 6, where the results obtained in real tests are included. In those real experiments, it will be seen that an arc with those characteristics needs around 10ms to reach the splitter area and 25ms for its extinction. Thus, it would have been very interesting to be able to consider longer simulation times, but unfortunately the computational logistic used to develop this thesis has not made it possible. The new simulation model developed in this thesis took around four days to solved 1ms of simulation (Table 6-5). Therefore, supposing a linear behaviour, simulating 25ms would take 100 days, which is not effective, sustainable or applicable.

Computational time is only explicitly mentioned in a few number of references, but it has to be considered that the publication year affects directly the computational time, as the PCs have improved over time. Some examples are [50] and [34], where it is indicated that the simulation took around 6 days, or 8 days in 8 clusters equipment for [2]. Thus, it can be said that the computational time required by the model developed in this thesis is a reasonable value.



Figure 5-43 Arc movement expressed by current density and temperature, for lower arc ignition, 50A input current and 1SP model, case C.2

### 5.4.3.3  Case C.3: Lower arc ignition, 100A input current and 0SP

In case C.3, case C.1 has been taken as reference and the input current has been changed from 50A to 100A. The results obtained for arc movement, expressed by current density and temperature, are shown in Figure 5-44 and Figure A-26.

These results differ from Figure 5-42 in the upwards movement of the arc. It is observed that with 100A the expansion and diffusion of the arc are greater.
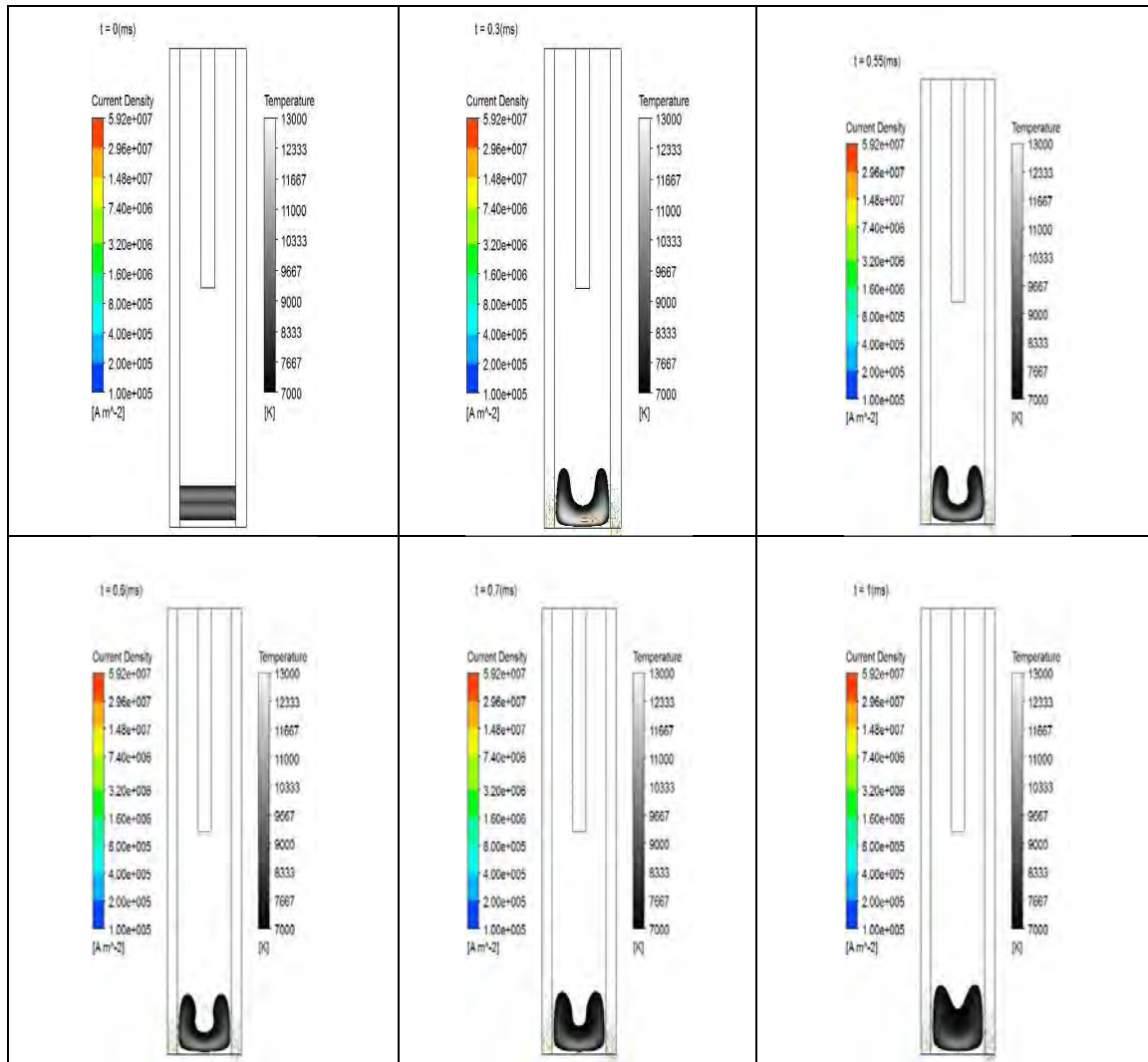
Figure 5-44 Arc movement expressed by current density and temperature, for lower arc ignition, 100A input current and 0SP model, case C.3

### 5.4.3.4  Case C.4: Lower arc ignition, 100A input current and 1SP

In this case C.4, case C.2 has been taken as reference and the current value has been increased to 100A. The arc movement results are shown in Figure 5-45 and Figure A-27. As in case C.2, simulation time is not long enough for the arc to reach the splitter plates so no difference is found between the results obtained in case C.3, without splitter plate, and in case C.4, with 1SP (Figure 5-44 and Figure 5-45).

Figure 5-45 Arc movement expressed by current density and temperature, for lower arc ignition, 100A input current and 1SP model, case C.4

### 5.4.3.5 Case C.5: Lower arc ignition, 200A input current and 0SP

In case C.5, a model with low arc ignition, 200A input current and 0SP has been analyzed. The model has been developed changing the input current of C.1 case. Results of the arc movement are shown in Figure 5-46 for certain timesteps and in Figure A-28 for the whole simulation time of 1ms.

As it has already been observed in C.1 and C.3 cases, expansion and diffusion of the arc are obtained as the input current increases. In this case, it is even clearer that arc does not move upwards as a cylinder as for 50A cases (case A) but it expands.

Besides, comparing Figure 5-46 with Figure 5-44 (case C.3) and Figure 5-42 (case C.1) it can be concluded that the higher the input current value, the higher the arc arrives in its way along the chamber, i.e., the expansion is bigger and the movement is faster. This way, for case C.5, at 0.5ms the arc has reached half of the chamber and at 1ms the arc has travelled three quarters of the total length.

The "nose" that appears in the centre of the arc displacement can be justified as explained in chapter 4 [42], where also the nose effect appears in both simulation and experiments.
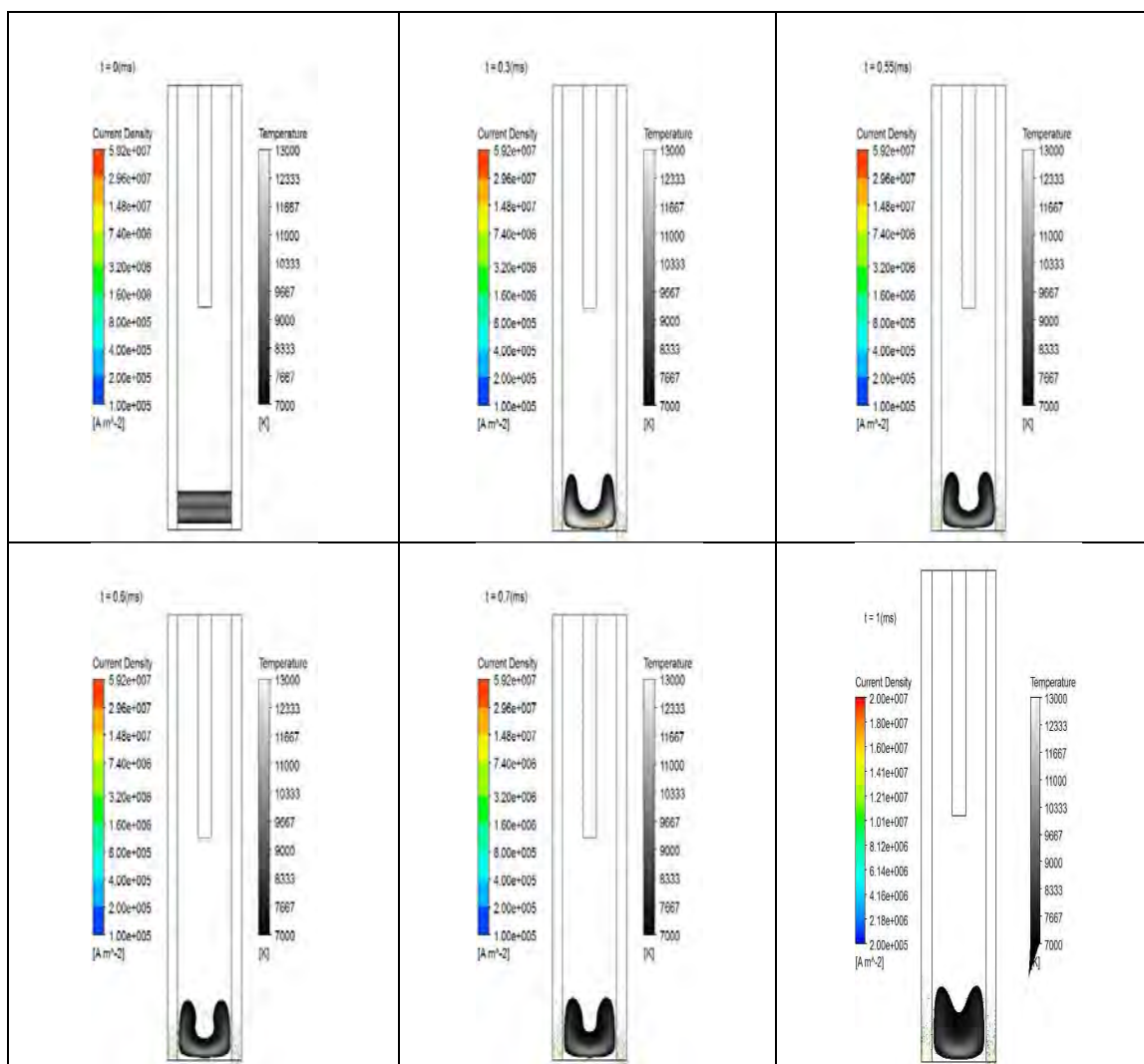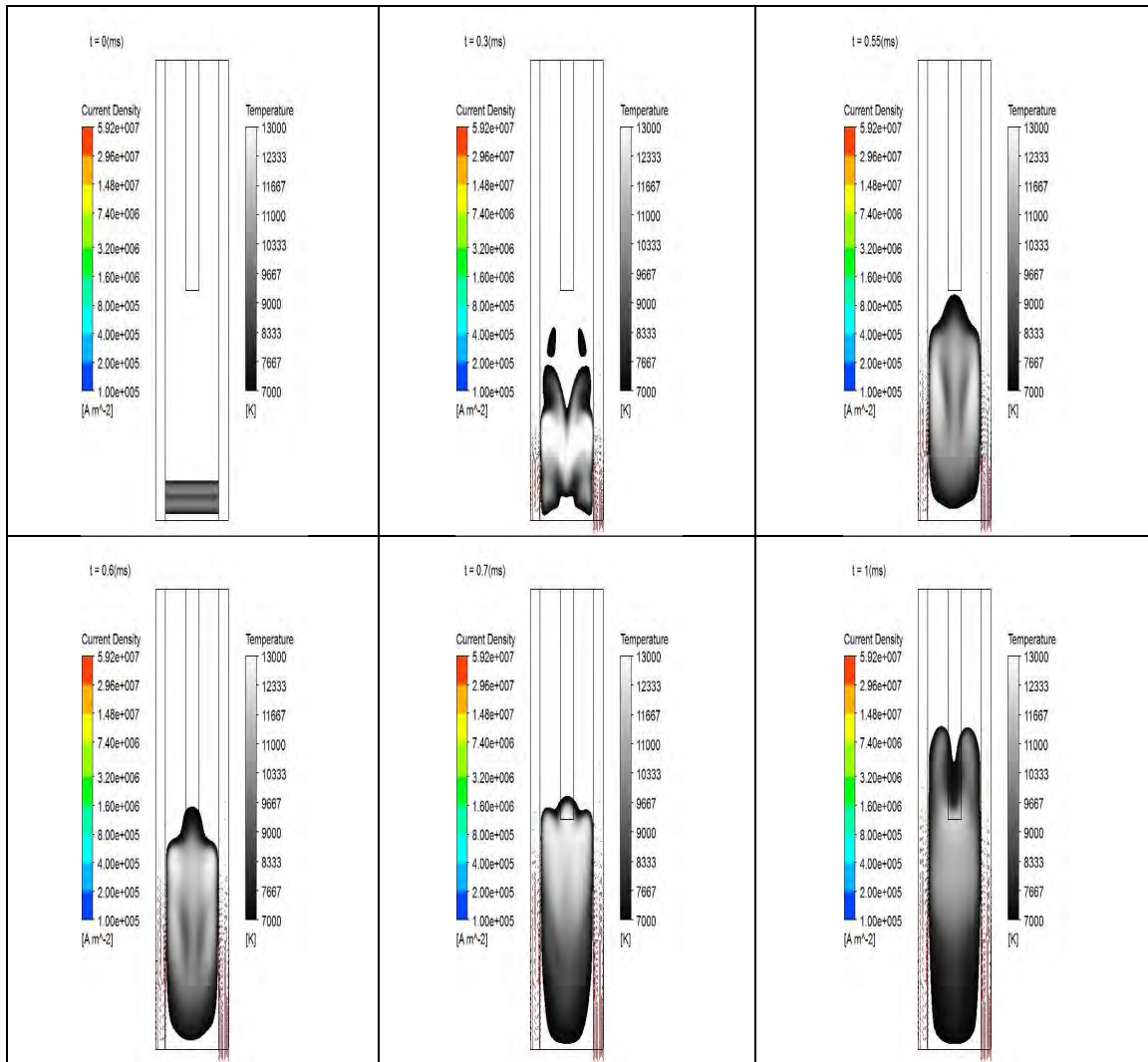
Figure 5-46 Arc movement expressed by current density and temperature, for lower arc ignition, 200A input current and 0SP model, case C.5

### 5.4.3.6  Case C.6: Lower arc ignition, 200A input current and 1SP

Finally, case C.6 is obtained from case C.2 increasing the input current to 200A. Results of the arc movement are shown in Figure 5-47 and Figure A-29, where expansion is observed as in case C.5 (Figure 5-46).

In this case, the arc reaches the splitter plate area before the simulation time ends. Thus, the bending of the arc around the plate is visible for the first time in case C. Starting at 0.8ms and up to 1ms (Figure A-29), the arc starts splitting in two around the plate. Thus, it is once again stated that a bigger input current makes the arc to expand and travel faster.
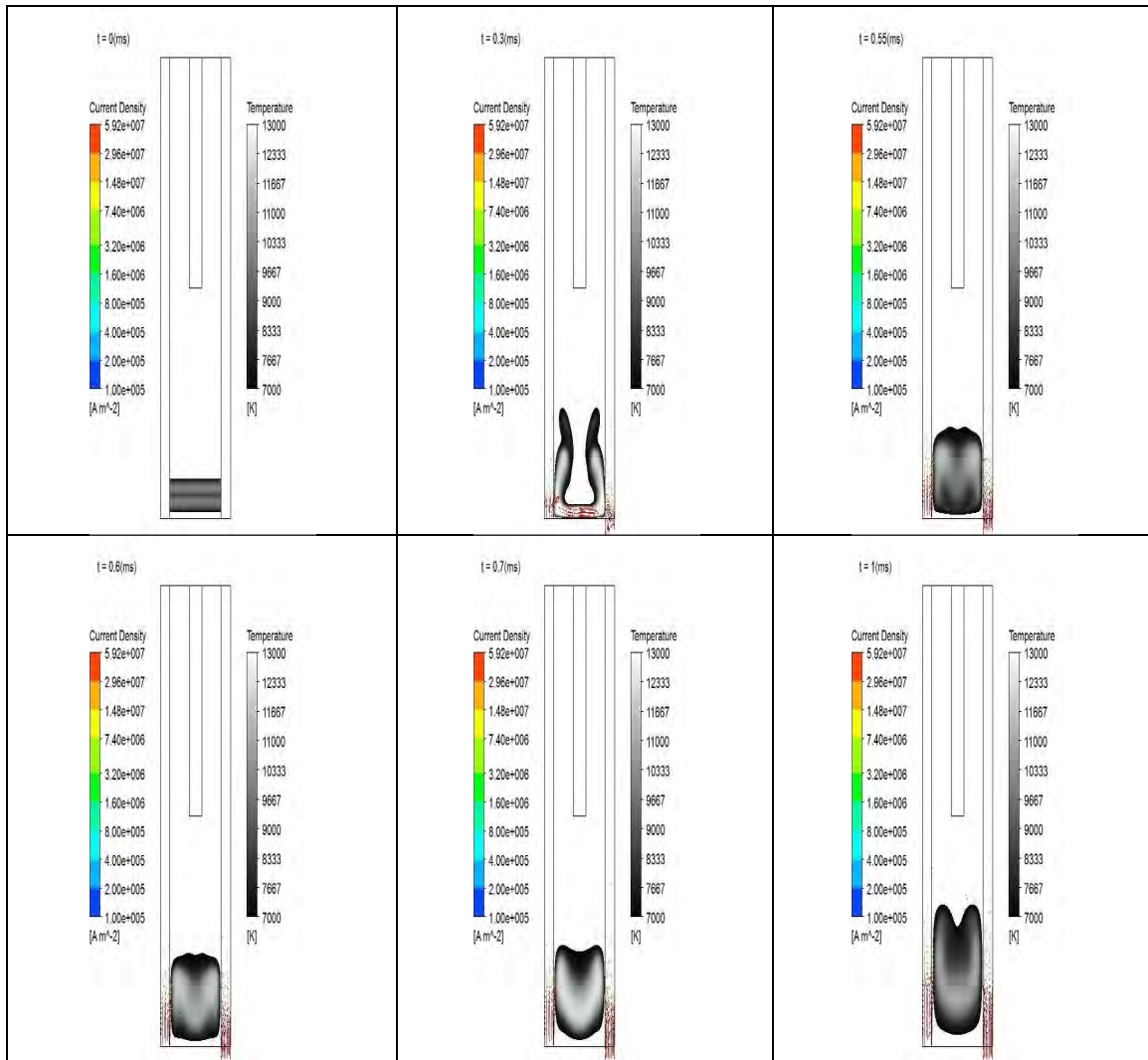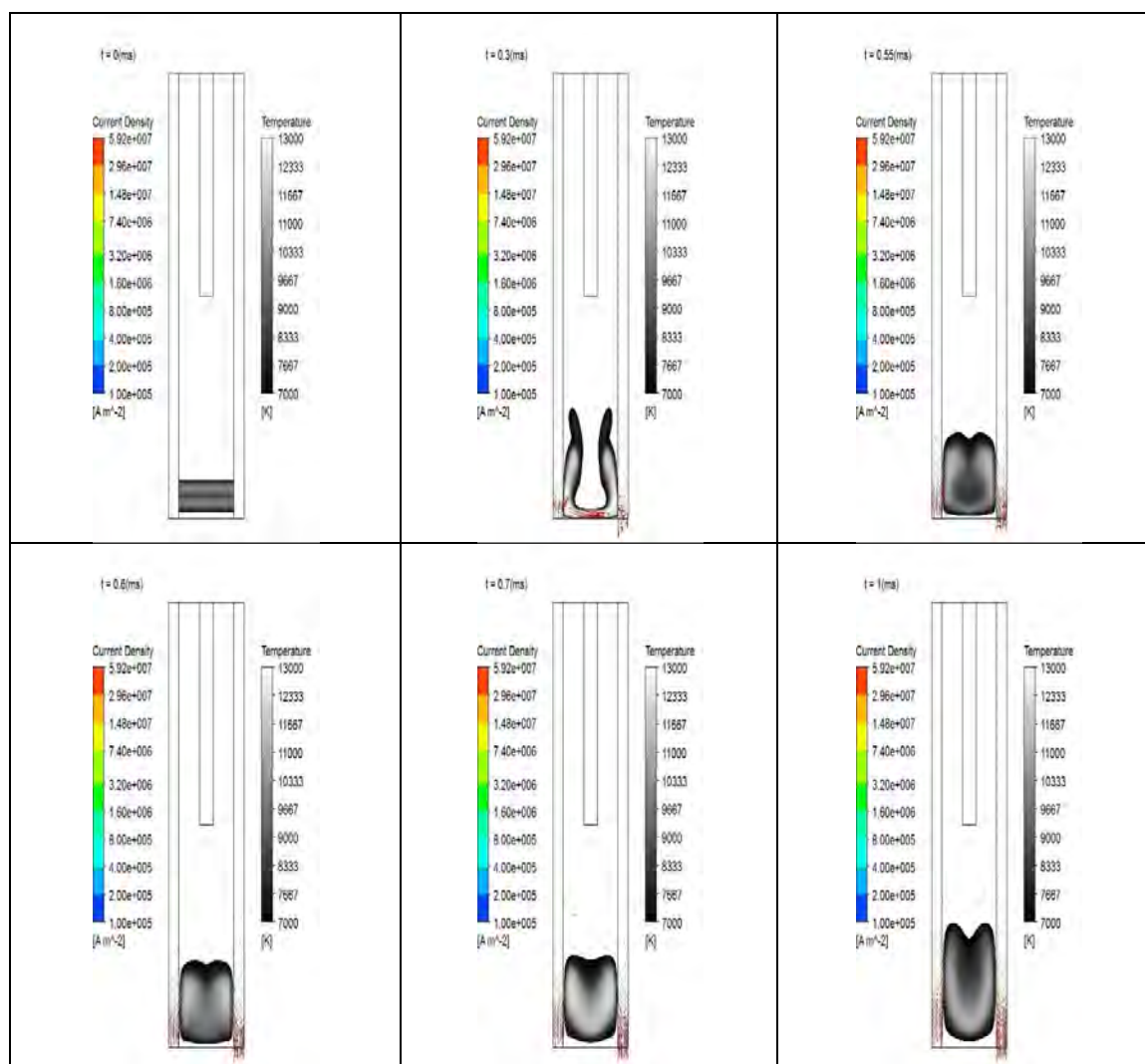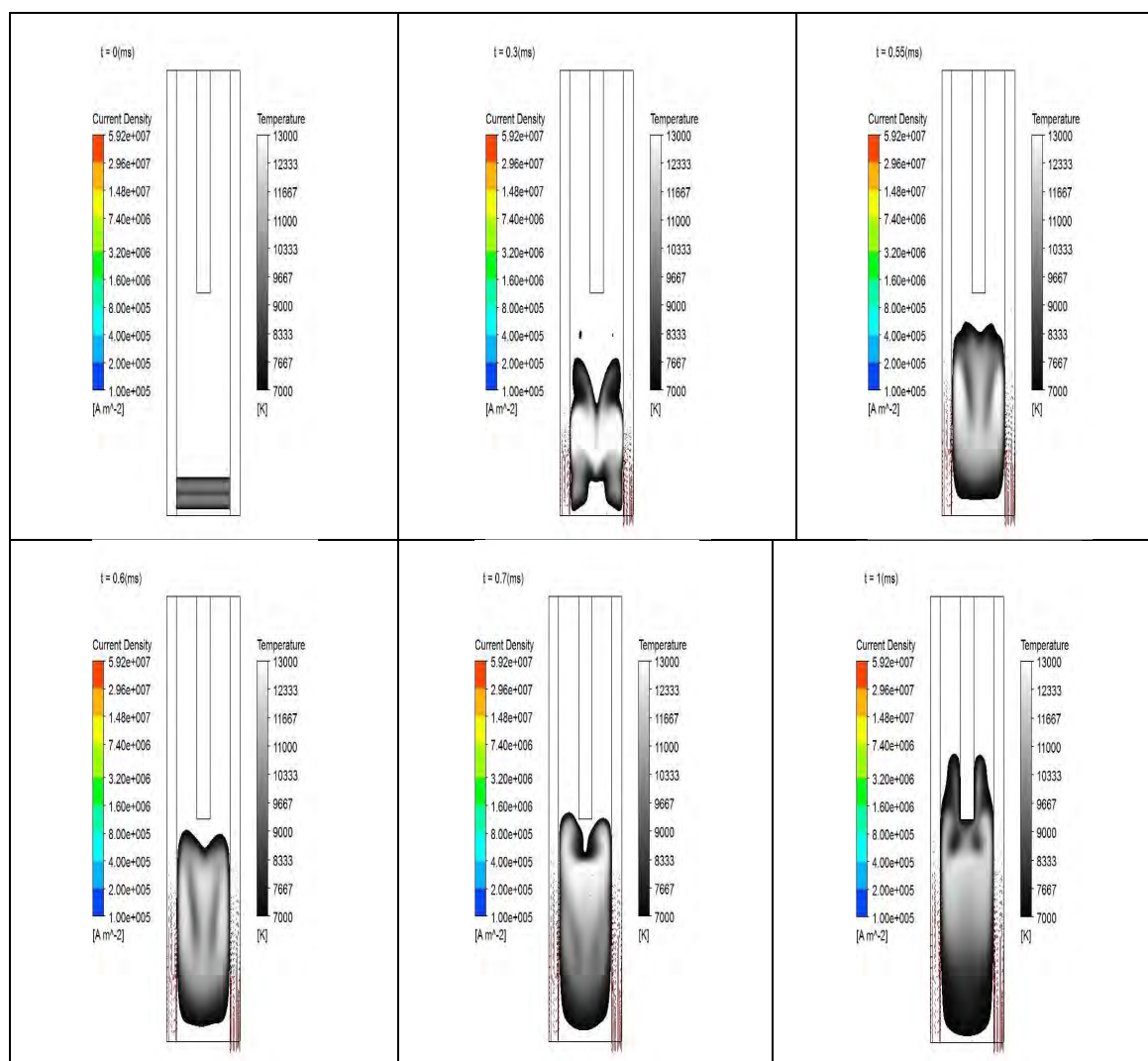
Figure 5-47 Arc movement expressed by current density and temperature, for lower arc ignition, 200A input current and 1SP model, case C.6

### 5.4.3.7   Comparative analysis

Finally, a comparative analysis of cases C.1 to C.6 is presented in this section. Voltage drop, maximum air temperature, maximum air pressure, maximum current density in the air and in the splitter plate are shown in Figure 5-48, Figure 5-49 and Figure A-30 to Figure A-32.

However, the information that can be extracted from those figures is limited, as 1ms of simulation is a short simulation time for these cases. Anyway, a general conclusion is fulfilled in all those results: the bigger the input current is, the higher the air temperature (Figure 5-48) and thus the electrical conductivity and the input power for the arc movement. This is proved comparing Figure 5-42 (50A, 0SP) to Figure 5-44 (100A, 0SP) and Figure 5-46 (200A, 0SP), and Figure 5-43 (50A, 1SP) to Figure 5-45(100A, 1SP) and Figure 5-47 (200A, 1SP), where a faster upwards diffusion for the arc is observed.
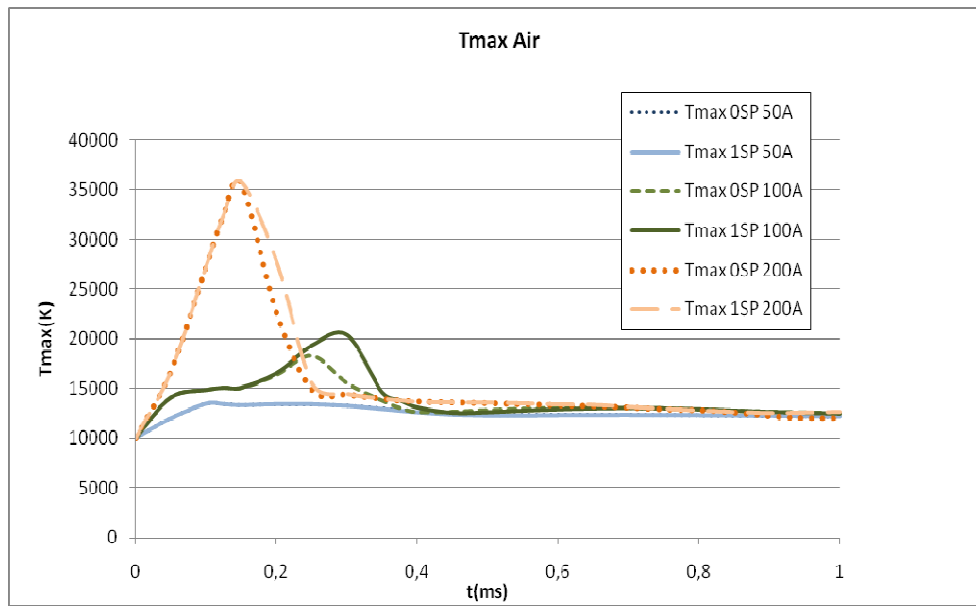
Figure 5-48 Maximum temperature in air for 50, 100 and 200A, 0SP and 1SP, case C

Regarding the arc voltage drop (Figure 5-49), it is clear that the arc voltage is higher the higher is the input current in the chamber. However, as the simulation time has not been long enough for the arc to bend around the splitter plate, due to the long computational time required, the additional voltage drop due to this phenomenon is not appreciable in that figure.
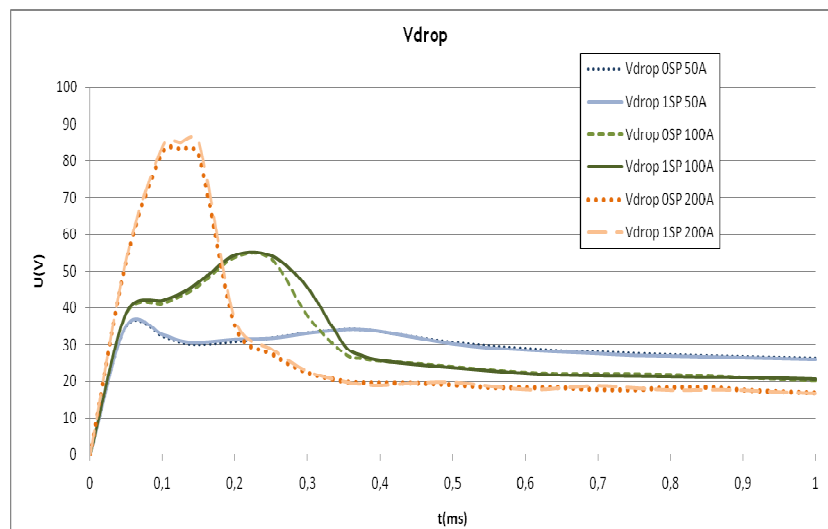


Figure 5-49 Arc voltage for 50, 100 and 200A, 0SP and 1SP, case C

These six cases C allow drawing conclusions from the impact of the arc ignition position and the input current value. Additionally, it has been possible to validate these cases of the new model by the real experiments presented in chapter 6.

### 5.4.4   CASE D: EXPANSION VOLUME

In this set of tests, D, the following geometrical changes have been introduced, with the aim of analyzing their impact on the arc movement:

- Case D.1: an additional volume in the upper part of the chamber (expansion volume) has been added to the original geometry of case A. Dimensions of the expansion volume are

7x11x2.5mm$^3$ and all its boundaries are defined as openings. The new geometry proposed for this case is shown in Figure 5-50. The expansion volume idea has been motivated by two reasons: on the one hand, it has been considered by Lindmayer [34, 51-53, 55, 57, 58, 60, 61, 65]. To evaluate the effect, the dimensions chosen for this expansion volume have been selected according to data of those references. On the other hand, this expansion volume allows analyzing the influence of a greater but further opening of the chamber on the arc movement.
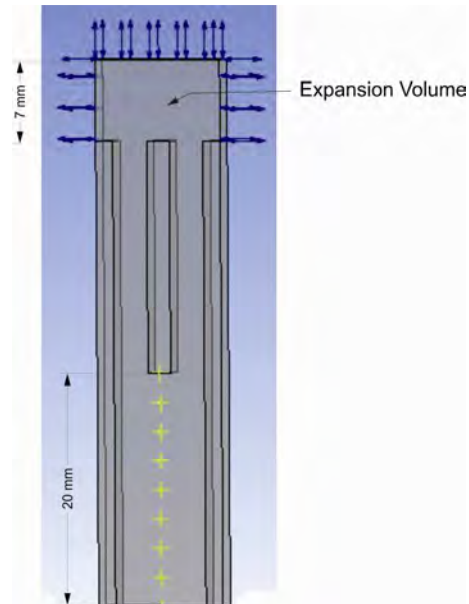


Figure 5-50 Geometry with expansion volume, Case D.1

- Case D.2: changes in the lower part of the circuit breaker have been applied. The position of the lower wall has been modified to reduce the space between the air down wall and the splitter plate from 20 mm to 7mm. This way, the total length of the chamber has been shortened. The geometry for this case is shown in Figure 5-51.
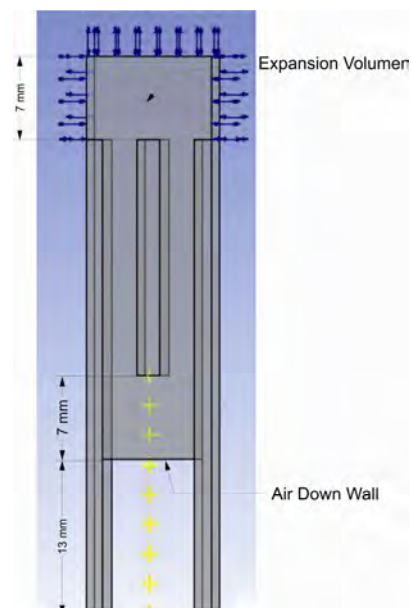


Figure 5-51 Geometry with expansion volume and air down wall higher, Case D.2

- Case D.3: finally, electrodes have been lengthened 7mm in the lowest part taking a base case D.1, but the distance between the air down wall and the beginning of the splitter plate is maintained equal to 20mm. The geometry is shown in Figure 5-52.

In both cases, D.2 and D.3, in the low part of the chamber where the electrodes have been lengthened or the down wall has been moved upwards, the boundary conditions applied have been defined as wall.
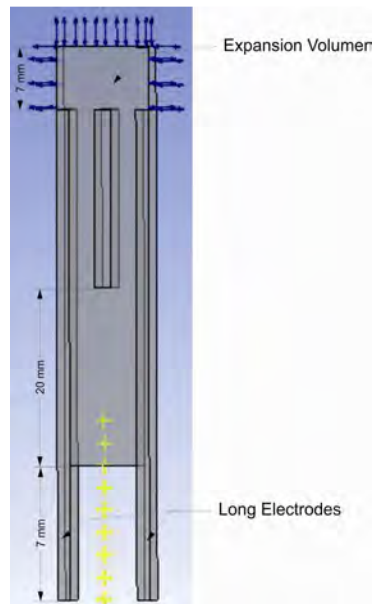


Figure 5-52 Geometry with expansion volume and longer electrodes, Case D.3

### 5.4.4.1 Case D.1: Expansion volume, base case

Results of the arc movement obtained are shown in Figure 5-53 for some timesteps and in Figure A-33 for the whole simulation time. At 0.3ms, the arc is approaching to the splitter plate but it has not arrived yet, while in case A (Figure 5-22) at 0.3ms the arc is already at the splitter plate. Besides, at 0.55ms in case D.1, the arc is still bending around the plate, as in case A (Figure 5-22). However, in case A the arc is higher and more bent.

In the next timestep, 0.65ms for case D.1, the arc continues bending while in case A is already splitted in two, and only at 0.75ms the total splitting is achieved for D.1, while for case A this is achieved at 0.6ms. Finally, at 1ms the arc has not still disappeared in case D.1 while in case A has disappeared at 0.8ms.

Thus, it can be affirmed that the expansion volume has a negative impact on the arc movement behaviour, making the displacement slower. However, it is a more realistic approach of the real geometry of a LVCB, as it implies greater flux convection with the outer medium.
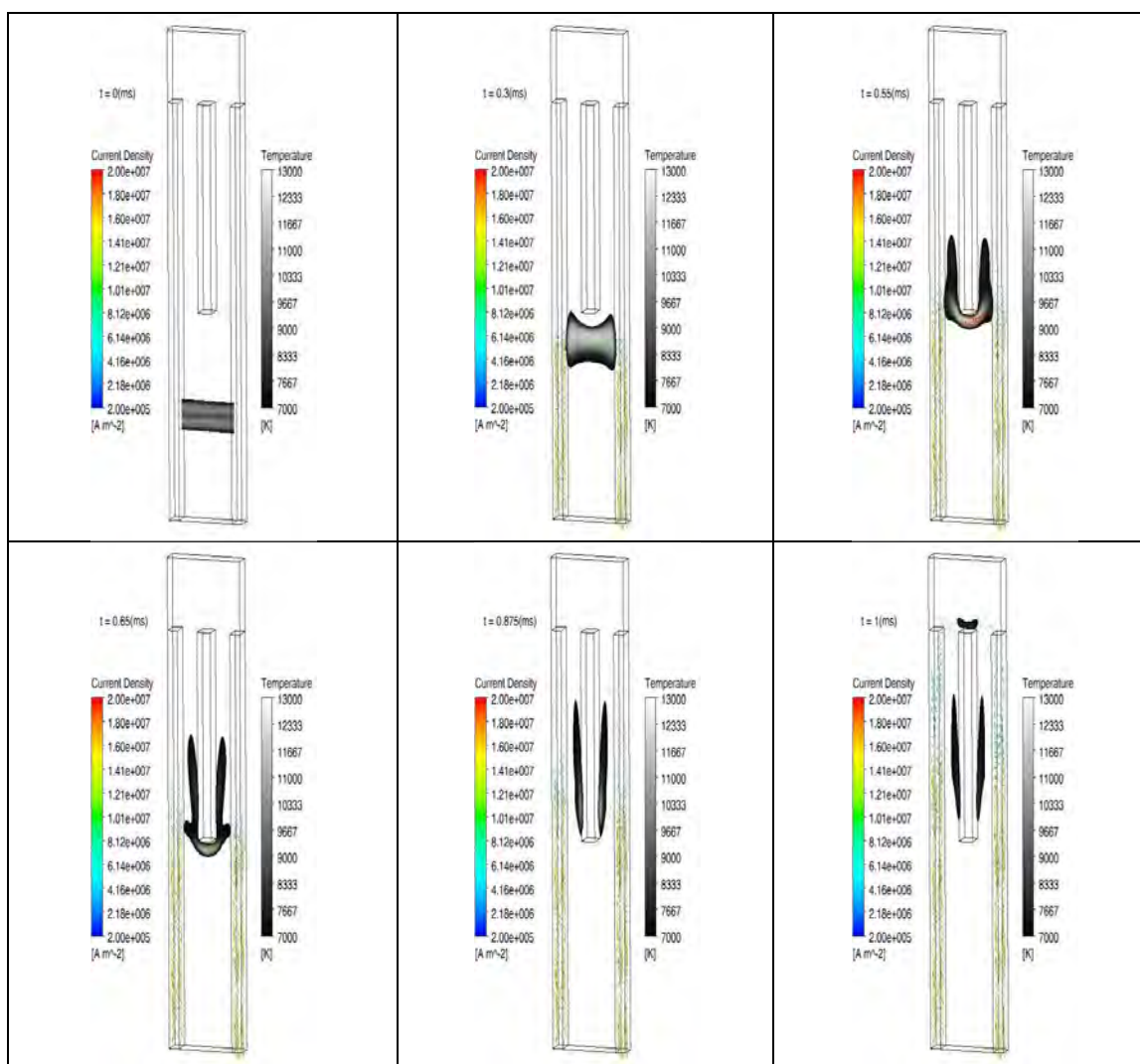
Figure 5-53 Arc movement expressed by temperature and current density, for expansion volume geometry, 50A input current and 1SP, case D.1

### 5.4.4.2 Case D.2: Expansion volume, higher air down wall

The expansion volume of case D.1 is maintained and, additionally, the lower face of the chamber has been changed, raising it 13mm. Thus, the distance between this wall and the beginning of the splitter plate is 7mm.

Results obtained for the arc movement are shown in Figure 5-54 and Figure A-34, for some timesteps and the whole simulation time, respectively. Analyzing the evolution of the arc movement, a similarity with cases C, lower ignition cases, is noticed. The ignition of the arc is very close to the bottom of the chamber and there is barely any air between the arc and the bottom of the circuit breaker. Thus, a smaller pressure is achieved to push the arc upwards. Therefore, by 1ms, the arc has barely started to bend around the splitter plate in case D.2. So, it can be concluded that this option does not contribute to the arc movement.
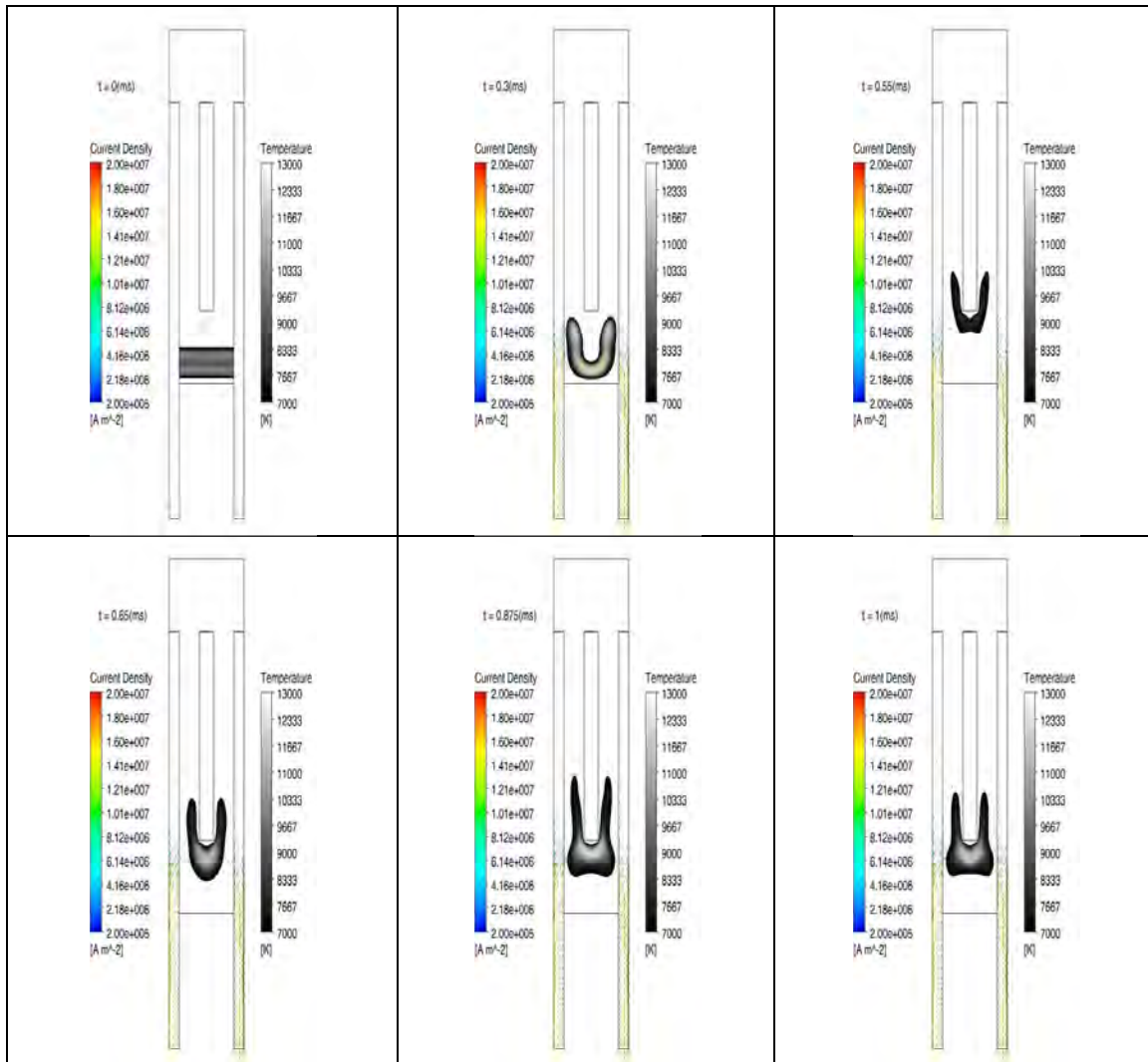
Figure 5-54 Arc movement expressed by temperature and current density for expansion volume and air wall down higher geometry, 50A input current and 1SP, case D.2

### 5.4.4.3  Case D.3: Expansion volume, longer electrodes

Taking as base case D.1 again, the influence of longer electrodes has been analyzed in case D.3. They have been lengthened 7mm in the lower part, as shown in Figure 5-52.

The results for the arc movement are shown in Figure 5-55 and Figure A-35. In this case, a great resemblance with case D.1 (Figure 5-53) is noticed, achieving the same height in the chamber, at the same timesteps. Thus, it can be concluded that lengthening the electrodes in the lower part does not lead to different results.
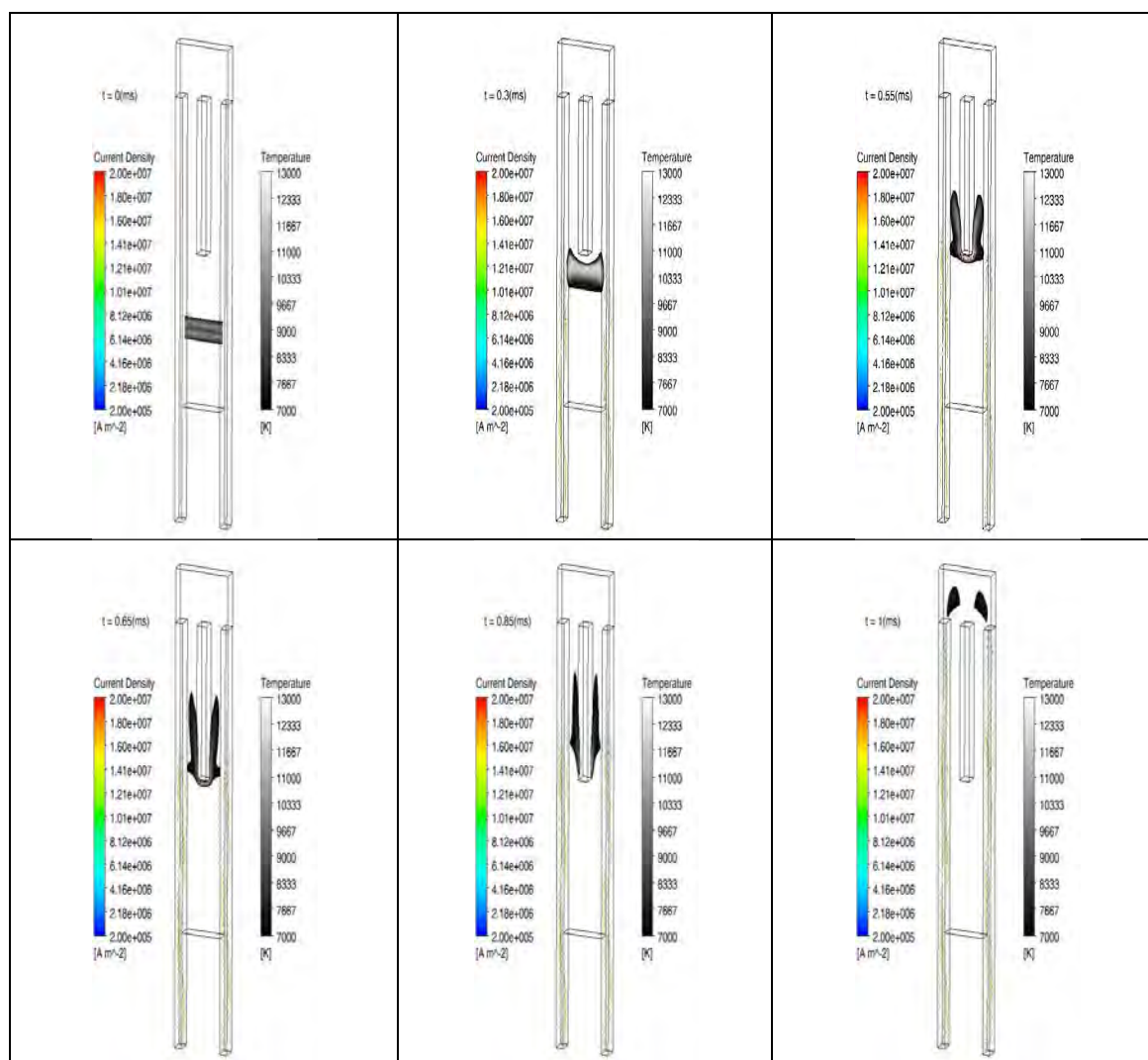
Figure 5-55 Arc movement expressed by temperature and current density for expansion volume and longer electrodes on the down side, 50A input current and 1SP, case D.3

### 5.4.4.4 Comparative analysis

Finally, arc voltage, air temperature, air pressure and current density in the air and in the splitter plate obtained in cases D.1 to D.3 are compared to case A. Results are shown in Figure 5-56 and Figure A-36 to Figure A-39.

In the simulation with expansion volume geometry, case D.1, the arc reaches the SP at 0.30ms, when starts to bend. At 0,875ms it is splitted in two smaller arcs. When the simulation ends at 1ms, the arc is not still extinguished. In fact, a third arc appears in the exhaust volume (Figure 5-53). The voltage drop from 0.3 to 0.875ms in this case increases around 70V (Figure 5-56), but it is delayed in comparison with case A, so it will lead to delayed extinctions.

In the simulation with expansion volume and higher down wall geometry, case D.2, the voltage drop obtained is very small. This result is logical, as the pressure of the air behind the arc is lower and the distance to the splitter plate small. Thus, the arc starts to bend from the beginning and the splitting and extinguishing of the arc are not produced.

Finally, in the simulation with expansion volume and longer electrodes, case D.3, a quite similar behaviour to case D.1 is obtained. So, attending to Figure 5-56, the voltage drop from 0.3 to 0.875ms increases around 80V.
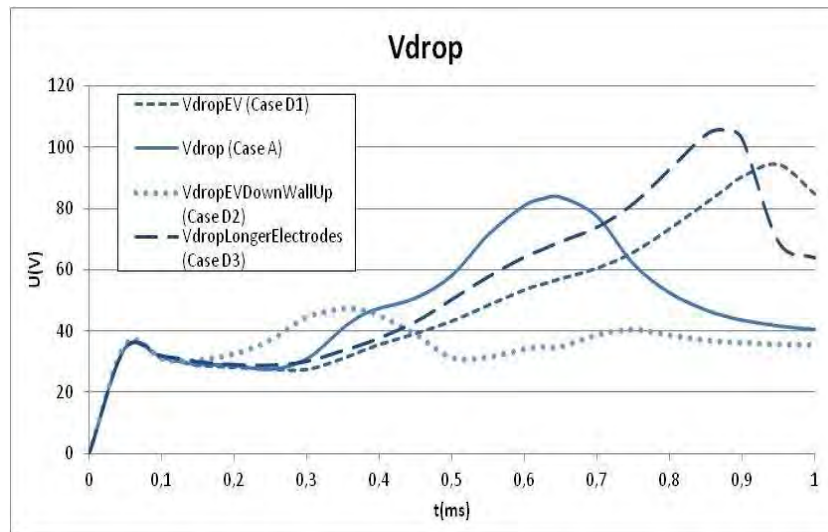


Figure 5-56 Arc voltage for 50A base case, expansion volume, longer electrodes and lower wall up, cases D and A

The rest of the parameters are presented in the Annex. So, after analyzing the influence of the geometrical new designs in the arc movement and arc voltage drop, it can be concluded that the geometrical changes proposed in this section, for D cases (D.1, D.2 and D.3) do not contribute to the improvement of the arc movement, but they have a negative influence on the arc movement, delaying it. However, expansion volume may be closer to actual geometries.

## 5.4.5   CASE E: ARC ROOTS

The approach proposed in [3] and [58, 60, 61] and applied in case A to model the arc roots using a non-linear resistance calculated from V-J curves shown in Figure 5-20, have not lead to effective results. Thus, a different approach has been modelled where in case E a different ohmic resistance is proposed. This V-J data should be obtained by a new experimental set-up, where the voltage drop inside the chamber and at both sides of the splitter plate should be measured. For this thesis, it has been impossible to obtain those data due to equipment limitation, but it is very recommendable as future work.

Therefore, in this case E, a constant value proposed by TU Ilmenau [87] for the contact resistance equal to $R = 1.4\ 10^{-06}\ \Omega\ m^2$ has been applied. This value is smaller than the ohmic resistance obtained from Figure 5-20.

### 5.4.5.1  Case E.1: Constant Ohmic resistance

Results obtained in the simulation for arc movement are shown in Figure 5-57 and Figure A-40, for some timesteps and the whole simulation time, respectively. In Figure 5-57, a rather similar behaviour to case A is observed but some differences arise comparing to Figure 5-22. Thus, in case E.1, the splitter plate is also achieved at 0.3ms, but the bending time is very short and the arc is quickly divided in two arcs. Then, the lengthening during the bending of the arc is limited, so the voltage drop is not as high as in case A (Figure 5-58) and the

extinction of the arc takes a longer time. As it is noticed, the arc is still in the chamber at 0.8ms (Figure 5-57).
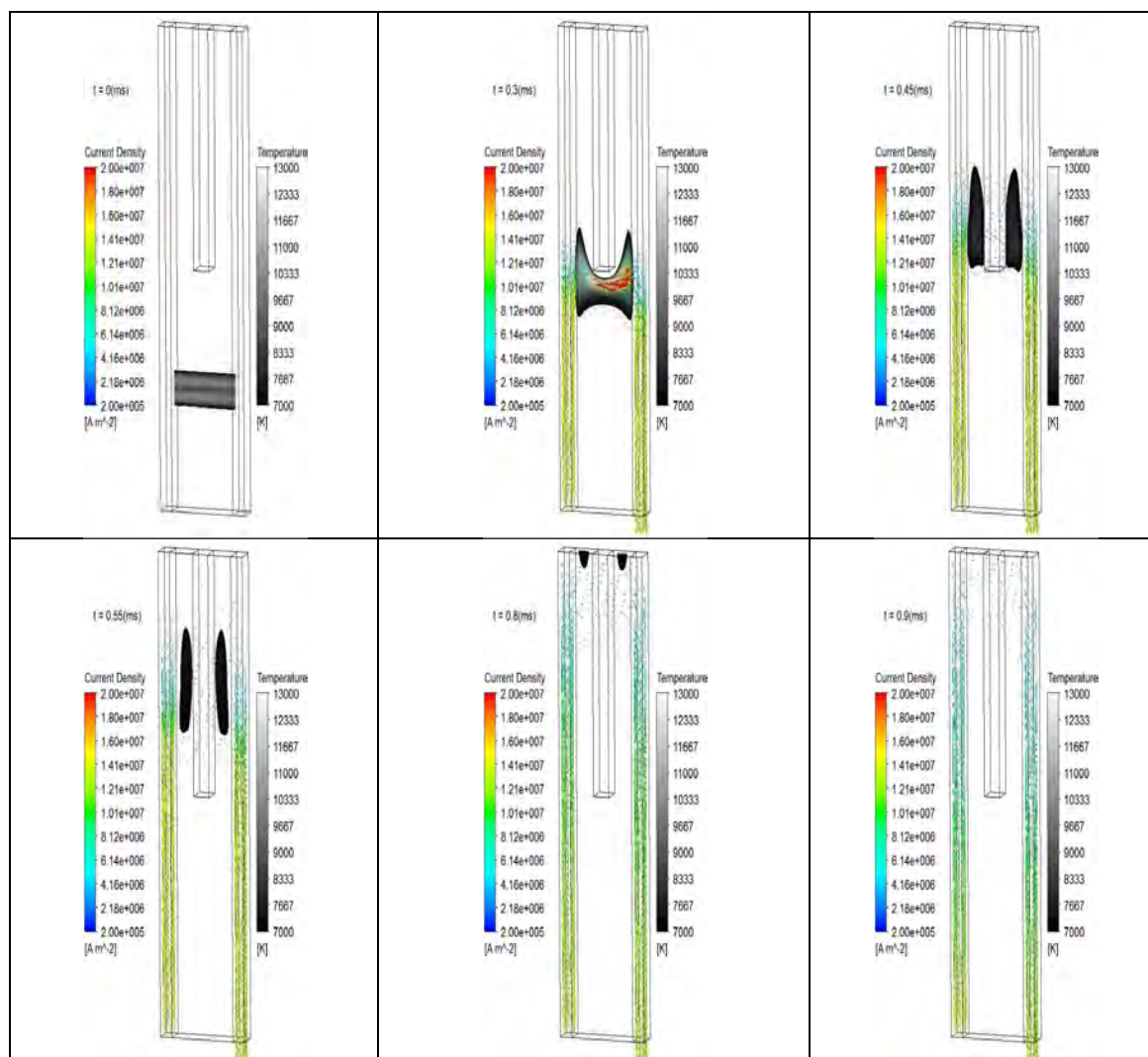


Figure 5-57 Arc movement expressed by temperature and current density 50A input current, 1SP and constant Ohmic resistance, case E.1

### 5.4.5.2   Comparative analysis

Results obtained in cases E.1 and A are shown in Figure 5-58 and Figure A-41 to Figure A-44. Figure 5-58 shows that the arc voltage in case E.1 is smaller than in case A, which leads to the following conclusion: the ohmic resistance application is correctly working, because when its value is changed a direct effect on the arc is observed. Thus, it is not the model but the input data considered which is not working correctly in case A. Therefore, as it has been stated, data from Figure 5-19 and consequently Figure 5-20 and Figure 5-21 should be reviewed.
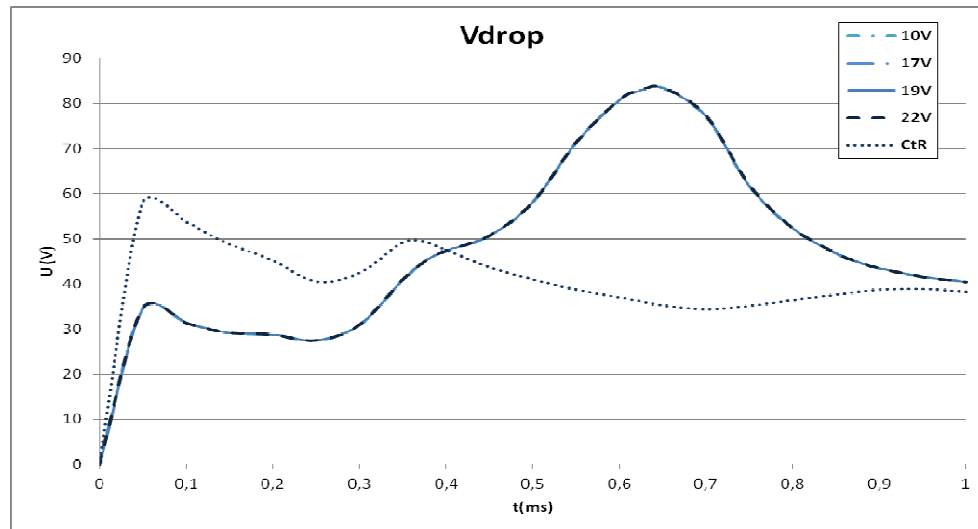
Figure 5-58 Voltage drop in the arc for 50A case E.1 (CtR) and the four case from case A (10V, 17V, 19V, 22V), case E

## 5.5    CONCLUSIONS

In this chapter, a new electric arc model for LVCBs has been proposed. The new model has been built based on reference [3] and the aim has been to include improvements on that previous model. This way, the new model built is a 40x11x2.5mm$^3$ chamber, with four domains (air, splitter plate, cathode and anode) where the electric arc is ignited at 10mm from the lower face of the chamber, as a hot channel at 10000K. The improvements that have been included in the new model are the following:

- A full 3D geometry where symmetry is not taken into account
- A fine hexahedral mesh of around 1000000 nodes
- Updated data for air properties
- Accurate radiation P1 model
- Vector magnetic potential formulation

Considering those improvements, the new arc model is presented in case A of this chapter. There, the four options presented in the reference model for arc root modelling [3] are considered, obtaining in the four cases just the same results for the new proposed model. This is explained by the operating point of those four curves in the present simulation. As said the current density magnitude around the plate is around 10$^7$ for the four cases and lead to the same voltage drop and therefore to the same ohmic resistance value for all of them.

The difference between the reference model and the new proposed model can be attributed to the symmetry simplification and a poor mesh quality in the reference model. Besides, from that first comparison, it can be said that in the new model the arc displacement is more constricted.

After the new model has been defined and compared with the reference one, several modifications and further tests have been developed. Following, the most relevant aspects are pointed out:

- In case B, the effect of splitter plates in the chamber has been analyzed, with the double aim of proving that the new model behaves according to the theoretical knowledge regarding arc, and to corroborate that the greater the number of splitter plates in the chamber, the better the interruption of the arc. This way, the model already proved for

one splitter plate (1SP) has been modified to consider zero splitter plate (0SP) and two splitter plates (2SP). Simulation shows that the voltage drop decreases when the number of splitter plates decreases and the opposite. Also, it has been proved that the interruption time increases when the number of splitter plates decreases.

- In case C, changes in the arc ignition location and input current value have been introduced, for a further validation of the new arc model proposed with real experimental data (chapter 6). In this case, the following conclusions can be extracted from those two modifications:

  – The arc ignition location has a great impact on the arc movement. The lower the ignition is, the less air volume below the arc and the slower the movement of the arc will be. Consequently, the interruption process will be longer. Therefore, an upper arc ignition is desirable for an optimal arc interruption.

  – The input arc current has also a direct and great impact on the arc development. As expected, the higher the current, the greater the diffusion of the arc. Also, its expansion movement is faster.

- Once the robustness of the new model has been proved, changes in the chamber geometry have been made, in order to analyze their impact on the arc movement and interruption. The modifications proposed for case D have consisted on: adding an expansion volume in the upper side of the chamber; shortening the distance between the down wall of the air and the beginning of the splitter plate, taking the lower face of the chamber higher; and finally lengthening the electrodes in the lower part. All these changes have not shown better performance and the influence performed on the arc displacement has been negative. Thus, those geometrical changes in the chamber can be taken into account for not being applied in new designs of LVCBs.

- Finally, in case E, another reference data for different ohmic resistance applied in the splitter plate has been tested. There, it has been proved that the model works properly but the data have to be reviewed.

Therefore, the new developed model reproduces adequately the general behaviour of the electric arc in LVCBs and so, it can be considered a good and robust model for electric arc analysis in LVCBs, as it will be validated in chapter 6.

# CHAPTER 6

## VERIFICATION AND VALIDATION OF THE NEW MODEL

6.1.- INTRODUCTION
6.2.- VERIFICATION OF THE MODEL
6.3.- VALIDATION OF THE MODEL
6.4.- CONCLUSIONS

# 6    VERIFICATION AND VALIDATION OF THE NEW MODEL

## 6.1    INTRODUCTION

This chapter presents the verification and validation processes of the new model proposed in chapter 5, for the analysis of the electric arc in LVCBs. Verification and validation can be considered separate activities to test the performance of a computational model, quantifying the uncertainty in a Computational Fluid Dynamics (CFD) simulation.

Verification means to take into account numerical errors, i.e. it is a code problem, so it relies on the mathematical side of the problem. According to [88], verification is the process of determining that a model implementation accurately represents the developer's conceptual description of the model.

In contrast, validation has to do with the scientific side of the analysis. It can be defined as the process of giving credibility to the simulation model, determining whether the domains, boundary conditions and, in general, the physics have been correctly defined [89].

For the new model proposed, verification process has been performed with mathematical tools, calculating errors and deviations for different mesh sizes and timespteps. Three different meshes have been tested, and the most appropriate one has been selected for the model presented in chapter 5. The three meshes tested have been hexahedral, with good quality parameters but with different densities: Low density (LD), medium density (MD) and high density (HD). The density of the mesh is related to the total number of nodes per volume in the mesh. Thus, the mesh with the better performance between precision and computational time has been selected (MD mesh).

Also, three timesteps have been tested on the same model. Once again, the timestep presenting better agreement between precision and computational time has been chosen $(2,5x10^{-6}s)$.

Besides, the same model has been analyzed for the three different radiation models presented in chapter 4, NECS, NEC and P1. Comparing the results obtained, it is concluded that P1 has a better and more precise behaviour in the electric arc model.

Finally, the validation process in the new model has been developed by comparing the simulation results obtained for case C (chapter 5) with a set of results obtained from real experimental tests. These experimental tests have been carried out in the laboratory of the Technical University of Ilmenau (Germany), having developed the following tests: Low arc ignition, for 50, 100 and 200A input currents, for geometries with 0SP and 1SP (according to case C, chapter 5).

After this validation process, it can be said that the new model developed in this thesis fulfils qualitatively the arc movement represented by the experimental data.

## 6.2    VERIFICATION

### *6.2.1 METHODOLOGY*

In all the steps involved in a CFD analysis, a certain amount of uncertainties and errors can arise depending on the complexity of the model. An uncertainty is generally defined as a potential deficiency of the computational model. This deficiency can arise either due to the lack of knowledge of the user, regarding the simulation tool or the value of some parameters, or due to the complexity of the physical process itself. An error is defined as recognizable deficiencies that are usually not caused by the lack of knowledge. In [90], a good description of all types of errors that may arise in a CFD computation can be found, structured as:

- Acknowledged errors: discretization or numerical errors, iteration or convergence errors and round-off errors
- Unacknowledged errors: user errors and code errors

Some of these errors, as iteration and round-off errors, are well understood and handled nowadays. But some problems may still arise in a computational model due to discretization errors. Being the fundamental purpose of the verification process the identification and quantification of the error in the computational model and its solution, this is usually done by comparing the solver results against highly accurate or different benchmark solutions. However, in the case of highly complex models or coupled problems, as the electric arc, this approach cannot be followed.

One of the main sources for errors in the verification process is the spatial and temporal discretization. Thereby, in order to perform the verification of a computational model, a systematically refinement of the grid size and the timestep is necessary. This way, the user can estimate the discretization error of the numerical solution and find the most suitable grid size and timestep. As both, cell size and timestep, approach to zero, the discretization error should also approach to zero. In [91], the authors have used a traditional error convergence analysis where the dependency between the exact results, $\phi_e$, and the approximate solution, $\phi_{(h)}$, is given by equation (6-1).

$$\left\| \phi_e - \phi_{(h)} \right\| \leq C \cdot h^p \qquad\qquad (6\text{-}1)$$

where:
C:      constant
h:      measure of mesh discretization
p:      order of convergence.

The main drawbacks of this method are the fact that the constant C is generally unknown and hard to define for every configuration and that the error is determined globally, while in real problems this error can vary locally a lot.

Another approach widely used in the CFD scientific community to estimate the results for "zero" element length and time step is the Richardson's extrapolation [92]. This method allows obtaining higher order estimations of the continuum value, of a series of lower-order discrete values. In order to provide a consistent way for reporting the results from discretization studies, also in [92] the usage of the Grid Convergence Index (GCI) is proposed by Roache. This index indicates an error band on how far away is the given solution from the asymptotic value. The value of the GCI, for non uniform refinement ratio, is defined by equation (6-2).

$$GCI^{21} = \frac{F_s\, e_a^{21}}{r_{21}^p - 1}$$                    (6-2)

where:

$F_s$:     safety factor equal to 3 when only two meshes are used and to 1.25 when three or more meshes are used in the analysis.

$r_{21}^p$:     mesh refinement ratio

$e_a^{21}$:     relative error

p:     order of convergence

These coefficients are defined by equations (6-3) to (6-7).

$$r_{21} = \frac{h_2}{h_1}$$                    (6-3)

$$e_a^{21} = (f_1 - f_2)/(f_1)$$                    (6-4)

$$p = \frac{|ln|f_{32} + f_{21}| + q(p)|}{ln\, r_{21}}$$                    (6-5)

$$q(p) = ln\left(\frac{r_{21}^p - s}{r_{32}^p - s}\right)$$                    (6-6)

$$s = sign(f_{32} - f_{21})$$                    (6-7)

where:

$f_i$:     solutions for a variable f of the flow field

$h_i$:     measures for the mesh discretization

In order to determine the correct value of p, equations (6-5), (6-6) and (6-7) can be solved using a fixed point iteration method, with the initial guess $q(p) = 0$. In equation (6-6), parameter $r_{21}^p$ represents the mesh refinement ratio between meshes 1 and 2, while $r_{32}^p$ between meshes 2 and 3.

Additionally, another parameter to evaluate the mesh density and timestep influence on the results obtained is the Courant-Friedrichs-Lewis (CFL) number, reported directly by the CFX solver [92, 93]. The CFL number is defined as shown in equation (6-8) and expresses the necessary condition for convergence of CFD problems, imposing the timestep criteria taking into account the velocity of the fluid flow and the density of the mesh.

$$CFL = \Delta t \sum_{i=1}^n \frac{u_{x_i}}{\Delta x_i}$$                    (6-8)

where:

u:     velocity of the fluid flow

Δt:     timestep

Δx:     mesh element length

The aim of this verification process has been to select the most appropriate mesh size and timestep for the model, and to evaluate the results obtained for the three mentioned radiation models (NECS, NEC and P1), selecting the most stable and realistic approach. For that aim, different simulations have been performed on the new model.

First of all, regarding the mesh size, three different meshes have been analyzed. Taking as reference a medium density mesh (MD), the mesh density has been increased to a high density mesh (HD) by multiplying the number of elements of the MD by 1.5, while the low

density mesh (LD) has been obtained by dividing the MD mesh by 2. The total number of elements obtained is presented in Table 6-1.

Table 6-1 Total number of elements for each mesh configuration

| Mesh | LD | MD | HD |
|---|---|---|---|
| Elements | 572273 | 1144546 | 1716819 |

For the timestep selection, three different timesteps have been considered for the analysis as shown in Table 6-2 ($1.25 \times 10^{-6}$, $2.5 \times 10^{-6}$ and $5 \times 10^{-6}$s). The additional data needed for the solver have been maintained constant, such as: the total simulation time, set as a transient run with a total simulation time of $1 \times 10^{-3}$s; the transient time scheme which has been selected as Second Order Backward Euler; the inner iteration numbers for each timestep, defined as 12 and the convergence criterion set to a Residual Target of $1 \times 10^{-4}$.

Besides, as said before, an additional analysis for the three different radiation models explained in chapter 4 has been carried out (NECS, NEC and P1).

Therefore, the influence of the timestep has been tested applying three different timesteps on the MD case, for the three radiation models. The influence of the mesh density has been tested applying three different mesh densities on the intermediate timestep case, $5.0 \times 10^{-6}$ s, for the three radiation models also. Thus, as shown in Table 6-2, a total number of 15 cases have been analyzed: 9 for MD mesh with three different timesteps over the three radiation models, and another 6 for $2.5 \times 10^{-6}$s timestep with three mesh densities over the three radiation models.

Table 6-2 Overview of performed simulations

| Radiation model | Δt Mesh density | $1.25 \times 10^{-6}$s | $2.5 \times 10^{-6}$s | $5.0 \times 10^{-6}$s |
|---|---|---|---|---|
| NECS | LD | | X | |
| NEC | MD | X | X | X |
| P1 | HD | | X | |

## 6.2.2 VERIFICATION RESULTS

In this section, the results obtained for the indexes CFL and GCI selected to analyze the results are shown. The variable taken as reference parameter has been the temperature. Thus, two values have been adopted: maximum value and volume average value of the temperature in air. The first one gives back the maximum temperature data existing in any cell of the selected domain and the second one makes a volume-weighted average of the temperature over all the cells of the chosen domain, air in the case considered.

As the tests have been performed considering the three radiation models, over different changes on mesh density and timestep, results are shown following that structure, in order to make the analysis clearer.

### 6.2.2.1 Mesh density influence

The tests performed on the new proposed model, with a constant timestep of $2.5 \times 10^{-6}$s and changing the mesh size over the three radiation models are presented and analyzed. Overall

results for each radiation model at different mesh densities are shown in Table 6-3 to Table 6-5

Table 6-3 Overall results for NECS radiation model, for different mesh densities

| NECS | Results | | |
|---|---|---|---|
| Mesh Density | LD | MD | HD |
| Max CFL | 55.4 | 44.2 | 17.6 |
| RMS CFL | 3 | 2.5 | 2 |
| Residual | $1.0 \times 10^{-3}$ | | |
| Total Computational time [s] | $9.840 \times 10^{4}$ | $1.709 \times 10^{5}$ | $3.153 \times 10^{5}$ |
| Total Computational time [d:h:m:s] | 1:03:20:1 | 1:23:28:19 | 3:15:35:33 |
| Computational time per Timestep [s] | 246.0 | 427.3 | 788.3 |
| Total number of Timesteps | 400 | 400 | 400 |

Table 6-4 Overall results for NEC radiation model, for different mesh densities

| NEC | Results | | |
|---|---|---|---|
| Mesh Density | LD | MD | HD |
| Max CFL | 18.7 | 17.9 | 20.7 |
| RMS CFL | 1.4 | 1.3 | 1.8 |
| Residual | $1.0 \times 10^{-3}$ | | |
| Total Computational time [s] | $9.80 \times 10^{4}$ | $2.15 \times 10^{5}$ | $2.62 \times 10^{5}$ |
| Total Computational time [d:h:m:s] | 1:03:13:07 | 2:11:43:11 | 3:00:24:24 |
| Computational time per Timestep [s] | 245.0 | 537.5 | 655.0 |
| Total number of Timesteps | 400 | 400 | 400 |

Table 6-5 Overall results for P1 radiation model, for different mesh densities

| P1 | Results | | |
|---|---|---|---|
| Mesh Density | LD | MD | HD |
| Max CFL | 11.5 | 11.1 | 12.3 |
| RMS CFL | 1.3 | 1.2 | 1.9731 |
| Residual | $1.0 \times 10^{-3}$ | | |
| Total Computational time [s] | $1.39 \times 10^{5}$ | $2.94 \times 10^{5}$ | $4,27 \times 10^{5}$ |
| Total Computational time [d:h:m:s] | 1.14:40:15 | 3:09:38:38 | 4:22:34:38 |
| Computational time per Timestep [s] | 348.0 | 734.8 | 1067.3 |
| Total number of Timesteps | 400 | 400 | 400 |

Attending to the computational time of each simulation, that simulation takes longer time the higher the density of the mesh, i.e., HD model takes longer time to be solved than MD, and this one takes longer time than LD, which makes sense, as the number of nodes increases. Besides, it can be noticed that the computational time for P1 radiation model is longer than for the other two radiation models. Additionally, between NECS and NEC the difference is not so clear. While in the case of LD and HD, computational time is almost the same for NECS and NEC cases, at MD case, the simulation time is surprisingly higher for NEC than for NECS case.

These results can be explained considering that the simulation time is not only related to the difficulty of the mathematical solution or the number of nodes, but also with the stability.

This way, sometimes worse stability leads to worse times, as the convergence is more difficult to reach.

Another factor shown in the previous tables is the CFL parameter. The value increases as the precision of the radiation model decreases, i.e., NECS has bigger CFL numbers than NEC, and NEC bigger ones than P1, which shows instability for those models with higher CFL values. Besides, a different pattern regarding the mesh for NECS, NEC and P1 cases, analyzing the CFL number is observed. In NECS case, the higher the mesh density is, the lower the CFL. But for NEC and P1 cases, the best option is the MD case.

Anyway, for a better analysis not only the maximum CFL numbers but the whole values along the simulation have to be considered. Figure 6-1 to Figure 6-6 show that the most bouncy and unstable simulation is obtained with the NECS radiation model, where the CFL rms values are completely bouncy (Figure 6-2) and the CFL max has the highest peaks (Figure 6-1).

In NEC radiation model case, the CFL numbers are also bouncy. But, for MD and HD densities, they follow the same trend. However, in the LD case, the values and the trend are completely different (Figure 6-3 and Figure 6-4).

Finally, for the P1 model, the trends for the three meshes are very similar for both CFL numbers, rms and max, and the bouncing is lower than in the previous cases (Figure 6-5 and Figure 6-6). Again, the most different one is the LD mesh case.
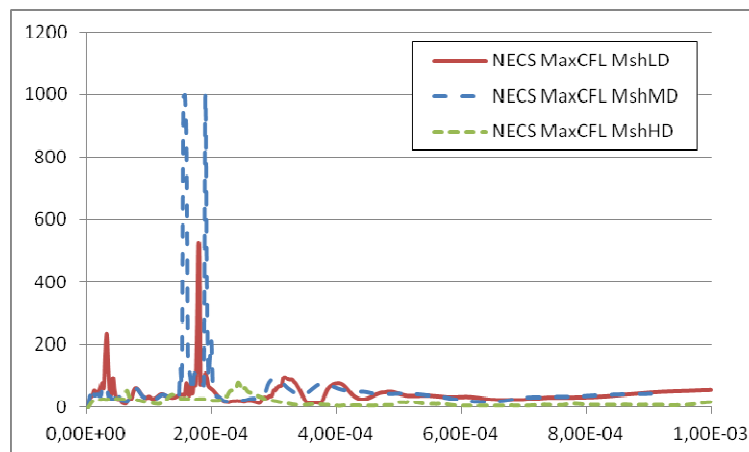


Figure 6-1 CFL max for NECS radiation model, for different mesh densities
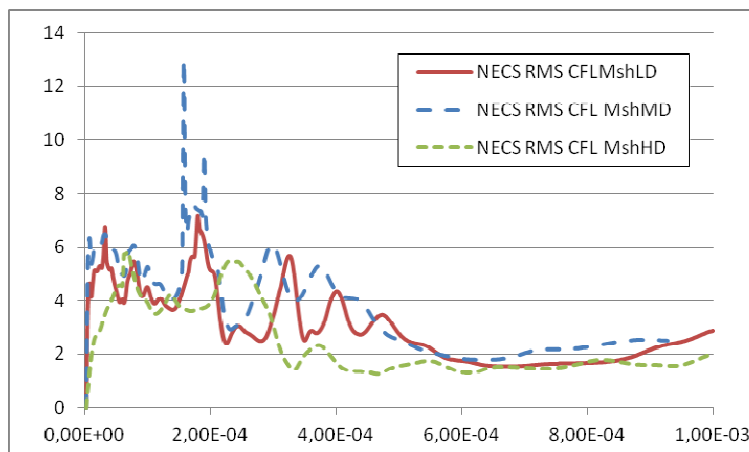


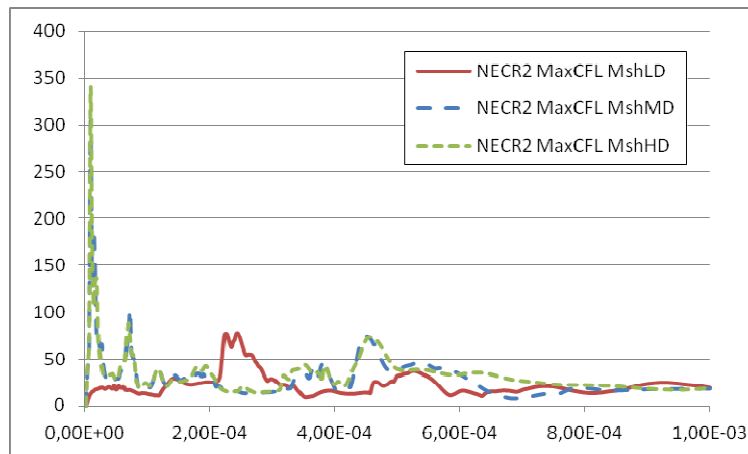Figure 6-2 CFL rms for NECS radiation model, for different mesh densities

Figure 6-3 CFL max for NEC radiation model, for different mesh densities
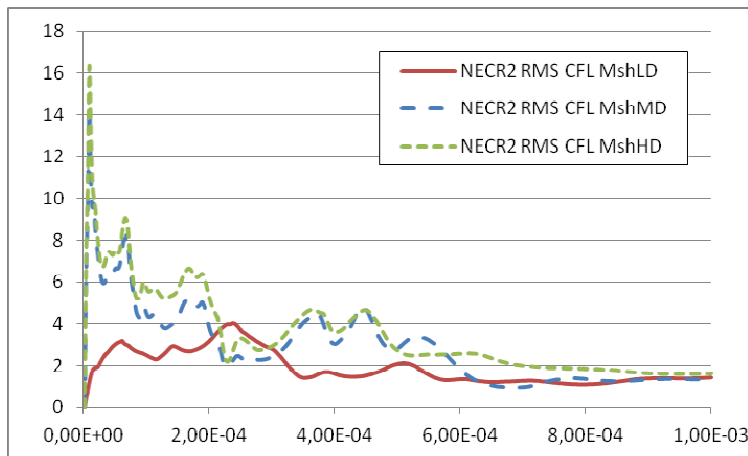


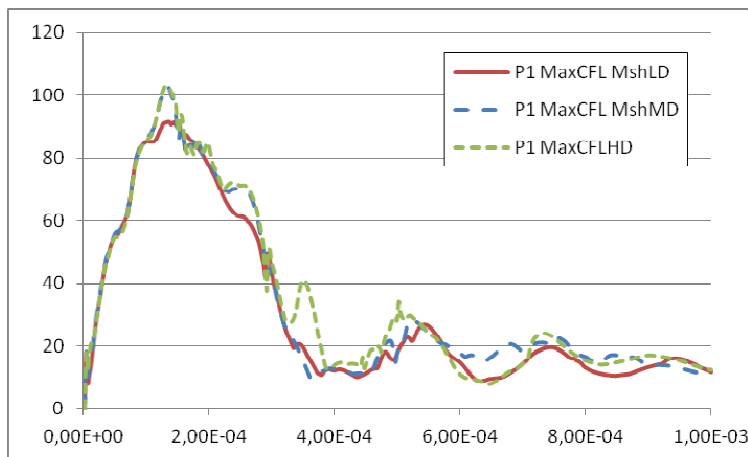Figure 6-4 CFL rms for NEC radiation model, for different mesh densities



Figure 6-5 CFL max for P1 radiation model, for different mesh densities
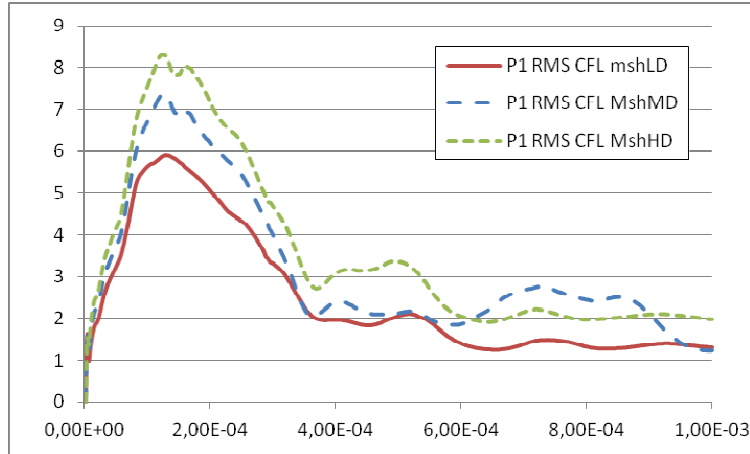
Figure 6-6 CFL rms for P1 radiation model, for different mesh densities

Analyzing the average values of maximum CFL ($CFL_{max}$) and root mean square CFL ($CFL_{rms}$), it can be observed in Table 6-6 that the most unstable case is again obtained with the NECS radiation model. For example, the $CFL_{max}$ value that has been reached for the MD mesh in the NECS configuration is $CFL_{max}$=53.22 which has a smaller value for NEC or P1 cases.

The same pattern is repeated for $CFL_{rms}$ parameter with higher values for NECS configuration than for NEC or P1. Thus, it can be concluded that the NECS radiation model is, by far, the worst option.

Table 6-6 Average value of CFLmax and CFLrms, for different mesh densities

|      |    | Ave(CFL$_{max}$) | Ave(CFL$_{rms}$) |
|------|----|------------------|------------------|
|      | LD | 42.53 | 2.92 |
| NECS | MD | 53.22 | 3.58 |
|      | HD | 15.17 | 2.36 |
|      | LD | 21.79 | 1.87 |
| NEC  | MD | 27.58 | 2.87 |
|      | HD | 31.43 | 3.46 |
|      | LD | 30.78 | 2.48 |
| P1   | MD | 32.91 | 3.18 |
|      | HD | 33.95 | 3.58 |

Following with the verification parameters, the GCI coefficient is analyzed. Table 6-7 shows the average value of GCI values obtained for the three radiation models, for the whole simulation time.

Table 6-7 Average value of GCI parameter, for maximum and volume average temperature

|      | Ave(GCI T$_{max}$) | Ave(GCI T$_{VolAve}$) |
|------|--------------------|------------------------|
| NECS | 0.098 | 0.00021 |
| NEC  | 0.268 | 0.0096 |
| P1   | 0.14  | 0.042 |

The GCI values obtained as a function of time are in the same range and show some regions of instabilities at different time points, as can be seen in Figure 6-7.
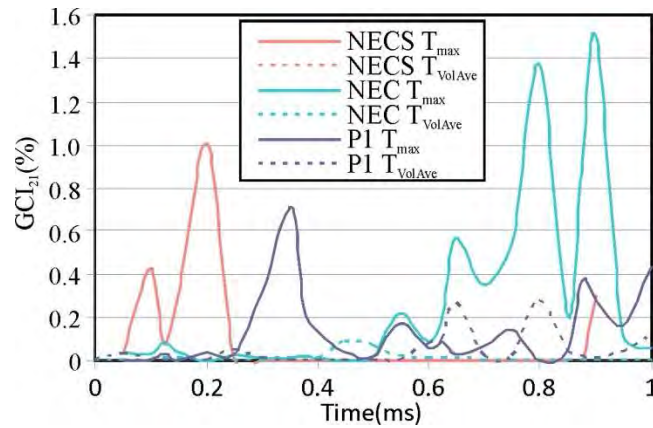
Figure 6-7 GCI coefficients obtained for the maximum and volume average temperature, obtained by performing a mesh density study

These results can be better explained by analyzing the volume average temperature trends used for calculation, presented in Figure 6-8 for NEC and P1 radiation models. For NEC case, a similar behaviour for the MD and HD meshes has been obtained, but the values computed for the LD mesh are lower. However, for P1 case the values for LD, MD and HD show the same behaviour. Therefore, the most stable solution is given by the P1 model.
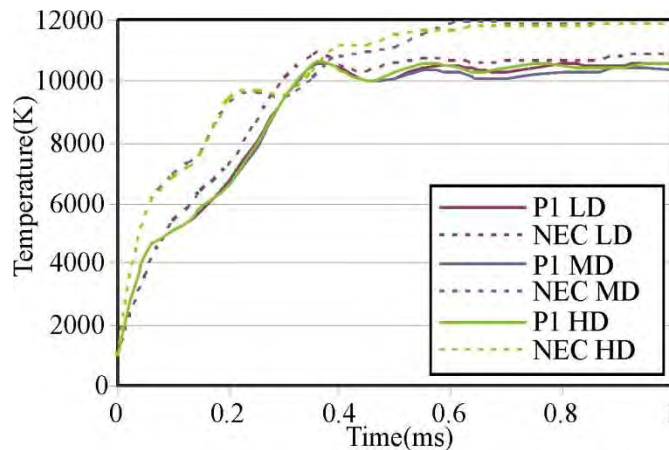


Figure 6-8 Transient volume average temperature behaviour for the P1 and NEC radiation models, by changing the mesh density

Concluding, the NECS radiation model is the most unstable of the three models analyzed. On the other hand, the P1 model is the one that gets better results in every case. Regarding the mesh density, LD has proved to be very unstable. Between MD and HD, it could be expected that HD should provide better results, but for the P1 model both MD and HD meshes show a similar behaviour (Figure 6-8). Also, MD has better CFL numbers and better computational time than HD. Thus, P1 and MD combination has been identified as the most efficient and stable choice for the new model developed in this thesis.

### 6.2.2.2 Timestep influence

Regarding the timestep influence, the overall results shown in Table 6-8 to Table 6-10 are obtained for the three different radiation models, all of them with MD mesh density but with three different timesteps.

Table 6-8 Timestep influence NECS-MD

| NECS radiation model – MD | Results | | |
|---|---|---|---|
| Timestep Δt [s] | $1.25 \times 10^{-6}$ | $2.50 \times 10^{-6}$ | $5,00 \times 10^{-6}$ |
| Max CFL | 28.7 | 44.2 | 88.8 |
| RMS CFL | 2 | 2.5 | 5 |
| Residual | $1.0 \times 10^{-3}$ | | |
| Total Computational time [s] | $3.555 \times 10^{5}$ | $1.709 \times 10^{5}$ | $1.075 \times 10^{5}$ |
| Total Computational time [d:h:m:s] | 4:02:45:24 | 1:23:28:19 | 1:05:50:51 |
| Computational time per Timestep [s] | 444.4 | 427.3 | 537.5 |
| Total number of Timesteps | 800 | 400 | 200 |

Table 6-9 Timestep influence NEC-MD

| NEC radiation model – MD | Results | | |
|---|---|---|---|
| Timestep Δt [s] | $1.25 \times 10^{-6}$ | $2.50 \times 10^{-6}$ | $5,00 \times 10^{-6}$ |
| Max CFL | 8.7 | 17.9 | 10.4 |
| RMS CFL | 0.7 | 1.3 | 2.5 |
| Residual | $1.0 \times 10^{-3}$ | | |
| Total Computational time [s] | $3.68 \times 10^{5}$ | $2.15 \times 10^{5}$ | $1.08 \times 10^{5}$ |
| Total Computational time [d:h:m:s] | 4:06:13:14 | 2:11:43:11 | 1:06:2:17 |
| Computational time per Timestep [s] | 460.0 | 537.5 | 540.5 |
| Total number of Timesteps | 800 | 400 | 200 |

Table 6-10 Timestep influence P1-MD

| P1 radiation model – MD | Results | | |
|---|---|---|---|
| Timestep Δt [s] | $1.25 \times 10^{-6}$ | $2.5 \times 10^{-6}$ | $5.00 \times 10^{-6}$ |
| Max CFL | 29.6 | 11.1 | 27.5 |
| RMS CFL | 2.4 | 1.2 | 3.7 |
| Residual | $1.0 \times 10^{-3}$ | | |
| Total Computational time [s] | $5.39 \times 10^{5}$ | $2,94 \times 10^{5}$ | $1.16 \times 10^{5}$ |
| Total Computational time [d:h:m:s] | 6:05:43:17 | 3:09:38:38 | 1:08:07:27 |
| Computational time per Timestep [s] | 688.1 | 734.8 | 578.0 |
| Total number of Timesteps | 800 | 400 | 200 |

From the data shown in these tables, it can be said that the smaller the timestep, the higher the computational time, i.e. $1.25 \times 10^{-6}$s involves higher computational time than the others, for all the radiation cases. Also, it can be noticed that the more complex the radiation model, the higher the computational time, i.e., computational times for P1 are longer than for NEC and NECS.

Moreover, considering the behaviour of the CFL number, it can be pointed out that the smaller the timestep, the smaller the CFL number, which means better behaviour for the model (NECS and NEC cases). This way, the option of $1.25 \times 10^{-6}$s gives better results than $2.5 \times 10^{-6}$s and $2.5 \times 10^{-6}$s better than $5 \times 10^{-6}$s. However, for P1 case the best results are obtained for the timestep of $2.5 \times 10^{-6}$s.

Also, the CFL values obtained and represented in Figure 6-9 to Figure 6-14 show a stronger dependency with the change in the timestep size. In fact, the dependency is bigger in the case of the variation of the mesh density. The highest values are recorded during the arc

expansion process, between 0.1(ms) and 0.35(ms), when the arc starts to move towards the splitter plate. This gives an idea about when the biggest instabilities of the model are produced.
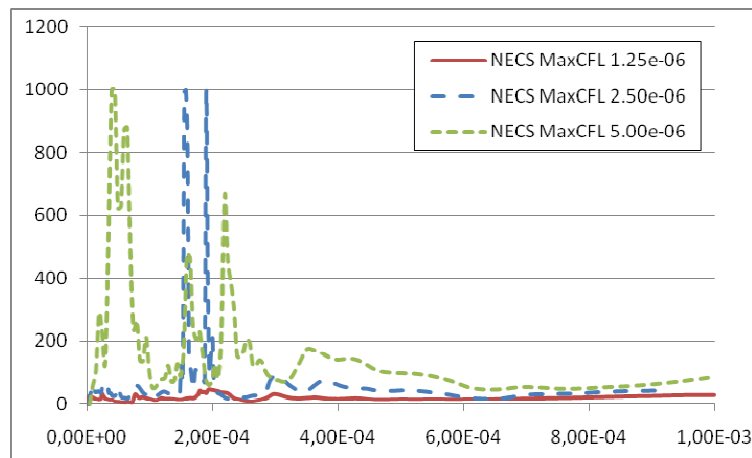


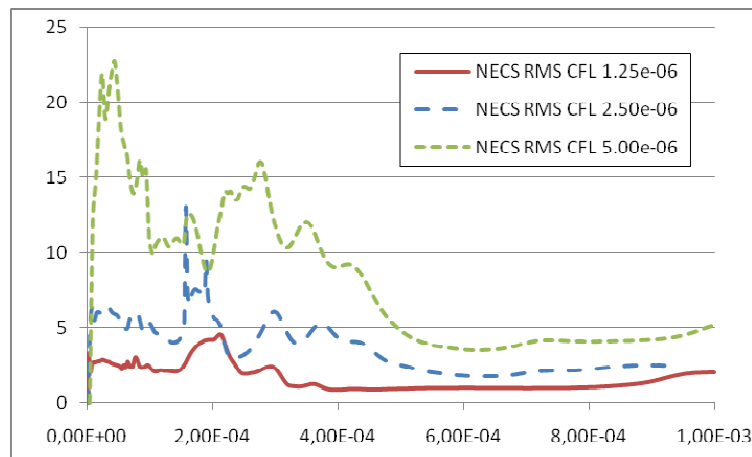Figure 6-9 CFLmax for NECS radiation, for different timesteps



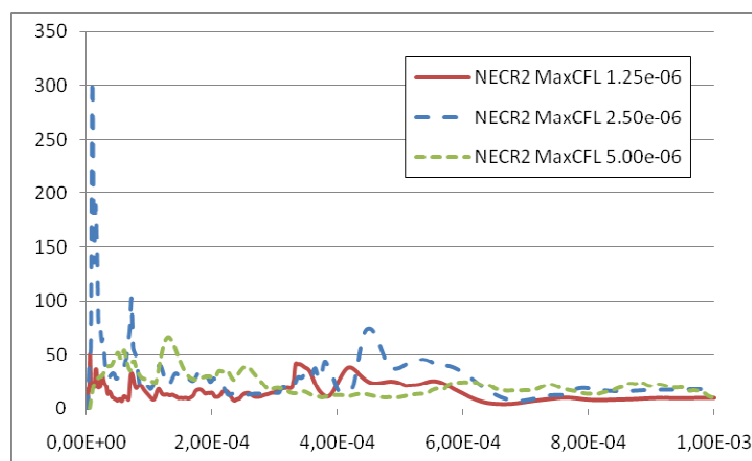Figure 6-10 CFLrms for NECS radiation, for different timesteps



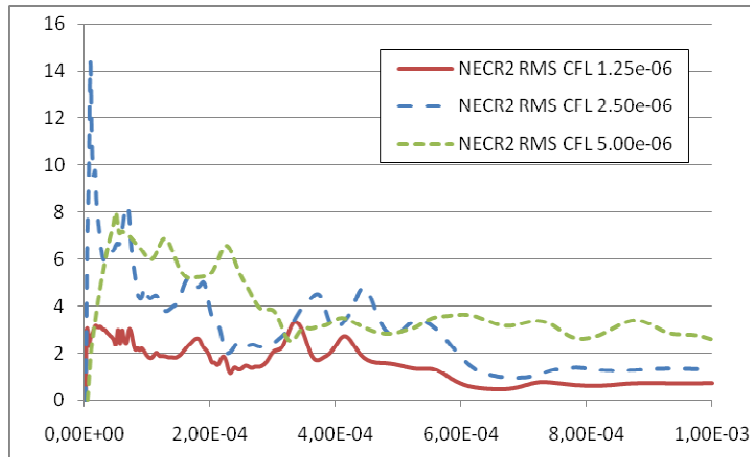Figure 6-11 CFLmax for NEC radiation, for different timesteps

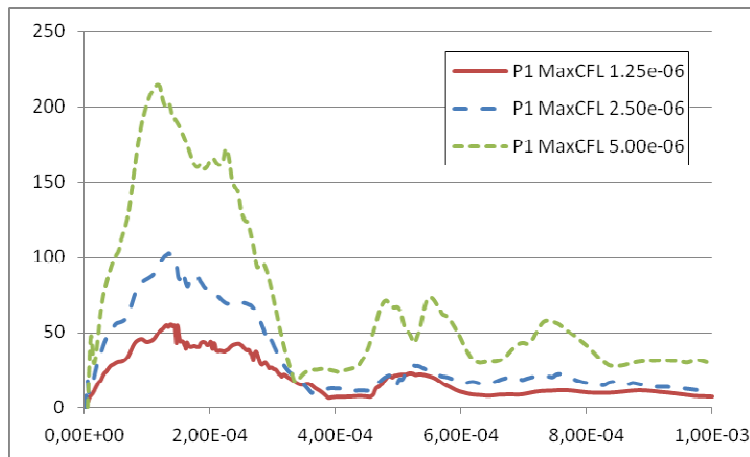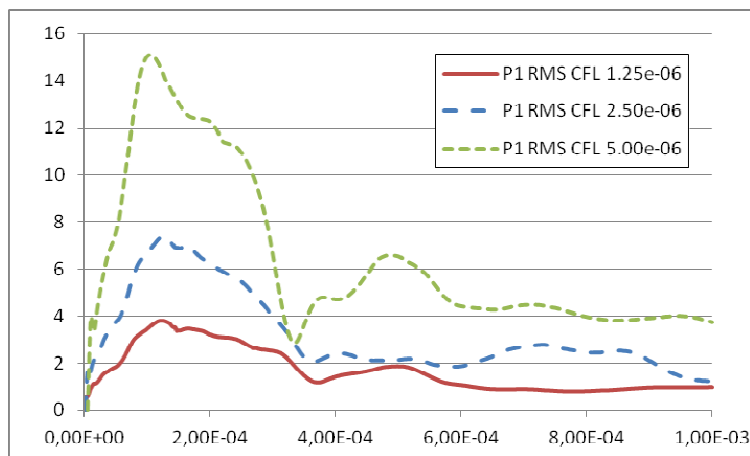Figure 6-12 CFLrms for NEC radiation, for different timesteps


Figure 6-13 CFLmax for P1 radiation, for different timesteps


Figure 6-14 CFLrms for P1 radiation, for different timesteps

Analyzing the average value of the CFL data, Table 6-11 shows that the most unstable case is again given by the NECS radiation model. In all cases both CFL values, maximum and rms, are higher for the NECS case than for NEC or P1 cases, no matter the timestep. Besides, another fact observed is that between the values for NEC and P1, the values for P1 radiation models are overall slightly higher, which makes P1 to be the best option.

Table 6-11 Average value of CFLmax and CFLrms for different timesteps and different radiation models for MD mesh model

| Timestep[s] | $1,25 \times 10^{-6}$ | | $2,5 \times 10^{-6}$ | | $5,0 \times 10^{-6}$ | |
|---|---|---|---|---|---|---|
| Coefficients / Radiation | $Ave(CFL_{max})$ | $Ave(CFL_{rms})$ | $Ave(CFL_{max})$ | $Ave(CFL_{rms})$ | $Ave(CFL_{max})$ | $Ave(CFL_{rms})$ |
| NECS | 20 | 1.7 | 53.22 | 3.58 | 132 | 7.9 |
| NEC | 15.2 | 1.4 | 27.58 | 2.87 | 22.3 | 3.8 |
| P1 | 19.5 | 1.7 | 32.91 | 3.18 | 70 | 6.4 |

In order to clarify these results, the time evolution trends of volume average temperature for P1 and NEC are shown for the three different timesteps (Figure 6-15). As the temperature trends for the three different timesteps for P1 radiation model have the same behaviour, it is clarified that P1 is the most stable option.
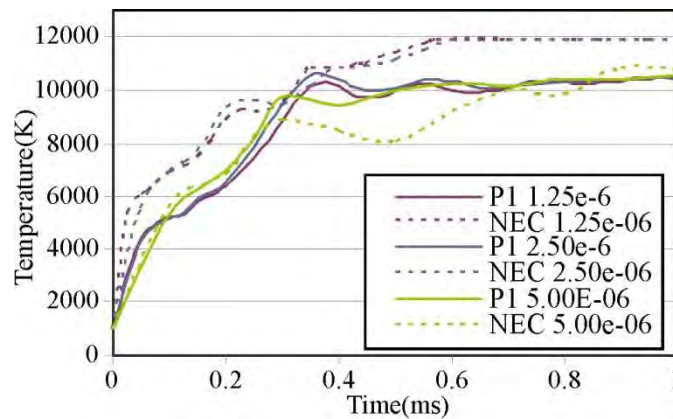


Figure 6-15 Transient volume average temperature behaviour for NEC and P1 radiation models, at three different timesteps

Regarding GCI coefficient values, results obtained for the GCI values of maximum and volume average temperature are presented in Figure 6-16 and Table 6-12. Again, the highest instabilities can be observed for the NECS case, while for the NEC and P1 cases the values of the GCI coefficients are smaller and ranging up to a maximum of 1, at 0.25ms (Figure 6-16). Those value differences between NECS, NEC and P1 can also be noticed in Table 6-12.
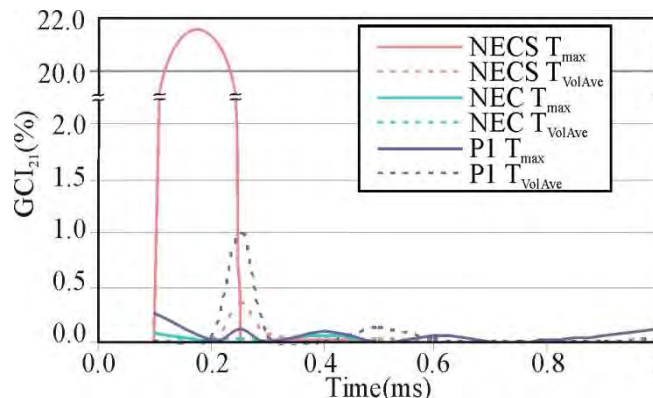


Figure 6-16 GCI coefficients for the maximum and volume average temperature for the three radiation models

Table 6-12 Average CGI for maximum and volume average temperature variable for the three radiation models

|      | Ave(GCI-$T_{max}$) | Ave(GCI-$T_{VolAve}$) |
|------|------|------|
| NECS | 2.31 | 0.044 |
| NEC  | 0.013 | 0.004 |
| P1   | 0.06 | 0.0104 |

Regarding the time behaviour of the GCI coefficient (Figure 6-16), as the CFL coefficients have previously indicated, a region of high instability up to 0.3ms can be observed, especially for the NECS values, in case of the maximum temperature, and for P1 values of the volume average temperature.

To summarize, after analyzing the overall behaviour of the simulation, its computational time, GCI and CFL parameters, it can be concluded that the most effective and precise results are obtained with P1 radiation model, where smaller GCI and CFL parameters are obtained. On the other hand, regarding the mesh and timesteps analysis, the poorest selection is LD mesh density and 5.0e-06s timestep, due to the instability and high CGI and CFL coefficients presented. Additionally, the computational time shows that MD and $2.5 \times 10^{-6}$s options are good enough for a not computationally expensive but precise model. Thus, the option chosen for the new model proposed in this thesis is a MD mesh density, with P1 radiation model and timestep of $2.5 \times 10^{-6}$s which leads to a computational time around four days.

## 6.3    VALIDATION

To validate the new model, a set of experimental tests has been developed at Technical University of Ilmenau (Germany). In particular, a total of six different tests have been carried out, with three different input current values (50A, 100A and 200A) and two different geometries (arc chamber without splitter plate (0SP) and with one splitter plate (1SP)). In all the tests (Table 6-13), the arc has been ignited at 1mm above the down wall of the air (low ignition).

Table 6-13 Experimental tests overview

| Model \ I(A) | 0 Splitter Plate (0SP) | 1 Splitter Plate (1SP) |
|------|------|------|
| 50   | X | X |
| 100  | X | X |
| 200  | X | X |

These six tests correspond to simulation cases denoted as case C, described in chapter 5. This way, it has been possible to validate the performance of the new model developed in this thesis.

### 6.3.1   LABORATORY SETUP

The experimental setup for the laboratory tests consists of the elements shown in Figure 6-17. First of all, an impulse generator, which provides and impulse waveform 10/350, with a maximum charging voltage of 10kV, has been used to provide the arc current. This impulse generator includes a DC source of 10kV maximum, two capacitors of 250μF each, in parallel with the source, and one inductance and two resistors in series. The inductance has a value of $L_{gen}$=5μH and the resistors $R_d$=9Ω and $R_e$=160kΩ.
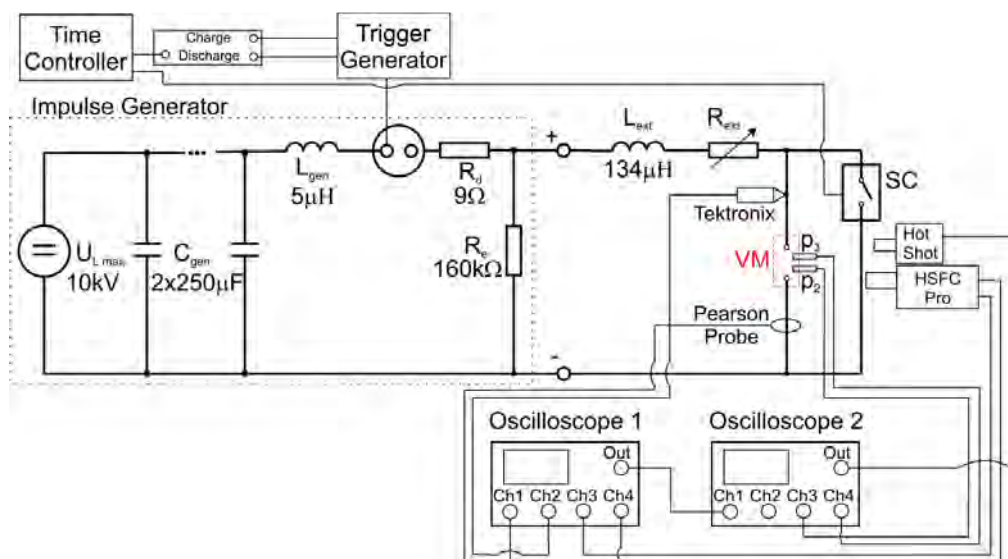
Figure 6-17 Scheme of the electrical circuit and measurement system used in the laboratory tests

The generator discharges over the series connection of the inductance $L_{ext} = 134\,\mu H$ and a variable resistance $R_{ext}$, at a given time specified in the Time Controller. Depending on the charging voltage and the value chosen for the variable resistor $R_{ext}$, different amplitudes of currents can be generated and applied in the experimental circuit. The current obtained has a small delay over time, allowing the testing of the desired configuration under DC arc conditions.

In order to protect the chamber for long arcing times, a normally open contactor is placed (SC) in parallel with the experimental setup. The contactor can be closed with a signal from the Time Controller.

The LCVB chamber is shown in the scheme in red colour and named as VM. Near the chamber, in order to record the evolution of the arc and the electrical magnitudes during the test, the following measurement equipment has been added to the circuit:

- Two high-speed cameras. Hot Shot high speed video camera and HSFC Pro high speed photo camera, located in the right side of the scheme and focusing directly to the arc chamber.
- Ampere meter. Pearson probe (division rate 1:1000), connected to the anode to measure the input current.
- Voltmeter. Tektronix probe P1065A (division rate 1:1000), connected in parallel with the arc chamber.
- Two pressure sensors. PCB Piezoelectrics sensors (p2 and p3) at 15 and 28mm above lower inlet (division rate 734 mV/bar).
- Two oscilloscopes. They are shown in the low side of the scheme as Oscilloscope 1 and Oscilloscope 2. In order to record the signals, the measured current form has been used as trigger for "Oscilloscope 1". The output signal of this "Oscilloscope 1" has been used, at the same time, as trigger signal for "Oscilloscope 2" where the pressure signals obtained from the piezoelectric pressure sensors have been recorded. Their characteristics are LeCroy, with a maximum recording rate of 5GS/s, to record the signals from the ampere meter, voltmeter and pressure sensors.

The settings for the measurement equipment used in the experimental set up for the tests are described in Table 6-14. However, the measures from the oscilloscopes have already been converted to real magnitude values in the data shown in the following subsection

Table 6-14 Settings for the measurement equipment

|      | Oscilloscope 1 | Oscilloscope 2 | HSFC Pro | HotShot |
|------|----------------|----------------|----------|---------|
| Ch1  | Tb:0.5ms/div 50V/div –trig. Offset: -150V | Tb:0.5ms/div 2V/div-trig. | Trig: extern Delay: 50000ns Opening t: 10ns Gain: 0dB | |
| Ch2  | 50V/div Offset: -150V | 2V/div | Trig: extern Delay: 200000ns Opening t: 10ns Gain: 0dB | Frames Per Second: 20000 Aperture:1/200000 Pict Size: 512x96 Trigg: Center 50% Noise: 0dB |
| Ch3  | 2V/div Offset: -6V | 180mv/div Offset: -546mV | Trig: extern Delay: 600000ns Opening t: 10ns Gain: 0dB | |
| Ch4  | 2V/div Offset: -6V | 180mv/div Offset: -546mV | Trig: extern Delay: 1000000ns Opening t: 10ns Gain: 0dB | |

The charging voltage of the generator and the chosen resistance for each value of the experimental current are presented in Table 6-15, for the different current values used in the tests.

Table 6-15 Test current values considering the charging voltage and the external resistance

| 50A | 100A | 200A |
|-----|------|------|
| $U_l$ = 1kV $R_{ext}$ = 18.6Ω | $U_l$ = 2kV $R_{ext}$ = 18.6Ω | $U_l$ = 4kV $R_{ext}$ = 18.6Ω |

An example of the current waveform obtained for 200A can be observed in Figure 6-18. As the current impulse disappears after a certain time, the arc extinction in all the experimental tests carried out is due to the disappearance of the current impulse, so no conclusions have been drawn. Neither has been possible at simulations to analyze the extinction for cases C.1 and C.2, because of the longer simulation time needed.
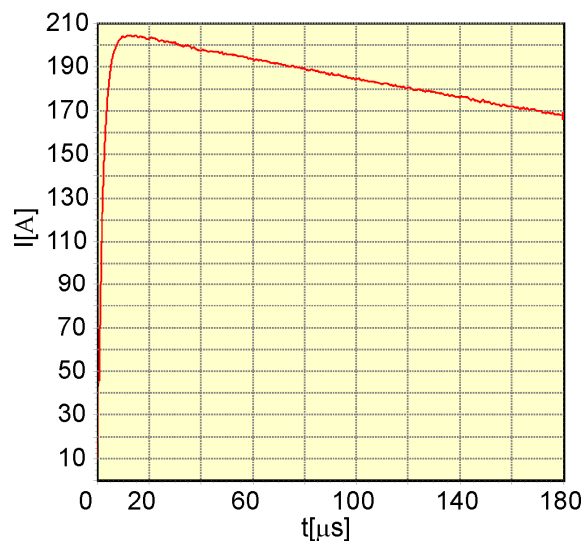


Figure 6-18 Test current for 200A

The experimental set-up used for the circuit breaker chamber is presented in Figure 6-19 which consists of two parallel copper arc rails. The electric arc is ignited between those two arc rails as a result of the melting of a carbon filament, 1mm above the lower inlet. This lower inlet has been considered to be fully closed. However, in the upper side, the geometry has been considered fully open without splitter plate (0SP), or only partially open when a splitter plate is considered (1SP). A quartz glass has been located in order to keep the arc inside the experimental chamber and to allow a good recording in a wide spectral band.

As it can be seen, geometry and dimensions of the experimental chamber are similar to those adopted for the simulated model in chapter 5 (Figure 5-8), with 8mm from anode to cathode and 40 mm length (17+23mm), which makes the validation possible.
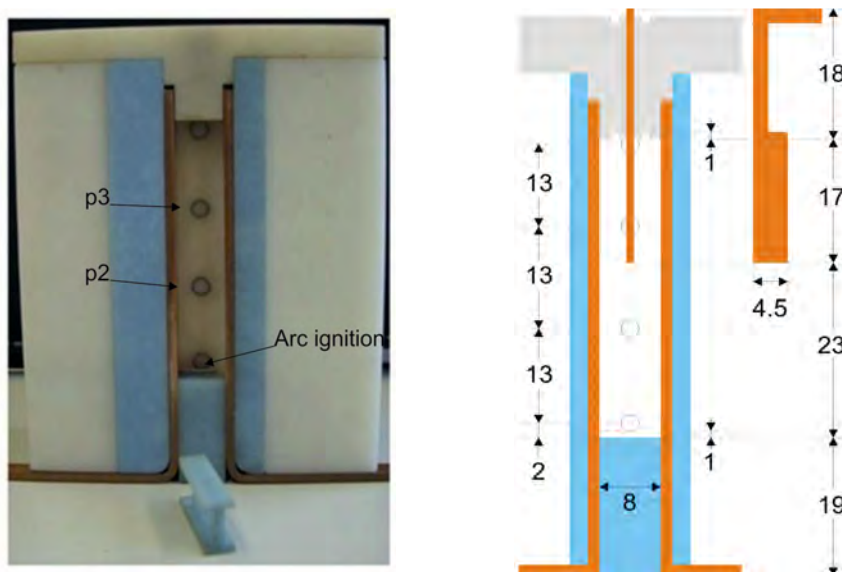


Figure 6-19 Experimental chamber (dimensions in mm)

## 6.3.2 VALIDATION RESULTS

In this section, the results obtained for each experimental test are presented. In all the cases, the input current, arc voltage and pressure data at two different points, p2 and p3, are shown. Additionally, arc movement images as recorded by the high-speed camera are included. These images have been compared to the arc movement obtained from the simulation results of case C, to validate the new model.

### 6.3.2.1 Test 1: 50A, 0SP

In the first test, the input current is 50A and no splitter plate is considered in the geometry. The data measured by the oscilloscopes (Figure 6-20), shows the input current with an impulse of 50A, the arc voltage starting at 40V and ending around 60V with some bouncing and the pressure with a peak value of 0.06bar.

Comparing these data with the results obtained in the simulation case C.1, (50A, 0SP), it can be seen that there is a good agreement between simulation and real tests for the arc voltage (Figure 5-49). In the results for case C.1, the voltage drop remains more or less constant with a value of 35V, while in the real data it ranges from 40 to 60V. But it has to be noticed that, looking at Figure 6-20, the voltage drop rising from 40V to 60V is not related with the arcing but with the current decrease. In these real tests, the current is produced as an impulse, unlike in the simulation. Therefore, its value goes down over time and so the voltage rises.
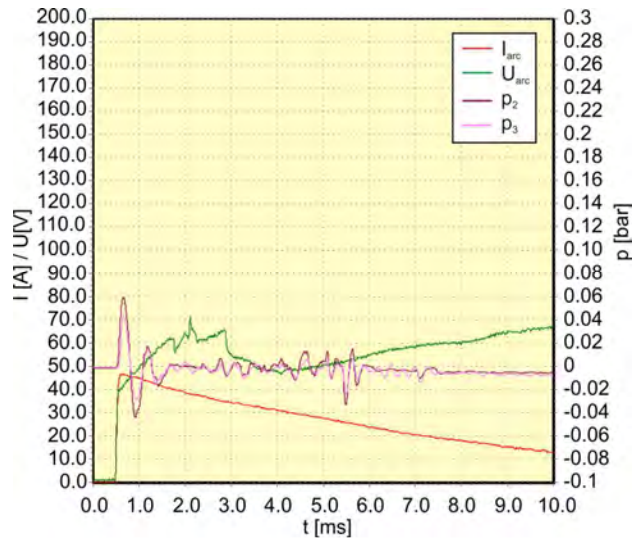
Figure 6-20 Arc current, voltage and pressure distribution for Test 1

Then, it is reasonable that if the current value would have been constant, instead of being an impulse, the voltage would remain also more or less constant, with the initial value of 40V which is very close to the value of 35V obtained in the simulation.

For pressure, the comparison is more difficult. First of all, because the data extracted from Ansys CFX and shown in Figure A-30, are the maximum pressure in the air, which for the case C.1 is around 0.2bar. But, the pressure in the real experiments has been measured at two specific points, p2 and p3, so they may not be maximum values. In this case, the maximum peak of those two measured pressures is 0.06bar. But, qualitatively, the trend of the pressure has the same shape as in the simulation: a peak at the beginning of the simulation and then it tends to zero, which validates the new model proposed.

The arc movement images recorded in this test are shown in Figure 6-21, where the slow upwards movement of the arc can be seen. Comparing these images with the simulation results for arc movement of case C.1 (Figure 5-42), again a good qualitative agreement can be observed as the arc barely moves up in both cases.
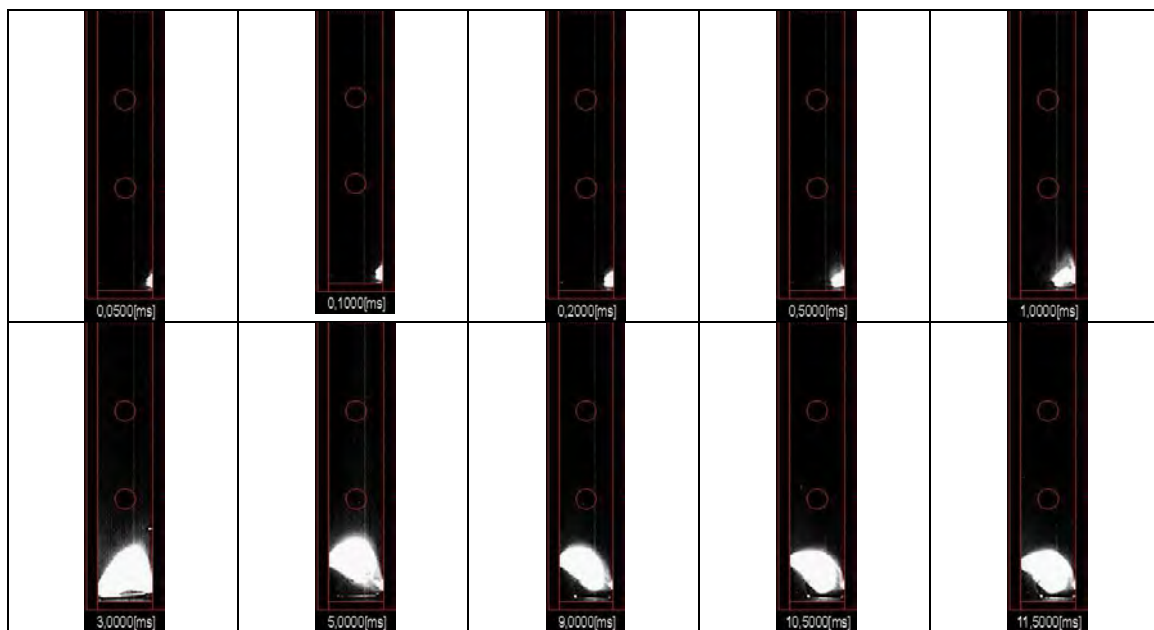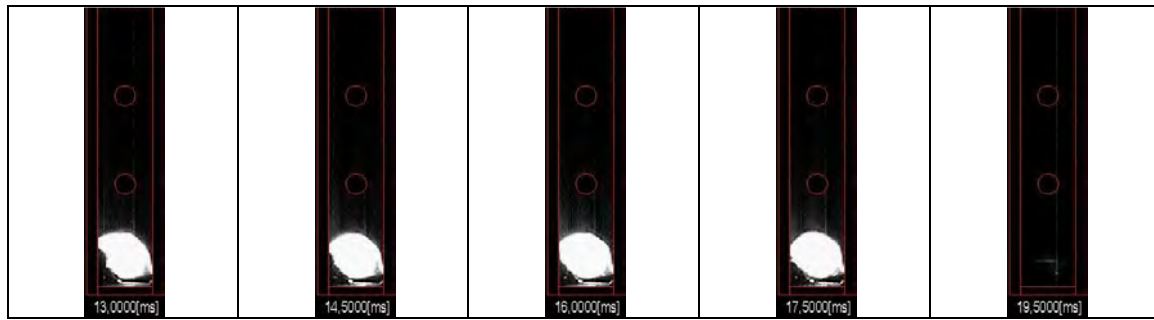
Figure 6-21 Arc movement images for test 1

## 6.3.2.2  Test 2: 50A, 1SP

In the second test, the input current is 50A and one splitter plate have been considered. Unfortunately, the oscilloscopes did not triggered this time and so, no voltage, current and pressure data was recorded. But, the arc movement, shown in Figure 6-22, was correctly recorded.

As in the simulation case (Figure 5-43, for case C.2) the results of this experimental test are almost similar to those achieved with 50A and no splitter plate. The reason is that the arc barely moves upwards, as shown in Figure 6-21. Then, it does not really matter whether the chamber has or not splitter plates, because the arc does not reach that area.
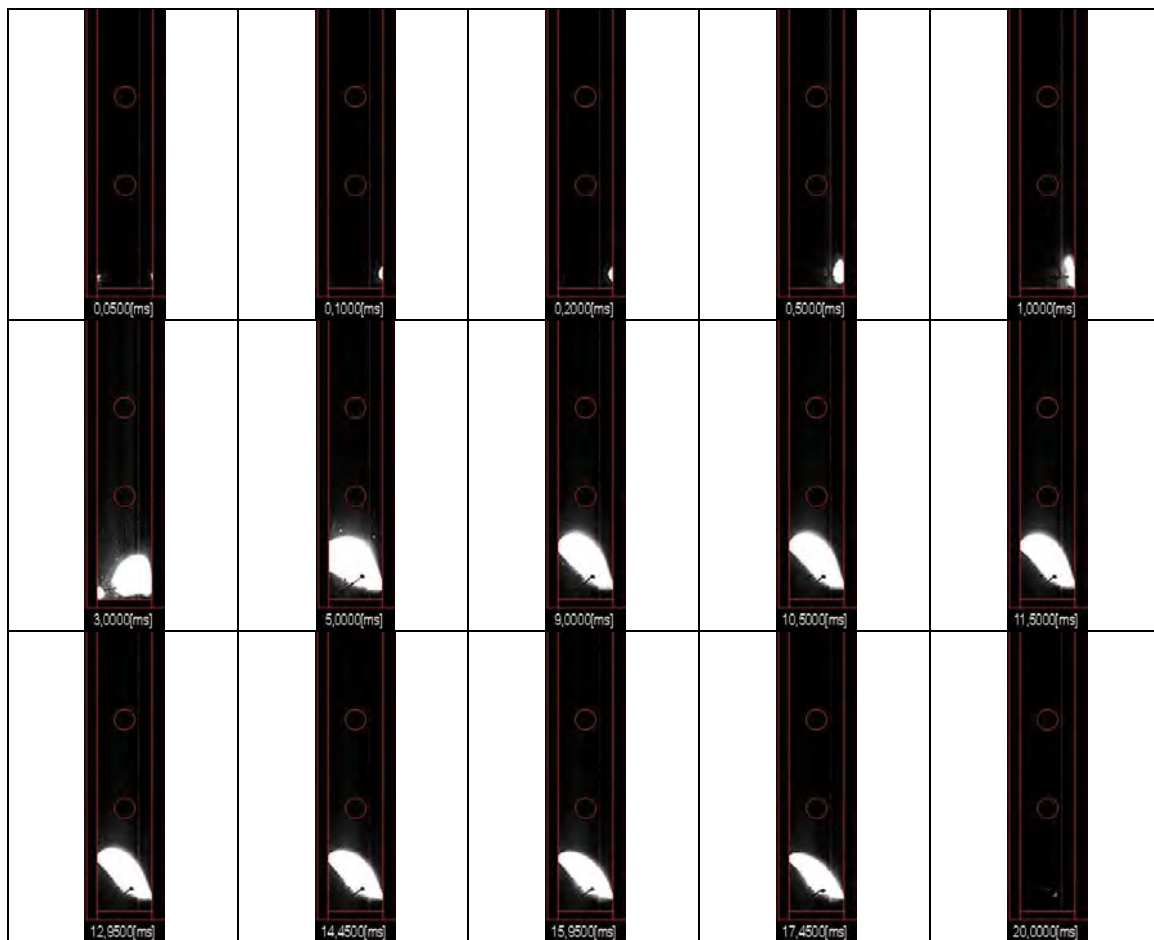


Figure 6-22 Arc movement images for test 2

### 6.3.2.3  Test 3: 100A, 0SP

The third test has been performed with an input current of 100A and without splitter plate. Results obtained are shown in Figure 6-23. The magnitudes obtained in this test lie around 120V for the arc voltage and 0.2bar for the pressure. Both values are higher than for 50A experimental tests. It is observed that the voltage has a peak between 2 and 2.5ms, which matches the instant when the copper filament completely burn and the arc is formed completely between the anode and the cathode.

In the simulation case C.3 (Figure 5-49 and Figure A-30) it can be observed that values for 100A are higher than for 50A. Regarding the magnitudes, the arc voltage achieved for 100A 0SP simulation lies around 55V (quite smaller) and the pressure around 0.2bar, which is similar. As an explanation, it has to be taken into account that although the new model proposed introduces several improvements, some aspects may also be adjusted.
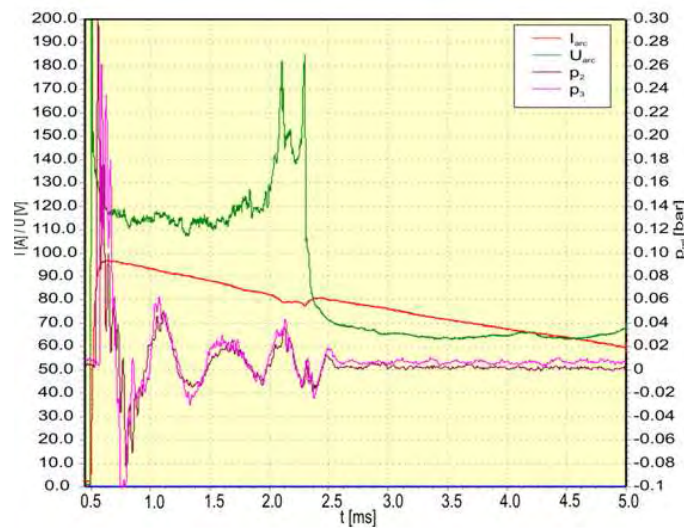


Figure 6-23 Arc current, voltage and pressure distribution for test 3

Regarding the images of the arc movement presented in Figure 6-24, the arc is faster for 100A, than for 50A. As the simulation shows, the arc moves upwards faster and more diffusely for 100A (Figure 5-43) than for 50A. This qualitative behaviour is again in good agreement with the new model proposed in this thesis.
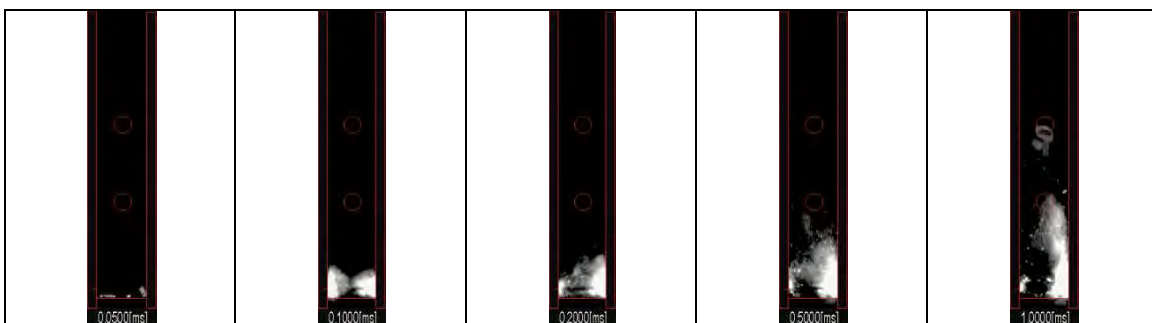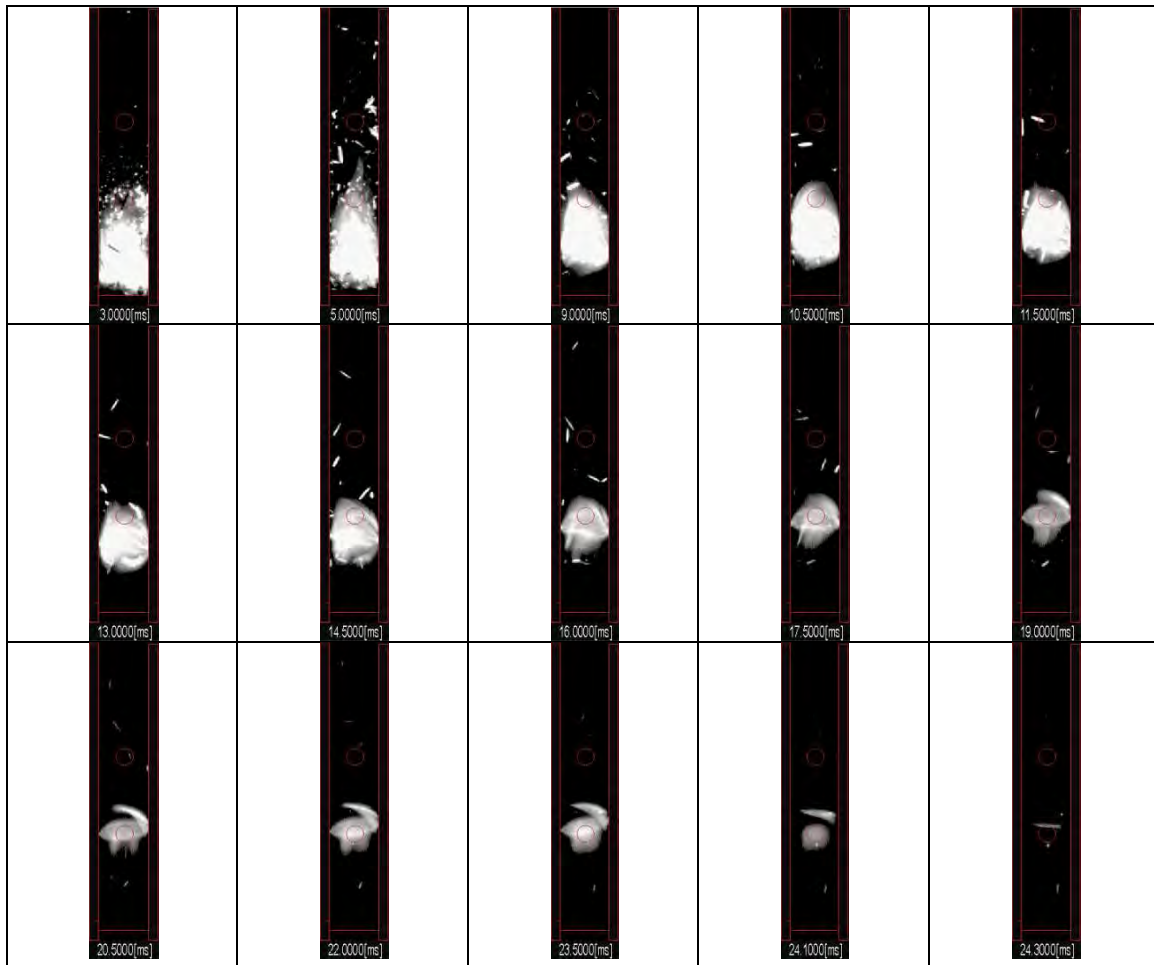
Figure 6-24 Arc movement images for test 3

### 6.3.2.4  Test 4: 100A, 1SP

In the fourth test, an input current of 100A and 1SP geometry have been considered. Arc voltage and pressure results are shown in Figure 6-25, where again the magnitudes obtained are around 120V for the arc voltage and 0.2bar for the pressure. So, similar results to those of test 3 (100A, 0SP) are obtained in Figure 6-26. Once again, the arc does not arrive the splitter plate area, so no real difference is observed for 100A tests with or without splitter plate. This is also proved by the simulation results obtained for case C.4 and shown in Figure 5-45.
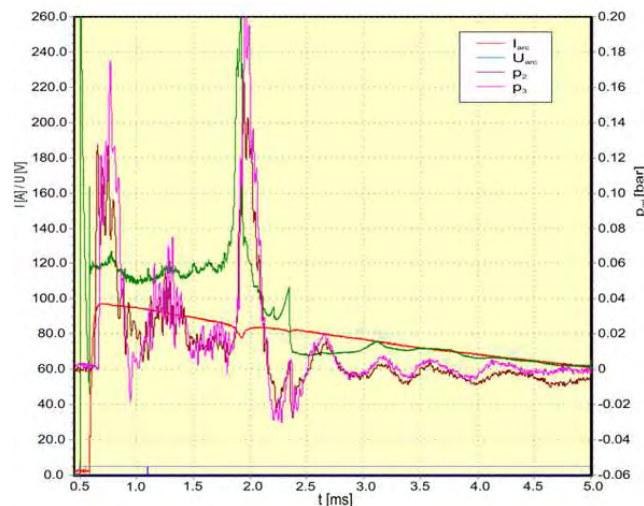


Figure 6-25 Arc current, voltage and pressure distribution for test 4
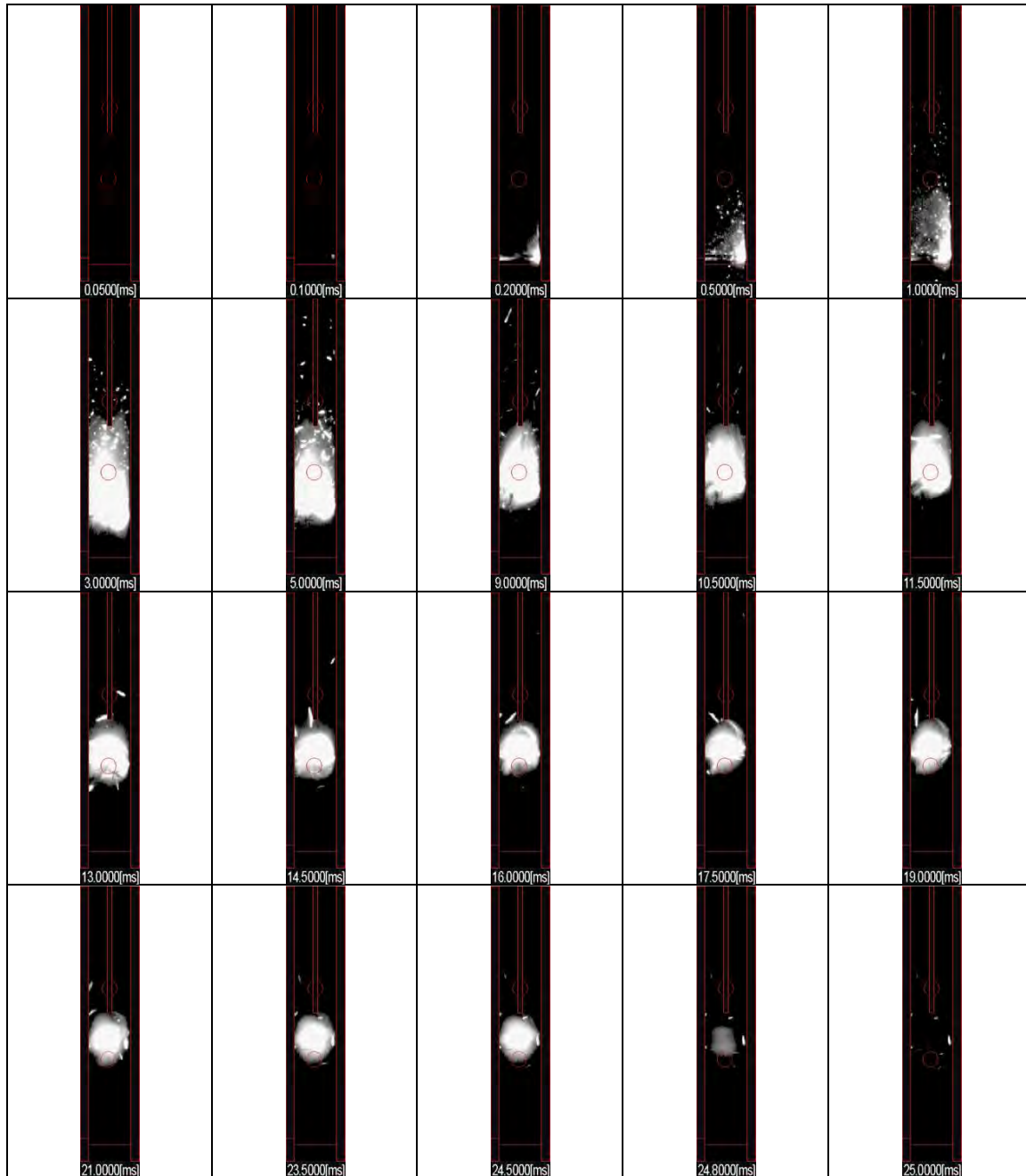
Figure 6-26 Arc movement images for test 4

### 6.3.2.5  Test 5: 200A, 0SP

This test is developed changing the input current to 200A. No splitter plate is included in the geometry and the data for arc voltage and pressure registered are shown in Figure 6-27 where an arc voltage around 160V peak and a pressure of 0.45bar is observed.

Looking at the simulation results obtained for case C.5 (Figure 5-49 and Figure A-30), values of 85V and 0.4bar are obtained. The arc voltage is again smaller in the simulation that in the real test, but qualitatively, it has increased as compared with the previous cases C.1, C.2, C.3 and C.4, as the real behaviour does.
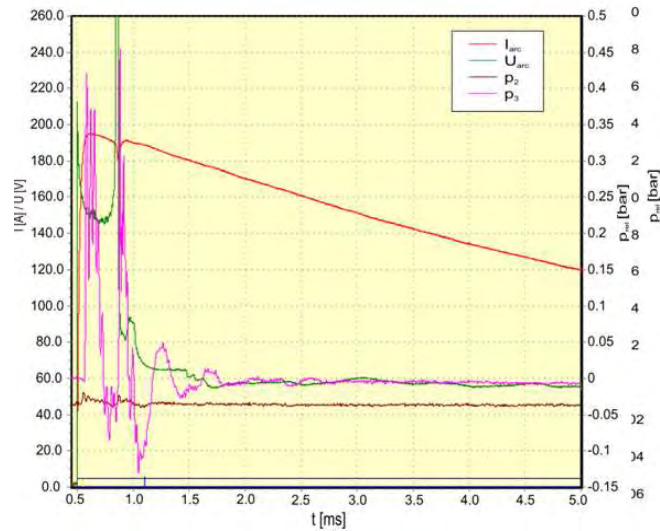
Figure 6-27 Arc current, voltage and pressure distribution for test 5

Regarding the arc movement images obtained with the high speed camera (Figure 6-28), with 200A the arc presents a more diffuse, expansive and faster upwards movement than in the previous analyzed experimental tests. This is once again in accordance with simulation results from Figure 5-46, where the same behaviour is observed.
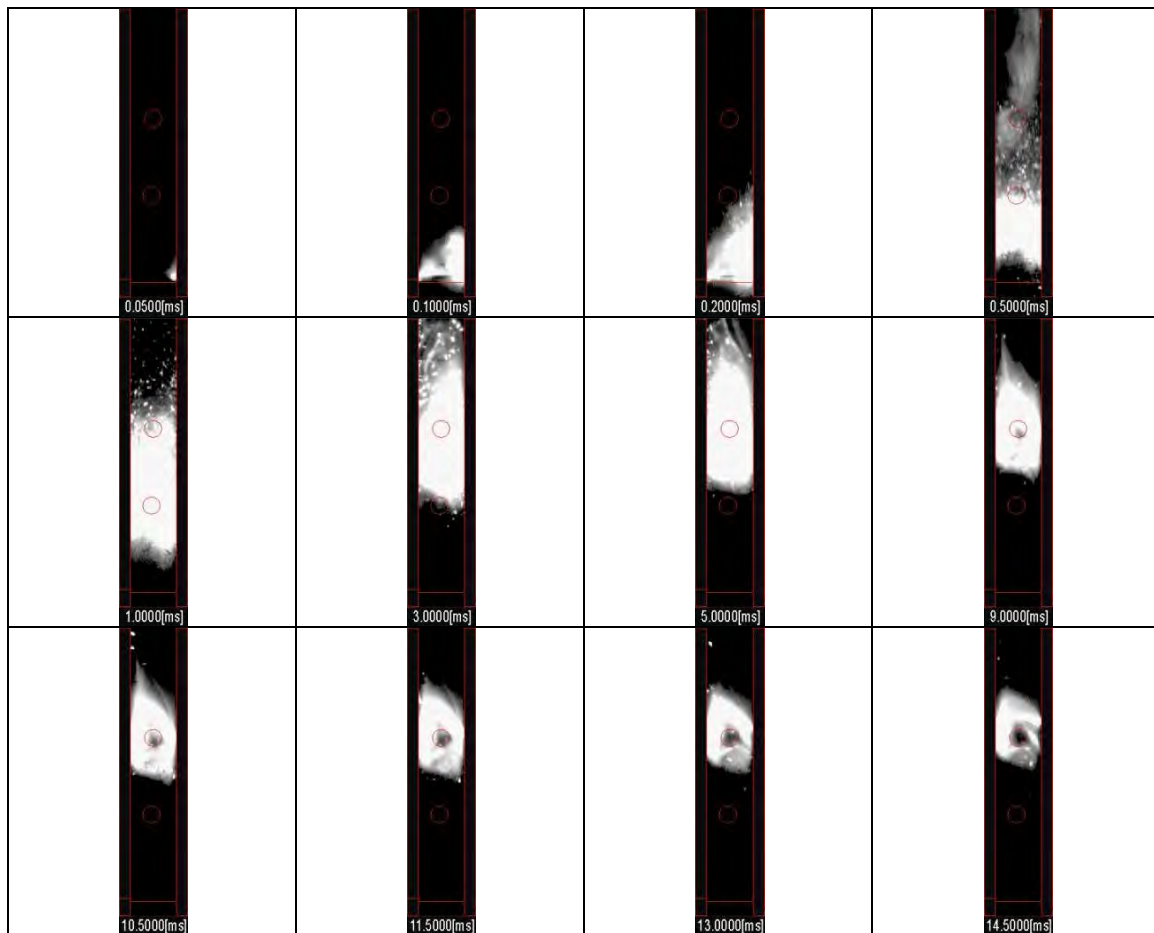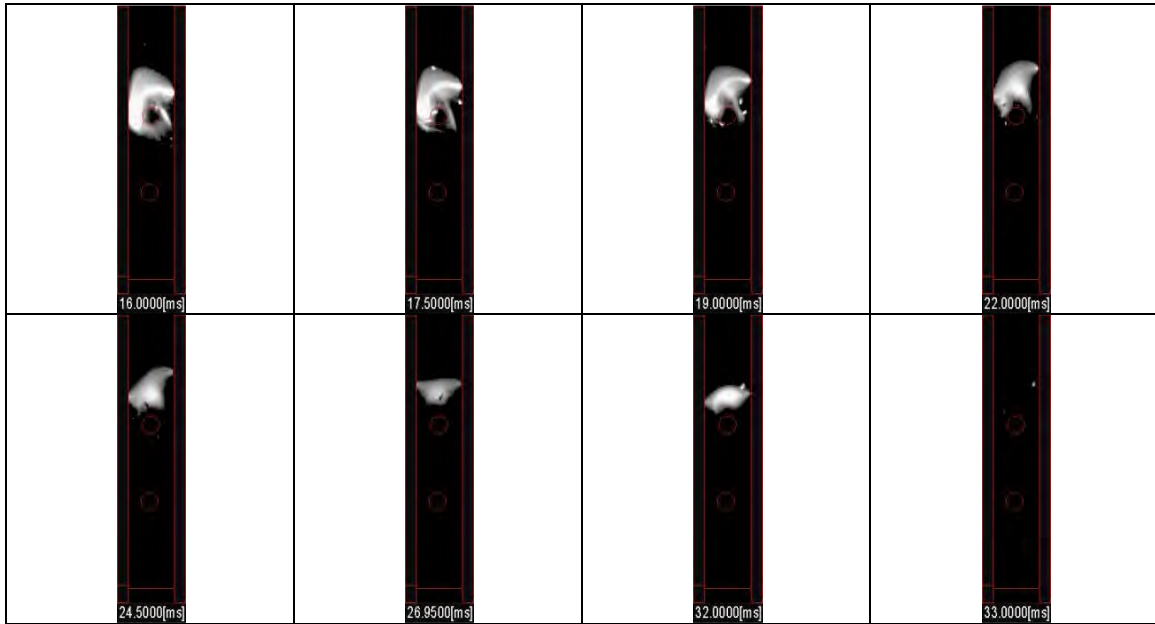
Figure 6-28 Arc movement images for test 5

### 6.3.2.6   Test 6: 200A, 1SP

The last experimental test has been carried out with 200A and 1SP geometry, obtaining the results shown in Figure 6-29. The arc voltage is around 200V peak and a pressure of 0.6bar is recorded.

Regarding simulation results of case C.6 (Figure 5-49 and Figure A-30), values of 86V and 0.5bar are obtained. The arc voltage is again smaller in simulation than in real tests.
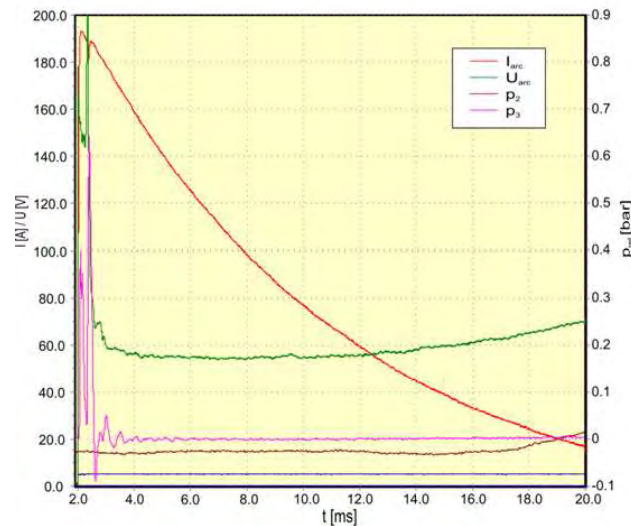


Figure 6-29 Arc current, voltage and pressure distribution for Test 6

Additionally, arc movement images recorded in this experimental test (Figure 6-30) show again a diffuse, expansive and faster arc. Also, this time the electric arc reaches to the splitter plate as in the simulation case C.6 (Figure 5-47).
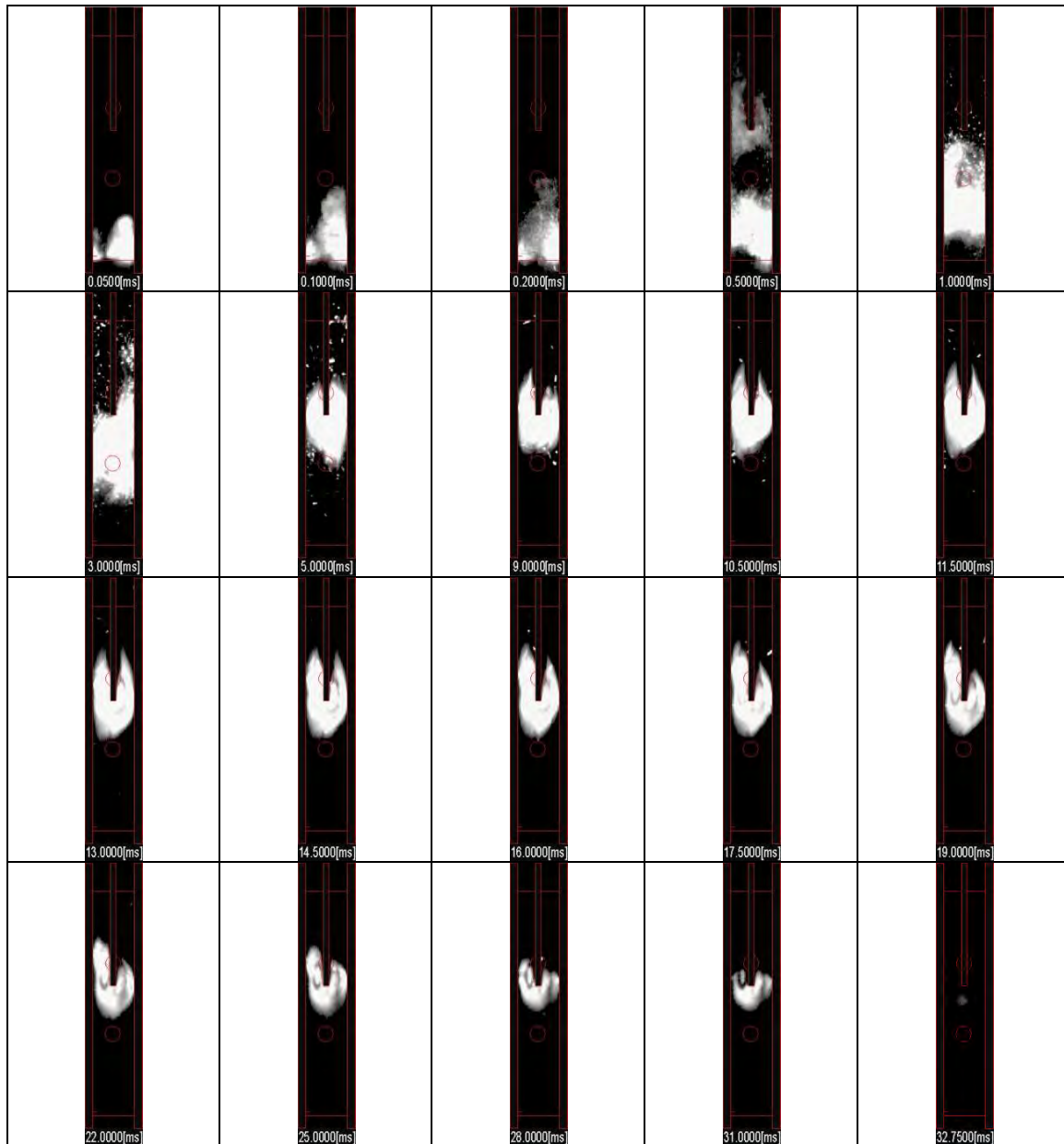
Figure 6-30 Arc movement images for test 6

## 6.4    CONCLUSIONS

In this chapter, verification and validation processes for the new model proposed in chapter 5 have been presented.

Verification of the model has been developed by analyzing a set of 15 simulations. This way, the influence of three different radiation models, mesh density sizes and timesteps have been evaluated. First of all, for the mesh size influence, a constant timestep equal to $2.5 \times 10^{-6}$s has been defined for the simulation model and three different mesh densities have been designed and tested with the three radiation models. After that, the timestep influence has been analyzed considering a constant mesh and three different timesteps for the three different radiation models.

The analysis of the results for the verification process has been developed considering CGI and CFL mathematical indexes. These coefficients are related to the stability and precision of the computational model, and obtaining small numerical values indicates that the model is

correct. After analyzing the values of CGI and CFL obtained for the 15 data set, the overall computational time of the simulations and some trends of parameters of interest, the most stable and efficient option has been chosen, which consists of P1 radiation model, MD mesh and a timestep of $2.5 \times 10^{-6}$s. Thus, those have been the parameters chosen to define the new model proposed in chapter 5.

On the other hand, the validation process has been carried out by performing experimental tests in the laboratory at Technical University of Ilmenau (Germany). In the experimental setup, a prototype from TU Ilmenau of a LVCB has been used. The geometrical dimensions are the same than in the new proposed model and six tests have been performed (geometries without splitter plate and with one splitter plate, for 50, 100 and 200A currents). In all the tests, the ignition of the arc is produced at 1mm above the down wall of the air as a result of the melting of a carbon wire.

From these experiments, arc voltage, pressure and arc movement have been registered and compared to the results obtained for the simulation case C, and shown in chapter 5, for the model validation.

From the experimental data obtained, the higher the current is, the higher the arc arrives in the chamber, and also the faster it moves. So, for an input current of 50A the arc barely moves from the low ignition location but for 100A and 200A the movement is more evident. In fact, for input currents of 50A and 100A the arc even does not reach the splitter plate area.

The comparison between experimental and simulation results shows that the arc movement images obtained in both cases are in good correspondence. Therefore, the new model responds correctly to the low ignition arc, where the arc barely moves from ignition location. Only when the current is increased, the movement starts to be remarkable and the arc becomes more diffuse and expansive.

Regarding the trends and numerical values obtained for arc voltage, the experimental trend is in accordance with simulation. The higher the input current is, the higher the arc voltage achieved. However, the numerical simulations values are lower than experimental ones. In the experimental results around 50V peak have been obtained for 50A, 120V for 100A test and 160V for 200A. While in the simulations a maximum arc voltage of 35V has been obtained for case C.1 and C.2, 55V for cases C.3 and C.4 and 85V for C.5 and C.6. But, it has to keep in mind that the simulation model is not yet a complete model to real demands, so differences are regular to achieve. Finally, the trends for pressure values are in accordance between experiments and simulations, obtaining values for the pressure inside the chamber between 0 and 0.6 bar in both cases. Again it can be observed that pressure peak values increases as the input current increases for both cases.

These results lead to conclude that the proposed model has a very similar behaviour toexperimental tests and so, that is correctly designed, even if still improvements in the arc physics definition may be made in future work.

# CHAPTER 7
## CONCLUSIONS AND FUTURE WORK

7.1.- CONCLUSIONS OF THE THESIS
7.2.- FUTURE WORK

# 7   CONCLUSIONS AND FUTURE WORK

## 7.1   CONCLUSIONS OF THE THESIS

Circuit breakers are responsible for the safety of equipment and human beings, being responsible for establishing or interrupting the electric current. They generally differ in the voltage level they are used for: low, medium or high voltage. But for all of them, the interruption process is ruled by the electric arc phenomenon.

The formation of the electric arc in a circuit breaker is due to the conduction of the electrical current through an interrupting medium. In the specific case of Low Voltage Circuit Breakers (LVCBs), the interrupting medium is usually air. This conduction starts when the contacts of the circuit breaker separate and the air became into ionized plasma. The elevation of the temperature is a necessary condition for the air to achieve plasma state and become conductive. Thus, an important factor in the appearance and maintenance of the electric arc is the temperature of the air. Besides, this temperature determines the values of some properties of the arc plasma, such as electrical conductivity, thermal conductivity and viscosity.

Another very important feature is the voltage drop in the arc, as it is directly related to its extinction in DC current cases, analyzed in the present thesis. In general, in a DC current circuit, the extinction is achieved when the arc voltage is greater than the source voltage. Thus, to achieve the arc extinction it is necessary to raise the arc voltage above the source voltage.

Therefore, in order to analyze and improve the knowledge of the electric arc phenomena and optimize the circuit breaker design, software simulation is a very interesting tool, as it presents high flexibility and it allows reducing the need of new prototypes. Among the simulation models for the electric arc (black box models, models based on graphics and diagrams and physical models) physical models are the most complete for understanding the evolution of the arc and for the improvement of LVCBs designs, as they focus their attention on the physical processes involved in the arc.

Considering these aspects, this thesis has proposed a new model for analyzing the behaviour of the electric arc in LVCBs, developed in ANSYS CFX. The model reproduces a simplified cahmber with the following dimensions 40x11x2.5mm$^3$, with four domains (air, splitter plate, cathode and anode) where the electric arc is ignited at 10mm from the lower face of the chamber by a hot channel of 10000K. This model is based on [3] but the following improvements have been introduced in this new model:

- A full 3D geometry with no symmetry simplifications
- A fine structured and hexahedral mesh of around 1000000 nodes has been designed
- Application of updated air data
- Radiation model has been improved to P1 model
- Calculation of magnetic field by vector magnetic potential formulation

The simulation of the model has lead to the following conclusions. First of all, the same four curves presented in the reference model [3] for arc root modelling have been considered, obtaining similar results in the four cases analyzed for the new proposed model. This is explained because the operation point is in the asymptotic region for all the cases which suggests that a review of the voltage-current density data should be developed. As an

alternative, a different ohmic resistance has been applied to model arc roots in the splitter plate, obtaining that the behaviour of the model reacts when changing the input data. Also, the effect of the splitter plates in the chamber has been analyzed proving that the new model responds well to the theoretical knowledge regarding the electric arc and that the higher the number of splitter plates in the chamber, the more efficient the interruption of the arc.

Besides, changes in the arc ignition location and input current have been applied. Regarding the impact of the arc ignition location on the arc movement, smaller movement of the arc when the ignition is lower has been achieved. Regarding the impact of the input current density, it has been concluded that the higher the current, the higher the diffusion and expansion of the arc, and also a faster movement.

Following, changes in the chamber geometry have been made. None of the changes have shown great influences and the influence, in any case, has been negative. Thus, those geometrical changes in the chamber should be taken into account not to be applied in the new LVCBs design.

Finally, verification and validation processes of the presented model have been developed. Verification has been achieved by analyzing a set of 15 simulations, where the influence of three different radiation models, three mesh density sizes and three timestep has been analyzed. This analysis has allowed choosing the most stable and efficient option which consist on the combination of P1 radiation model, MD the density mesh and a timestep equal to 2.5e-06s. These parameters have been applied to the new model presented in chapter 5.

For the validation process, an experimental setup at Technical University of Ilmenau (Germany) has been performed, considering geometries without splitter plate and with one splitter plate for 50, 100 and 200A input currents. In all the tests, the ignition of the arc is carried out at 1mm above from the lower face of the chamber, by melting a carbon wire. From the comparison of experimental and simulation results, it is observed that the arc movement is in correspondence. The new proposed model responds correctly to the low ignition arc, where the arc does not get high pressure push to move due to the small air volume behind. Only by increasing the current, the arc movement starts to be remarkable, being the arc more diffuse and expansive. So, it can be said that the new proposed model is correctly designed, and it is a good and robust tool for the electric arc analysis in LVCBs.

Finally, it can be highlighted that some of the works carried out during the development of this thesis have been published in the following conferences and journals:

- "Considerations for Simulation of the Switching Arc" Przeglad Electrotechniczny (Electrical Review), Vol. 88, No. 1a 2012, pp. 104-107, 2012.
- "Analysis of the Discretization Errors in Different Electric Arc Configurations" XIXth International Conference on Gas Discharge and its Applications, Beijing, China, 2012.
- "Analysis of Spatial Discretization for Electric Arc Simulations" XIIIth International Conference on Optimization on Electrical and Electronic Equipment, Brasov, Romania, 2012.
- "Numerical Analysis of the electrical Arc simulation using Ansys CFX" XXVIth International Conference on Electrical Contacts, Beijing, China, 2012.
- "Analysis of the electric Arc in Low Voltage Circuit Breakers" International Conference on Renewable energies and Power Qualities, Gran Canaria, Spain, 2011.

Additionally, a research project in this field has been developed, entitled "Optimización de la interrupción del arco eléctrico en dispositivos de baja tensión" funded by the University of the Basque Country (UPV/EHU), from december 2009 to december 2011.

## 7.2   FUTURE WORK

Regarding the future work that can be developed in this research field, several ideas arise:

- Further research about the formation of the arc roots is needed, due to their influence on the arc voltage and so, in the extinction process. This aspect will have to be developed by experimental tests in laboratory.

- Longer simulation times. Nowadays, the computational time required of the presented model to simulate 1ms is around four days, so it would be interesting to run simulations faster and be able, for example, to simulate the whole range of 25ms that is needed for experimental set-up in the tests presented in chapter 6.

- Analysis of the arc contact movement during the opening time.

- Improvement of all the assumptions made at the beginning of chapter 5 to define the new model, including the gravity effect; metal vapours and plastic ablation, introducing the rates in the MHD formulation; turbulence flow; a non symmetrical ignition of the arc; a more realistic geometry; etc, [94-96]

- Finally, regarding the experimental setup, changes in the arc ignition location could be considered or even different geometries and materials.

# REFERENCES

# REFERENCES

[1] W. F. Giménez Gutiérrez, "Modelización de interruptores eléctricos de potencia," Ph.D. dissertation, Universitat Politècnica de Catalunya, Spain, 2000.

[2] M. Anheuser, T. Beckert and S. Kosse, "Electric arcs in switchgear - theory, numerical suimulations an experiments," in *XIXth Symposium on Physics of Switching Arc,* Nové Město na Moravě, Czech Republic, 2011, pp. 3-15.

[3] M. Lohse, A. Spille-Kohoff, M. Schnick and U. Füssel, "Implementation of Lindmayer Sheath Model for Arc Simulation using ANSYS CFX," CFX Berlin Software GmbH; TU Dresden, Germany, 2009.

[4] M. Cortes Cherta, "Curso de aparamenta eléctrica," Centro de Formación Merlin Gerin. 1990.

[5] T. E. Browne, *Circuit Interruption: Theory and Techniques*. Ed. New York: Marcel Dekker, Inc., 1984.

[6] K. Nakanishi, *Switching Phenomena in High-Voltage Circuit Breakers*. Ed. New York: Marcel Dekker, Inc., 1991.

[7] L. Van der Sluis, *Transient in Power Systems*. Ed. Chichester: John Wiley & Sons, 2001.

[8] P. G. Slade, *Electrical Contacts: Principles and Applications*. Ed. Florida: CRC Press, 1999.

[9] W. Rieder, "Circuit breakers Physical and engineering problems I - Fundamentals," *Spectrum, IEEE*, vol. 7, pp. 35-43, 1970.

[10] R. D. Garzon, *High Voltage Circuit Breakers: Design and Applications*. Ed. New York: Marcel Dekker, 2002.

[11] J. W. McBride and P. M. Weaver, "Review of arcing phenomena in low voltage current limiting circuit breakers," *Science, Measurement and Technology, IEE Proceedings -,* vol. 148, pp. 1-7, 2001.

[12] C. W. Brice, R. A. Dougal and J. L. Hudgins, "Review of technologies for current-limiting low-voltage circuit breakers," *Industry Applications, IEEE Transactions on,* vol. 32, pp. 1005-1010, 1996.

[13] T. Mitsuhashi, M. Takahashi, Y. Wada and S. Yamagata, "Development of a new current limiting technique by 3D nonlinear analysis of magnetic fields in arc chambers and its application to LV circuit breakers," in *Industry Applications Conference, 1996. Thirty-First IAS Annual Meeting, IAS '96., Conference Record of the 1996 IEEE,* 1996, pp. 2269-2274 vol.4.

[14] IEEE Std 1015, "IEEE recommended practice for applying low voltage circuit breakers used in industrial and commercial power systems," Institute of Electrical and Electronics Engineers, Inc., Ed. New York, 2006.

[15] F. W. Kussy and J. L. Warren, *Design Fundamentals for Low-Voltage Distribution and Control*. Ed. New York: Marcel Dekker, 1987.

[16] C. Rümpler, F. Reichert, F. Berger, H. Stammberger and P. Terhoeven, "Simulation and verification of the arc behaviour in quenching chambers with splitter plates," in *XVIIth Symposium on Physics of Switching Arc,* Nové Mesto na Morave, Czech Republic, 2007, pp. 181-184.

[17] P. Dohnal, "Calculation of magnetic force in low voltage circuit breaker," in *XVth Symposium on Physics of Switching Arc*, Nové Mesto na Morave, Czech Republic, 2003, pp. 55-61.

[18] K. Nakayama, Y. Yokomizu, T. Matsumura, E. Kanamori and K. Kawamura, "Mechanism of voltage rise of high-current arc at atmospheric pressure due to deion plates," *Electrical Engineering in Japan,* vol. 145, pp. 17-24, 2003.

[19] E. Debellut, D. Cajal, F. Gary and A. Laurent, "Phenomena generated by splitter plates on low-voltage electric arc dynamics," in *50th IEEE Holm Conference on Electrical Contacts and the 22nd International Conference on Electrical Contacts,* 2004, pp. 355-361.

[20] V. Kapustin, D. Podolsky and V. Mestcherjakov, "Arc penetration to the arc chute and arc chute plates erosion," in *Proceedings of the 42nd IEEE Holm Conference on Electrical Contatcs and 18th International Conference on Electrical Contacts,* Chicago, USA, 1996, pp. 50-9.

[21] V. Behrens and T. Honig, "Arc splitter for an arcing chamber," US20080135524 A1, 2005.

[22] K. J. Lim, S. H. Kang, U. Y. Lee and H. C. Song, "3-D finite element analysis of magnetic force on the arc for arc chamber design of molded case circuit breaker," *The European Physical Journal, Applied Physics*, vol. 14, pp. 183-186, 2001.

[23] J. Valenta, "Modelling of electrodynamic forces in Modeion circuit breaker," *Student EEICT,* vol. 1, pp. 95-97, 2003.

[24] P. Dohnal, "Arc body force in splitter-plates chamber," *Student EEICT,* 2003.

[25] P. Dohnal and J. Valenta, "Diagnostics of LV arc blasting," in *XVIth Symposium on Physics of Switching Arc,* Nové Město na Moravě, Czech Republic, 2005, pp. 245-249.

[26] P. Rodriguez, J. Didier, G. Bernard and S. Rowe, "Arc-contact-insulating wall interactions in low voltage circuit-breakers," *Power Delivery, IEEE Transactions on,* vol. 13, pp. 480-488, 1998.

[27] Working Group 13.01 of the Study Committee 13, "State of art of circuit-breaker modelling," *Cigre,* Report N°135,1998.

[28] J. A. Martinez Velasco, "Representación avanzada de interruptores mediante el EMTP," in *4°Jornadas Luso Espanholas De Engenharia Electrotécnic,* Porto, Portugal, 1995, pp. 253-260.

[29] G. Bizjak, P. Zunko and D. Povh, "Circuit breaker model for digital simulation based on Mayr's and Cassie's differential arc equations," *Power Delivery, IEEE Transactions on,* vol. 10, pp. 1310-1315, 1995.

[30] P. H. Schavemaker and L. Van der Sluis, "The arc model blockset," in *2nd IASTED International Conference Power and Energy Systems (EuroPES),* Crete, Greece, June 25-28, 2002, pp. 644-648.

[31] H. A. Darwish and N. I. Elkalashy, "Universal arc representation using EMTP," *Power Delivery, IEEE Transactions on,* vol. 20, pp. 772-779, 2005.

[32] L. Ghezzi and A. Balestrero, "Modeling and Simulation of Low Voltage Arcs," Ph.D. dissertation, Technische Universiteit Delft, Netherlands, 2010.

[33] M. S. Benilov, "Understanding and modelling plasma–electrode interaction in high-pressure arc discharges: a review," *Journal of Physics D: Applied Physics,* vol. 41, pp. 01-31, 2008.

[34] F. Karetta and M. Lindmayer, "Simulation of arc motion between divergent arc runners," in *Proceedings of 19th International Conference on Electric Contact Phenomena,* 1998, pp. 361-7.

[35] M. F. Modest, *Radiative Heat Transfer.* Ed. New York: McGraw-Hill, 1993.

[36] M. Melot, J. Trépanier, R. Camarero and E. Petro, "Comparison of Two Models for Radiative Heat Transfer in High Temperature Thermal Plasmas," *Modelling and Simulation in Engineering,* vol. 2011, pp. 1-7, 2011.

[37] A. Gleizes, J. J. Gonzalez and P. Freton, "Thermal plasma modelling," *Journal of Physics D: Applied Physics,* vol. 38, pp. 153-183, 2005.

[38] Naghizadeh-Kashani, Y., Cressault, Y., and Gleizes, A., "Net emission coefficient of air thermal plasmas," *Journal of Physics D: Applied Physics,* vol. 35, pp. 2925-2934, 2002.

[39] A. Gleizes, Y. Cressault and P. Teulet, "Mixing rules for thermal plasma properties in mixtures of argon, air and metallic vapours," *Plasma Sources Science Technology,* vol. 19, pp. 055013-055026, 2010.

[40] V. Aubrecht and M. Bartlova, "Radiation transfer in thermal plasmas of air, N2 and CO2," in *17th International Conference on Gas Discharges and their Applications,* Cardiff, United Kingdom, 2008, pp. 393-396.

[41] F. Reichert, C. Rumpler and F. Berger, "Application of different radiation models in the simulation of air plasma flows," in *17th International Conference on Gas Discharges and their Applications,* Cardiff, United Kingdom, 2008, pp. 141-144.

[42] F. Yang, Y. Wu, M. Rong, H. Sun, A. Murphy, Z. Ren and et al., "Low-voltage circuit breaker arcs—simulation and measurements," *Journal of Physics D: Applied Physics,* vol. 46, pp. 273001-273020, 2013.

[43] G. Meunier and A. Abri, "A model for the current interruption of an electric arc," *Magnetics, IEEE Transactions on,* vol. MAG-20, pp. 1956-1958, 1984.

[44] G. Meunier, J. C. Sabonnadière, J. L. Coulomb and E. Belbel, "Magnetic field computation for electric arc modelling," *Magnetics, IEEE Transactions on,* vol. MAG-19, pp. 2593-2595, 1983.

[45] S. Ito, Y. Takato, Y. Kawase and T. Ota, "Numerical analysis of electromagnetic forces in low voltage AC circuit breakers using 3-D finite element method taking into account eddy currents," *Magnetics, IEEE Transactions on,* vol. 34, pp. 2597-2600, 1998.

[46] S. Ito, Y. Kawase and H. Mori, "3-D finite element analysis of magnetic blowout forces acting on the arc in molded case circuit breakers," *Magnetics, IEEE Transactions on,* vol. 33, pp. 2053-2056, 1997.

[47] S. Ito, Y. Kawase and H. Mori, "3-D finite element analysis of repulsion forces on contact systems," *Magnetics, IEEE Transactions on,* vol. 32, pp. 1677-1680, 1996.

[48] P. A. Jeffery, J. K. Sykulski and J. W. McBride, "3D finite element analysis modelling of the arc chamber of a current limiting minature circuit breaker," *COMPEL,* vol. 17, pp. 244-251, 1998.

[49] M. Ziólkowski, "Arc spot trajectories over ferromagnetic plates of extinguishing chambers," *COMPEL,* vol. 17, pp. 506-5015, 1998.

[50] F. Karetta and M. Lindmayer, "Simulation of the gasdynamic and electromagnetic processes in low voltage switching arcs," *Components, Packaging, and Manufacturing Technology, IEEE Transactions on,* vol. 21, pp. 96-103, 1998.

[51] M. Lindmayer, "Complete simulation of moving arcs in low-voltage switchgear," in *XIV International Conference on Gas Discharges and their Applications,* Liverpool, UK, 2002, pp. 01-06.

[52] M. Lindmayer and M. Springstubbe, "Three-dimensional-simulation of arc motion between arc runners including the influence of ferromagnetic material," *Components and Packaging Technologies, IEEE Transactions on,* vol. 25, pp. 409-14, 2002.

[53] M. Lindmayer, E. Marzahn, A. Mutzke and M. Springstubbe, "Low-voltage switching arcs-experiments and modelling," in *XVth Symposium on Physics of Switching Arc,* Nové Mesto na Morave, Czech Republic, 2003, pp. 01-16.

[54] M. Lindmayer, E. Marzahn, A. Mutzke, T. Ruther and M. Springstubbe, "The process of arc-splitting between metal plates in low voltage arc chutes," in *50th IEEE Holm Conference on Electrical Contacts and the 22nd International Conference on Electrical Contacts,* Seattle, USA, 2004, pp. 28-34.

[55] M. Lindmayer, A. Mutzke, T. Rüther and M. Springstubbe, "Some aspects of arc behavior in low-voltage arc chutes," in *XVIth Symposium on Physics of Switching Arc,* Nové Mesto na Morave, Czech Republic, 2005, pp. 278-292.

[56] M. Lindmayer, "Simulations of switching devices based on the general transport equation," in *International Conference on Electrical Contacts Swiss Federal Institute of Technology,* Zurich, Switzerland, 2002, pp. 01-07.

[57] T. Rüther, A. Mutzke, M. Lindmayer and M. Kurrat, "The formation of arc roots on a metallic splitter plate in low-voltage arc chambers," in *23rd International Conference on Electrical Contacs,* Sendai, Japan, 2006, pp. 01-06.

[58] A. Mutzke, T. Rüther, M. Kurrat and M. Lindmayer, "Simulation of the arc splitting proccess at a spitter plate," in *XVIIth Symposium on Physics of Switching Arc,* Nové Mesto na Morave, Czech Republic, 2007, pp. 01-04.

[59] C. Rümpler, "Lichtbogensimulation für Niederspannungsschaltgeräte," PhD thesis, Fraunhofer Verlag, 2009.

[60] A. Mutzke, T. Ruther, M. Kurrat, M. Lindmayer and E. D. Wilkening, "Modeling the arc splitting process in low-voltage arc chutes," in *53rd IEEE Holm Conference on Electrical Contacts,* Pittsburgh, USA, 2007, pp. 175-182.

[61] A. Mutzke, T. Rüther, M. Lindmayer and M. Kurrat, "Arc behavior in low-voltage arc chambers," in *24th International Conference on Electrical Contacts* St. Malo, France, 2008, pp. 01-06.

[62] J. Riß, M. Lindmayer and M. Kurrat, "Considerations to simplify the numerical gas flow simulation of low voltage arcs," in *XIXth Symposium on Physics of Switching Arc,* Nové Město na Moravě, Czech Republic, 2011, pp. 299-302.

[63] J. Riß, M. Lindmayer and M. Kurrat, "Simplification of the arc splitting process in numerical gas flow simulations," in *26th International Conference on Electrical Contacts,* Beijing, China, 2012, pp. 245-249.

[64] L. Xingwen, C. Degui and W. Qian. Simulation on the arc plasma behavior in low voltage circuit breaker. pp. 1-6. 2005. Available: http://www.paper.edu.cn/index.php/default/en_releasepaper/downPaper/200503-21.

[65] M. Lindmayer, E. Marzahn, A. Mutzke, T. Ruther and M. Springstubbe, "The process of arc splitting between metal plates in low voltage arc chutes," *Components and Packaging Technologies, IEEE Transactions on,* vol. 29, pp. 310-317, 2006.

[66] J. Yos, "Revised transport properties for high temperature air and its components," *Avco Space System Divison,* 1967.

[67] W. Yi, R. Mingzhe, Y. Qian and H. Guangxia, "Numerical analysis of the arc plasma in a simplified low-voltage circuit breaker chamber with ferromagnetic materials," *Plasma Science and Technology,* vol. 7, pp. 2977-2981, 2005.

[68] Y. Wu, R. Mingzhe, J. Li and L. Jianyong, "Calculation of electric and magnetic fields in simplified chambers of low-voltage circuit breakers," *Magnetics, IEEE Transactions on,* vol. 42, pp. 1007-10, 2006.

[69] Y. Qian, R. Mingzhe, A. B. Murphy and W. Yi, "The influence of medium on low-voltage circuit breaker arcs," *Plasma Science and Technology,* vol. 8, pp. 680-685, 2006.

[70] B. Swierczynski, J. J. Gonzalez, P. Teulet, P. Freton and A. Gleizes, "Advances in low-voltage circuit breaker modelling," *Journal of Physics D: Applied Physics,* vol. 37, pp. 595-609, 2004.

[71] Y. Wu, M. Rong, Z. Sun, X. Wang, F. Yang and X. Li, "Numerical analysis of arc plasma behaviour during contact opening process in low-voltage switching device," *Journal of Physics D: Applied Physics,* vol. 40, pp. 795-802, 2007.

[72] L. Xingwen, C. Degui, D. Ruicheng and G. Yingsan, "Study of the influence of arc ignition position on arc motion in low-voltage circuit breaker," *Plasma Science, IEEE Transcations on,* vol. 35, pp. 491-498, 2007.

[73] L. Xingwen, G. Chen, Y. Wu and R. Dai, "A comparison of the effects of different mixture plasma properties on arc motion," *Journal of Physics D: Applied Physics,* vol. 40, pp. 6982-6988, 2007.

[74] L. Xingwen, L. Rui, S. Hao, K. Tusongjiang and C. Degui, "Ferromagnetic Material Effects on Air Arc Behavior," *Plasma Science, IEEE Transactions on,* vol. 37, pp. 463-469, 2009.

[75] R. Mingzhe, Y. Fei, W. Yi, A. B. Murphy, W. Weizong and G. Jin, "Simulation of Arc Characteristics in Miniature Circuit Breaker," *Plasma Science, IEEE Transactions on,* vol. 38, pp. 2306-2311, 2010.

[76] M. Lindmayer, "Modeling of contact heating and erosion under arc influence," in *24th International Conference on Electrical Contacts,* Saint Malo, France, 2008, pp. 37-42.

[77] C. Fievet, M. Barrault, P. Petit, P. Cheviere, C. Fleurier and v. Andre, "Optical diagnostics and numerical modelling of arc re-strikes in low-voltage circuit breakers," *Journal of Physics D: Applied Physics,* vol. 30, pp. 2991, 1997.

[78] C. Fievet, M. Barrault, P. Chevrier and P. Petit, "Experimental and numerical studies of arc restrikes in low-voltage circuit breakers," *Plasma Science, IEEE Transactions on,* vol. 25, pp. 954-60, 1997.

[79] E. Domejean, P. Chevrier, C. Fievet and P. Petit, "Arc-wall interaction modelling in a low-voltage circuit breaker," *Journal of Physics D: Applied Physics,* vol. 30, pp. 2132-2142, 1997.

[80] H. Rachard, P. Chevrier, D. Henry and D. Jeandel, "Numerical study of coupled electromagnetic and aerothermodynamic phenomena in a circuit breaker electric arc," *International Journal of Heat Mass Transfer,* vol. 42, pp. 1723-34, 1999.

[81] J. Wild, J. Y. Battandier and C. Fievet, "Magneto hydrodynamic simulation coupled with network in low voltage circuit breakers," in *International Conference on Power System Technology,* 2004, pp. 1954-1959.

[82] L. Piqueras, D. Henry, D. Jeandel, J. Scott and J. Wild, "Three-dimensional modelling of electric-arc development in a low-voltage circuit-breaker," *International Journal of Heat Mass Transfer,* vol. 51, pp. 4973-4984, 2008.

[83] R. Günther, C. Lüders, M. Hein and M. Anheuser, "System simulation of the behavior of electric arcs in molded case circuit breakers (MCCB)," in *XVIIIth Symposium on Physics of Switching Arc,* Nové Mesto na Morave, Czezh Republic, 2009, pp. 49-55.

[84] M. Anheuser and C. Lüders, "Numerical arc simulations for low voltage circuit breakers," in *XVIIIth Symposium on Physics of Switching Arc,* Nové Mesto na Morave, Czech Republic, 2009, pp. 1-11.

[85] J. Lowke, "Simple theory of free-burning arcs," *Journal of Physics D: Applied Physics,* vol. 12, pp. 1873-1887, 1979.

[86] ANSYS Inc., "ICEM CFD 13.0 User Manual," 2010.

[87] F. Reichert, "Private comunication," Technical University of Ilmenau, 2011.

[88] American Institute of Aeronautics and Astronautics (AIAA), "Guide for the Verification and Validation of Computational Fluid Dynamics Simulations," *American Institute of Aeronautics and Astronautics (AIAA),* 1998.

[89] P. J. Roache, *Verification and Validation in Computational Science and Engineering.* Ed: New Mexico, USA: Hermosa publishers, 1998.

[90] M. Casey and T. Wintergerste, *ERCOFTAC Special Interest Group on" Quality and Trust in Industrial CFD".* Ed: European Research Community on Flow, Turbulence and Combustion, 2000.

[91] A. Hauser and S. Kosse, "Numerische konvergenz in der lichtbogensimulation," in *20. Albert-Keil Kontaktseminar,* Karlsruhe, Germany, 2009, pp. 125-128.

[92] P. J. Roache, "Quantification of uncertainty in computational fluid dynamics," *Annual Review of Fluid Mechanics,* vol. 29, pp. 123-160, 1997.

[93] I. ANSYS, "ANSYS CFX Manual," 2010.

[94] M. Rong, Q. Ma, Y. Wu, T. Xu and A. B. Murphy, "The influence of electrode erosion on the air arc in a low-voltage circuit breaker," *Journal of Physics D: Applied Physics,* vol. 106, pp. 023308-023318, 2009.

[95] F. Yang, M. Rong, Y. Wu, A. B. Murphy and et al., "Numerical analysis of the influence of splitter-plate erosion on an air arc in the quenching chamber of a low-voltage circuit breaker," *Journal of Physics D: Applied Physics,* vol. 43, pp. 434011-434023, 2010.

[96] C. Rumpler, H. Stammberger and A. Zacharias, "Low-voltage arc simulation with out-gassing polymers," in *57th Holm Conference on Electrical Contacts (Holm),* Minneapolis, USA, 2011, pp. 1-8.

# ANNEX

ANNEX



(a)  (b)
(a)  (b)
(a)  (b)
(a)  (b)
(a)  (b)
(a)  (b)
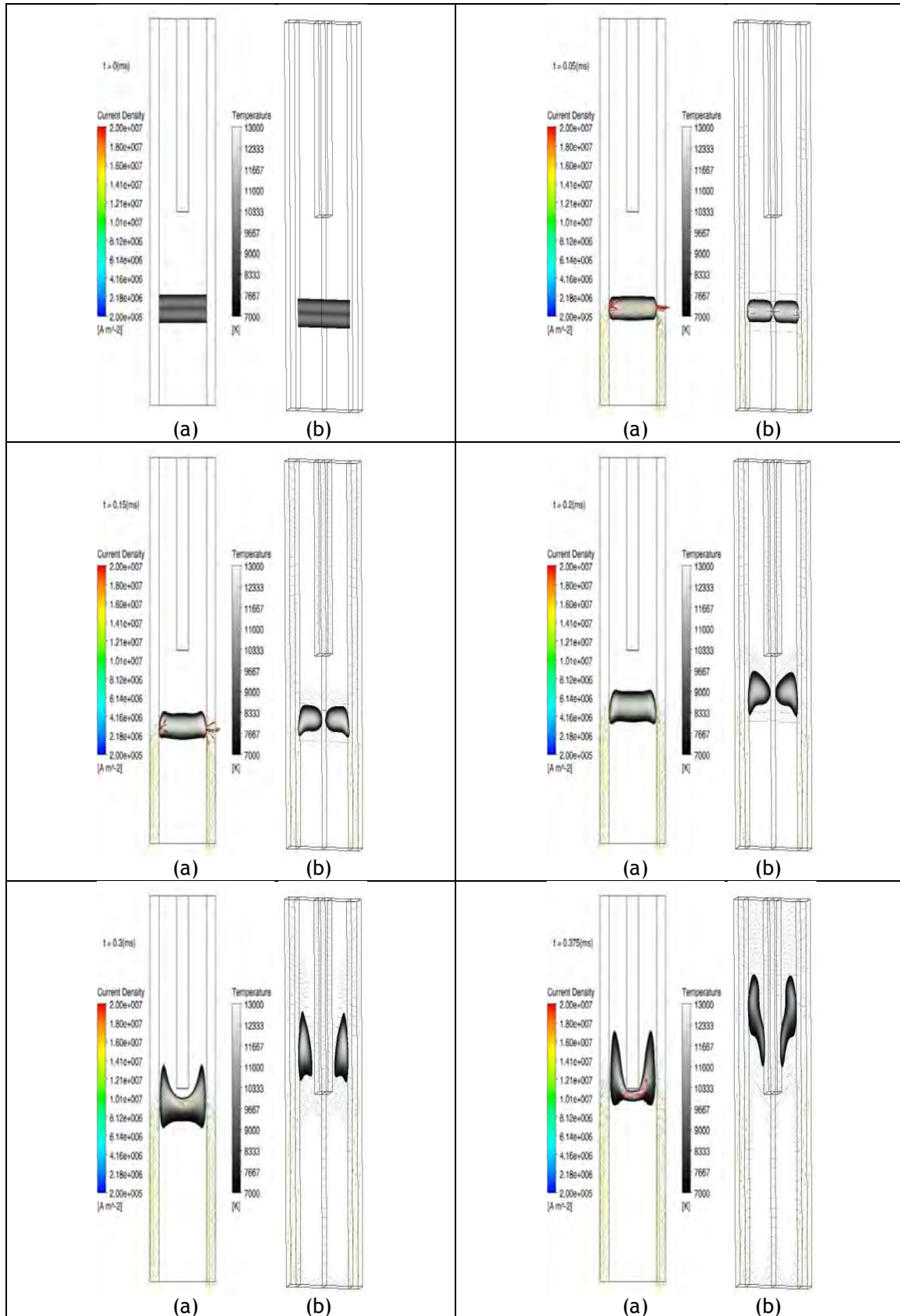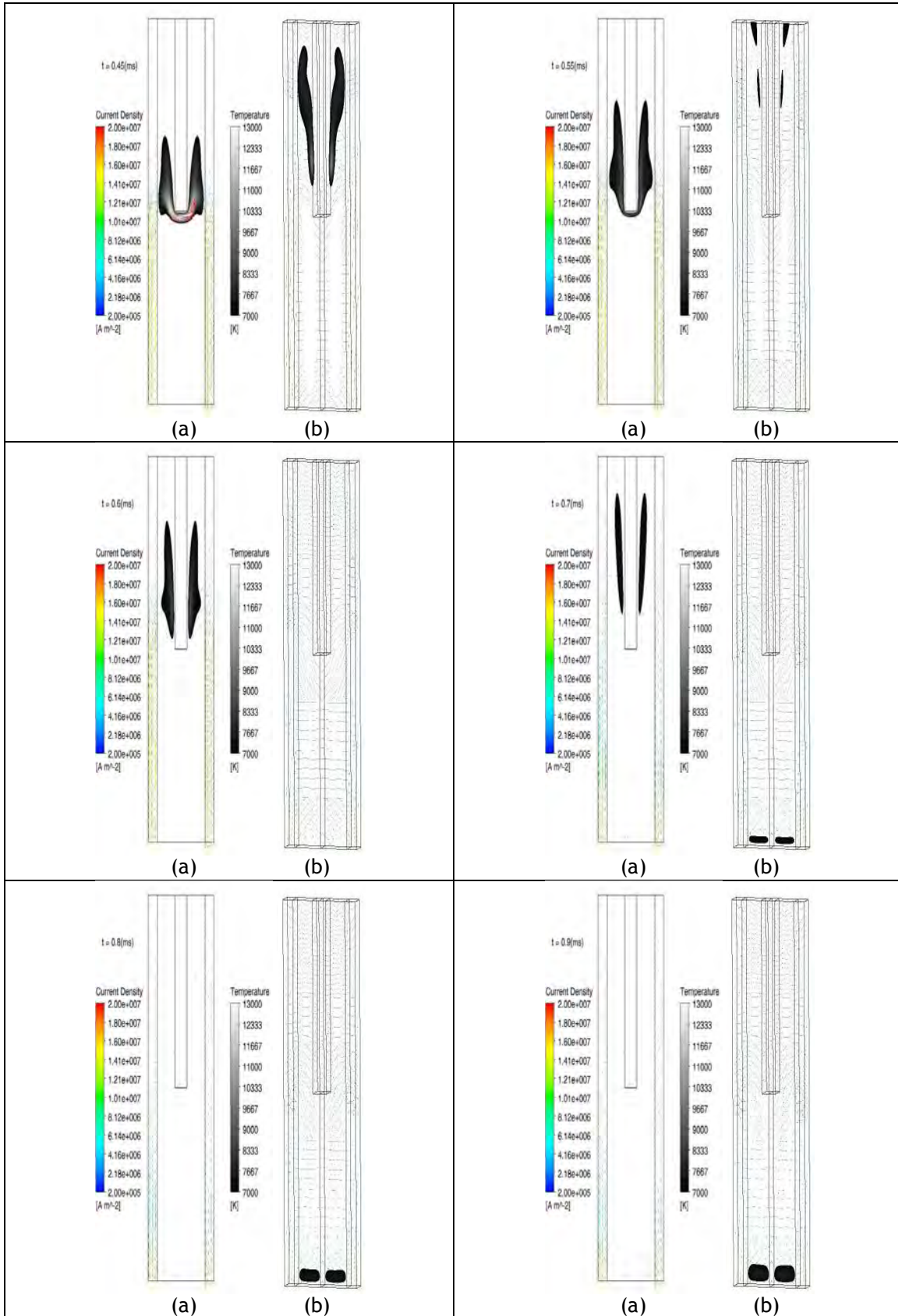
Figure A-1. Arc movement, represented by temperature and current density on a model without symmetry (left) and with (right)
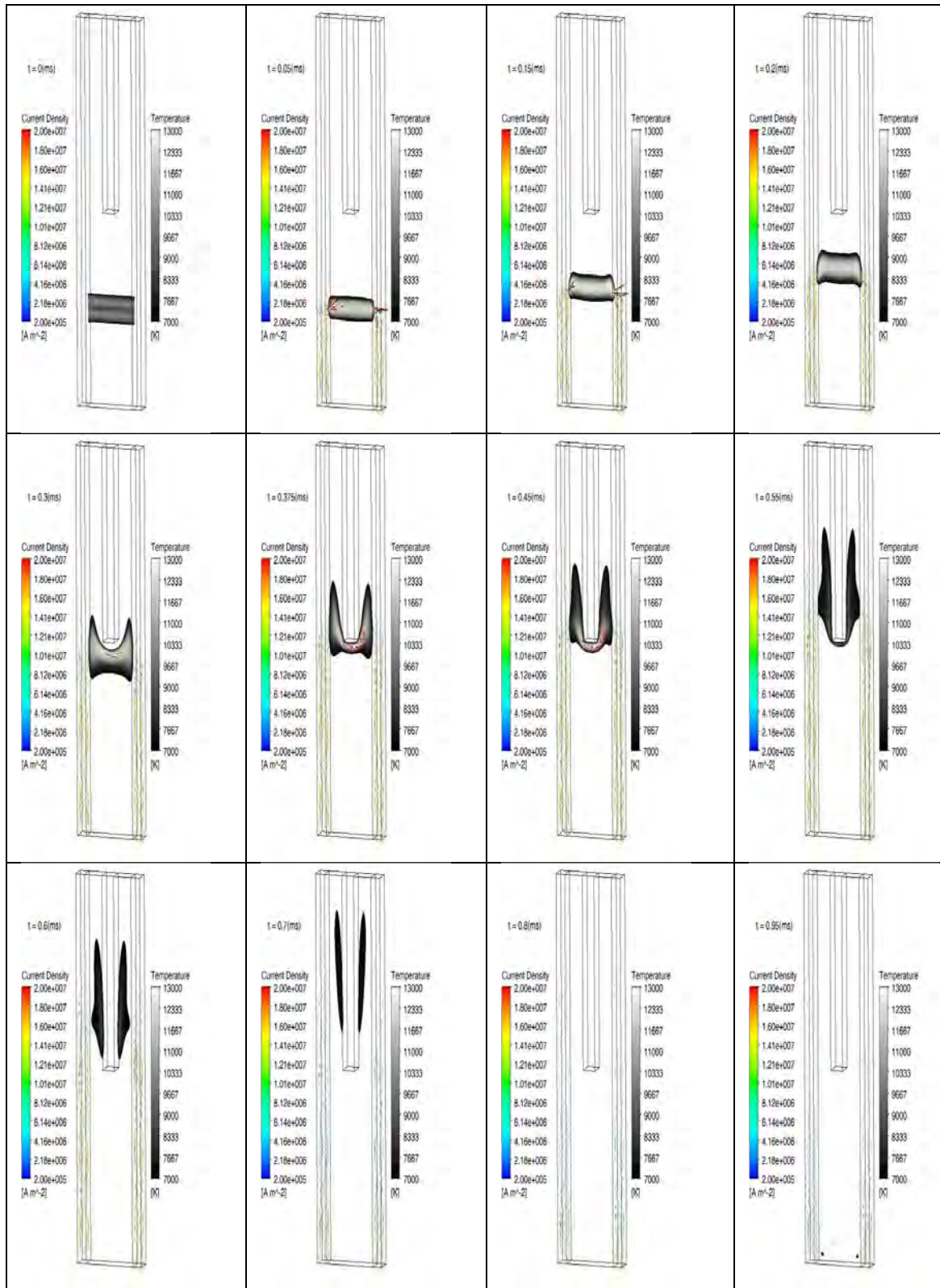
Figure A-2 Arc movement behaviour, expressed by temperature and current density for case A.1, 50A, 1SP and V-J arc root curve for 10V peak
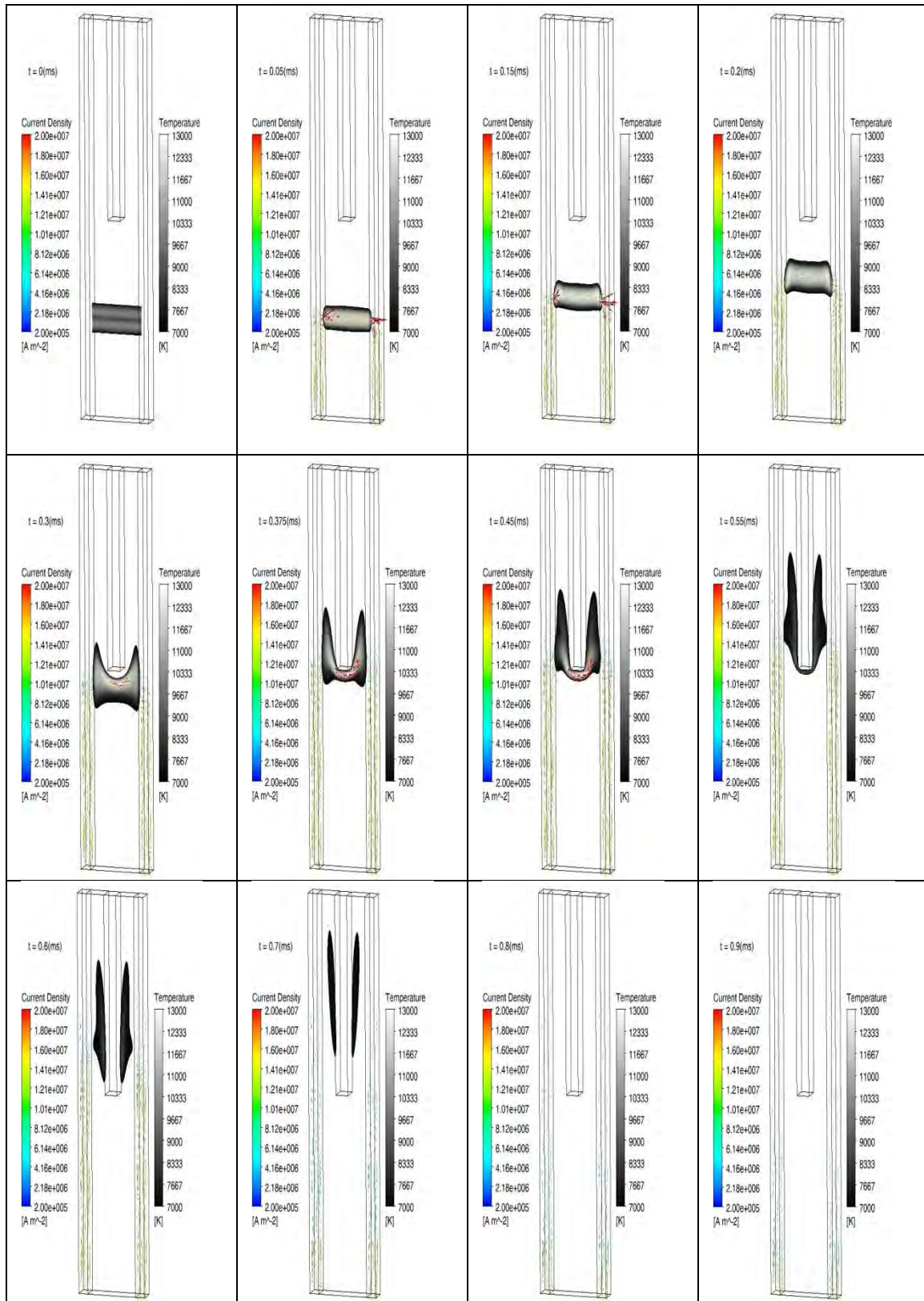
Figure A-3 Arc movement behaviour, expressed by temperature and current density for case A.2, 50A, 1SP and V-J arc root curve for 17,1V peak
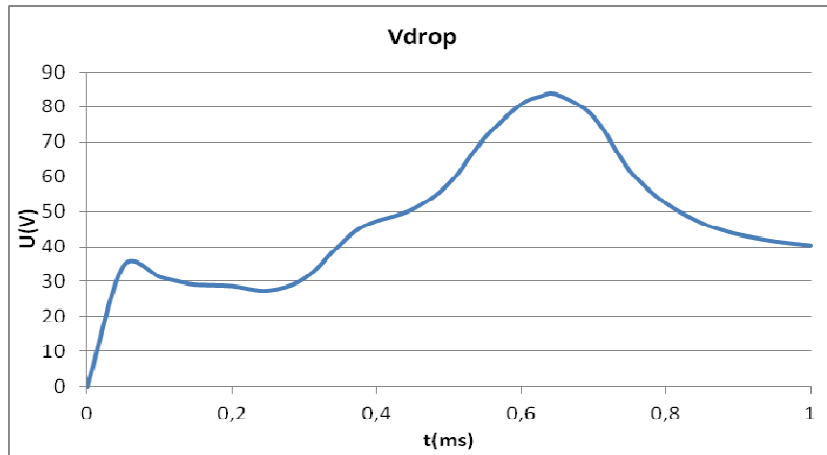
Figure A-4 Arc voltage for 50A 1SP model, V-J arc root curve for 17,1V peak, for case A.2
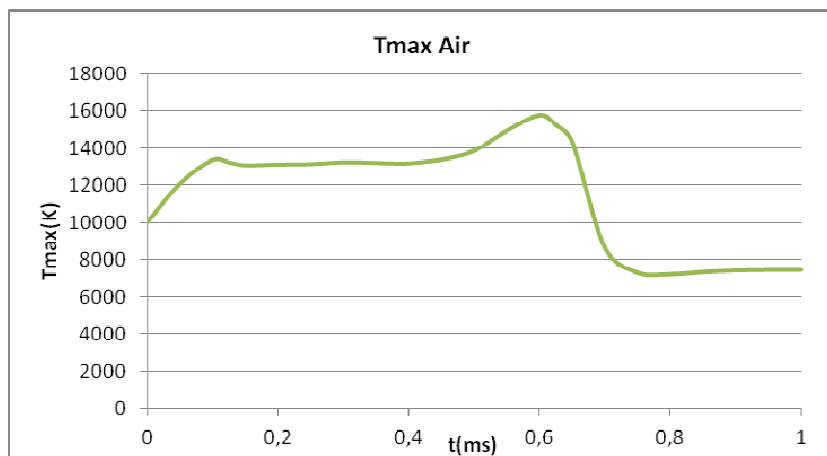


Figure A-5 Maximum temperature in air for 50A 1SP model, V-J arc root curve for 17,1V peak, for case A.2
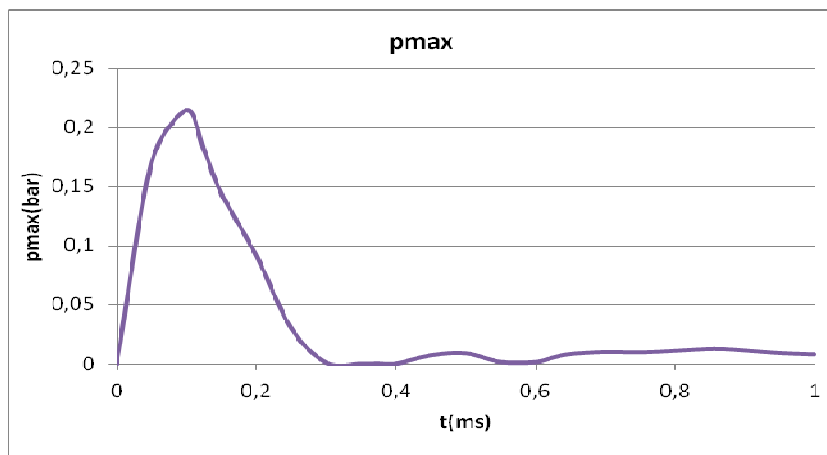


Figure A-6 Maximum pressure in air for 50A 1SP model, V-J arc root curve for 17,1V peak, for case A.2
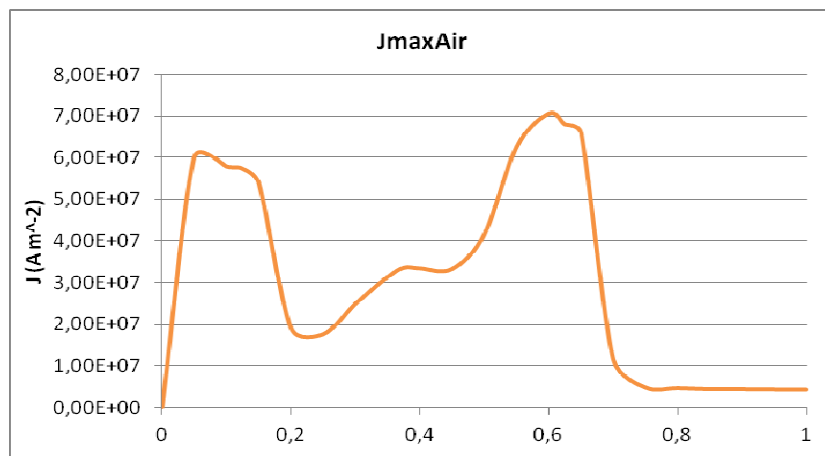
Figure A-7 Maximum current density in air for 50A 1SP model, V-J arc root curve for 17,1V peak, for case A.2
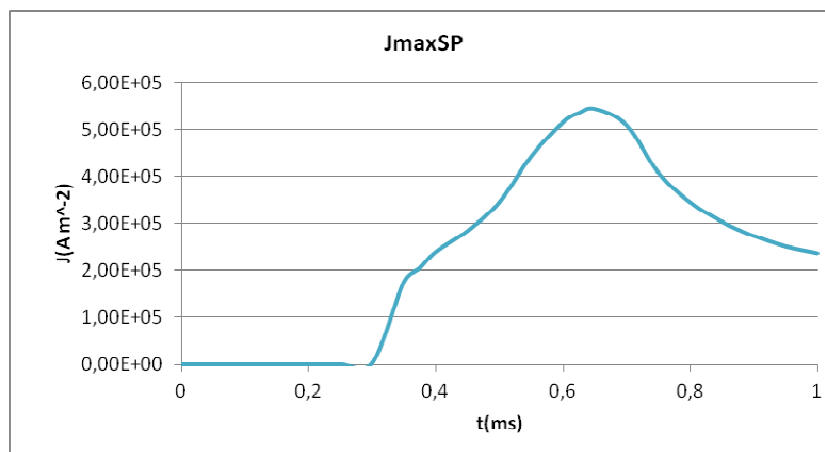


Figure A-8 Maximum current density in SP for 50A 1SP model, V-J arc root curve for 17,1V peak, for case A.2
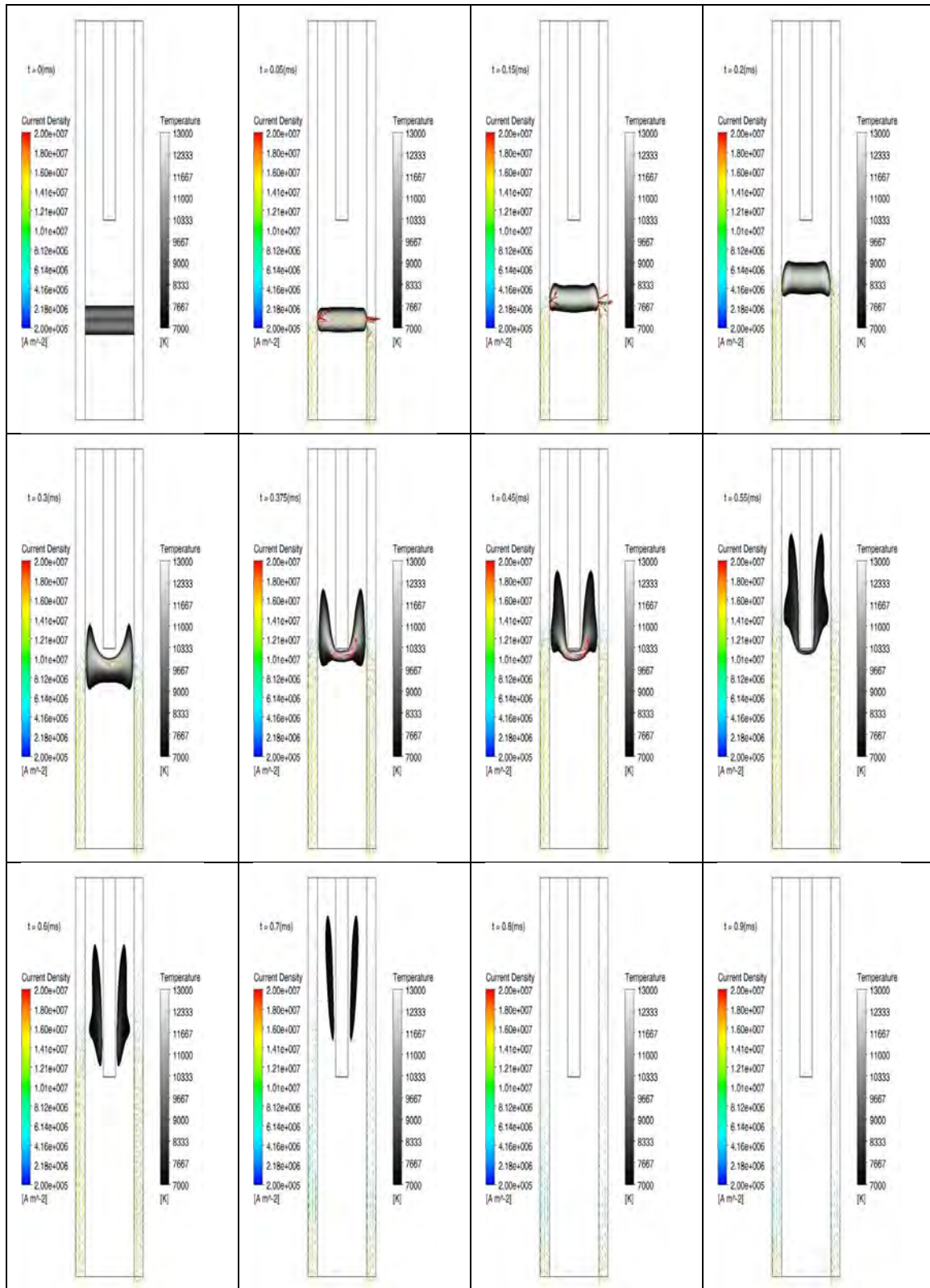
Figure A-9 Arc movement behaviour, expressed by temperature and current density for case A.3, 50A, 1SP and V-J arc root curve for 19,7 peak
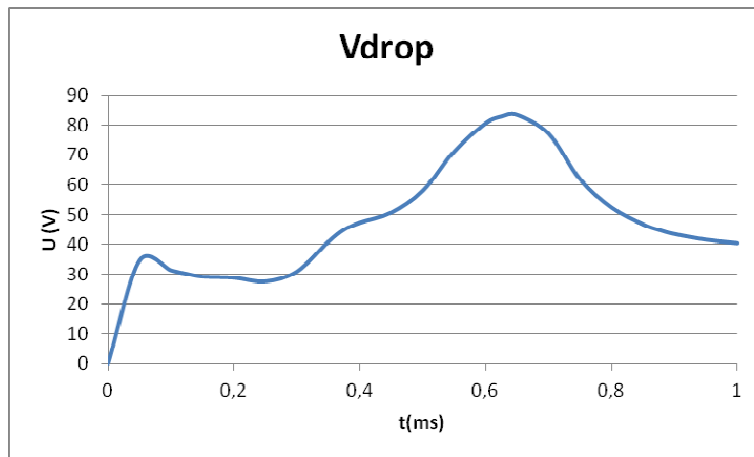
Figure A-10  Arc voltage for 50A 1SP model, V-J arc root curve for 19,7V peak, for case A.3
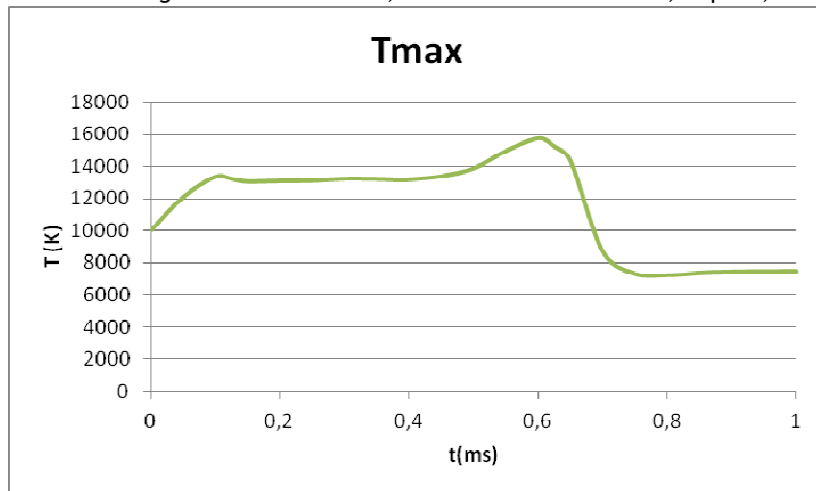


Figure A-11 Maximum temperature in the air for 50A 1SP model, V-J arc root curve for 19,7V peak, for case A.3
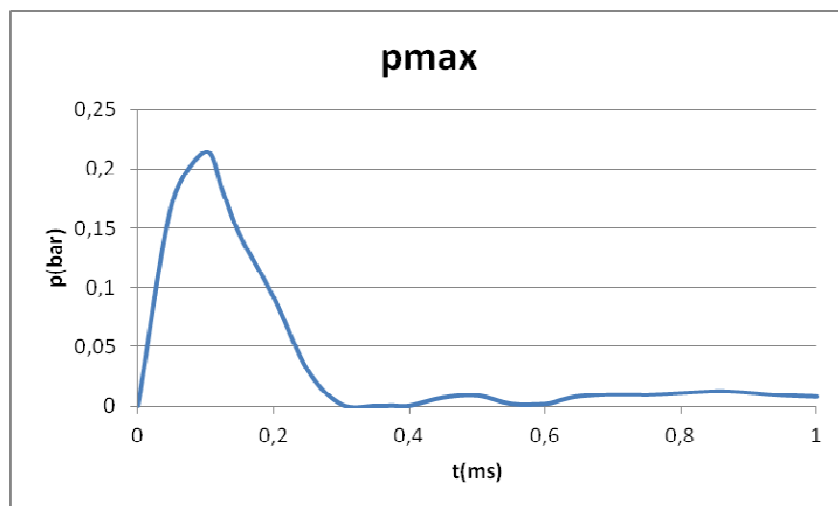


Figure A-12 Maximum pressure for 50A 1SP model, V-J arc root curve for 19,7V peak, for case A.3
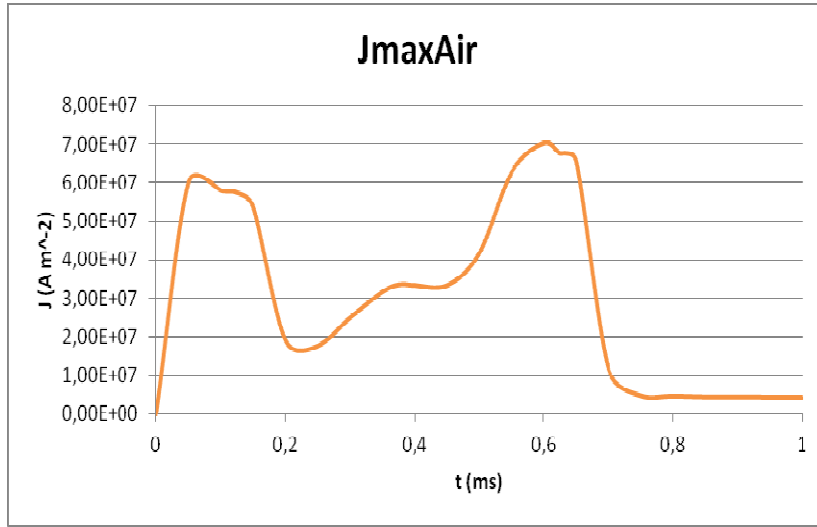
Figure A-13Maximum current density in air for 50A 1SP model, V-J arc root curve for 19,7V peak, for case A.3
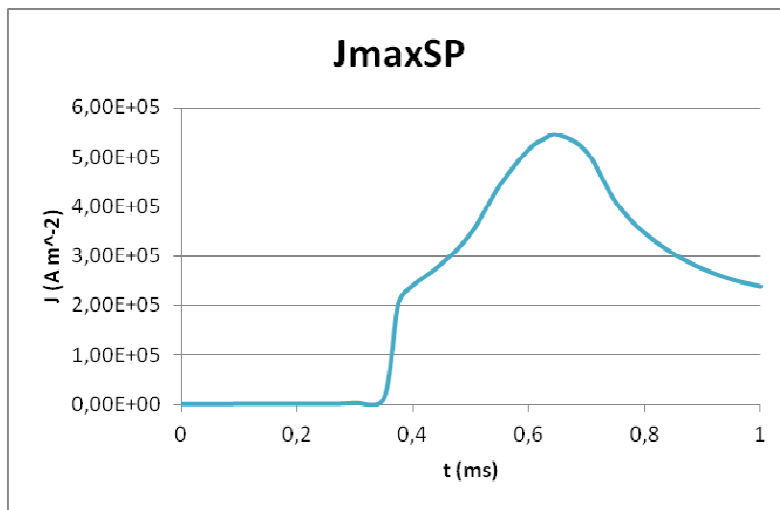


Figure A-14 Maximum current density in splitter plate for 50A 1SP model, V-J arc root curve for 19,7V peak, for case A.3
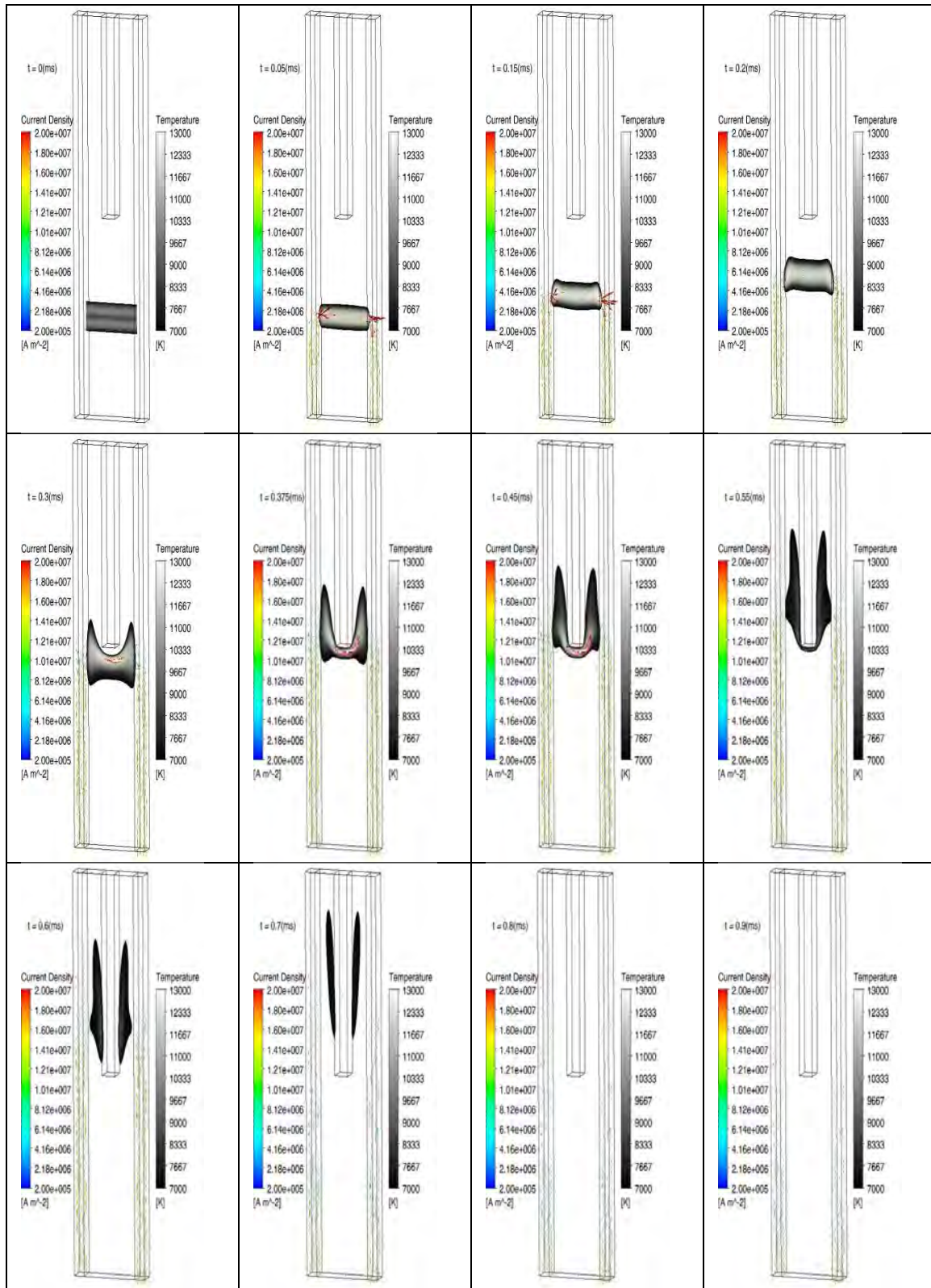
Figure A-15 Arc movement behaviour, expressed by temperature and current density for case A.4, 50A, 1SP and V-J arc root curve for 22,3 peak
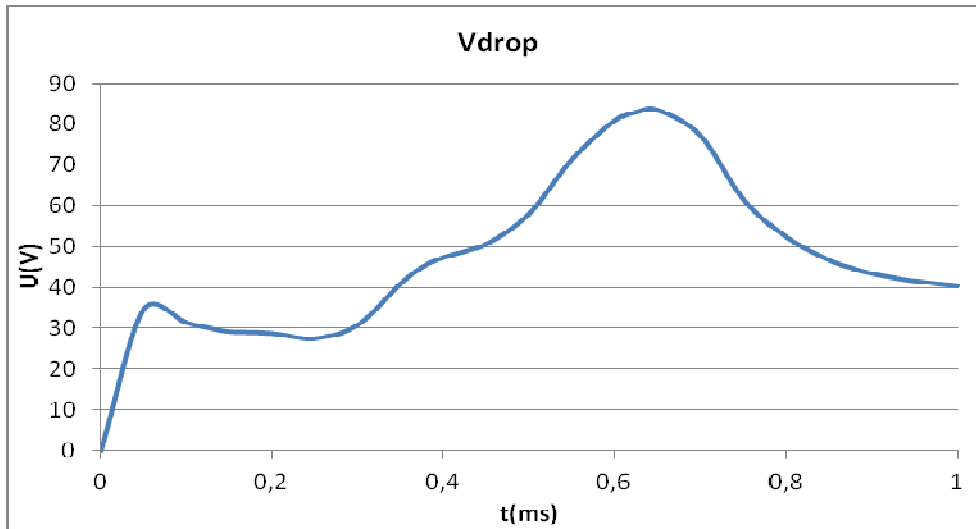
Figure A-16 Voltage drop for 50A 1SP model, V-J arc root curve for 19,7V peak, for case A.4
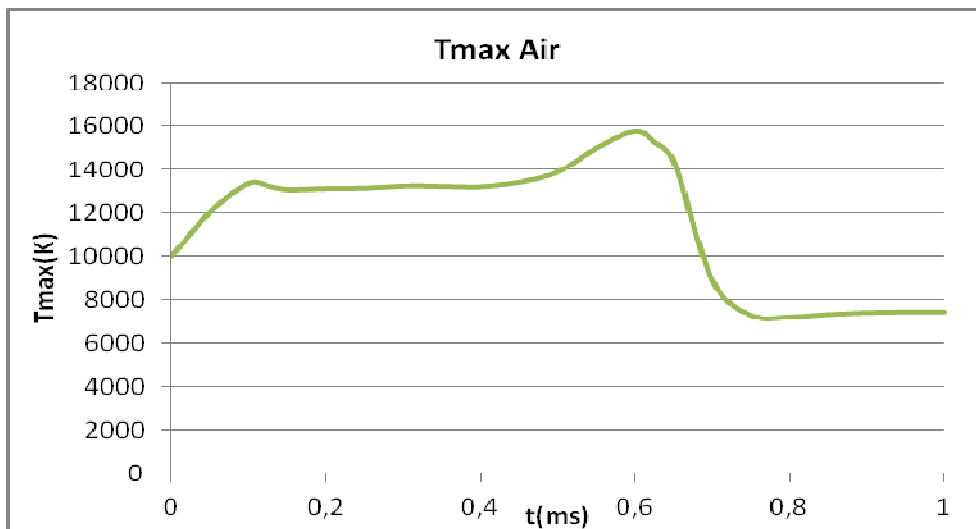


Figure A-17 Maximum temperature in air for 50A 1SP model, V-J arc root curve for 22,3V peak, for case A.4
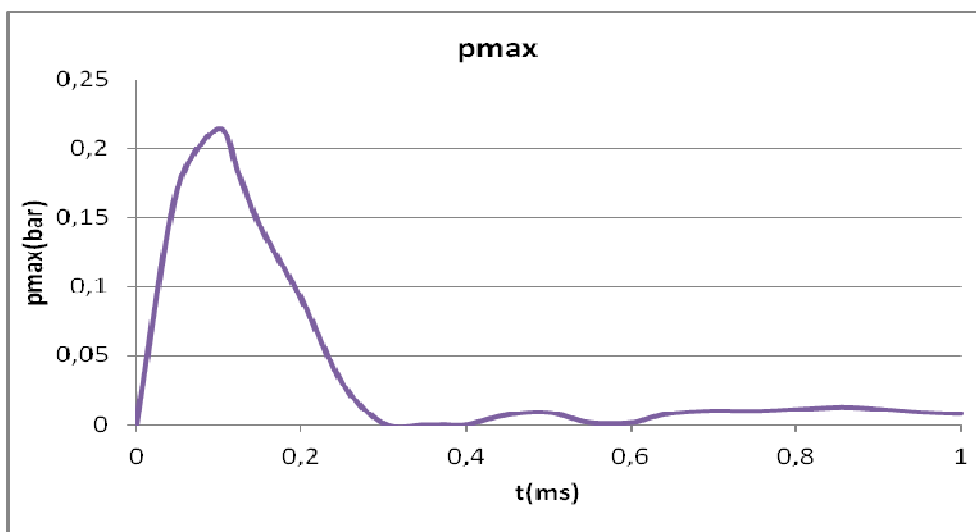


Figure A-18 Maximum pressure for 50A 1SP model, V-J arc root curve for 22,3V peak, for case A.4
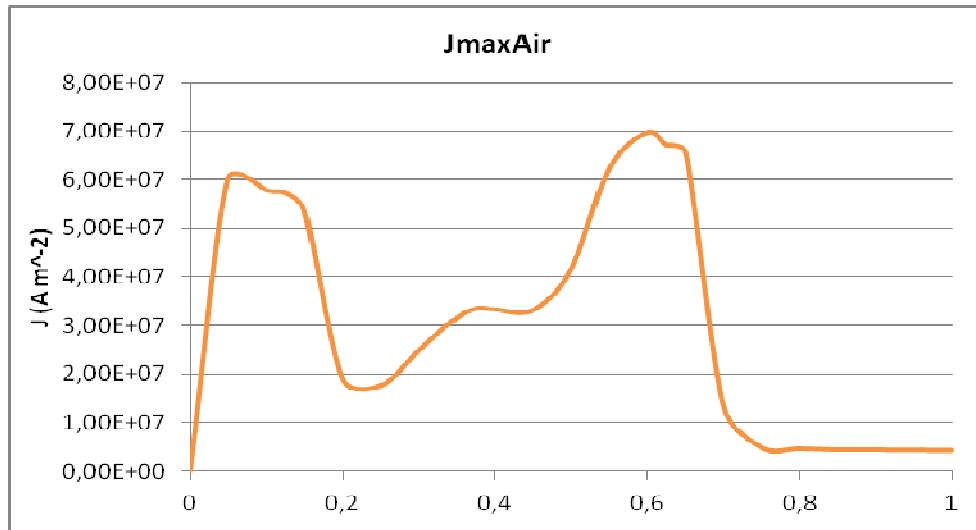
Figure A-19 Maximum current density in air for 50A 1SP model, V-J arc root curve for 22,3V peak, for case A.4
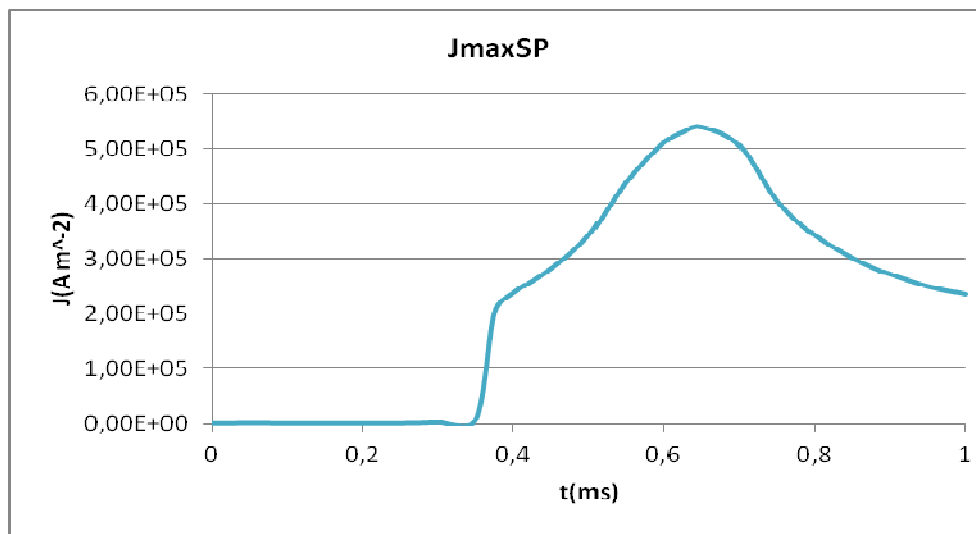


Figure A-20 Maximum current density in splitter plate for 50A 1SP model, V-J arc root curve for 22,3V peak, for case A.4
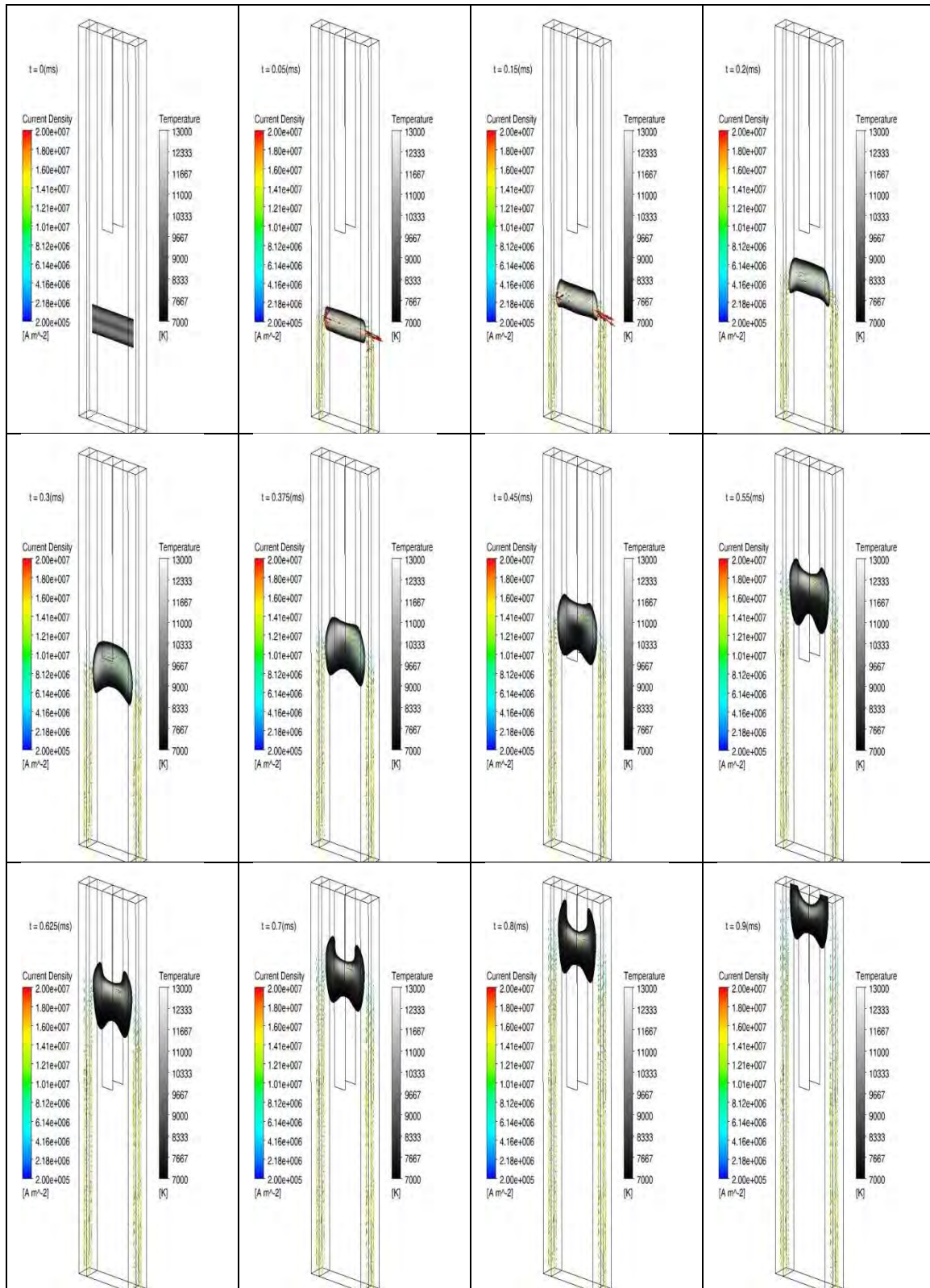
Figure A-21 Arc movement expressed by current density and temperature for 50A and zero splitter plate (0SP), case B.1
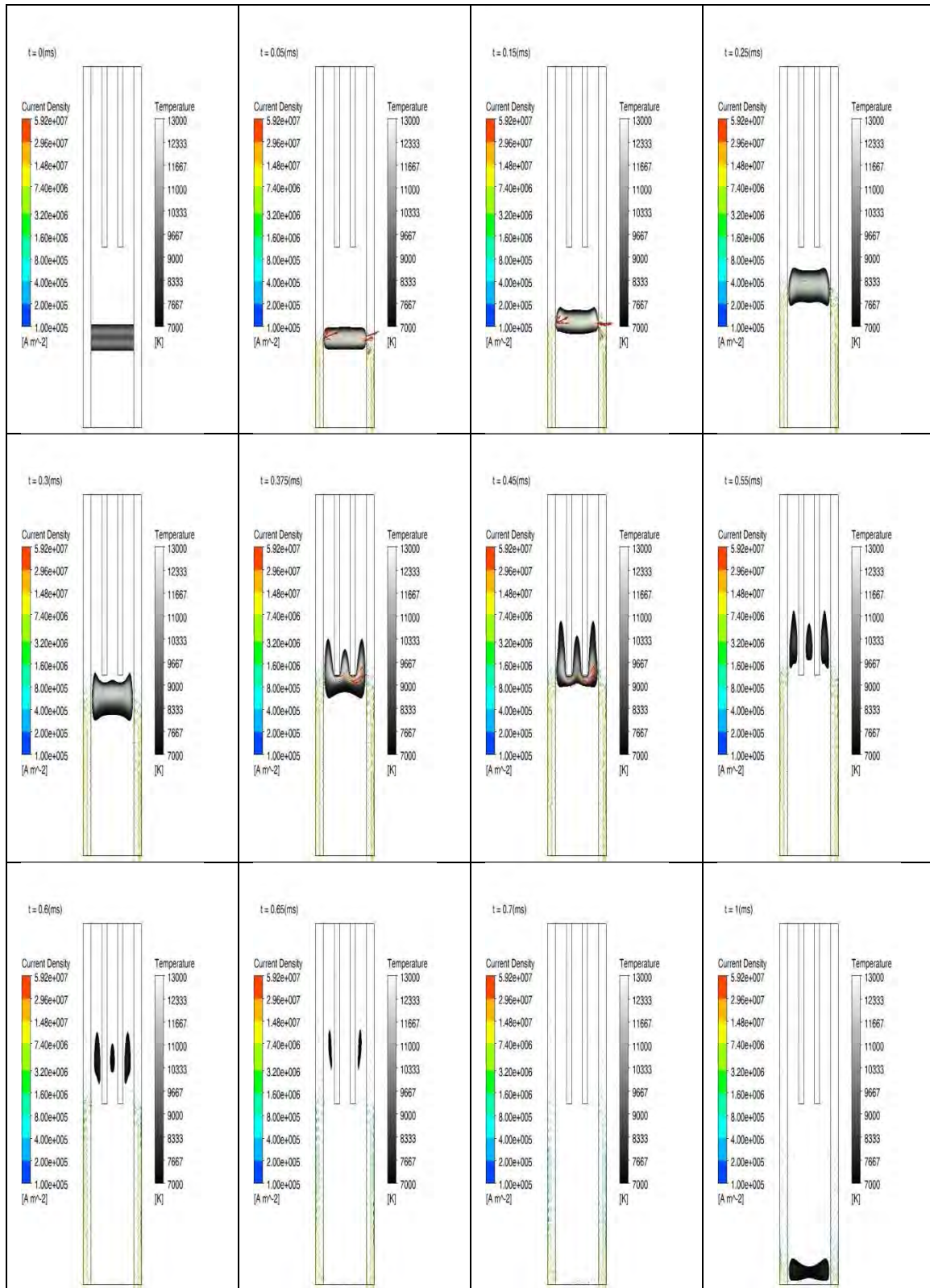
Figure A-22 Arc movement expressed by current density and temperature for 50A and two splitter plate (2SP), case B.2
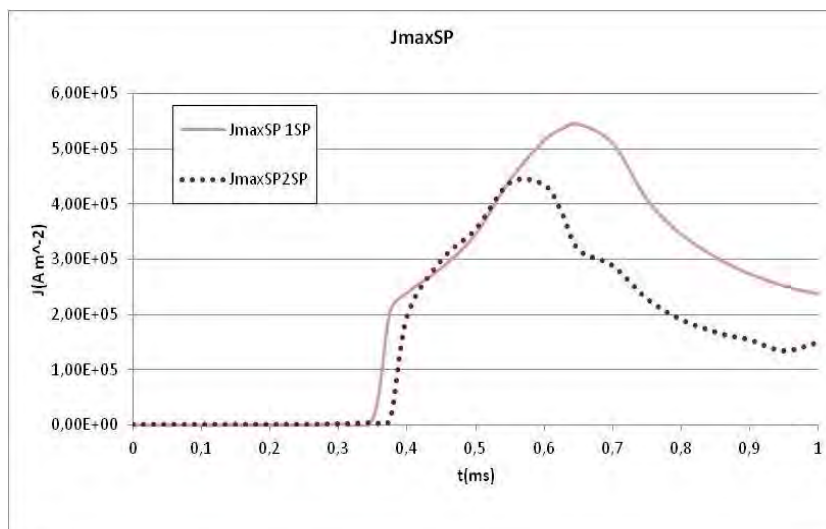
Figure A-23 Maximum current density in splitter plate for 50A model, SP comparison, case B
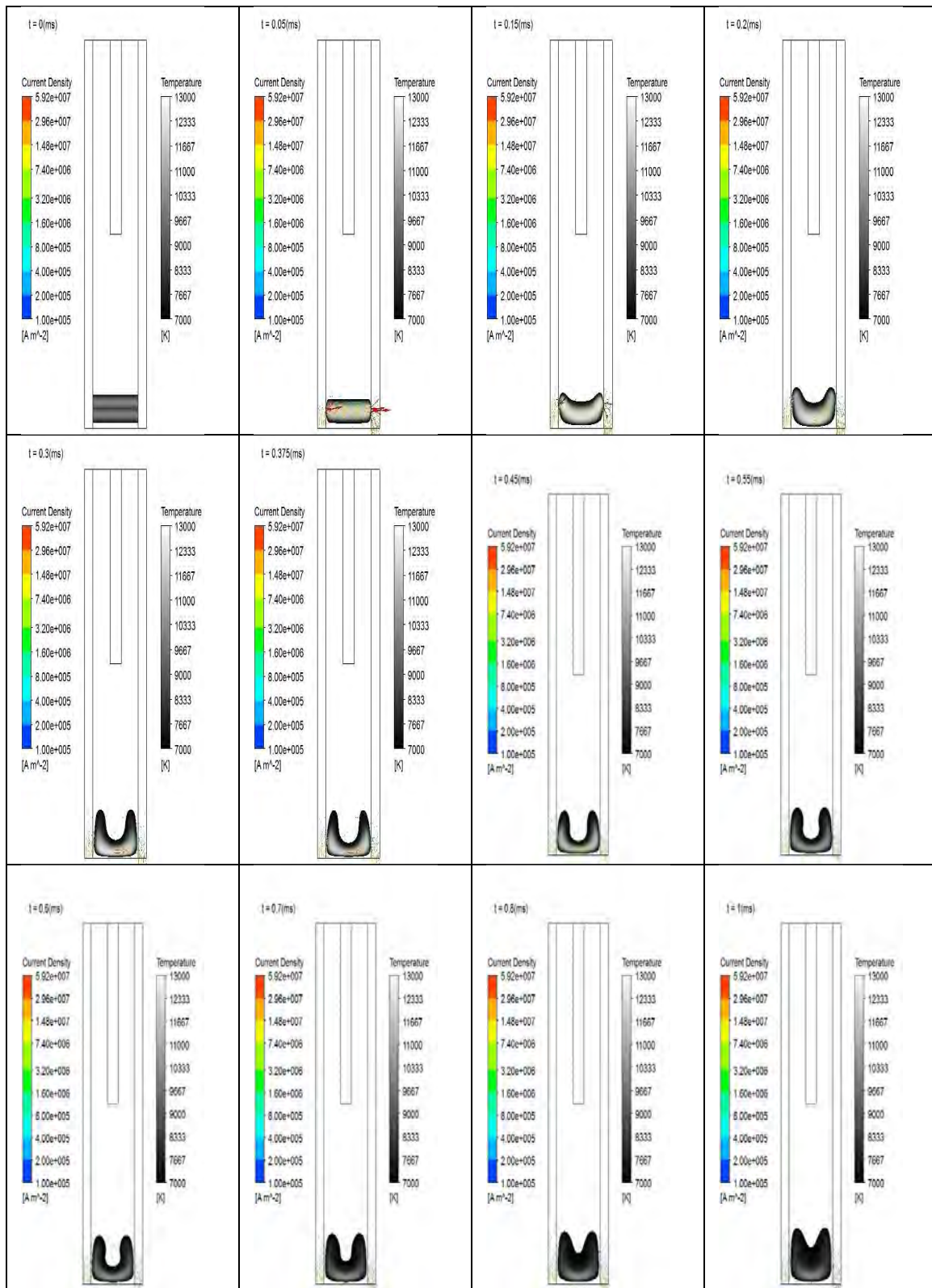
Figure A-24 Arc movement expressed by temperature and current density for lower arc ignition, 50A input current and 0SP, case C.1
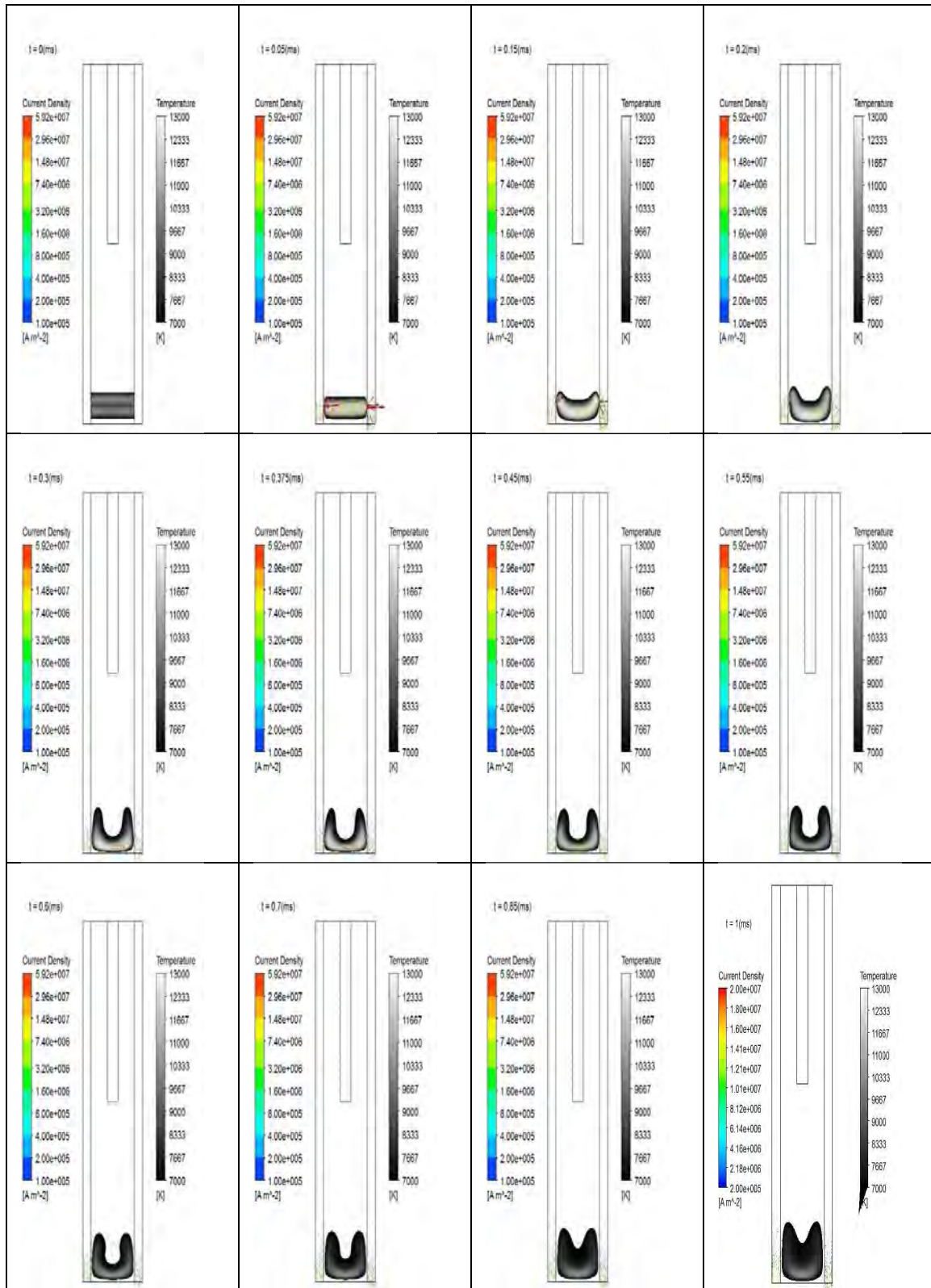
Figure A-25 Arc movement expressed by temperature and current density for lower arc ignition, 50A input current and 1SP, case C.2
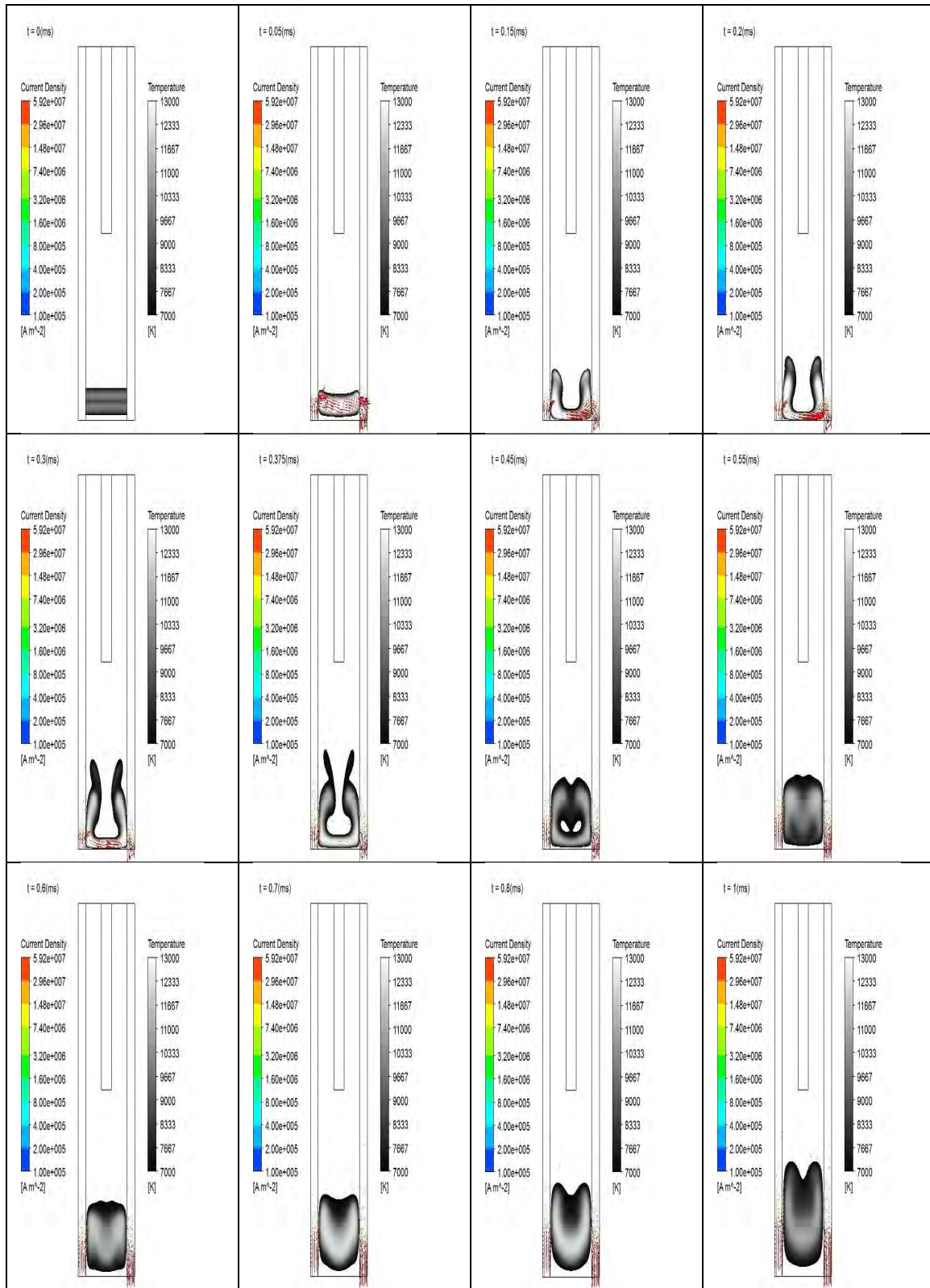
Figure A-26 Arc movement expressed by temperature and current density for lower arc ignition, 100A input current and 0SP, case C.3
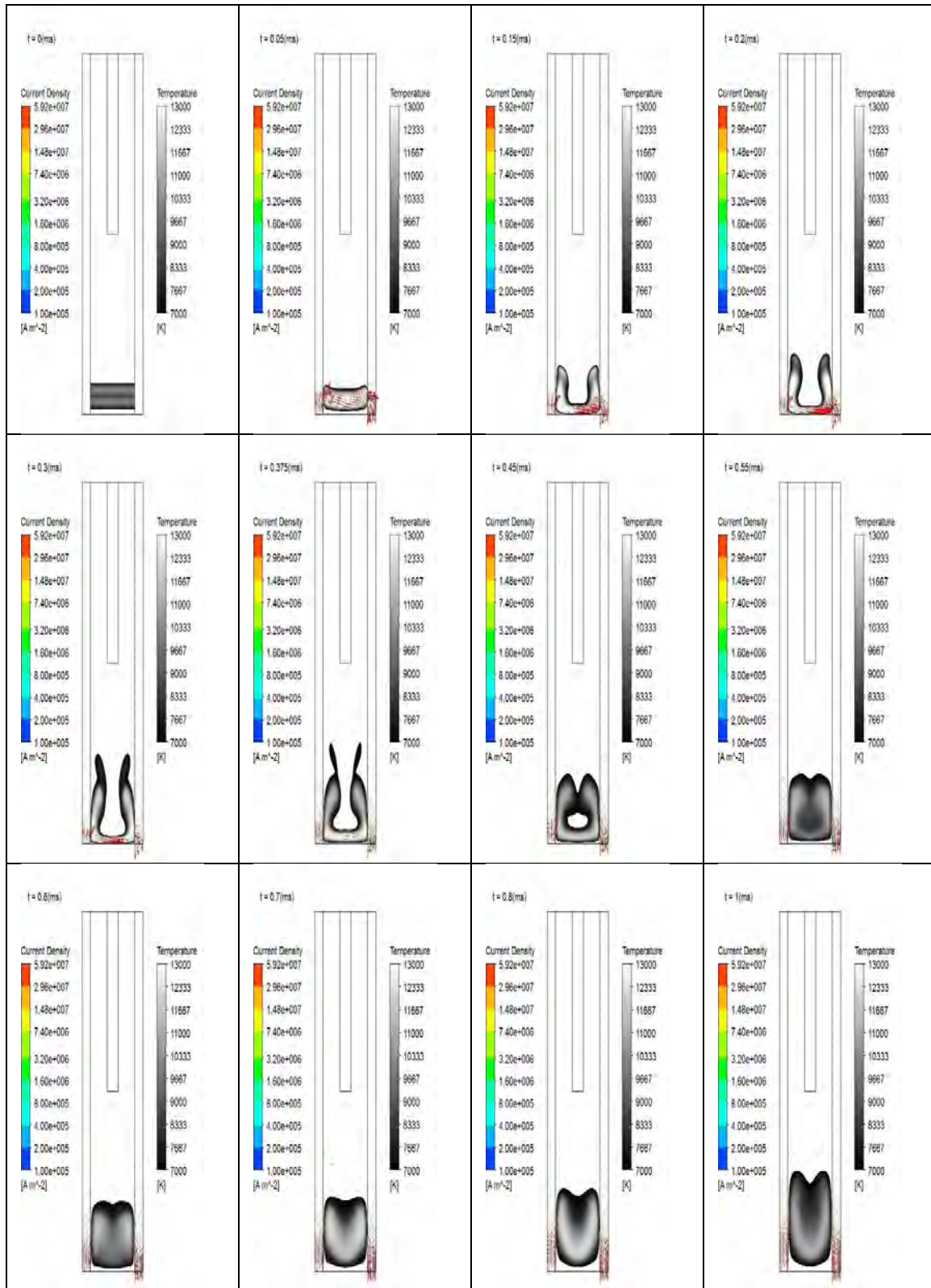
Figure A-27 Arc movement expressed by temperature and current density for lower arc ignition, 100A input current and 1SP, case C.4
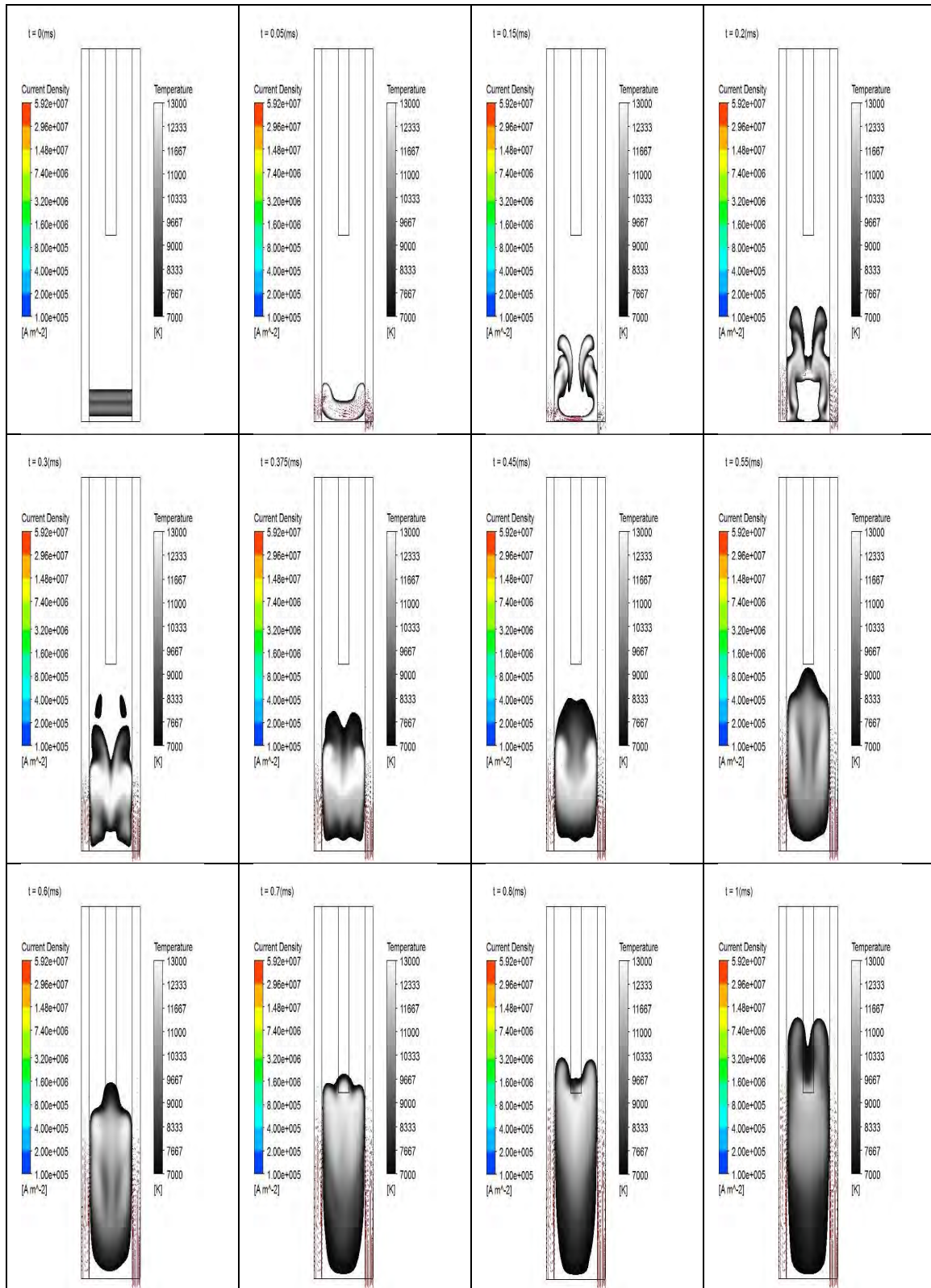
Figure A-28 Arc movement expressed by temperature and current density for lower arc ignition, 200A input current and 0SP, case C.5
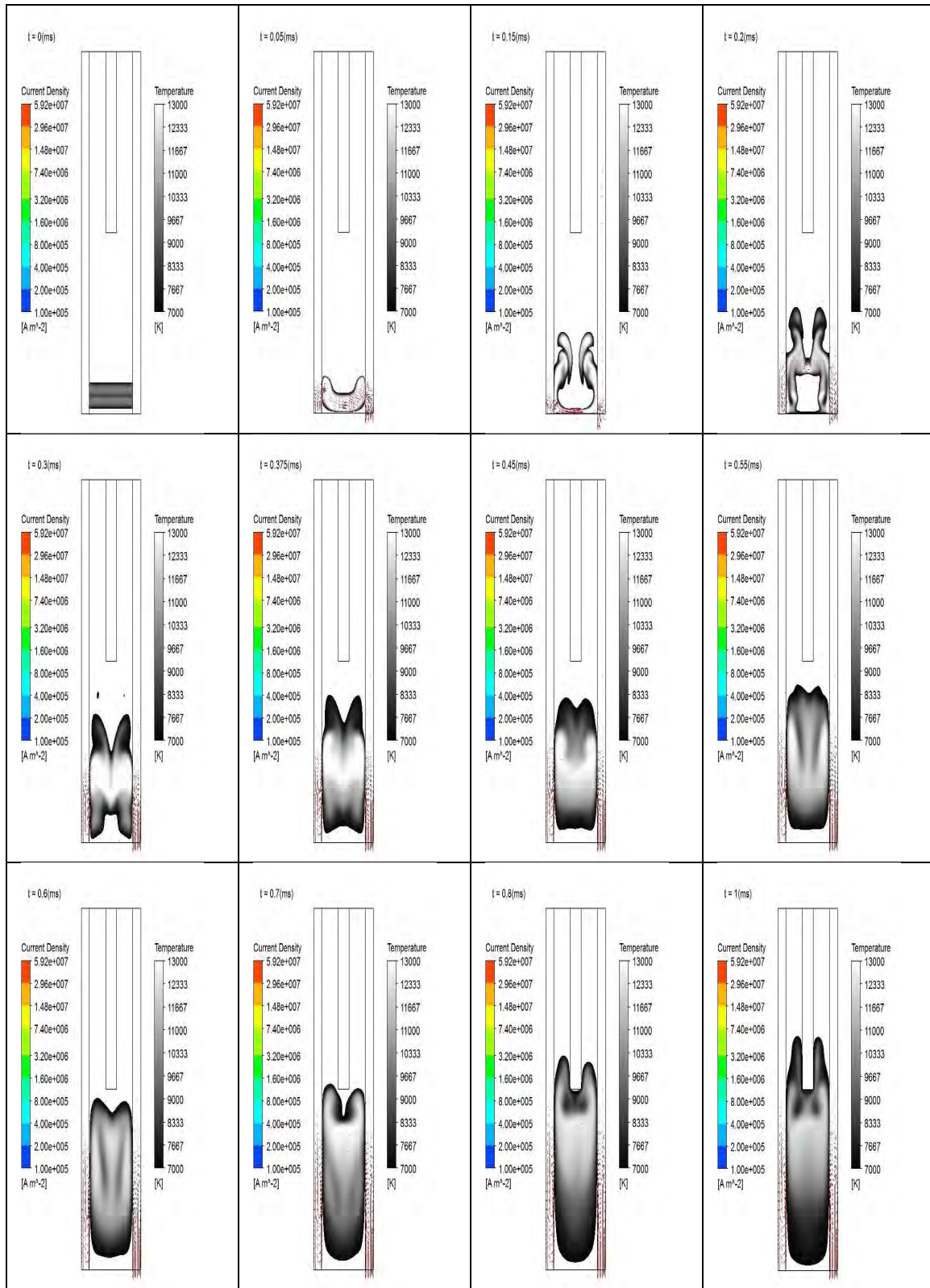
Figure A-29 Arc movement expressed by temperature and current density for lower arc ignition, 200A input current and 1SP, case C.6
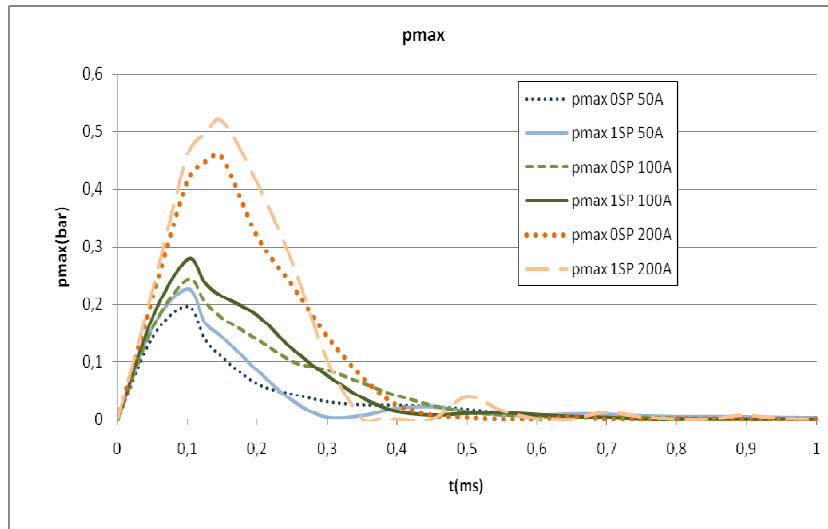
Figure A-30 Maximum pressure in air for 50, 100 and 200A, 0SP and 1SP, case C
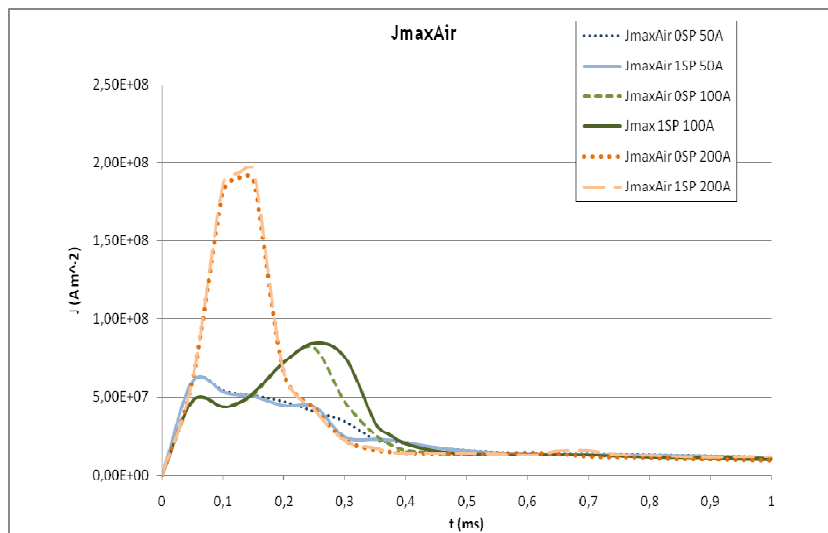


Figure A-31 Maximum current density in air for 50, 100 and 200A, 0SP and 1SP, case C
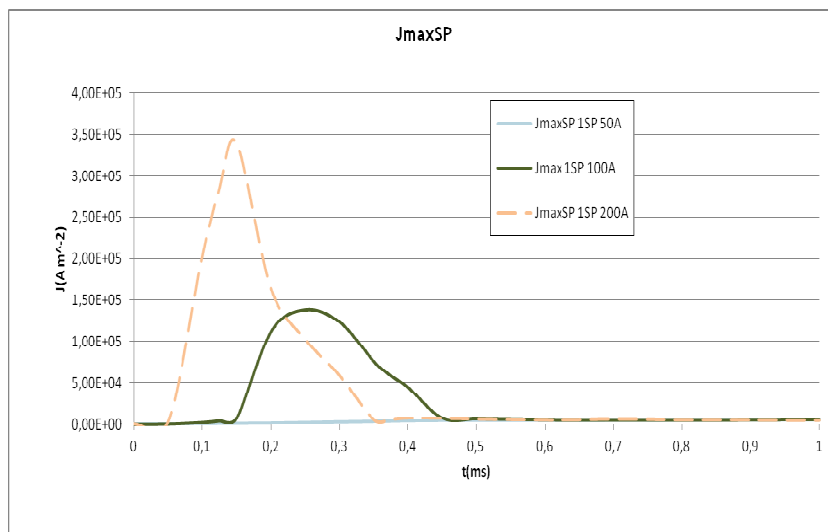


Figure A-32 Maximum current density in splitter plate for 50, 100 and 200A, 0SP and 1SP, case C
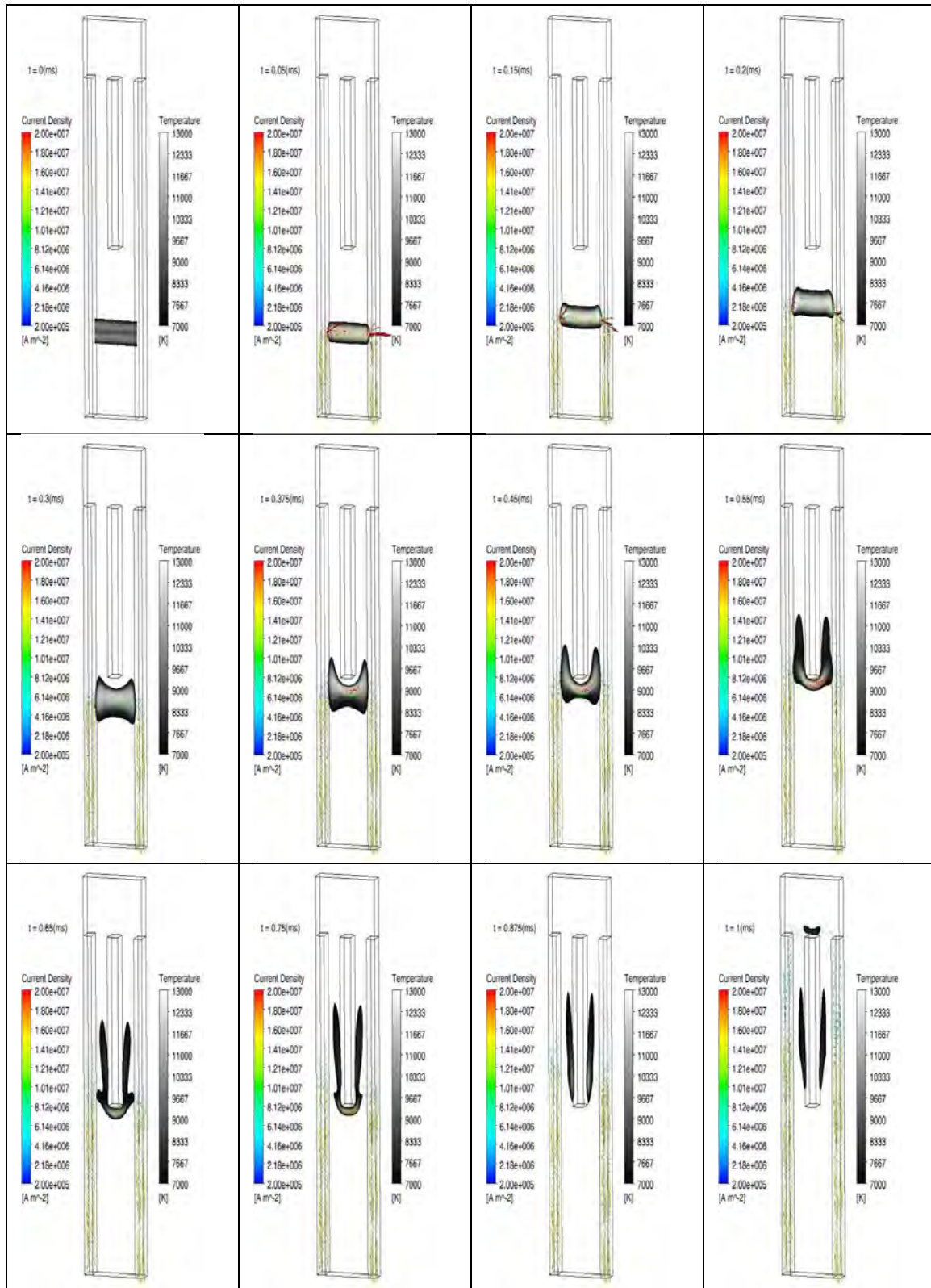
Figure A-33 Arc movement expressed by temperature and current density for expansion volume geometry, 50A input current and 1SP, case D.1
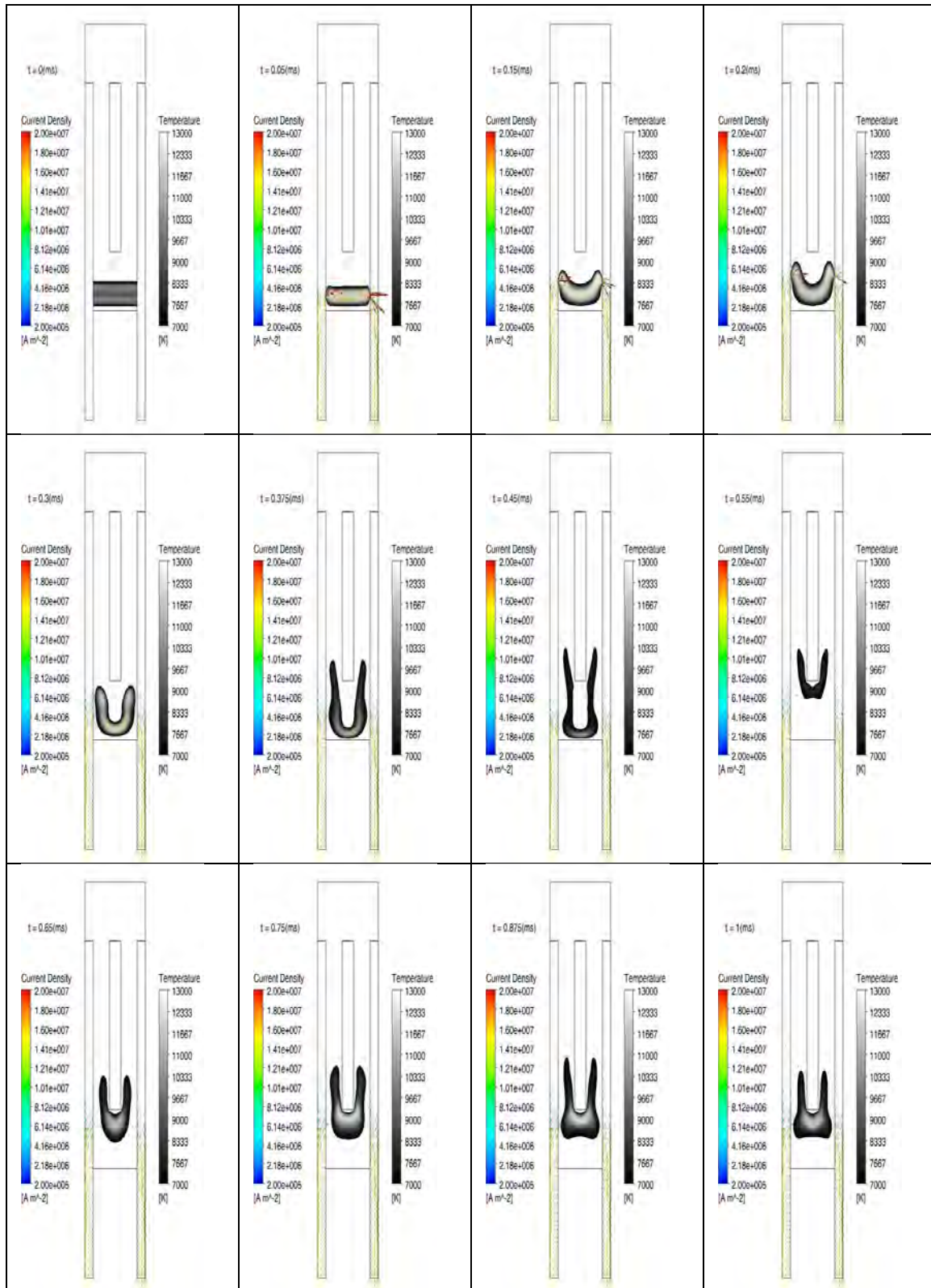
Figure A-34 Arc movement expressed by temperature and current density for expansion volume and air wall down higher geometry, 50A input current and 1SP, case D.2
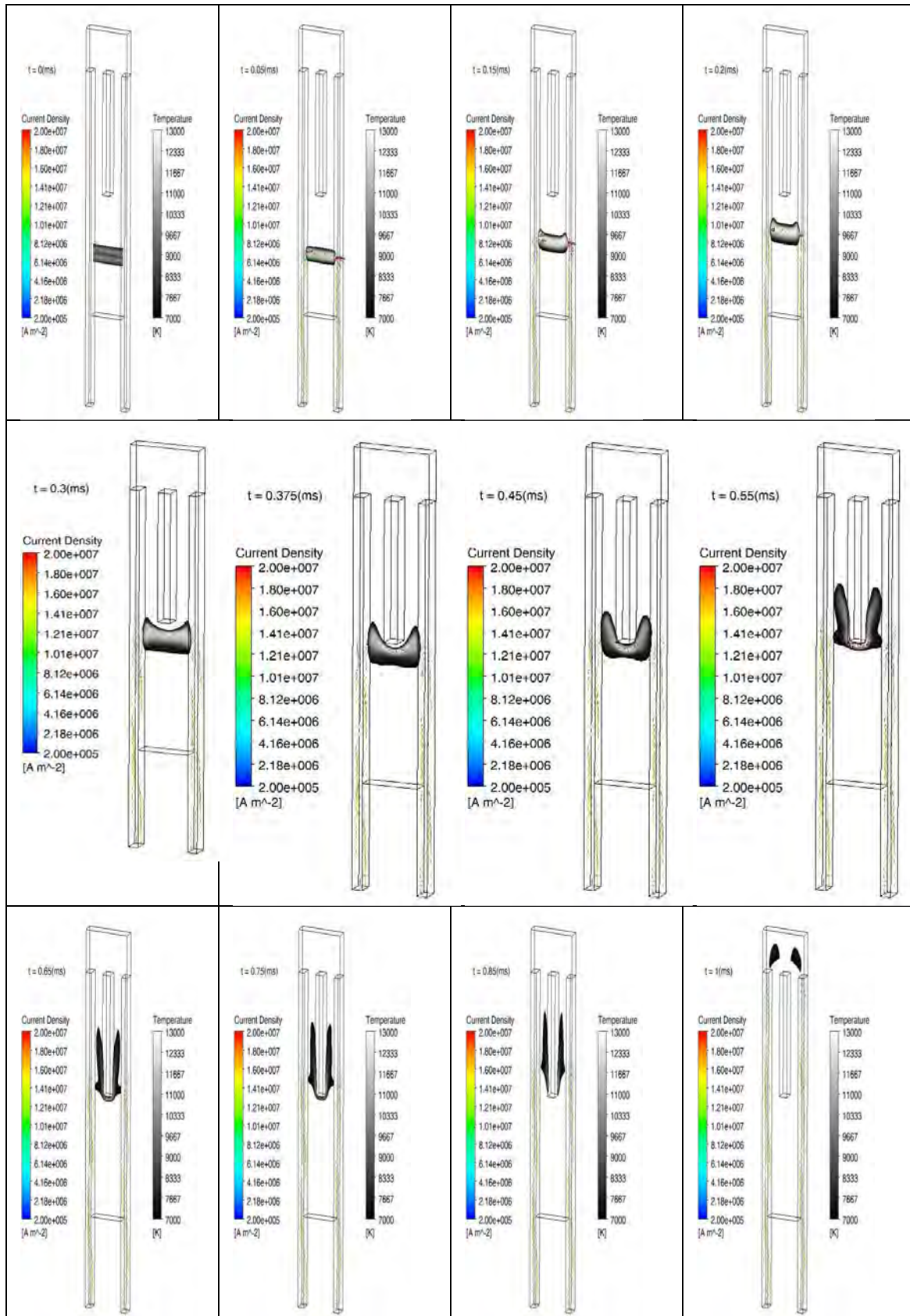
Figure A-35 Arc movement expressed by temperature and current density for expansion volume and longer electrodes on the down side, 50A input current and 1SP, case D.3
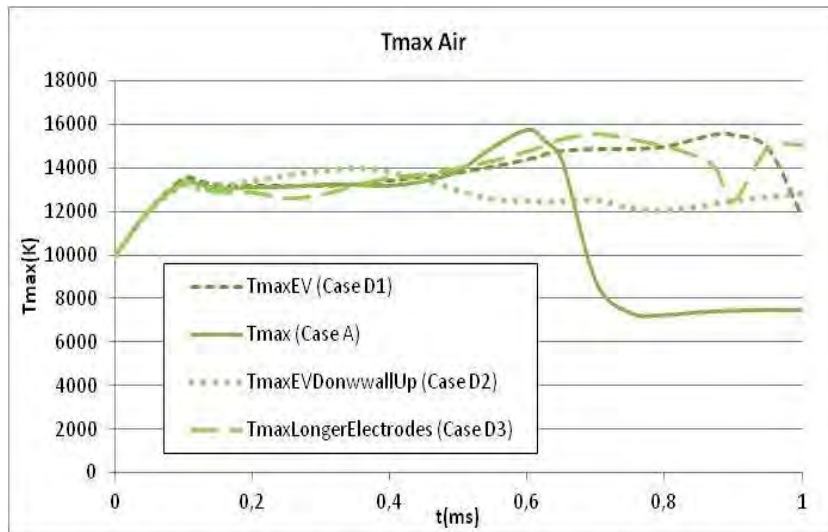
Figure A-36 Maximum temperature in air for 50A base case, expansion volume, longer electrodes and lower wall up, cases D and A
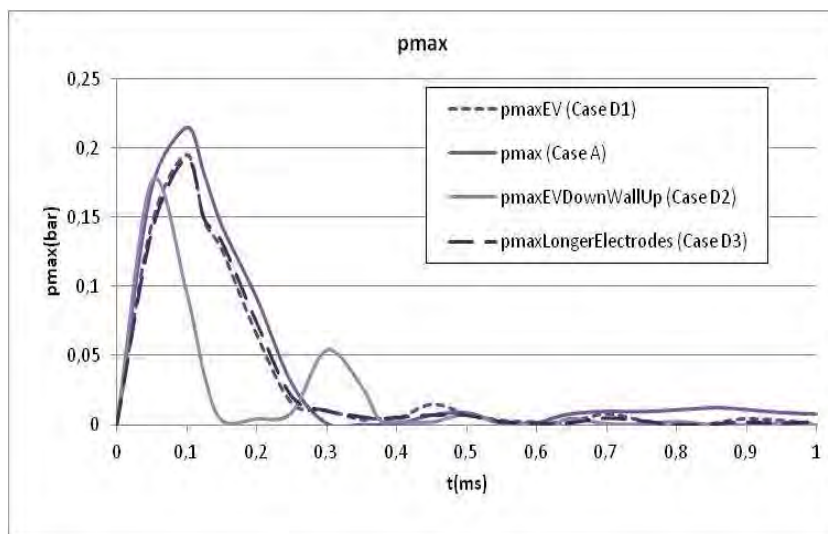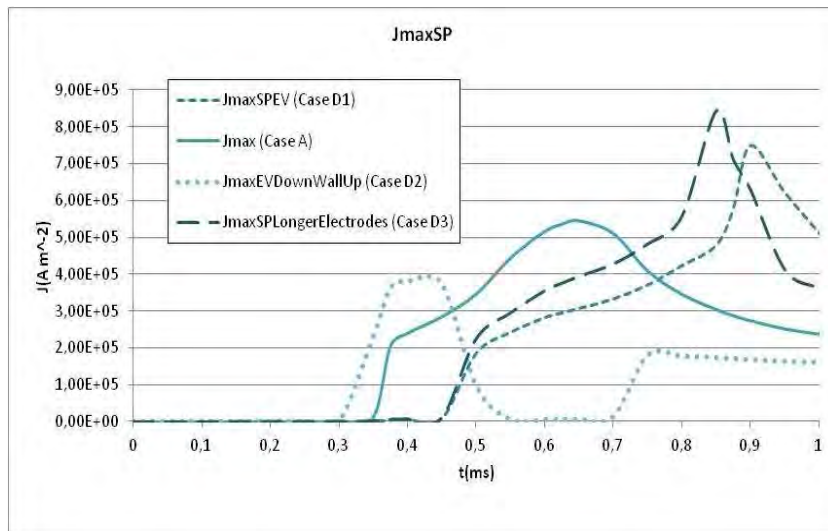


Figure A-37 Maximum pressure in air for 50A base case, expansion volume, longer electrodes and lower wall up, cases D and A
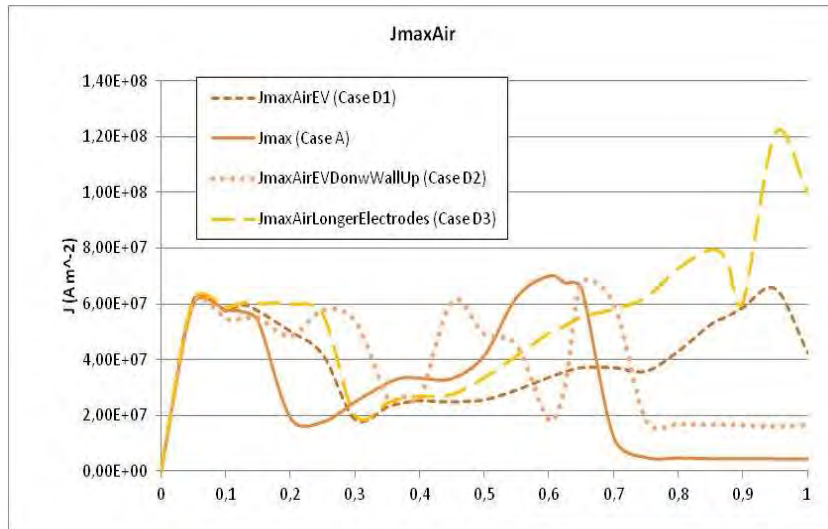
Figure A-38 Maximum current density in air for 50A base case, expansion volume, longer electrodes and lower wall up, cases D and A
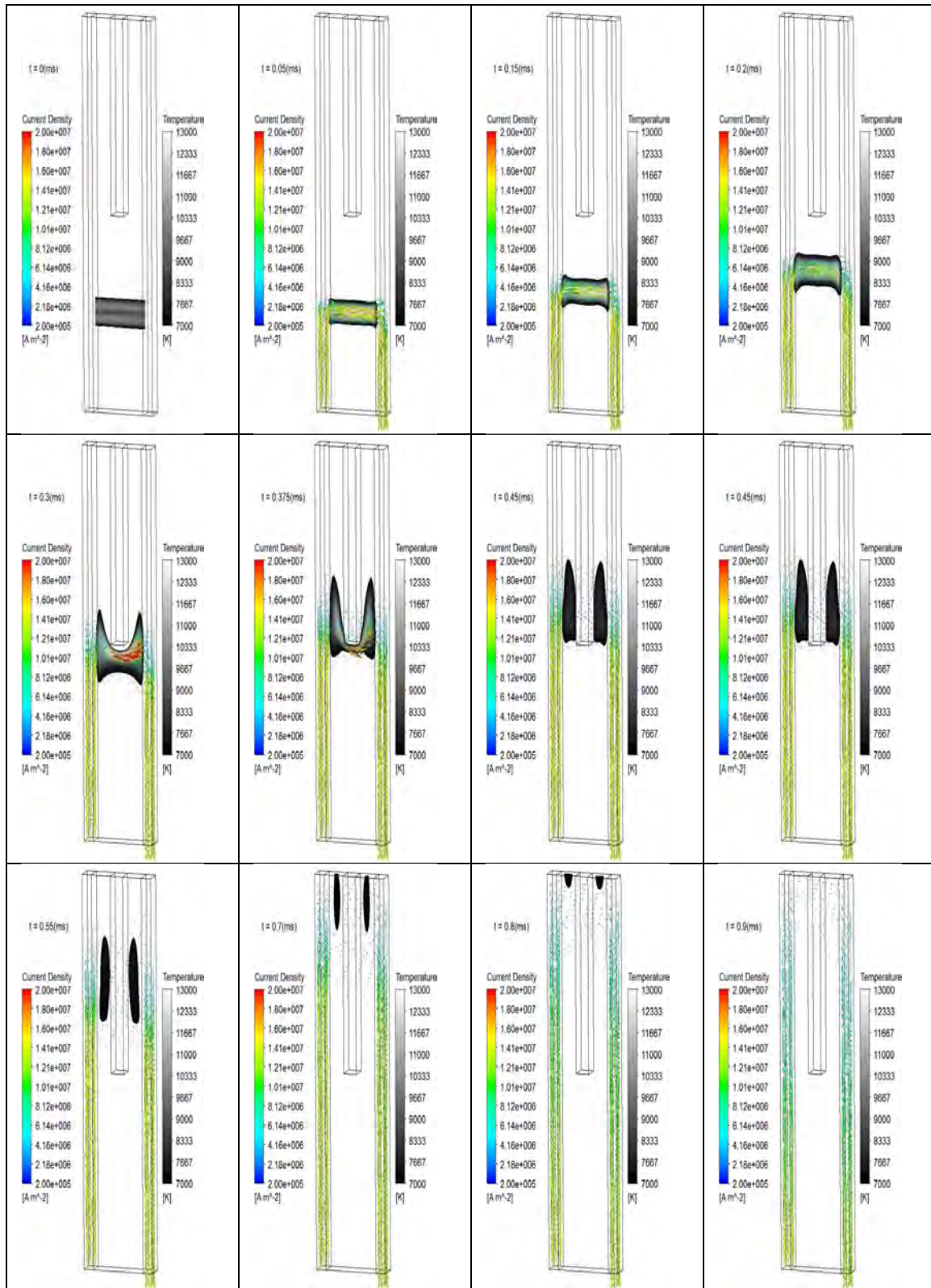


Figure A-39 Maximum current density in splitter plate for 50A base case, expansion volume, longer electrodes and lower wall up, cases D and A

Figure A-40 Arc movement expressed by temperature and current density for 50A input current, 1SP and constant Ohmic resistance, Case E.1
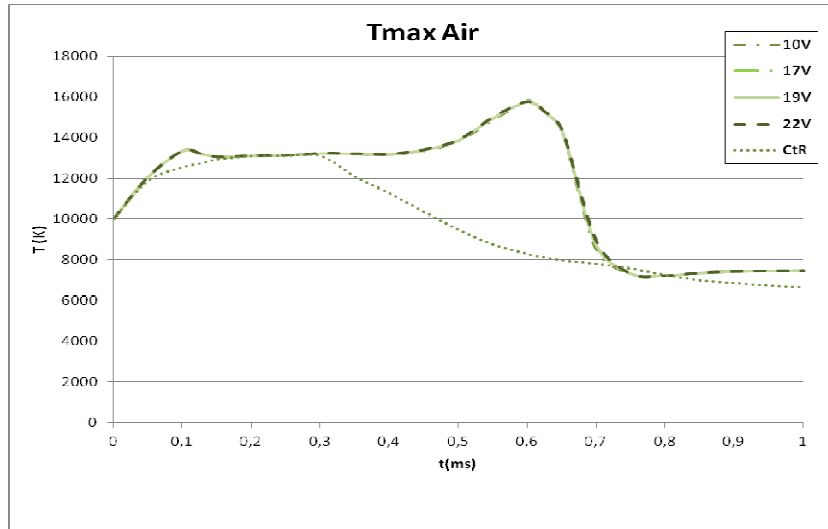
Figure A-41 Maximum temperature in air for 50A constant and variable Ohmic resistance, case E
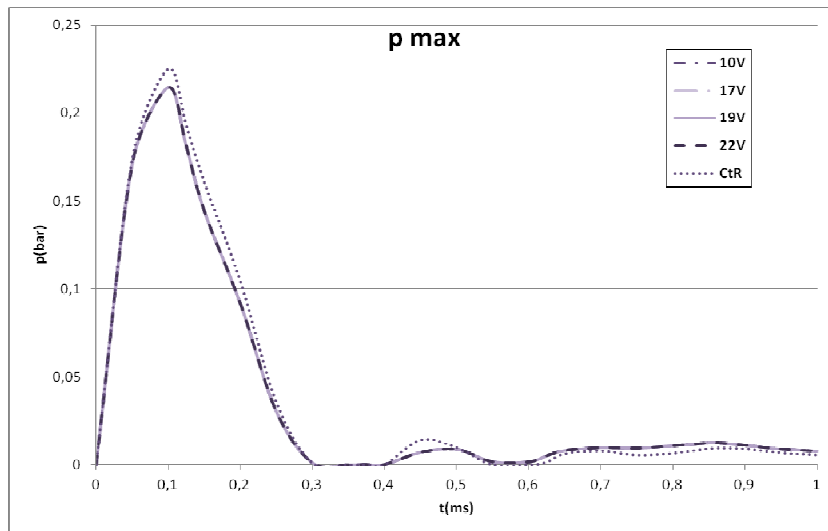


Figure A-42 Maximum pressure in air for 50A constant and variable Ohmic resistance, case E
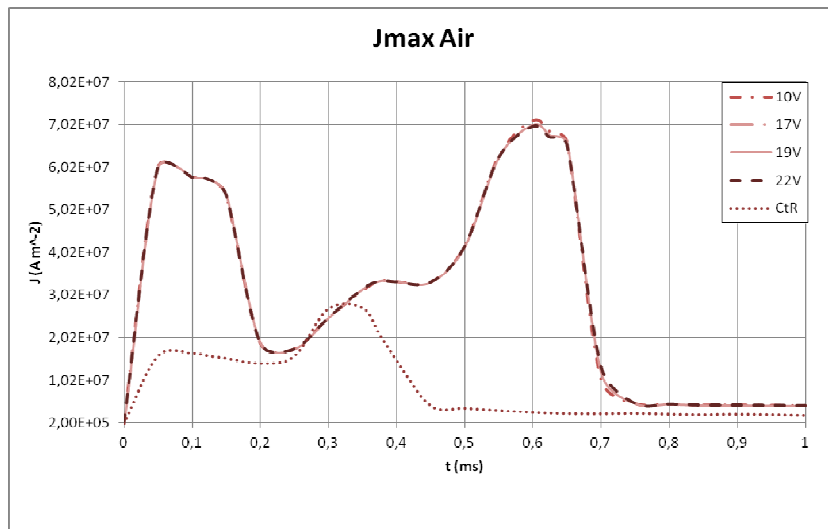


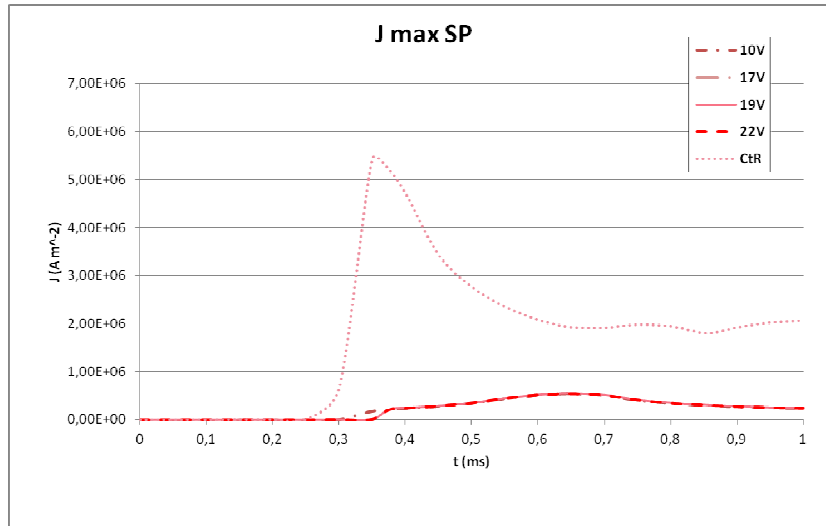Figure A-43 Maximum current density in air for 50A constant and variable Ohmic resistance, case E

Figure A-44 Maximum current density in splitter plate for 50A constant and variable Ohmic resistance, case E